RHODES UNIVERSITY

Where leaders learn

Constraining the role of carbonate assimilation on spinel stability in oxide ores of the Flatreef, Bushveld Complex, South Africa

By

Siyasanga Dyan (Ms)

Submitted in fulfilment of the requirements for the degree of:

Master of Science

at

Rhodes University

Department of Geology

October 2020

Declaration

I, Siyasanga Dyan, declare that the thesis titled "Constraining the role of carbonate assimilation on spinel stability in oxide ores of the Flatreef, Bushveld Complex, South Africa" is my unaided work. Information obtained from other sources is thoroughly acknowledged accordingly. This thesis is submitted for the fulfilment of the Master of Science at Rhodes University.

Signature

22/02/2021

Date

Acknowledgments

There are no words to express the amount of pleasure of having accomplished this thesis, and sincere gratitude goes to the endless guidance of my supervisors.

I am truly grateful for my principal supervisor, Prof. Steve Prevec, for his never-ending patience, guidance, and willingness to impart knowledge whenever I would show up in his office unannounced. I am honored by the number of hours he put in, providing careful revisions and thorough feedback amid a pandemic.

I extend my gratitude to my co-supervisor, Dr. Nicolas Tonnelier, for his recommendation for this thesis. I am most thankful for his advice, impromptu availability, and vast knowledge he provided for this study.

The support of the DSI-NRF Centre of Excellence for Integrated Mineral and Energy Resource Analysis (DSI-NRF CIMERA) towards this research is hereby acknowledged. Opinions expressed and conclusions arrived at are those of the author, and are not necessarily to be attributed to the CoE.

I am grateful to Ivanhoe Mines Ltd for facilitating access to their courtyard and providing samples for this study. I thank Danie Grobler and Albie Britz for imparting their knowledge and eagerness of the Flatreef.

I thank Rhodes University for access to the Electron Microprobe, special thanks to Dr. Deon van Niekerk for his assistance with the analyses and patience with specific requests I had. I am also thankful for the University of Johannesburg Analytical Facility (Spectrum) for granting me access to their Electron Microprobe to analyse the remainder of my samples and Dr. Christian Reinke for his assistance with the analyses.

I would like to extend my gratitude to Rhodes University EMU for their access to the Scanning Electron Microprobe and Marvin Randall for his assistance. I also thank Prof Steffen Büttner for his assistance with the EDS data acquisition and processing.

I am grateful to the Geology Department technical staff, Andrea King, and Thulani Royi for their help with sample preparations. I am grateful for Willie Deysel at the courtesy of Nelson Mandela University for his further assistance with thin section preparations.

To my family and friends, I am indebted for your constant support throughout this thesis. Many thanks to my supportive friends, Siyasanga Macholi, Hulisani Booi, Zilungile Buhlingu. And lastly, special thanks to Katlego Matlou for the support, motivation, and assistance throughout this project

Abstract

The northern limb of the Bushveld Complex shows significant evidence for footwall rock-magma interaction, as a result of the emplacement of magmas onto the Transvaal Supergroup sediments. The Platreef of the northern limb is known to have involved extensive contamination of the magma. The lateral extension of the Platreef, the Flatreef, is less contaminated and comprises PGE-mineralization and thick chromitite layers. This enables successful stratigraphic correlation to the Upper Critical Zone of the eastern and western limbs of the Bushveld Complex. This study aims at addressing the influence of dolomitic floor rock contamination on the formation of spinels of the Flatreef and how they may differ to their occurrences in the Bushveld Complex elsewhere.

Three main drill cores (UMT-345, UMT-335, and UMT-094) from the deep drilling program by Ivanhoe Mine, north of Turfspruit, were logged and sampled. The drill cores contained rocks contaminated by dolomite in varying degrees, depending on the proportion of carbonate xenoliths present. A total of sixty-two samples were obtained from the UG-2-equivalent chromitite seam, down into the hybrid contaminated units (Footwall Assimilation Zone; FAZ). Petrographic examination of the drill cores revealed that the feldspathic pyroxenite and chromitite layers are the most pristine lithologies in the Flatreef. The chromitite layers occur as a semi-massive to massive ores. The FAZ rocks are mainly dominated by the abundance of Al-rich Cr-spinels ($Mg\#_{30-80}$), clinopyroxenes with a high Ca-Tschermak component (up to 35 mol.%), olivines (Fo_{72-84}), and plagioclase (An_{31-78}).

Geochemical characteristics of the feldspathic pyroxenite and chromitite seams include low CaO/Al_2O_3 and Ca/SiO_2 ratios, the low abundance of REE and HFSE. In contrast, the FAZ samples display high CaO/Al_2O_3 and CaO/SiO_2 ratios, suggesting mobilization of CaO-rich fluids derived from the associated dolomite xenoliths. Observations from lithostratigraphic element profiles indicate spikes in CaO within FAZ units relative to the feldspathic pyroxene, indicating a secondary source of CaO linked to proximity to carbonate xenoliths intersected in the core.

The assimilation-fractional crystallization model performed with the Upper Critical Zone parental melt and dolomite produced assemblages dominated by spinel, olivine, clinopyroxene, and plagioclase, relating to those of the most contaminated rocks of footwall assimilation zones. The model also showed that large quantities of CO_2 were produced during assimilation. High amounts of CO_2-fluids mobilized in the melt would have

interacted with the melt and increased the overall oxidation conditions. Oxygen fugacity (fO_2) values were constrained from the spinels in the FAZ and chromites in chromitite seams. Spinels within the most contaminated rocks of the FAZ recorded relatively high fO_2 values ranging between NNO-0.2 and NNO+1.8 (relative to the Nickel-Nickel-Oxide buffer. High fO_2 values in spinels from the FAZ suggest that the melt interacted with greater amounts of oxidative CO_2-fluids during decarbonation reactions. Such high redox conditions could have triggered the saturation and crystallization of spinels.

Comparison of mineral compositions and fO_2 of UG-2 chromites from the Flatreef with UG-2 from the eastern limb, western limb, chromitites from the Platreef and Uitkomst Complex reveal that Flatreef chromites are of most similar to those of the Platreef Uitkosmt Complex. The northern limb and Uitkomst Complex chromites have high fO_2 values (NNO+0.3 to NNO+1.2), indicating their apparent link to the Malmani dolomite. Interaction of magma with the Malmani dolomite would have produced high quantities of CO_2, triggering an increase in oxidizing conditions. Such an effect is most prominent in the Flatreef chromitites that are in contact with the FAZ. The chromites are characterised by high fO_2 (NNO+1.2) and distinct compositions (low Cr_2O_3, high Fe^{3+}/Fe^{total}, and TiO_2). Thus, it is proposed that carbonate assimilation in the Flatreef triggered the precipitation of these distinctive chromites proximal to FAZ, due to liberation of substantial amounts of CO_2-rich fluids with a highly oxidative capacity. Carbonate assimilation in layered intrusions can be used as a monitor potential precipitation of chromites.

Table of contents

List of Figures

Chapter 1. : Introduction

1.1 Problem statement

The topic of the formation of chromitite ore deposits in mafic-ultramafic layered intrusions remains debated to date. This is mainly because chromitite ores are generated as multiple ~1 m thick massive to semi-massive layers generated by magmas that crystallize minor proportions of chromite from trace amounts of Cr (~0.15 wt.% Cr_2O_3 in the Bushveld Complex). Thus, a mechanism that would increase the chromite/silicate ratios in the magma to form thick chromitite layers remains poorly understood. Amongst many models proposed for the formation of chromitite layers is an increase in oxygen fugacity in the melt with relatively little or no change in the temperature (Ulmer, 1969; Murck and Campbell, 1986), and contamination of primitive magma by crustal material during ascent and emplacement of the magma ((Irvine, 1975; Kinnaird et al., 2002; Friedrich et al., 2019; Lesher et al., 2019)). Many oxide-mineralized layered intrusions are hosted on sedimentary floor rocks and show significant evidence for magma interaction with the floor rock material (e.g. Bushveld Complex, Uitkomst Complex, Panzhihua intrusion, and Jacurici Complex) (Harris and Chaumba, 2001; Harris et al., 2005; Ganino et al., 2008; Filho and Araujo, 2009; Maier et al., 2018; Friedrich et al., 2019).

Generally, assimilation of carbonate country rock material into mafic-ultramafic magmas may impact the melt in various ways, including shifts in the redox conditions, promote spinel saturation, and change mineral compositions. Previous work on carbonate-hosted layered mafic-ultramafic intrusions show that significant amounts of carbonate material (CO_2) liberated during assimilation elevated the overall oxidation environment of the magma, subsequently promoting early saturation of spinels (e.g. Cameron and Desborough, 1969; Pang et al., 2008; Ganino et al., 2008; Friedrich et al., 2019; Tanner et al., 2019). Ganino et al (2008) argue that large quantities of CO_2-rich volatile fluids interact with the host magma and increase the overall oxygen fugacity by about 1 log unit relative to the fayalite-magnetite-quartz buffer (FMQ). Such high oxidation conditions will potentially increase the overall Fe^{3+}/Fe^{2+} ratio of the magma, therefore, promoting the crystallization of Fe-Ti-type ore deposits. High oxidation conditions also play a major role in the precipitation of chromites by lowering the solubility of Cr in the magma.

1.2 Research aims and objectives

The main aim of this study is to test a previously largely unrecognized mechanism for the precipitation of chromite as being driven by carbonate assimilation. This mechanism is inspired by studies on magnetite spinels from the Panzhihua Intrusion (e.g., Ganino *et al.*, 2008), suggesting that carbonate wall-rock contamination in the melt can potentially trigger Fe-Ti-V-type deposits. This study will adapt the premise of their study to evaluate the influence of carbonate material on the stability of Cr-spinels of the Flatreef in the northern limb of the Bushveld Complex.

The main objectives of this studies are:

- ..Assess and quantitatively model local carbonate contaminations; in an attempt to determine the relationship between spinel abundance, texture, and compositions.
- ..Constrained redox state equilibria of Cr-spinels to determine the influence carbonate assimilation has on the stability of these oxides. This will help discern between genetic models relating to crustal contamination and numerous other genetic models e.g., variations in pressure, magma mixing.
- ..Correlate compositions and redox conditions of Cr-spinels from chromitite ores to those of the Bushveld Complex elsewhere and Uitkomst Complex to monitor the influence of extensive contamination on spinel formation.

One of the most fundamental implications this study will have is in exploration purposes. Examining the role of carbonate assimilation as a trigger for the formation of spinel may offer a guide to future exploration targets for Cr-Fe-Ti-V-PGE-type ore deposits. The exploration target would involve the identification of the association of carbonate floor rocks, carbonate xenoliths that have experienced high temperature reactions, and also an abundance of Ca-bearing phases.

Three main drill cores showing evidence for magma-dolomite interaction were examined and sampled from the Upper Critical Zone at the courtesy of the Ivanhoe deep drilling program. The three drill cores comprise varying degrees of contamination, from least contaminated to most contaminated based on the proportion of dolomite xenoliths observed.

Chapter 2. : Overview on carbonate assimilation

2.1 Context of carbonate assimilation as a driver of spinel stability

2.1.1 Role of carbonate as an oxidizing agent

The release of CO_2-rich fluids during carbonate assimilation has been proposed by various researchers as a mechanism to increase oxidation conditions of the surrounding melt (e.g. Cameron and Desborough, 1969; Ulmer, 1969; Wenzel *et al.*, 2002; Pang *et al.*, 2008). Wenzel *et al.* (2002) performed a series of calculation experiments, which proved that these CO_2-rich fluids are highly oxidizing, with oxygen fugacity conditions equal to that of the HM-buffer. Therefore, decarbonation reactions involving the release of CO_2 are sufficient to bring about increased oxidation that may result in the crystallization of spinels. How the stability of spinel is influenced by fluctuations in oxidation conditions will be explored more in depth in the sections below. The oxidation process can be represented through a simple reaction (1), in which cation accumulation of CO_2 will increase valence of Fe^{2+} ions to Fe^{3+} through bonding with oxygen upon donating an electron to stabilize C:

$$CO_2 + 2FeO \rightarrow Fe_2O_3 + C \quad \text{---------- (1)}$$

In contrast, the oxygen fugacity of the melt can be lowered by assimilating graphite (pure C), derived from carbonaceous shales. Such a case has been reported by Yudovskaya *et al.* (2013) to have taken place in the Lower Zone of the Platreef in the northern limb, which has led to the absence of chromite spinels. It has long been argued that consumption of C can drastically lower oxygen fugacity, such that the addition of about 100 ppm of C will reduce 0.13 ppm of Fe_2O_3 to FeO (Sato, 1978; Sato and Valenza, 1980). The added carbon will react with O^{2-} species to form a carbonate melt, thus causing the reduction of Fe_2O_3 to FeO species (reaction 2). However, this reaction can only transpire in the absence of H_2O in the melt or when the activity of water is low. This is because H_2O will plausibly react with carbon, and the release of H_2 gas will oxidize carbon to either CO or CO_2, which will induce the overall oxidation on the magma rather than reduction (Sato, 1978).

$$C + Fe_2O_3 + O^{2-}_{(melt)} \rightarrow 2FeO + CO^{2-}_{3(melt)} \quad \text{----------(2)}$$

2.1.2 Effect of oxidation on spinel stability

An increase in the O_2 content of a previously reduced magma will result in the oxidation of iron, oxidizing Fe^{2+} to Fe^{3+} (reaction 1). In the case where the magma is highly concentrated in Cr_2O_3, early saturation of chromian spinels will occur (Hill and Roeder, 1974). This results in the precipitation of chromite because Cr^{3+} in an oxidized magma has higher preference energy for the

octahedral site compared to other +3 cations (e.g. Fe^{3+}, Al^{3+}) (Hill and Roeder, 1974). In the case where the magma is depleted in the Cr_2O_3, such as in an evolved liquid, Cr-poor spinel should become more stable and precipitate as magnetite (De Waal, 1975).

Furthermore, experimental work conducted by Cameron and Desborough (1969); Ulmer (1969); and Snethlage and Gruenewaldt (1977) showed that increasing fO_2 in a $MgO\text{-}SiO_2\text{-}Cr_2O_3$ magmatic system will shift the liquid from the cotectic line into the chromite-only stability field. In turn, fractionation of chromite will lower the fO_2 conditions of the melt and will shift the residual liquid composition back to the cotectic. According to Hill and Roeder (1974), the composition of spinel precipitating in a melt can also be a function of the fO_2 and temperature. Basically, under conditions of high oxygen fugacity, Fe^{3+} will become highly insoluble. Fe^{3+} -rich chromite will tend to stabilize, provided the concentration of Cr in the melt is high enough, and if Cr-undersaturated, magnetite spinel (Ti-V-Fe oxide) will precipitate instead (Hill and Roeder, 1974).

2.1.3 Effect of oxidation on spinel composition

The composition and stability of spinel in a magmatic system correspond to the availability of spinel partitioning major elements, such as Cr^{3+}, Fe^{2+}, Fe^{3+}, Mg, and some minor V and Ti^{4+}. It has been reported that the stability field of chromite spinel, concerning both the position on the liquidus and equilibrium composition, is defined by the availability of Cr^{3+} in the melt, which in turn has major implications on the stability of V in spinel (Papike et al., 2015). Cr^{3+} is affected by dramatic shifts in the oxygen fugacity. For instance, the elevation of the oxygen fugacity from the IW-buffer to the QFM-buffer would increase the Cr^{3+}/Cr^{total} ratio in the melt (Barnes, 1986; Canil, 1999; Papike et al., 2015). Nevertheless, such an increase may have no significant effects on the Cr content chromite content. This can solely be attributed to the response of the spinel structure with changes in oxidation conditions.

Under low fO_2, spinel will be present as a normal spinel structure $\mathbf{AB_2O_4}$. This is composed of 16 octahedral sites (A) that are occupied by trivalent cations (Cr^{3+}, V^{3+}, Al) and 8 tetrahedral sites (B) occupied by divalent cations (Mg, and Fe^{2+}) (Deer et al., 1992; Papike et al., 2015). Spinel transitions to an inverse structure $\mathbf{B(AB)O_4}$ under elevated oxygen fugacity, allowing for the accommodation of $Fe^{3+}$and other highly charged cation species (V^{4+} and Ti^{4+}).

2.1.4 Proxies of oxygen barometers

The oxygen fugacity of the crystallizing magma can be constrained using various proposed oxygen barometers. These include Fe^{3+}/Fe^{total} ratios of basaltic magma or quenched glass (e.g. Kress and Carmichael, 1991), ratios of redox-sensitive/insensitive elements, such as V/Sc and V/Ga (e.g. Canil, 1999; Mallmann and O'Neill, 2009), partitioning of redox-sensitive elements (e.g. V) in

minerals during magma differentiation (e.g. Canil, 1999; Herd, 2006; Mallmann and O'Neill, 2009), as well the use of a mineral pair equilibria oxybarometer such as olivine-spinel pair (O'Neill and Wall, 1987; Ballhaus et al., 1991).

(i) Fe^{+3}/Fe^{+2} ratios

The most widely recognized and straightforward proxy for oxygen fugacity is the Fe^{3+}/Fe^{2+} or Fe^{3+}/Fe^{total} ratio (Kress and Carmichael, 1991). This proxy is based on the notion that Fe is the most redox-sensitive major element in magmatic systems. Changes in the redox state of Fe as a result of a shift in the oxidation state of the magma will drastically affect the compositions of Fe-bearing phases (Hill and Roeder, 1974). One of the problems associated with this oxybarometer is that it can only be applied to glasses. This is because Mg-bearing silicic magma tends to stabilize Fe^{2+} even under oxidizing conditions and Fe^{3+} under reducing conditions (Sato, 1978). This characteristic makes the use of the Fe^{3+}/Fe^{2+} ratio slightly inaccurate. In addition, the Fe^{2+}/Fe^{3+}ratio is highly affected by subsolidus and post-cumulus modifications, such as reaction with the liquid, metamorphism, alteration, etc. (Canil, 2002).

(ii) Cr/V ratio

A proxy that has recently been receiving quite a bit of attention is V partitioning in spinel and silicate minerals (Canil, 1999; Toplis and Corgne, 2002; Herd, 2006; Mallmann and O'Neill, 2009; Papike et al., 2013). This oxybarometer is based on the fact that V has a wide range of redox states (V^{2+}, V^{3+}, V^{4+}, V^{5+}), which makes it the most sensitive element to changes in the oxidation state of the magma. According to Mallmann and O'Neill (2009), assessment of the partition coefficient ($D_V^{crystal/melt}$) is one of the approaches taken to extract redox information on vanadium through experimental calibrations. Partitioning of V into a crystal structure is controlled by the availability of V^{3+} or V^{4+} in the melt and oxygen fugacity. For instance, an increase in oxygen fugacity of the melt will lower the proportions of V^{3+}, whereas that of V^{4+} will increase (Toplis and Corgne, 2002). Calibration of $D_V^{spinel/melt}$ (for both Al- and Cr-spinels) is only proven to work for conditions above QFM-5.7, which suggests that the most reduced state (V^{2+}) was not taken into consideration during calibrations (Mallmann and O'Neill, 2009).

The V partitioning proxy is mostly used in association with chromite spinels. This is due to the correlated behaviors of V^{3+} and Cr^{3+} in terms of the similar ionic radii and charges, and also their preference for the octahedral site in the normal spinel structure (Papike et al., 2013, 2015). Changes in the spinel structure with fluctuating fO_2 will also affect D_V. This means that V^{4+} will have higher preference energy for the octahedral site with increasing fO_2 (Canil, 1999). The fundamental advantage of using this oxybarometer is because of the immobile nature of vanadium, thus less sensitive to secondary modifications. The use of V alone as an oxybarometer does estimate shifts

in oxygen fugacity of spinel, however, it fails to give information about the magnitude of the shifts. This limits its usefulness as a solo proxy, as it needs to be used in conjunction with a mineral equilibria oxybarometer or a geothermometer.

(iii) V/Sc ratio

As mentioned earlier, V is one of the most redox-sensitive elements, whereas Sc is not, hence the V/Sc ratio can be applied to constrain oxygen fugacity. This proxy is based on the fact that V and Sc behave similarly during mantle melting, therefore their relative abundance and effect of fractional crystallization may be used as a sensor for redox conditions (Mallmann and O'Neill, 2009). However, the use of V/Sc as a proxy requires constraints on source mineralogy, the concentration of trace elements, and the degree of melting (Lee et al., 2005). Alongside Sc, V/Ga ratio can also be used to estimate the redox condition of a melt. Ga also behaves similarly to V and Sc during melting, and more advantageous to use than Sc because its partitioning is more similar to V than Sc (Canil, 1999). Both V and Ga are incompatible elements in silicate systems, but are very compatible in spinel.

(iv) Olivine-spinel compositional equilibria

An oxybarometer that is widely used and accepted is the olivine-spinel oxygen barometer proposed by Ballhaus et al. (1991). This approach has been calibrated using several experiments with olivine (Fo>85) + spinel + orthopyroxene on the liquidus under different temperatures, pressure, and the activity of water. The olivine-spinel barometer is often adopted to estimate fO_2 of a magma or mantle source conditions, as it is viable even when orthopyroxene is incorporated in the calculation or not. The olivine-spinel oxybarometer was initially calibrated to estimate partial melting conditions of the upper mantle, then later applied to magma differentiation processes (Ballhaus, 1993). However, calibrations of this method were carried out under high pressure and close to water-saturated conditions, such that it tends to overestimate fO_2 under low pressure and low water content by up to 1-1.5 log units (Fomin et al., 2013). Corrections to this model were recently devised by Nikolaev *et al.* (2016) for low pressure and low water content conditions.

2.1.5 Proposed geological environment for carbonate assimilation

Carbonate contamination has been recently been proposed (Zhou et al., 2005; Ganino et al., 2008; Xing et al., 2012) to be a trigger for spinel stability, in the Panzhihua intrusion in China. The reason behind this suggestion lies in the proximity of marbles of the Dengying Formation to the adjacent magmatic rock units, and their texture and compositions, which have been used to propose that they underwent partial melting. The low density and viscosity of both partial melts and CO_2-H_2O-rich fluids formed through decarbonation reactions enabled them to migrate into the magma chamber (Pecher et al., 2010). Moreover, as the fluids migrated upwards through the intrusions,

they dehydrated the magma, producing supercooled silicate phases and promoting early crystallization. The fluids further induced oxidation of the magma, thereby promoting the crystallization of magnetite ores. Elevated fO_2 was the prime reason behind the early crystallization and settling of Fe-Ti oxides in the Panzhihua intrusion. fO_2-temperature extrapolations performed by Pang *et al.* (2007) suggested that Fe-Ti oxides from the Panzhihua intrusions were above the QFM-buffer, by approximately 1.5 log units. These oxidation conditions are mildly elevated and are suitable to trigger precipitation of magnetites.

The effect of water on these melts was also proposed to have played a role in the stabilization of the Fe-Ti oxides (Xing et al., 2012; Howarth and Prevec, 2013). Xing *et al.* (2012) argue that H_2O is derived from fractionating minerals and country wall rock. H_2O in the magma will dissociate into O^{2-} and H^+ and then be released as H_2 gas (reaction 2). The release of H_2 gas will result in the overall oxidation of the melt, and this will induce early crystallization of Fe-rich oxides (Xing et al., 2012). Accumulation of large amounts of H_2O and CO_2 from the crystallization of magnetite induced early stabilization of anhydrous pyroxene and plagioclase, thus elevating the total H_2O in the melt. This suggests that fluids derived from the wall rock alone did not necessarily trigger early crystallization of magnetite.

The role played by CO_2 on a magmatic system has been studied in detail in the Ioko-Dovyren intrusion in Eastern Siberia by Wenzel et al. (2001, 2002). Their investigations focused on how mafic magma interacts and assimilates calcareous limestone, in particular the petrology and mineralogy of the xenoliths within mafic-ultramafic intrusion. They found that the entrained xenolith blocks are composed of dolomitic limestone skarns with dominant Al-diopside, and were incorporated during the emplacement of the intrusion. Rapid heating of the dolomite by mafic magma resulted in the decomposition of dolomite into calcite and periclase, thus releasing CO_2 fluids. This release of CO_2-rich fluids increased the overall oxygen fugacity of the magma (Wenzel et al., 2002). Close to dolomite xenoliths, the oxidized melt crystallized olivine and spinel.

2.2 Geological Overview

2.2.1 Overview of Bushveld mafic igneous rocks

The Bushveld Igneous Complex (BIC) is the largest known layered intrusion, emplaced around 2,540 Ma (Scoates and Friedman, 2008) into the Kaapvaal Craton in the north-eastern part of South Africa (Eales and Cawthorn, 1996). This intrusion extends for about 450 km east-west and 350 km north-south, covering an area of approximately 65 000 km^2 (Eales and Cawthorn, 1996). The BIC is composed of four distinctive igneous suites, namely, early mafic sills, Rooiberg felsites, Rustenburg Layered Suite (RLS), and the Lebowa Granite Suite (Sharpe, 1981; Button and Cawthorn, 2015). The mafic-ultramafic RLS is divided into five segments; the Eastern, Western,

southeastern (Bethal), Far western, and Northern Limbs (Figure 2-1) (Eales and Cawthorn, 1996). The Bethal Limb is covered by Karoo sedimentary rock and has been identified only employing gravity survey drill cores (Eales and Cawthorn, 1996), the Eastern and Western Limb are fairly symmetrical, while the Northern Limb forms a sinuous outcrop separated from other limbs by the Thabazimbi-Murchison Lineament (TML).

The mafic-ultramafic Rustenburg Layered Suite is further subdivided into five major zones from bottom to top based on the mineralogy of the rocks; namely the Marginal Zone, Lower Zone (LZ), Critical Zone (CZ), Main Zone (MZ), and the Upper Zone (UZ). Collectively these layers make up a stratigraphic thickness of ca. 7-9 km (Eales and Cawthorn, 1996). However, the thicknesses may vary from limb to limb. For instance, the stratigraphic units of the western and eastern limbs are thicker than the northern limb (3-5 km).

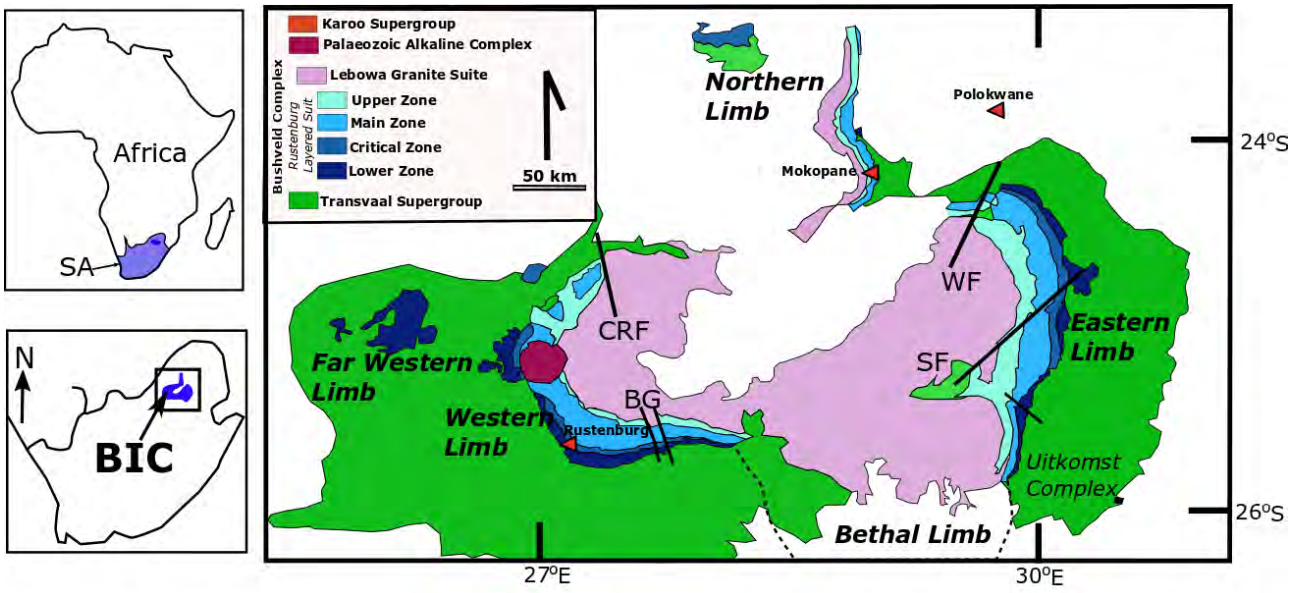

Figure 2-1: Geological map of the Bushveld Complex showing the five compartments; far western, western, eastern, northern, and Bethal limb; and the contemporaneous Uitkomst Complex. ***CRF*** *Crocodile River fault,* ***BG*** *Brits graben,* ***SF*** *Steelport fault,* ***WF*** *Wonderkop fault. Modified from* Barnes and Maier (2002)

2.2.2 Stratigraphic succession of the Bushveld Complex

The Marginal Zone is the most enigmatic of the zones, composed of about 800 m of heterogeneous medium-grained noritic rock units that form the basal contact of the complex. Contacts of the Marginal Zone with the Magaliesberg quartzite are covered by thick quartzite scree. The upper contact of this zone is ultramafic and rarely exposed. It has variably fine-medium-grained norite units that show poor layering. Grain-size variation and thickness of this unit may imply multiple magma injections (Cawthorn, 2015). Nevertheless, the evidence from depleted incompatible elements would suggest that it has partial cumulate characteristics. According to Eales and Cawthorn (1996), this zone cannot be used as a parental melt to the Lower Zone, as it may represent

multiple stages of magma injections. The marginal zone is characterized by pronounced evidence for contamination, from the Transvaal Supergroup quartzite and dolomite.

In the Clapham Section, in the north-eastern part of the Eastern Limb, Wilson (2015) discovered a Basal Ultramafic Succession (BUS) occurring below the Marginal Zone. The Bus is postulated to be compartmentalized into the Olifants River, Clapham, and Bugerstort compartments (Wilson, 2015; Scoon and Tiegler, 1993**).** The BUS is defined by basal quartzite floor rocks, in contact with a chilled zone, and with about 200 m thick harrisitic-textured layers above the chilled zone. Wilson (2015) interpreted these features to be representative of an early stage magma replenishment into the Bushveld Complex. Tanner et al (2019) correlated the BUS to the mineralized Volspruit Sulphide Zone in the northern limb.

The Lower Zone (LZ) is made up of basal orthopyroxenite, followed by an interlayered succession of harzburgite, dunite, and bronzite, approximately 1700 m thick (Eales and Cawthorn, 1996). Plagioclase is rarely found as a cumulus phase in this zone. It is best exposed and preserved in the Olifants River Trough, and this area is unique in that it is the only area where all the LZ units are well developed (Eales and Cawthorn, 1996). However, some of its sections are also well developed in the central sector of the eastern limb, western limb, far western limb, south of Mokopane (northern limb) (Hulbert and Von Gruenewaldt, 1985)**,** and it has also been reported to be present in the Platreef on the Turfspruit property in the northern limb as well (Yudovskaya et al., 2013). Van Der Merwe (1976) states that the lower zone is separated from the rest of the zones in that it is either intruded into or below the Transvaal sediments. South of Mokopane the LZ consists of about 1600 m of 37 cyclic units of chromite>harzburgite>pyroxenite (Hulbert and Von Gruenewaldt, 1985)**.** The units in this area differ from the LZ units from elsewhere in the BIC in that the orthopyroxene is highly enstatitic and olivine is highly fosteritic (Van Der Merwe, 1976)**,** and that the zone itself was in a trough-like depression of the Transvaal rocks and Archean granite (Yudovskaya et al., 2013)**.** The upper contact of the zone is poorly defined. Cameron (1978) defined the contact between this zone and the Lower Critical Zone based on the increase in modal abundance of interstitial plagioclase from 2 to 6 %, whereas Teigler and Eales (1996) recommended the contact to be just above the uppermost harzburgitic unit. Yudovskaya *et al.* (2013) reported varying amounts of interstitial plagioclase in different units within the LZ and lower CZ. Meaning that the amount of plagioclase present cannot be used as a reliable marker for the upper LZ boundary. This makes the uppermost harzburgitic unit a more reliable boundary marker for the upper LZ.

The Critical Zone is subdivided into the Lower Critical Zone (C_LZ) and the Upper Critical Zone (C_UZ) based on the presence of cumulus plagioclase. The C_LZ is 700 – 800 m thick, consisting of

predominantly orthopyroxenite (86 %) with chromitite layers (0.5 %) and rare olivine (11 %) layered units (Figure 2-2) (Eales and Cawthorn, 1996). Within this zone, there are nine major chromitite seams, divided into the Lower Group seams (LG 1 – 7) and Middle Group seams (MG 1 – 2) numbered from the base upwards. The LG 6 seam is the only reliably economic seam amongst these groups and one of the largest chromite reserves on Earth (Crowson, 2001). In the western part of the complex, there is an extensive gap between the LG and MG seams (MG 1 – 4), while LG and MG in the eastern part consist of short intervals (Charlier et al., 2015).

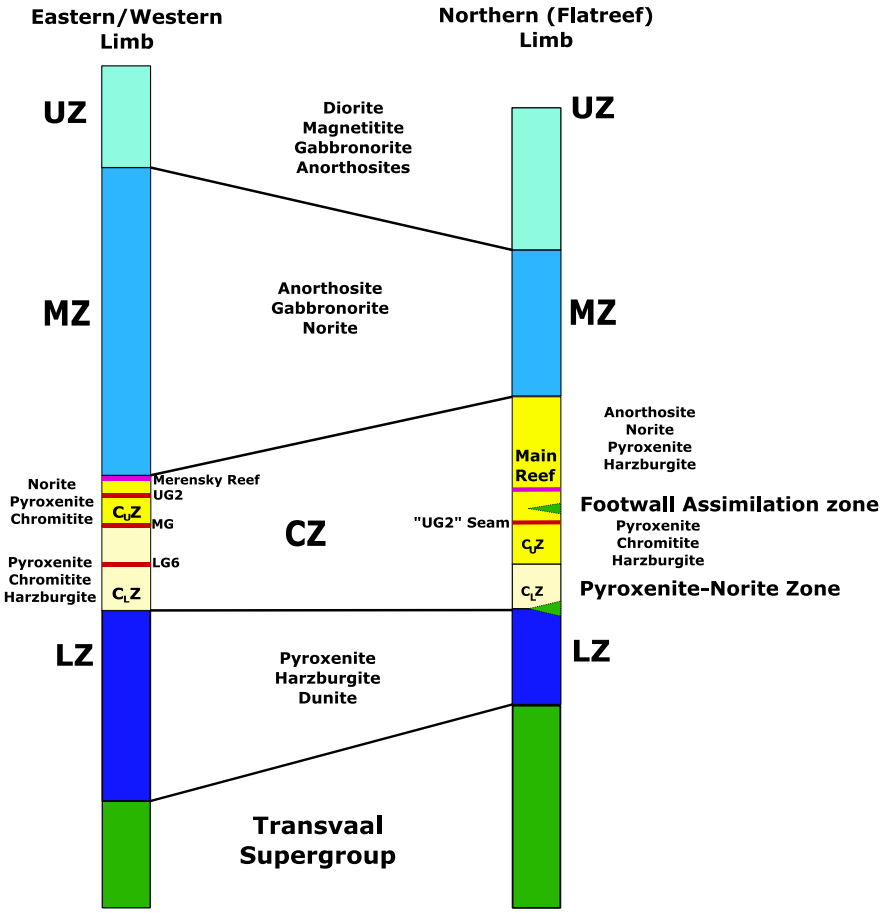

Figure 2-2: Stratigraphic succession of the Bushveld Complex comparing the eastern/western limb with the Northern Limb Flatreef geology. The eastern and western limb geology is adapted and modified from Eales and Cawthorn (1996)*, and the northern limb Flatreef stratigraphy is modified after* Grobler et al. (2018).

The Upper Critical Zone has a thickness of ~500 m, and comprises orthopyroxenite, norite, and anorthosite. In the Western and Eastern Limbs, the transition from the C_LZ to the C_UZ is defined by the appearance of basal cumulus plagioclase between the MG 2 and MG 3 seams (Eales and Cawthorn, 1996). Conversely, in the Northern Limb, the C_UZ rocks overlie harzburgitic rocks belonging to the LZ, indicating the absence of the C_LZ (Figure 2-2). The basal contact between the LZ and C_UZ is dominated by dolomite and quartzite xenoliths (Yudovskaya et al., 2011). A characteristic feature of the C_UZ is the presence of cyclic units with sequences of chromitite, harzburgite, pyroxenite, and anorthosite (Eales and Cawthorn, 1996). Each of these units

comprises an ultramafic rock with a sharp basal contact, overlain by progressively more feldspathic rocks (i.e. norite then anorthosite) (Eales and Cawthorn, 1996; Maier *et al.*, 2013). Within these units, the thickness varies between a few millimeters to tens of meters. There are four major chromitites seams in the C_UZ, including the MG (MG 3 – 4) and Upper Group (UG 1 – 2) seams, along with several minor seams and stringers.

The Main Zone (MZ) is a 2 – 3 km thick zone, composed of predominantly massive norites, gabbronorites, and anorthosites (Figure 2-2) (Eales and Cawthorn, 1996). The anorthosites are restricted to Subzone A and are subordinate in volume to the other rock types. The MZ is homogeneous, lacking the fine-scale layering and lithological diversity of the CZ. 300 m above the basal contact of the MZ, augite, and pigeonite sequentially become cumulus phases. According to Nex et al. (2002), orthopyroxene replaces pigeonite as a cumulus phase at about ~2000 m above the base. This reappearance of orthopyroxene marks the base of a prominent melanocratic layer termed the Pyroxenite Marker (Eales and Cawthorn, 1996).

The Upper Zone is an approximately 1 – 2 km (Figure 2-2) thick zone and has been subdivided into three subzones, namely Subzone A; B; and C. Subzone A is composed of magnetite, low-Ca pyroxene, and cumulus plagioclase. In Subzone B olivine has become an additional cumulus phase. Subzone C is defined by the appearance of cumulus apatite and the occurrence of country rock xenoliths (Maier et al., 2013). Cyclic units of magnetite, gabbronorite, and anorthosites are characteristic of Subzone A, and B. Subzone C is defined by the cyclic units of Fe-oxide with granular ilmenite that are overlain by ferrodiorites (Molyneux, 1970; Von Gruenewaldt, 1971). In the northern limb, the number of recorded magnetite layers is 16, whereas in the Eastern and Western Limbs up to 26 layers have been recorded. In the Eastern Limb, the fourth layer from the bottom is 1 – 2 m thick and is the known as the Main Magnetite Layer, from which about 50 % of the world's vanadium is produced (Crowson, 2001).

2.2.3 Geology of the northern limb

The Northern Limb crops out as a sinuous, north-west striking sequence with a length of 100 km and a maximum width of 15 km (Figure 2-3) (Van Der Merwe, 1976). This limb is separated from the rest of the complex by the Thabazimbi-Murchison Lineament (TML). The Ysterberg-Planknek and Zebedial faults (Figure 2-3) are expressions of the TML, and they tend to compartmentalize the Northern Limb. The emplacement style of the Northern Limb differs from that of the Eastern and Western Limbs. The latter two limbs overlie the Magaliesberg quartzites, while the Northern Limb is regionally transgressive (Grobler et al., 2018). For instance, the southernmost sector of the Northern Limb is emplaced into the Transvaal sediments and transgresses until it overlies Archean basement towards the north. As with the emplacement relationships, the geological

sequences also vary from north to south. The Transvaal Supergroup comprises the Chuniespoort and Pretoria Groups (Button, 1975). The Chuniespoort Group in the Northern Limb is composed of Black Reef quartzites, Malmani dolomite, and Penge Banded Iron Formation, while the Pretoria Group comprises the Duitschland and Timeball Hill shales, and the Magaliesberg quartzites (Button, 1975).

The Flatreef is described as a sub-horizontal succession characterized by major changes in geology with a remarkably rich and extensive PGE mineralization layer (ca. 19 m) with world-class deposits (Yudovskaya et al., 2017). This reef was discovered by Ivanhoe Mines, through their deep drilling program in 2007 on the Turfspruit farm, as a result of which the geologists noted that at a depth of 600 m, the Platreef temporarily flattens out for about 1-2 km (Grobler et al., 2018). The topmost package of the Flatreef occurring at the basal contact of the Main Zone is composed of anorthosites-norite-pyroxenite cycles (Figure 2-3). The underlying layer to these cycles is termed the Middling unit, comprising a group of the latter cycles and a feldspathic pyroxenite. Yudovskaya et al. (2017) grouped medium-grained pyroxenite, poikilitic harzburgite, and pegmatoidal pyroxenite into the Main Reef (Figure 2-3.)

The Footwall to the Main Reef is termed the footwall cyclic unit. This unit is composed of alternating pyroxenite-norite-anorthosite cyclic units (Figure 2-3). The unit is characterized by the appearance of chromite stringers and disseminated BMS (base-metal sulphides), with abundant sedimentary xenoliths of the Transvaal Supergroup. It has been noted that this zone contains abundant magma-sedimentary interactions (e.g. Grobler et al., 2018), such that assimilation zones have been described as abundant. Lithologies noted for this unit are norites with shale-hornfels xenoliths and parapyroxenites/paraharzburgite. The latter rocks are characterized as a mixture of partially undigested dolomitic rocks, pyroxenite igneous rocks, and serpentinites at Sandsloot Mine (Harris and Chaumba, 2001). They are also characterized by abundant diopside-clinopyroxenites enriched in metamorphic olivine (McDonald et al., 2005).

A thick, laterally extensive pyroxenite unit occurs below the Footwall Cyclic Unit. It is mostly characterized by the presence of a ~1 m massive chromite seam. The footwall to this unit is a pegmatoidal pyroxenite/harzburgite. The succession within this unit and the chromitite seam has been correlated to that of the UG-2 of the western and eastern limbs based on the mineralogy present and its stratigraphic location below the PGE-mineralised Merensky Reef (Figure 2-2) (Grobler et al., 2018). The unit is underlain by a pyroxenite-norite zone, composed of pyroxenites and norites with intercalated hornfels xenoliths. The lithological package within this zone is correlated to that of the C_LZ of the rest of the Bushveld Complex. The transition from the Flatreef to the Lower Zone comprises interlayered hornfels (up to 300 m thick), fine-grained norites, and

feldspathic pyroxenite. The Lower Zone is made up of about 800 m thick cyclic units of dunite, harzburgite, and pyroxenite (Figure 2-2) (Yudovskaya et al., 2013; Grobler et al., 2018).

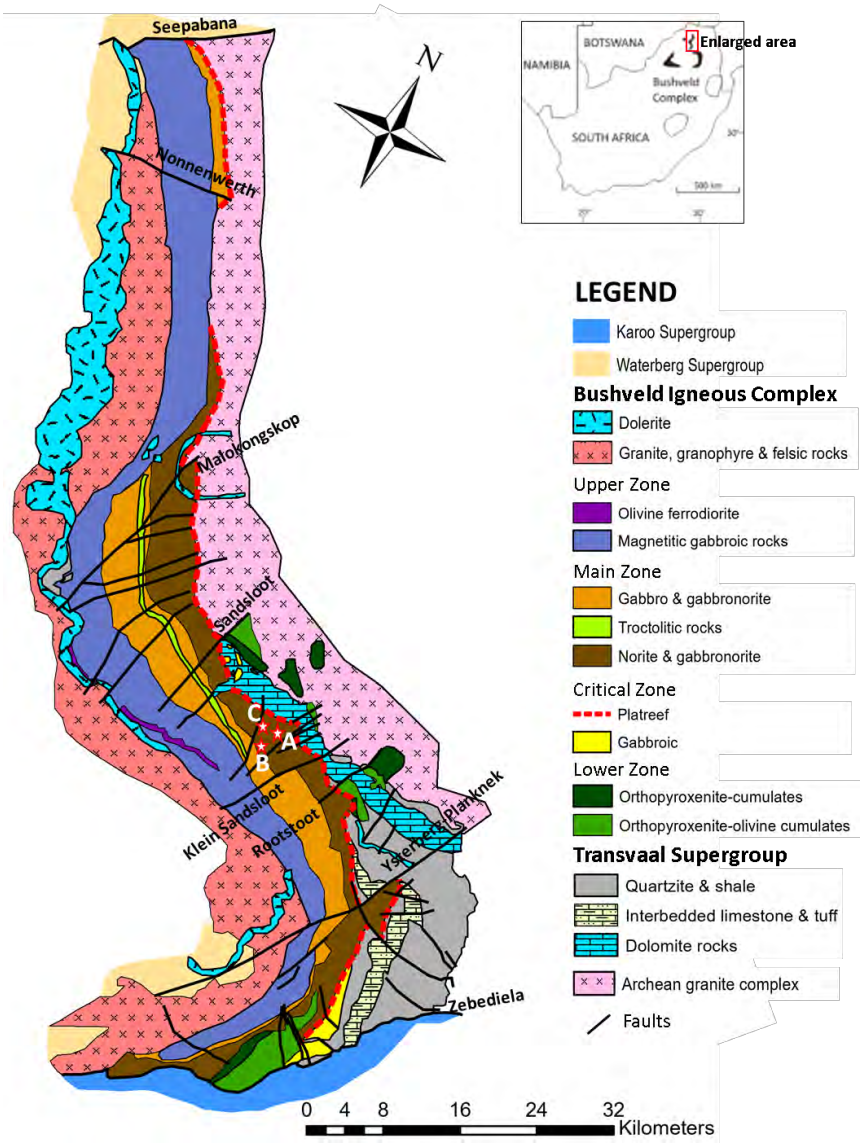

*Figure 2-3: Geological map of the northern limb of the Bushveld Complex showing locations of the analyzed boreholes on the Turfspruit Farm: **A** represents UMT-094 and **B** is UMT-345, and **C** is UMT-335 Geological map is modified after Kruger (2005), and the location of the boreholes from Grobler et al. (2018).*

2.2.4 Overview of Upper Critical Zone chromite mineralization models

(i) Crustal contamination

In the early 1970s, Irvine proposed that granitic crustal contamination could serve as a trigger for chromite precipitation to account for stratiform chromitite reefs in layered intrusions including the Muskox, Bushveld, Stillwater, and Great Dyke occurrences (Irvine, 1975). He argued that the addition of granitic material to a primitive melt (Figure 2-4), perhaps derived from the roof of the magma chamber, will shift the bulk composition of the contaminated liquid off the olivine-chromite cotectic and towards the SiO_2 apex into the chromite-only stability field (Figure 2-4). Pure chromite will, thus, crystallize, subsequently driving the residual liquid bulk composition

away from the chromite compositional apex until the liquid returned to the cotectic curve (Irvine, 1975). He later rejected the effectiveness of this idea, by postulating that geologically improbable amounts of granitic melts would be required to induce the changes in crystallization (Irvine, 1977), replacing this model with an elegant magma mixing model based on the same phase relationship principles (see below). However, there is independent evidence for granitic contamination of Bushveld rocks, including elevated REE concentrations and Ce/Sm ratios (consistent with crustal-like LREE-enrichment), and Sr, O, and Nd isotopic compositions consistent with significant crustal involvement (Maier et al. n.d.; Harris and Chaumba, 2001). Many believe that crustal contamination may have occurred during emplacement into the upper crust at the current level (e.g. Scoon and Tiegler, 1994). Some believe that contamination could have occurred during the ascent of the Bushveld magma through Kaapvaal crust (Harris and Chaumba, 2001). And others believe contamination could have occurred in a deeper staging chamber (e.g. Eales and Costin, 2012). All of these mechanisms would be consistent with similarly uncontaminated, non-crustal Sr isotopic signatures observed below (FW) and above (HW) a massive chromitite layer, within which crustal contributions are recorded.

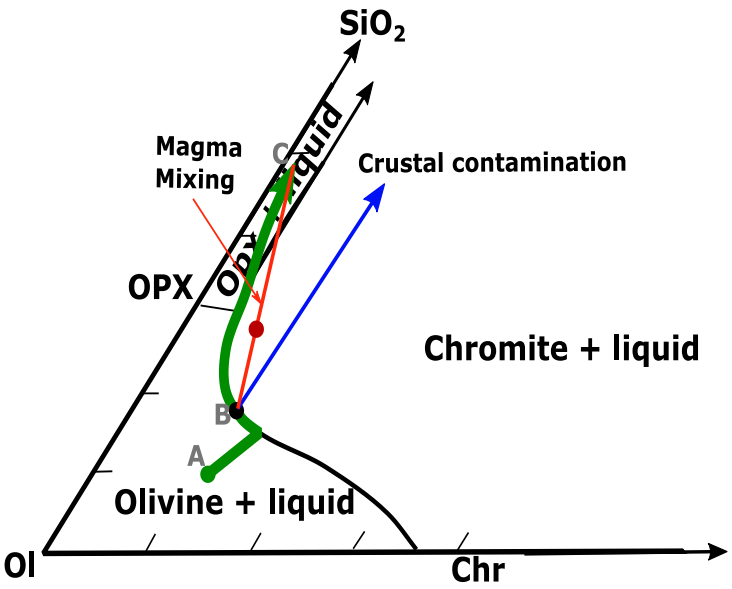

Figure 2-4: Phase diagram showing chromite stability as a result of granitic contamination and magma mixing. Modified from Irvine (1975, 1977). *Point **A** to **B** represents sole olivine to olivine-spinel cotectic fractionation path of an uncontaminated melt, the addition of SiO_2 from granitic material will drag the path towards the SiO_2 apex into the sole chromite stability field (blue line), fractionation of the magma will move the bulk composition of the melt to the orthopyroxene field. The red line represents the mixing of a slightly evolved orthopyroxene-dominated magma and a primitive magma produces a hybrid liquid (red dot) that is in the chromite stability field similar to Figure 2-5.*

(ii) Magma mixing

The magma mixing model was proposed by Irvine (1977) as an alternative to his granitic crustal contamination model. This model argues for chromite crystallizing in a magma chamber through mixing of compositionally dissimilar magmas, either crystallizing a chromite-only layer *in situ* in

the same manner as in Figure 2-4 (Irvine, 1977), or forming by magma mixing elsewhere in the chamber and then settling by the influence of gravity forming a massive chromitite layer (e.g., Scoon and Tiegler, 1994; Kinnaird et al., 2012). Figure 2-5 shows a mixing curve of a primitive chromium-saturated magma (point A) that mixes with an evolved chromium-saturated (point B), and forms a hybrid melt that is over-or supersaturated with chromium (point X) (Irvine, 1977; Murck and Campbell, 1986). It is important to note that chromite will only crystallize once the melt composition is in the field of chromite-only stability (chromite plus coexisting liquid). In both the contamination and magma mixing models, chromite occurs as the sole liquidus phase in the hybridized magma, thus allowing the formation of, ideally in situ, thicker, and thinner chromitite layers as a result of magma replenishment. The advantage of the magma mixing model is that it avoids the phase stability problems envisioned by Irvine (1977) introduced by granitic crustal contamination, and it removes the need for an external contribution to the magma to induce chromite precipitation.

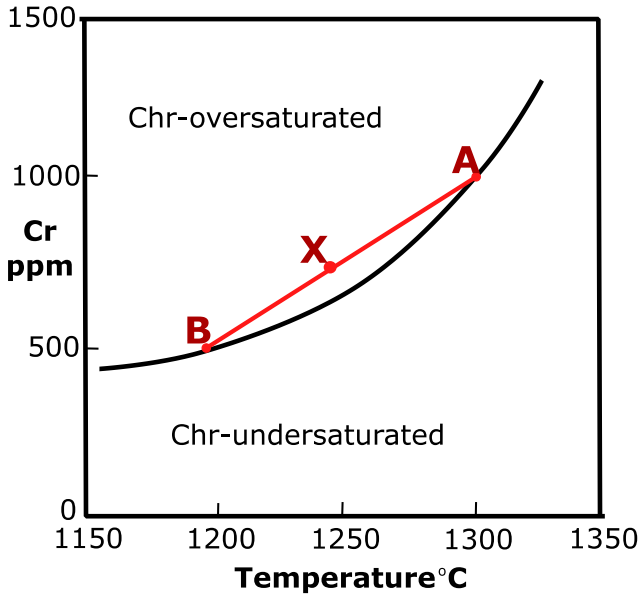

Figure 2-5: Representation of a typical magma mixing model, where a Cr-saturated primitive melt A mixes with a Cr-saturated melt B to produce a hybrid melt X that is Cr-oversaturated. Adapted from Murck and Campbell (1986).

(iii) Ephemeral pressure changes

A model based on ephemeral changes in pressure was previously postulated by Cameron (1977) for the formation of Bushveld chromitites and later developed in detail by Lipin (1993) based on the Stillwater Complex chromitites. This model envisages that temporal changes in pressure as a result of nucleation of CO_2 bubbles will induce a shift in the cotectic boundary of chromite within a magma chamber (Lipin, 1993). This model has the attraction of more easily explaining the vast lateral extents of many massive chromitite layers as a consequence of the instantaneous effect and transmission of pressure throughout the entire magma chamber (Mondal and Mathez, 2007).

However, Mondal and Mathez (2007) comment that this model fails to account for the lack of sensitivity on phase boundary and Cr-stability a result of changing pressure.

(iv) Pressure decrease during magma ascent

Latypov et al. (2018) have recently proposed that massive chromitites originate from the saturation of chromite induced during the early stages of magmatic processes. They suggest that a deep-seated magma in equilibrium with enstatite ± chromite will become oversaturated in chromite during ascent, as a result of a depressurization. As the magma ascends to shallower crustal settings, the plagioclase stability field will expand at the expense of enstatite, promoting chromite stability (Latypov et al., 2018). This notion is based on experimental data and thermodynamic modeling. Massive chromitites hosted in orthopyroxene in layered intrusions can be explained by the crystallization of only chromite as an early phase, forming layers such as the LG 6 in the Bushveld Complex.

(v) Magma hydration

The magma hydration model was proposed by Nicholson and Mathez (1991) for the Merensky Reef. This model envisages that the reef formed from the reaction of a hydrous melt with a partially molten pyroxenite hanging wall and norite footwall, as presented in Figure 2-5. Vapour (H_2O-CO_2-rich) exsolved from a crystallizing interstitial liquid will migrate upwards until it encounters a fluid-unsaturated crystal mush. The dissolution of the fluid into the melt component of the mush will result in sulphide saturation and eventually induce partial melting by liquidus depression of the fluxed melt (Boudreau, 2016). Consequently, orthopyroxene and plagioclase will be resorbed, and the increasing Cr content in the melt chromite will crystallize (Nicholson and Mathez, 1991; Mondal and Kinzler, 2017; Boudreau 1999, 2019). This mechanism would produce the observed reef sequential units: norite – anorthosite – chromitite – then the pegmatoidal feldspathic pyroxenite (Nicholson and Mathez, 1991). However, the perceived problem with this model is that it would require unrealistically large amounts of the underlying host rock to be scavenged, or unrealistic concentrations of Cr in those rocks, to account for the observed volumes of Cr in the Critical Zone (Mondal and Mathez, 2007).

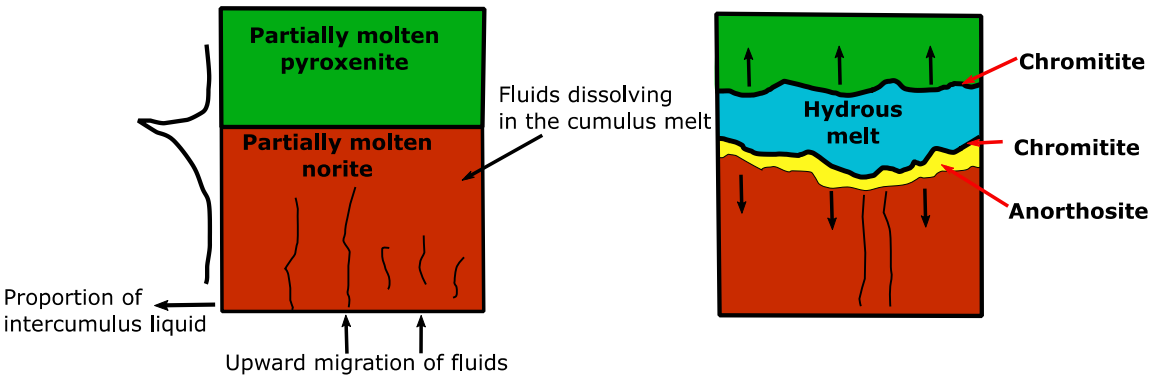

Figure 2-6: Diagram representing hydration of the melt for the formation of the Merensky Reef. The figure on the left shows upward migration of fluids in a partially molten norite with the aid of fractures. The figure on the right shows a fluid-saturated zone, with chromite forming at the hydration from with anorthosites in the footwall and pyroxenite forming in the hanging wall. After Nicholson and Mathez (1991).

(vi) Injection of a chromite-saturated magma

A Cr-saturated slurry model was proposed by Eales (2002) in an attempt to explain the imbalance in Cr between the Lower Zone and Critical Zone in the Bushveld Complex. Calculations by Eales (2002) showed that the Critical Zone (Cr_2O_3 ~ 1.4 wt.%) required a magma with a Cr_2O_3 content of 0.15 wt.% with a thickness of 15 km, which is almost double the thickness of the ultramafic-mafic sequence. This mass balance problem is thought to be overcome by elevation of Cr content of the initial magma (Naldrett et al., 2012) or by high volumes of magma, which would later be removed from the chamber (Kruger, 2005). Naldrett et al. (2012) proposed that the injected magma was already saturated with Cr, and upon emplacement, massive chromitites will be produced through gravitational settling.

Mondal and Mathez (2007) found that the Cr content in the hangingwall and footwall to the UG-2 chromitite in the Bushveld Complex has similar compositions. Thus, proposed that the UG-2 chromitite was formed by injection of a chromite slurry with suspended orthopyroxene and chromite crystals, followed by mechanical sorting and then the accumulation of chromite on the magma chamber floor. The recent work of Latypov et al. (2017) invokes a similar mechanism for massive chromitites. They argue that a chromite-saturated magma added during magma replenishment would account for the mass balance enigma most models fail to explain. In addition, this model also attempts to explain the different geochemical signatures of chromitites from those of silicates above and below the chromitite layers (Latypov et al., 2017).

2.2.5 Carbonate contamination in the Bushveld

2.2.5.1 Uitkomst Complex

The BIC-related Uitkomst Complex was emplaced into the dolomitic footwall, as was the BIC Northern Limb (Gauert et al., 1995). It has been established to be of the same age as the Bushveld Complex (Maier et al., 2018). De Waal *et al.* (2001) interpreted the parental melt to be similar to

that of the B1 magma of the Bushveld Complex. This complex is interpreted to be a conduit that feeds into an eroded or unexposed layered intrusion (Gauert et al., 1995). The complex intrudes the Transvaal Supergroup sedimentary rocks including Malmani dolomite, sulfidic shale, and chert, as well as the Timeball Hill shale (Gauert et al., 1995). Hulley (2005) observed evidence of contamination through the presence of reaction rims within the xenoliths in contact with magmatic units. This signifies the migration of fluids from the neighboring dolomite into the magma conduit.

The assimilation of carbonate material in the Uitkomst Complex has been associated with the prevalence of diopside over olivine (Steenkamp, 2012)**.** This is associated with the overall increase in CaO in the magma, thus crystallizing Ca-rich minerals, including Ca-amphibole and diopside. Maier et al (2018) pointed out that the carbonate material that was assimilated upon emplacement probably played a major role in the formation of mineralization in the Uitkomst Complex, generating Ni-Cu-PGE-Cr-V-type ore deposits. PGE-mineralization is proposed to have been a consequence of a lowered S saturation as oxidation conditions increased with mobilization of volatile fluids (Gauert, 2001; Hulley, 2005). Similarly, the precipitation of primary magnetite was induced by high oxygen fugacity (Gauert, 2001).

2.2.5.2 Platreef

According to Pronost *et al.* (2008) the Platreef was affected by fluid-rock interaction to a much greater degree than the rest of the Bushveld Complex. Their conclusions are based on their investigations on $\delta^{18}O$ isotopes. They found elevated values of $\delta^{18}O$ in the dolomite country rock, of up to 24‰ (e.g. Harris and Chaumba, 2001), proximal to magmatic units. However, the analysis of entrained xenoliths and calc-silicates exhibits lower values, which is consistent with the dissolution of CO_2-rich fluids from the dolomite into the melt. High $\delta^{18}O$ isotopic compositions in the Platreef analyzed by Harris and Chaumba (2001) also suggest evidence for carbonate contamination. The assimilation of the dolomite played a vital role in the origin and mineralization of BMS and oxides (Gain and Mostert, 1982; Tanner et al., 2019). The existence of BMS in the pyroxenite and metacarbonate parapyroxenite is further assumed to be evidence for transportation of BMS during fluid migration (Pronost et al., 2008). De Waal (1975) argues that dissolution of CO_2 and H_2O from country footwall could have increased the fO_2 conditions of the melt, thus creating an environment capable of precipitating oxides and lower the S-saturation. Tanner et al. (2019) also argue that emplacement of the magma into a dolomitic footwall caused chromite saturation upon increased fO_2, followed by sulphide precipitation.

In the Sandsloot area, carbonate contamination has been associated with an increase in the abundance of the olivine and clinopyroxene closer to the dolomitic footwall (Appiah-nimoh, 2004). Both olivine and clinopyroxene are attributed to an overall increase in CaO in the melt.

Appiah-nimoh (2004) further argues that orthopyroxene was converted to diopside and augite, such that the Fe and Mg content stabilized olivine. These olivines have a lower forsteritic content due to crystallizing from an Fe-rich residual liquid at relatively lower temperatures. The widespread distribution of water is also linked to dolomitic contamination, such that it enhances a high abundance of serpentine and calcic-amphibole (Buchanan and Nolan, 1979; Buchanan et al., 1981).

Additionally, the effects of contamination have been reported in the Flatreef. This is attributed to the circumstances of how the Flatreef was emplaced, directly into the dolomites, shales, and iron-stone bearing rock units. The melt was reduced upon assimilation of organic carbon from the underlying shale units, which resulted in the suppression of chromite crystallization (Yudovskaya et al., 2013; Grobler et al., 2018). Potholing observed within the magmatic units has been associated with the interaction of the sedimentary footwall with the magma upon emplacement (Grobler et al., 2018). Devolatization of the dolomite released CO_2 into the surrounding melt, thus lowering the viscosity of the melt, and thereby enhancing hydrodynamic erosion of the footwall cumulates (Grobler et al., 2018).

Chapter 3. : Methods

3.1 Sampling

3.1.1 Sampling strategy

Samples were obtained from three different drill cores (UMT-345, UMT-094, and UMT - 335), provided by Ivanhoe Mines Ltd. in Mokopane, South Africa. The drill cores were obtained from the deep Flatreef extension, which is an extension of the Platreef. UMT-345 and UMT-094 were drilled along the same transect, about 400 m apart, while UMT-335 was drilled along a transacting that is 1 km apart from the two. The drill cores that were sampled had varying amounts of contamination, from extensively contaminated (UMT-094), medium contamination (UMT-335) and least contaminated (UMT-345). Core-logging of the drill cores took place in the core yard before sampling. Samples were collected at intervals of 20 m, from the upper Platreef just below the main chromitite (UG-2 lookalike) up to the footwall cyclic unit (lower Platreef) to retain the uniformity of the samples.

Sampled drill cores were near-vertical (see figure 1c in Grobler *et al.*, 2018) with varying lengths. UMT-094 was sampled between 1331.4 and 1423.2 m with a total of 22 samples. UMT-335 was sampled between 1715.5 and 1765.4 m with a total of 23 samples obtained while UMT-345 was sampled between 1517.8 and 1595.3 m with a total of 16 samples obtained.

3.1.2 Sample preparation

Once the samples were all collected, they were transported to the Geology Department at Rhodes University for further processing. A total of 62 sections were cut into blocks to make thin sections. Forty of those blocks were sent to the sample preparation laboratory to prepare thin sections at Rhodes University. The remaining 22 samples were sent to Nelson Mandela University to optimise the available time. All the thin sections were polished for petrographic description under reflected light as well as for SEM and EPMA analysis.

For the crushing stage, the samples were cleaned and dried before crushing to avoid possible contamination by extraneous dust and dirt. Since the samples were quarter core blocks, instead of using a crusher, they were wrapped in clean sample bags and hammered into smaller chips suitable to be milled. Each sample was placed into a manganese-steel vessel and milled for four minutes using a Herzog swing mill machine. After milling each sample, the mill was thoroughly cleaned by wiping and brushing, and then by crushing quartzite (silica) chips, to remove any remainder of the sample and minimize further contamination, after which the vessel was cleaned and dried using acetone and compressed air.

The strategy used for crushing each sample was to group similar lithologies together and crush them in continuous sessions. Once each sample was crushed, it was bottled and labelled. The packaging was done in Styrofoam to prevent damaging to the bottles, and they were ready for shipping.

3.2 Sample analysis

3.2.1 Electron Microprobe Analysis

(i) Rhodes University JEOL JXA-8230

Quantitative mineral chemical analyses of magnetite, chromite, and Ca-rich pyroxene were obtained by using four wavelength dispersive spectrometers on a JEOL JXA-8230 electron probe micro-analyser at Rhodes University. The beam was generated by a Tungsten cathode, and excited with 15 kV accelerating potential at 20 nA current. Beam sizes between 1-10 μm were used depending on the beam sensitivity of the material. Elements were measured on K-alpha peaks except for Sr and Ba on Lα. Overlap of Ti-Kβ on V-Kα, and V- Kβ on Cr-Kα was corrected for. Counting times were 10s on peak and 10s total on background for all elements, except in spinels for Ti, V, Fe, Cr, and in pyroxene for Ca. Ti, V, and Fe were counted for 60s on peak and 60s on background; Cr was counted for 30s on peak and 30s on background. Calcium was counted 60s on peak and 60s on background. Commercial "SPI" standards were used for intensity calibration, and are shown in Table 1. The data was collected with JEOL software (PC EPMA 1.9.2.0) and its ZAF matrix algorithm (Heinrich/Duncumb-Reed with FFAST-2005 MACs) was applied to correct for differential matrix effects. Oxygen was calculated by stoichiometry. Samples were polished down to 20-micron abrasive before analyses, and vacuum carbon-coated to 25 nm (+/-5) thickness.

(ii) University of Johannesburg Cameca SX-100

Quantitative analysis of a few samples was also performed using a CAMECA SX-100 microprobe for Chromites, magnetites, pyroxenes, plagioclase and olivine at the courtesy of University of Johannesburg SPECTRAU Labs. The silicates were analysed using an accelerating voltage of 20 kV, a beam current of 20 nA, and a counting time of 20s on peak and 10s on background. These settings were only applied for plagioclase and pyroxene. For olivine, these settings were changed to lower the detection limit of Ca, since it was of interest. The accelerating voltage was 20 kV and beam current was 40 nA. Counting for all other elements was 20s on peak and 40s on background, whereas Ca was counted for longer, at 60s on peak and 30s on background. These settings lowered the detection limit of Ca from 500 ppm with the former settings, down to 30 ppm. The detection limit was reasonable and lower than the average concentration of Ca in olivine of 400 ppm. For oxides, an acceleration voltage of 20 kV, a beam current of 40 nA and counting time of 16s on peak and 8s on background was used, except for Ti, V and Cr. Ti and V were counted for 50s on peak and 25s on background, while Cr was counted for 20s on peak and 10s on background.

Table 1:

Mineral	*JEOL JXA-8230 Standards*	*CAMECA SX-100*
Olivine	Pyrope (Mg, Si, Fe, Ca), Hematite (Fe), Nickel metal (Ni), Manganese metal (Mn)	Diospide (Mg, Si, Ca), Hematite (Fe), Manganese oxide (Mn), Nickel metal (Ni)
Pyroxene	Pyrope (Mg, Si, Fe, Ca), Hematite (Fe), Nickel metal (Ni), Manganese metal (Mn), Albite (Na)	Diospide (Mg, Si, Ca), Hematite (Fe), Manganese oxide (Mn), Nickel metal (Ni), Almandine (Al)
Plagioclase	Plagioclase (Ca, Al), Pyrope (Ca, Fe), Chromite (Al), Kaersutite (Al), Albite (Na), Orthoclase (K)	Diopside (Ca, Si), Phlogopite (K), Albite (Na), Almandine (Al)
Spinel	Chromite (Al, Cr), hematite (Fe), Pyrope (Mg), Vanadium metal (V), Rutile (Ti)	Chromite (Cr, Fe), Hematite (Fe), Vanadium metal (V), Manganese metal (Mn), Ilmenite (Ti)

Some of the accessory minerals were identified using the energy-dispersive spectrometers on the scanning electron microprobe (SEM) at Rhodes University EMU. Back-scattered-electron (BSE) images were obtained on both the EPMA and SEM instruments.

3.2.2 Whole-rock geochemistry

A total of 61 powdered samples were weighed to 5 g each and were shipped to the Ministry of Northern Development and Mines (MNDM) Geoscience Laboratory (GeoLabs) in Sudbury, Canada. Major elements were analysed by an X-Ray fluorescence (XRF) spectrometer for TiO_2, CaO, Fe_2O_3, MnO, K_2O, Al_2O_3, Cr_2O_3, P_2O_5, SiO_2, MgO and Na_2O. Duplicate analysis was done on 6 random samples to ensure the reproducibility and precision of the data. The duplicate samples have a precision between 0 and 3% for most oxides, except for K_2O (13%). Reference material used to assess the quality of the data includes inhouse reference material (OKUM-1) certified reference material (UB-N, Orca-1, BHVO-2, AGV-2 and GSP-2). Two reference material and their standard deviations are shown in Table 2.

Table 2: Comparison of the OKUM-1 and UB-N reference material used to assess the quality of the XRF data.

	OKUM-1 (INHOUSE RM)			**UB-N (CRM)**		
	Average from all runs	working values	std deviation	Average from all runs	working values	std deviation
Al_2O_3	8.00	*8.00*	*0.00*	*3.00*	*3.00*	*0.00*
CaO	7.90	*7.90*	*0.10*	*1.20*	*1.20*	*0.10*
Cr_2O_3	0.40	*0.30*	*0.00*	*0.30*	*0.30*	*0.10*
Fe_2O_3	12.00	*12.00*	*0.00*	*8.00*	*8.00*	*0.00*
K_2O	0.00	*0.00*	*0.00*	*0.00*	*0.00*	*0.00*
MgO	21.30	*21.00*	*0.00*	*36.00*	*35.00*	*1.00*
MnO	0.20	*0.20*	*0.00*	*0.10*	*0.10*	*0.00*
Na_2O	1.00	*1.00*	*0.00*	*0.00*	*0.00*	*0.00*
P_2O_5	0.00	*0.00*	*0.00*	*0.00*	*0.00*	*0.00*
SiO_2	44.00	*44.00*	*0.00*	*40.00*	*39.00*	*1.00*
TiO_2	0.40	*0.40*	*0.00*	*0.10*	*0.10*	*0.10*

3.2.3 ICP-MS (digestion) analysis

The 61 samples were also analysed for trace elements analysis using Inductively Coupled Plasma Mass Spectrometry (ICP-MS) method at MNDM labs. The samples were prepared using a closed vessel multiple-acid digestion method for analysis with the ICP-MS. The ICP-MS method analysed concentrations of large ion lithophile, high field strength, and rare earth elements. Full details on the accuracy, precision and detection limits of the method code (IMC-100) used for ICP-MS are presented by Burnham (2008). Duplicate analyses were performed on 6 random samples across the three drill cores. The precision of the data falls within 15%. Most data agree within 10% of the CRM (certified reference materials), excluding Cr and V that deviate by about 13 and 11%, respectively.

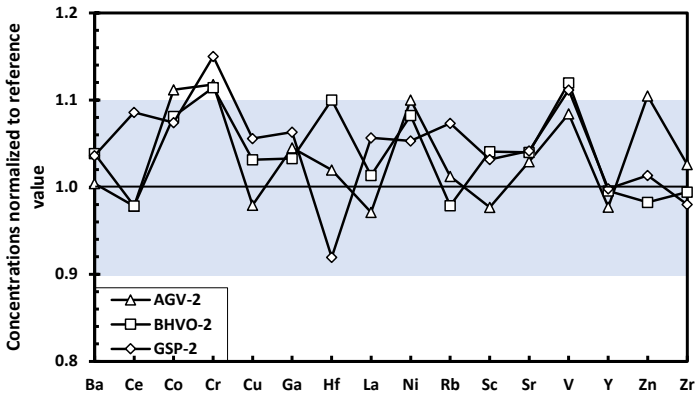

Figure 3-1:Comparison of a crm standards used for ICP-MS on a few selected elements.

3.3 Oxygen fugacity calculations

Oxygen fugacity was constrained using vanadium partitioning calibrations from Mallmann and O'Neill (2009), using the equation:

$$D_{\Sigma V}^{crystal/melt} = \frac{\begin{array}{l}(D_{V^{2+}}^{c/m} \times (K'_{\hom(6a)})^{-1} \times (f_{O2})^{-3/4}) + \\ (D_{V^{3+}}^{c/m} \times (K'_{\hom(6b)})^{-1} \times (f_{O2})^{-1/2}) + \\ (D_{V^{4+}}^{c/m} \times (K'_{\hom(6c)})^{-1} \times (f_{O2})^{-1/4}) + D_{V^{5+}}^{c/m}\end{array}}{\begin{array}{l}((K'_{\hom(6a)})^{-1} \times (f_{O2})^{-3/4}) + \\ ((K'_{\hom(6b)})^{-1} \times (f_{O2})^{-1/2}) + \\ ((K'_{\hom(6c)})^{-1} \times (f_{O2})^{-1/4}) + 1\end{array}}$$

Where $D_{\Sigma V}^{crystal/melt}$ is the partitioning coefficient of the total V oxidation states in the crystal; $K'_{\hom}$ represents the equilibrium constants of +2, +3+and +4 vanadium redox states; and the partition coefficient of each redox state is represented by $D_{V^{2+}}^{c/m}, D_{V^{3+}}^{c/m}, D_{V^{4+}}^{c/m}$ and $D_{V^{5+}}^{c/m}$. The values to these parameters are listed in Table 6 in Mallmann and O'Neill (2009). The equation was then rearranged to obtain the unknown fO_2.

Chapter 4. : Results

4.1 Lithostratigraphy and petrography of the Flatreef

A total of three drill cores (UMT-345, UMT-335 and UMT-094) were selected for logging, based on the proportion of dolomitic xenoliths and the degree of contamination present on the sections. The samples from the Ivanhoe Mines were obtained from the Turfspruit farm. Predominant magmatic lithologies encountered in these cores include the feldspathic pyroxenite, olivine gabbronorite and chromitite. The logged sections are described from the bottom to the top. The top of each core comprises the hangingwall feldspathic pyroxenite to the 'UG-2' chromitite.

The logged cores exhibit varying amounts of contamination, from least to most contaminated, as estimated by the volume of xenoliths present in the cores. The most prevalent rock type in all drill cores is feldspathic pyroxenite, followed by variably contaminated rock types. The latter units are mostly referred to as para-pyroxenite or para-harzburgite, depending on the degree of serpentinization of olivine. However, in this study, the term para-harzburgite is disregarded, to distinguish different types of lithologies arising from the degree of contamination. Specifically, plagioclase+olivine-rich and clinopyroxene-poor rocks are designated as troctolite, olivine+clinopyroxene-rich ± plagioclase rocks are wehrlites, and the clinopyroxene+plagioclase-rich and olivine-poor rocks are designated as parapyroxenites.

4.1.1 Core Logs

(a) UMT-345 (least contaminated)

The logged section of the drill core is 80 m thick and contains predominantly feldspathic pyroxenite (Figure 4-1). The base of the drill core comprises a 43 m thick feldspathic pyroxenite, from a depth of 1597 m to 1554 m. It comprises cumulus orthopyroxene, oikocrystic clinopyroxene grains, interstitial plagioclase and minor disseminated sulphides (Figure 4-2a). The olivine-bearing gabbronorite unit is defined by a gradational contact with the underlying feldspathic pyroxenite (Figure 4-2b). The unit is mostly made up of coarse-grained orthopyroxene, clinopyroxene and olivine with interstitial plagioclase. Thus, the unit consists of disseminated sulphide and chromite mineralization, which increases in proportion towards the top contact of the unit. The upper contact is marked by a sharp transition into a calc-silicate xenolith at a depth of 1531 m. This xenolith has a mottled texture, is banded in places, and is fine-to medium-grained although it may locally be pegmatoidal (Figure 4-2c-d).

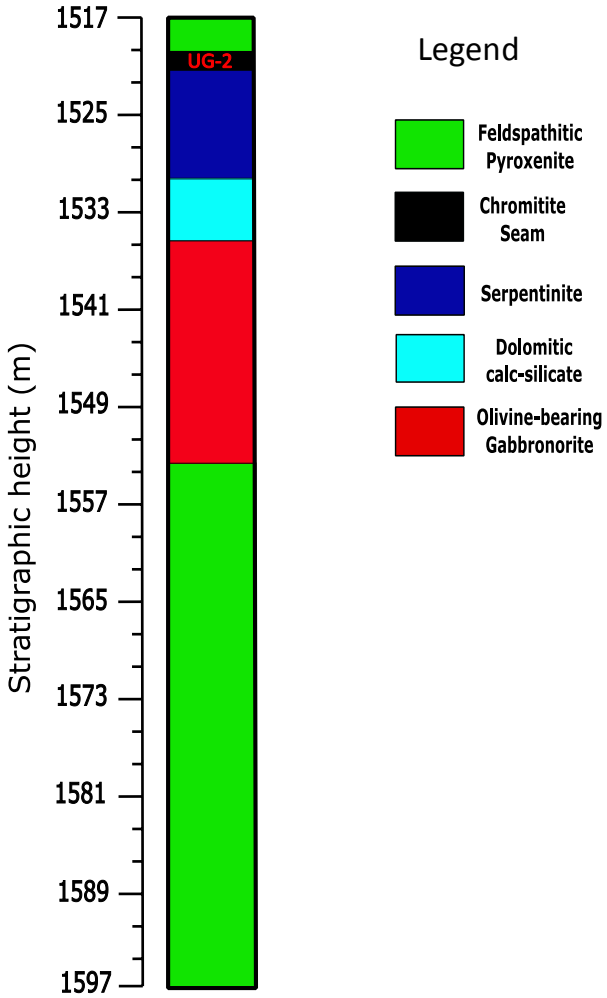

Figure 4-1: Lithostratigraphic section logged from UMT-345

The calc-silicate is truncated by an intensely serpentinized rock that is mineralized with disseminated sulphide and chromites. This section of UMT-345 has the thickest recorded unit of serpentinite unit (5.1 m) of all logged drill cores. The unit exhibits a black colour and comprises coarse grains of anhedral serpentine pseudomorphs after olivine and partly preserved green-coloured grains of clinopyroxene. In places, this unit contains higher proportions of plagioclase-rich zones with a pegmatoidal texture.

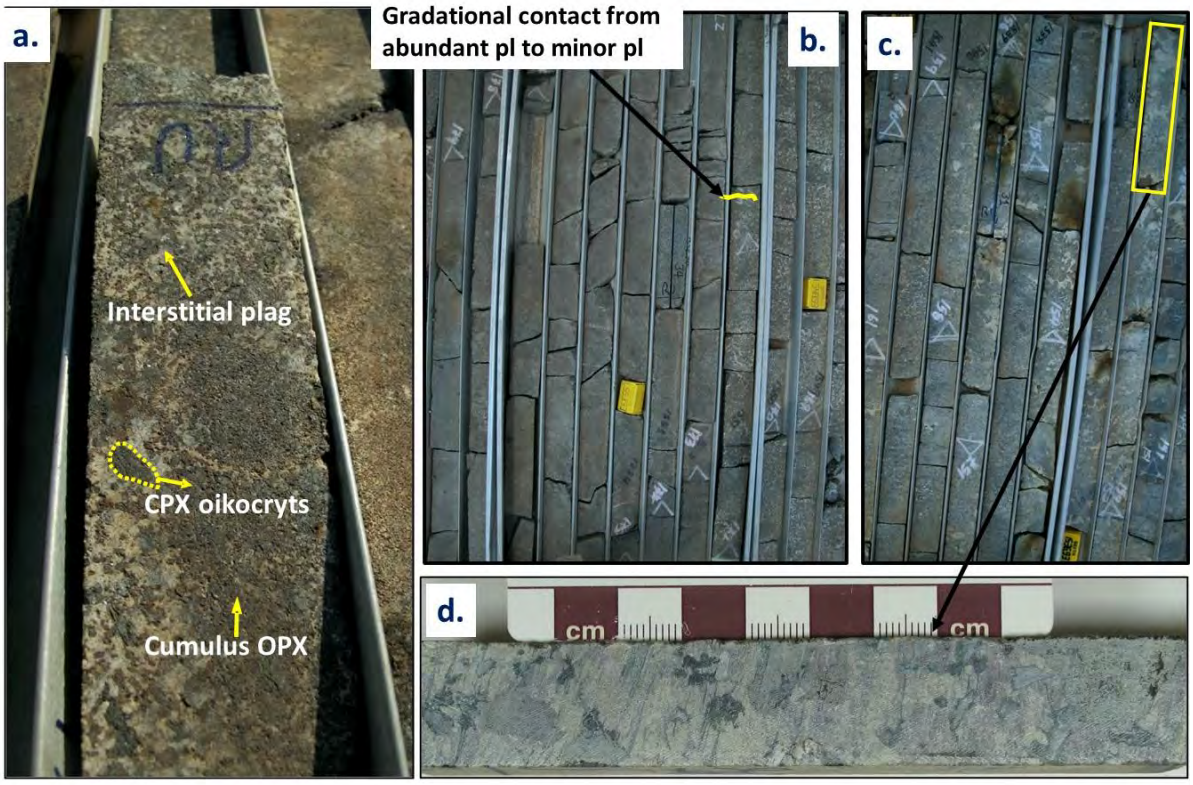

*Figure 4-2: Images from UMT-345 showing **A** feldspathic pyroxenite with cumulus orthopyroxene, clinopyroxene oikocrysts, interstitial plagioclase and disseminated sulphides. **B** a gradational contact between feldspathic pyroxenite and olivine gabbronorite. **C** a metamorphosed dolomitic xenolith into a calc-silicate skarn. **D** a close up of the sampled calc-silicate showing intense alteration of clinopyroxene and olivine.*

The economically important unit in this section comprises a thick, heavily disseminated chromitite belonging to the UG-2 chromitite, from a depth of 1532.9 m to a depth of 1519 m. The chromitite comprises chromite distributed as densely disseminated zones, horizontal seams, and stringers, with minor interstitial orthopyroxene, clinopyroxene and plagioclase. A sharp and linear contact marks the boundary to the hangingwall feldspathic pyroxenite. The grains in the hanging wall are medium-grained and coarsen upwards with increasing proportions of plagioclase.

(b) UMT-335 (moderately contaminated)

Drill core UMT-335 is a moderately contaminated core, comprising uncontaminated sections of feldspathic pyroxenite with chromitite seams and contaminated units made up of wehrlites and para-pyroxenites (Figure 4-3). Sedimentary xenoliths include dolomitic calc-silicates and hornfels.

Drill core UMT-345 is defined by a medium-grained pyroxenite devoid of plagioclase at the base of the drill core between 1769 m and 1763.2 m. Moving upwards, there is a gradational increase in feldspathic content resulting in a pegmatoidal unit with disseminated sulphides (Figure 4-4b). This transitions into a coarse-grained parapyroxenite unit with a green colour to about 1761 m. Above this, there is a sharp contact into the calc-silicate unit, defined by abundant carbonate phases and green pyroxene (diopside), also with abundant sulphides. There is a sharp contact above this

unit into an olivine-rich rock, which is 13 m thick. A 3 cm thick disseminated chromite zone is observed at 1752 and 1554.7 m. These layers are defined as large-grained (2-3 cm) clinopyroxene oikocrysts and highly fractured olivine and are mostly plagioclase-poor. However, at a depth of 1752.3 m, there is abundant milky-white plagioclase interstitial to olivine and clinopyroxene (Figure 4-4d). At a depth of 1747.6 m, this unit has abundant disseminated chromitites.

A 1 m thick calc-silicate xenolith occurs just above the olivine-bearing rock, at 1745.5 m (Figure 4-4c). The xenolith comprises a coarse-grained and pegmatoidal dolomite, with a milky-white altered interstitial plagioclase with granoblastic (3 cm) clinopyroxene crystals and disseminated sulphide. A parapyroxenite unit, at a depth of 1743.4 m, is marked by the occurrence of green clinopyroxene grains in a matrix of altered plagioclase and disseminated sulphide phases. Moving upwards, between 1743.6 and 1739 m, there is a pegmatoidal zone of parapyroxenite with varying proportions of plagioclase. The top contact grades transitionally into a calc-silicate unit with plagioclase, carbonates, and clinopyroxene grains.

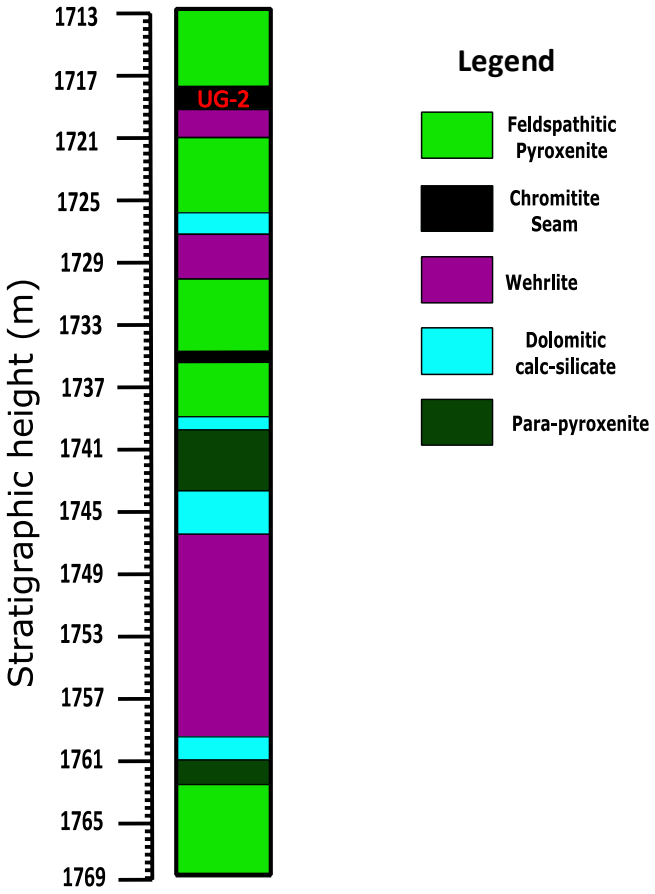

Figure 4-3: Lithostratigraphic section logged from drill core UMT-335.

From the calc-silicate, there is a sharp contact with the hangingwall feldspathic pyroxenite at 1739 m. The feldspathic pyroxenite is characterized by sulphide and chromite stringers, orthopyroxene laths, clinopyroxene oikocrysts, and interstitial plagioclase. This layer continues up

to a depth of 1731.9 m. There is a 0.6 m thick chromite layer at a depth of 1734.1 m, marked by a gradational bottom contact and a sharp upper contact with the feldspathic pyroxenite unit. There is a rather sharp contact at 1731.9 m with a serpentinized wehrlite that is pegmatoidal in places. This unit is defined by pegmatoidal zones that overprint clinopyroxene crystals that are 2-3 cm in size and disseminated sulphides and chromites. The wehrlite grades into an overlaying calc-silicate unit that has abundant clinopyroxene and minor carbonates.

At a depth of 1725.5 m, there is a feldspathic pyroxenite unit that is defined by a rather sharp contact. It comprises fine-grained pyroxenite with minor proportions of plagioclase and oikocrystic clinopyroxene grains. At a depth of 1721.8 m, there is a parapyroxenite unit with high proportions of plagioclase and clinopyroxene. This unit is marked by gradational contact into the 'UG-2' chromitite, which contains a series of chromitite stringers of 2-5 cm thick with heavily disseminated chromites in between (Figure 4-4a). The top contact to the 'UG-2' is defined by a sharp contact into the UG-2 hanging wall of feldspathic pyroxenite.

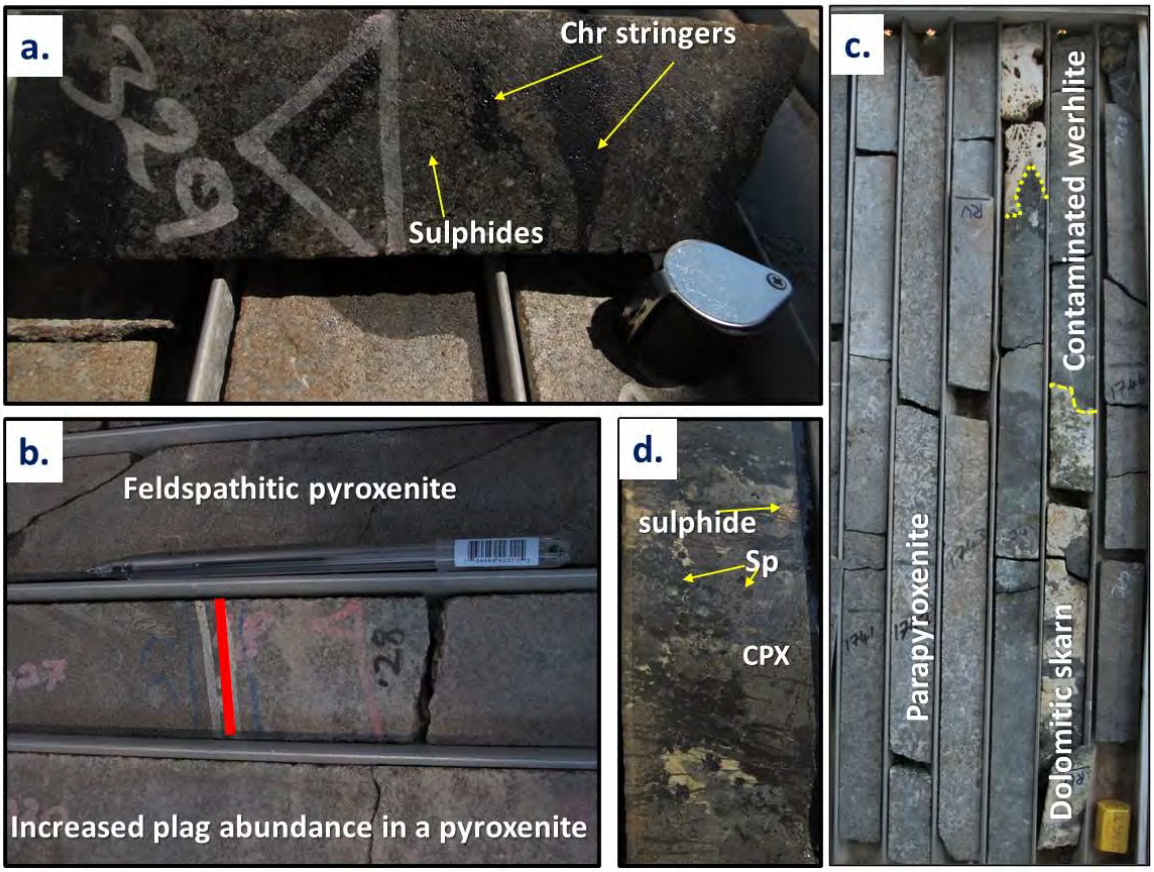

*Figure 4-4: **A**. UG-2 chromitite showing chromite stringers and associated sulphides, **B**. a sharp transition between a plagioclase-rich and plagioclase-poor pyroxenite. **C.** metamorphosed dolomitic xenolith showing sharp but irregular contact with wehrlite units and the overlying parapyroxenite unit. **D** large clinopyroxene oikocrysts are associated with anhedral olivine grains and minor interstitial plagioclase (white portion) and disseminated spinel and sulphide grains.*

(c) UMT-094 (most contaminated)

The logged section of UMT-094 is 94 m thick (Figure 4-5). Most of this drill core is made up of contaminated wehrlitic units, with serpentinized olivine, plagioclase, clinopyroxene, and spinels. The base of this drill core is made up of dolomitic calc-silicates (Figure 4-6e). In as much as the dolomite has been metamorphosed, it still retains primary layering, which has been preserved as highly contaminated layers. The dolomitic xenolith close to the magmatic layer is highly altered and has haloes of sulphides and spinels. At a depth of 1408.3 m to 45 m there is a sharp magmatic contact thick serpentinized wehrlite unit. The base of this unit contains coarse-grained clinopyroxene, serpentinized olivine, disseminated sulphides, and spinels, and it is devoid of plagioclase. The grains decrease in size upwards up to a depth of 1391.2 m, locally containing pegmatoidal zones. From the depth of 1385.5 m, there is a gradational increase in interstitial plagioclase and clinopyroxene grain-size (Figure 4-6a). At 1385.9 m there is a plagioclase-olivine pegmatoid with abundant disseminated spinel and sulphides. Plagioclase decreases in modal proportions to about a depth of 1372.4 m. Between depths of 1372.4 m and 1367 m, there is a highly pegmatoidal zone with characteristic spinel stringers.

A 0.8 m-thick chromitite seam is present between a depth of 1364.5 and 1363 m. It grades upwards into a coarse-grained troctolite unit with predominant plagioclase and olivine with minor proportions of subhedral clinopyroxene grains. This unit grades from coarse to fine upwards into a serpentinized zone at 1355.2 m, comprising ~0.5-1 cm sized disseminated spinel grains. At a depth of 1352.9 m, this unit transitions into orthopyroxene- and plagioclase-rich pyroxenite unit with minor interstitial plagioclase. This unit continues at 1337.8 m depth. It is characterized by a series of pegmatoidal zones, plagioclase-free zones, and varying grain size. A massive 3 cm chromitite stringer that consists of 0.5 cm thick sulphide stringers occurs at the depth of 1350.4 m (Figure 4-6b). At the depth of 1346.3 m, there is a 30 cm-sized serpentinized unit with interstitial plagioclase and a series of 1 cm sized chromite stringers. Above this zone, the unit coarsens upwards into plagioclase-free and olivine-rich zones (Figure 4-6c). Plagioclase increases into the UG-2 hanging wall unit, defined by a pegmatoidal texture of the plagioclase-olivine-pyroxene rich unit. The footwall contains high proportions of disseminated chromite and sulphide, with a series of chromite 2-3 cm thick stringers. The contact to the UG-2 chromitite is defined by a gradational transition, containing serpentinized olivine and oikocrystic clinopyroxene-rich wehrlite unit (Figure 4-6d). The top contact to this unit is defined by a rather sharp contact into an olivine-free feldspathic pyroxenite hangingwall.

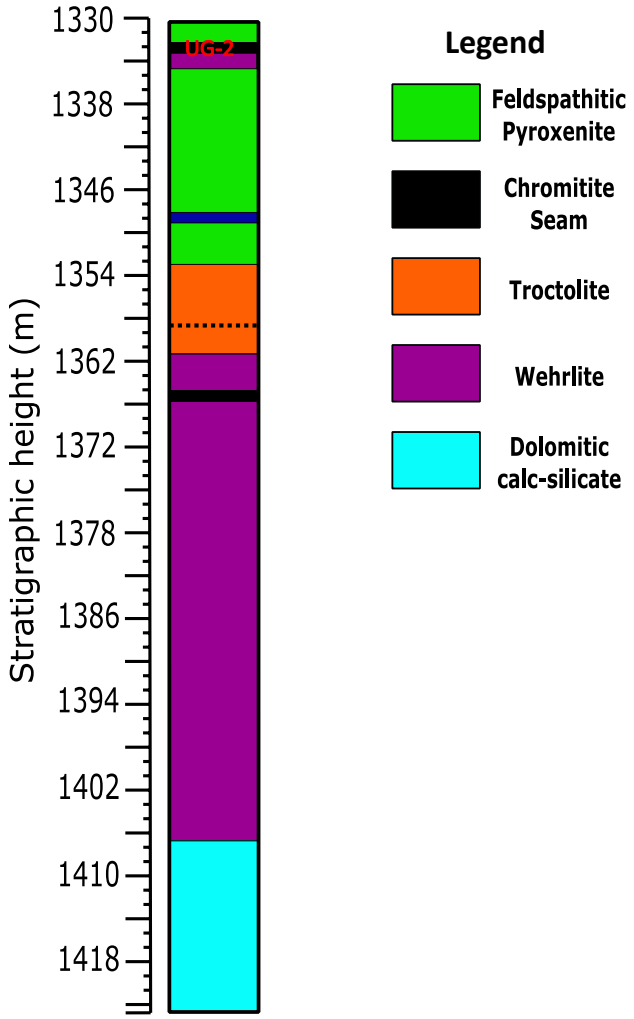

Figure 4-5: Lithostratigraphic section logged from drill UMT-094

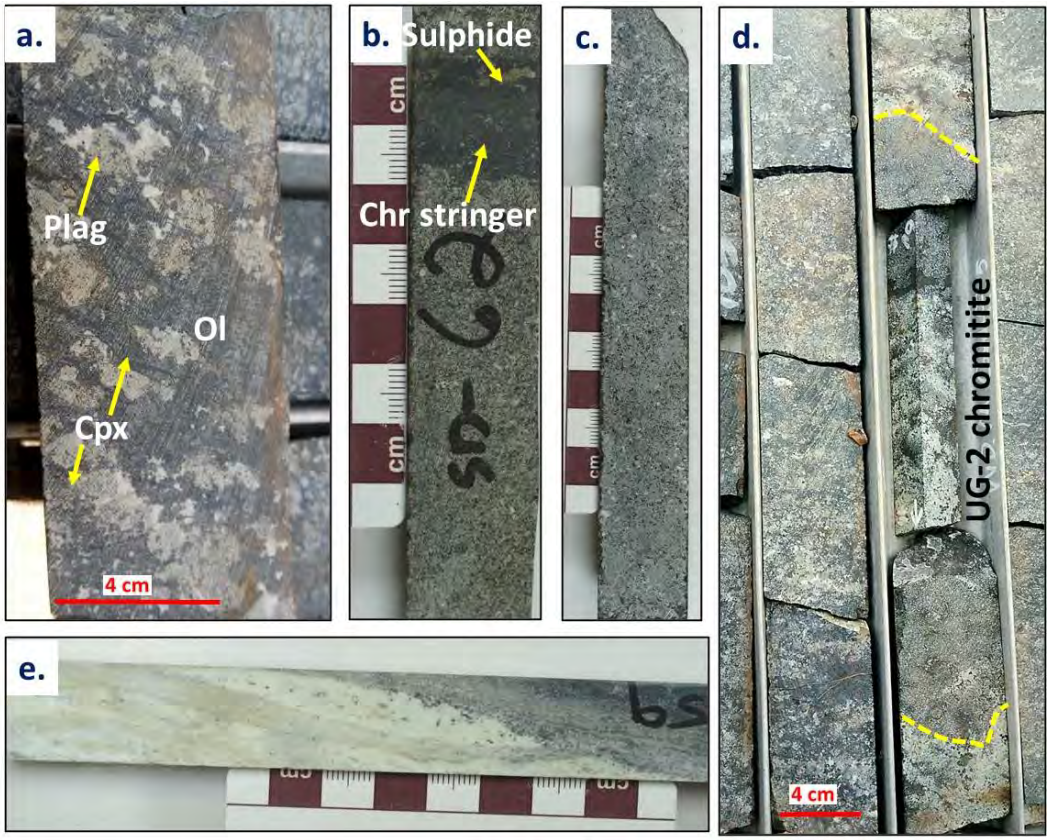

*Figure 4-6: **A**. Plagioclase-poor (Plag) wehrlite unit with coarse-grained anhedral olivine (Ol), clinopyroxene (Cpx). **B** shows a chromite stringer with a thin sulphide band in the feldspathic pyroxenite. **C** plagioclase-poor feldspathic pyroxenite. **D.** heavily disseminated UG-2 chromitite, with massive stringers in parts. and **E**. a layered dolomitic xenolith.*

4.1.2 Petrography

(i) Feldspathic pyroxenite and pegmatoidal pyroxenite

Feldspathic pyroxenites are medium- to coarse-grained lithologies that consist of mainly euhedral orthopyroxene (40-70 modal %), minor clinopyroxene oikocrysts (2-10 modal %), interstitial plagioclase (5-20 modal %), and sometimes containing sulphide phases (up 5 modal %) and disseminated spinels (up to 5 modal %). Feldspathic pyroxenite present in the Flatreef rocks commonly has pegmatoidal varieties, which may contain up to 40 modal % of plagioclases.

Orthopyroxene (0.5-2 mm) crystals show annealing of grains and triple junction boundaries defined by straight boundaries (Figure 4-7a-b). Where a triple junction is present, the elongated grains lack a preferential orientation. The most prevalent texture of the pyroxene is the presence of exsolution lamellae. Exsolution lamellae are predominantly thin in clinopyroxene, while both blebby and thin are present in orthopyroxene. Clinopyroxenes are 2-3 mm coarse-grained oikocrysts that are subhedral, enclosing orthopyroxene, plagioclase, and sometimes chromite. In addition, clinopyroxene is also found along the rims of orthopyroxene as optically-discontinuous thin phases (Figure 4-7a). Olivine phases have been observed only in UMT-094 in minor proportions (<5 modal %) (Figure 4-7c). These phases are mostly interlocked with orthopyroxene, sometimes containing partly consumed plagioclase grains.

Plagioclase is predominantly and intercumulus phase. It often forms a tricuspidate shape, with inward curved grain boundaries (Figure 4-7d), where sandwiched between orthopyroxene grains. Plagioclase is also found as partially resorbed grains enclosed in cumulus orthopyroxenes (Figure 4-7e).

Proximal to chromitite layers, these rocks can exhibit a high proportion of disseminated Cr-spinel grains. These grains are enclosed in orthopyroxene and clinopyroxene. The chromites are less common in these units, but where present, may occur as fine-grained (<0.1-0.3 mm) euhedral inclusions in pyroxenes, and, rarely, in olivines. Sulphides are more abundant (up to ~5 modal %) than spinels in these units and occur as anhedral interstitial phases, and sometimes as inclusions in plagioclase.

The most dominant alteration products are saussurite after plagioclase and uralite (actinolite) after orthopyroxene (Figure 4-7f). Saussuritization varies from spotted patches to highly altered regions. Prehnitization is also observed in a few samples, either as aggregates of replacement products or within thin veins that crosscut both pyroxene and plagioclase. Pyroxene exhibits alteration to actinolite, in which actinolite can occur as both aggregated to subhedral grains depending on the degree of alteration of the rock. The degree of alteration within these silicates depends on the stratigraphy and footwall and hanging wall lithology. For example, in samples close to

serpentinites or xenoliths, there is a high degree of alteration, and lower degrees of alteration within samples further away. Minor amounts of chlorites are present within veinlets or patches in actinolite. Phlogopite is also present as an accessory phase, occurring either within saussiritizied patches in plagioclase or associated with disseminated chromite.

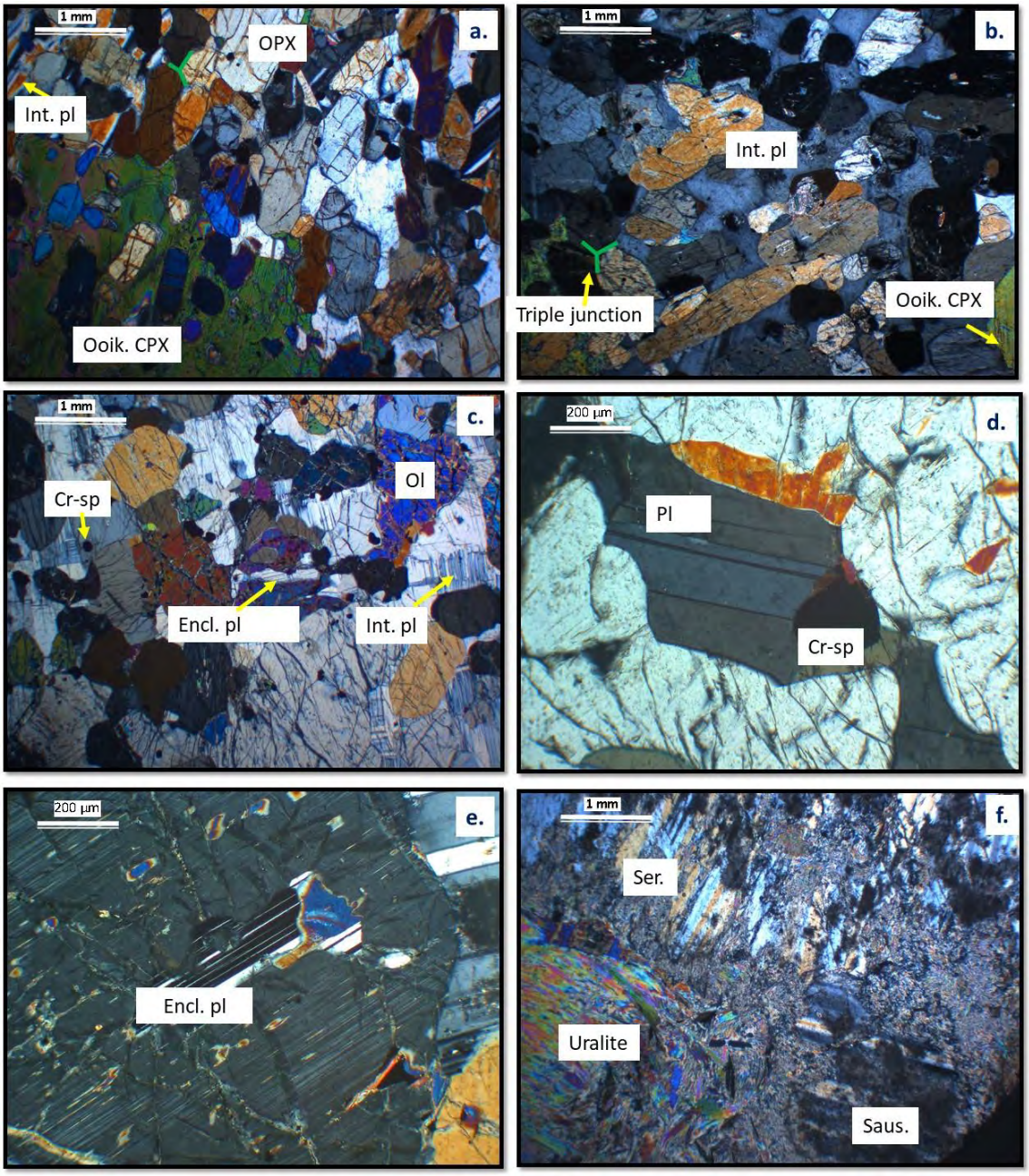

Figure 4-7:: Photomicrographs showing textural relationships present in a feldspathic pyroxenite. ***a-b*** *Sample SD-38 showing clinopyroxene oikocryst (Cpx oik.) with enclosed orthopyroxene crystals (Opx), orientated orthopyroxene (Opx) laths within tripe junction boundaries in places, within interstitial olivine (Int. plag);* ***c*** *Sample SD-45 with disseminated spinel (Cr-sp) minor olivine (Ol) grains that are interlocked with orthopyroxene and contain enclosed plagioclase (Encl. plag) within interstitial plagioclase;* ***d*** *Sample SD-46 showing coarse-grain orthopyroxene that comprises of clinopyroxene rims in places and disseminated spinel grains,* ***e*** *Sample SD-46 showing orthopyroxene-enclosed grains of partially resorbed plagioclase,* ***f*** *Sample SD-44 showing tricuspidate grains of plagioclase defined by concave inward grain interface. (all pictures are taken under transmitted light).*

(ii) Pyroxene – bearing troctolite

This rock unit is composed of mainly olivine (60-80 modal %) and plagioclase (20-40 modal %), chromite spinels () and minor clinopyroxene (<5 modal %). Olivine exhibits two populations. The first population (Ol_1) occurs as subhedral to anhedral grains ranging between 1 mm and 2 cm. It often shows interlocking grain boundaries and constitute consumed plagioclase inclusions and has the largest number of enclosed spinel grains. Interestingly, Ol_1 often shows thin peritectic-orthopyroxene rims. The second population (Ol_2) comprises 0.5 mm olivine xenomorphs that are sometimes found as chadacrysts in clinopyroxene grains associated with spinel grains. Plagioclase grains occur as interstitial grains that sometimes interlock with olivine grains. Plagioclase is also sometimes found as relict grains with partly resorbed grain boundaries hosted in olivine. A few enclosed plagioclase grains exhibit Carlsbad-twinning, however, in most cases they show simple polysynthetic albite-law twinning (Figure 4-8a.). It is sometimes difficult to distinguish between interstitial and enclosed plagioclase, due to the interlocking texture observed in plagioclase and olivine. In most cases, stress-twins in interstitial phases can distinguish them from the partly consumed enclosed phases.

Clinopyroxene is present as 1-2 mm subhedral elongated grains with thin exsolution lamellae (Figure 4-8b). These grains sometimes exhibit zoning and simple twinning. Where they are in contact with Ol_1 there is often decomposed grain boundaries. Cr-spinels in this unit are present as opaque 0.3 mm disseminated grains. They range in shape depending on the enclosing phase from euhedral in plagioclase to anhedral in olivine and clinopyroxene (Figure 4-8 d.). Sulphide phases are often present within spinel grains filling fractures.

In this unit, olivine is the most serpentinized phase with distinct differences between the two populations Ol_1 and Ol_2; the degree of serpentinization in Ol_2 is much lower than that of Ol_1 (~60 %). Plagioclase shows minor saussuritization as well. Pyroxene has experienced little alteration, occasionally incompletely replaced by actinolite. Magnetite is found within the fractures of olivine as unformed aggregates. It is also commonly found as thin and patchy rims and veinlets in Cr-spinels, especially those that are enclosed in olivines.

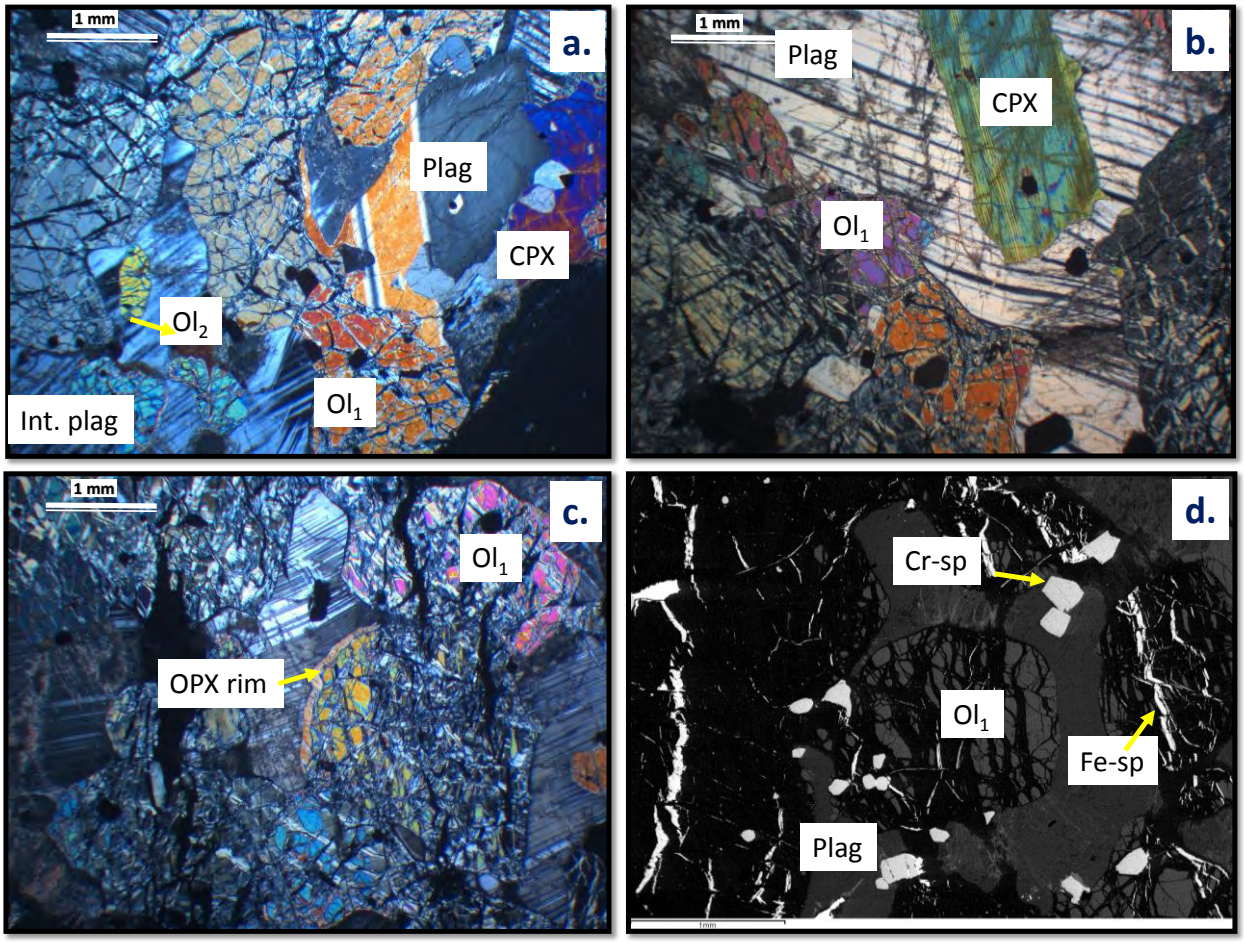

Figure 4-8: Photomicrographs showing textural relationships found in troctolite. ***a*** *First generation of olivine (Ol_1) that is serpentinized containing enclosed plagioclase (Plag) in intercumulus plagioclase and the second generation of xenomorphic olivine (Ol_1) XPL.* ***b*** *Anhedral olivine enclosing minor plagioclase chadacrysts and laths of clinopyroxene grain enclosed in interstitial plagioclase containing minor deformation twins;* ***c*** *Type 1 olivine with thin orthopyroxene rims and anhedral partially consumed plagioclase grains;* ***d*** *a BSE image showing subhedral olivine associated with disseminated fine-grained spinels and the anhedral olivine with predominant magnetite (Fe-sp) along fractures.*

(iii) Olivine bearing Gabbronorite

These rocks are typically equigranular, ranging from medium to very coarse-grained. They comprise cumulus assemblages of olivine (~20 – 40 modal %), orthopyroxene (~20 modal %), and clinopyroxene (~30 modal %). Olivine adcumulates (1 – 3 mm) exhibit a subhedral to anhedral shape with inclusions of plagioclase and minor chromite chadacrysts in some samples. In some of the samples, olivine shows embayed grain boundaries. Orthopyroxene (0.5-1.5 mm) grains are euhedral to less commonly subhedral, and they most often exhibit exsolution lamellae, and often found enclosing plagioclase and sometimes chromite. Orthopyroxene is also observed as thin optically-continuous rims along the boundaries of olivines (Figure 4-9a.), and sometimes are present in partly resorbed chadacrysts in olivine. Plagioclase is present as interstitial phases and small resorbed chadacrysts in olivine. The former plagioclase grains tend to show deformation twins.

Chromites in these rocks are less than 10 % in modal compositions and tend to be disseminated. They occur as enclosed grains (<0.3 mm) with euhedral shape, and sometimes exhibit an atoll-like texture, in which they contain minor enclosed silicate grains. Disseminated chromite often exhibits a subhedral shape with corroded grain boundaries and contain no inclusions. However, they may be slightly replaced by sulphides along the rims. Sulphides observed in these rocks are solely anhedral interstitial phases. The proportions of the sulphide minerals present are typically pentlandite > pyrrhotite > chalcopyrite.

The degree of alterations observed in olivines differs between cumulus olivine and enclosed olivine. The serpentinization in cumulus olivine is about 30 %, with most of the alteration occurring within fractures and, sometimes, but less commonly, along rims. Enclosed olivine grains on the other hand are virtually completely altered (> 90 %). Pyroxenes exhibit minor prehnitization and, occasionally, serpentinization that is restricted to fractures. Plagioclase also shows moderate alteration to saussurite and minor sericite in these rocks. Minor alteration to chlorite, talc and actinolite is observed in some thin sections, especially for samples close to the calc-silicate.

(iv) Chromitite seam

The lower chromitite seam and the UG-2 chromitite seams in the Flatreef vary from heavily disseminated to semi-massive to massive. The massive chromitite comprises chromites that are characterised by re-crystallization and annealed textures, often showing well-developed triple junction orientated at 120^{o} angles. Chromite grains comprise straight to slightly curved grain boundaries. Chromitites that are found as semi-massive to heavily disseminated are significantly fractured. The fractures are often filled with secondary magnetite phases. Silicate inclusions in chromite are very rare, however, a few grains of pyroxenes and carbonates have been observed. Atoll-like and embayed chromites are observed as well. The contact between chromitites and the footwall and hanging wall lithologies tends to be sharp (Figure 4-9 b.). Sulphide phases mostly occur as interstitial phases within plagioclase, or along the boundaries of chromite grains (Figure 4-9c & d). They also occur as veinlets within the re-crystallized and annealed boundaries of chromite.

The only alteration assemblage observed within these rocks is saussurite in plagioclase.

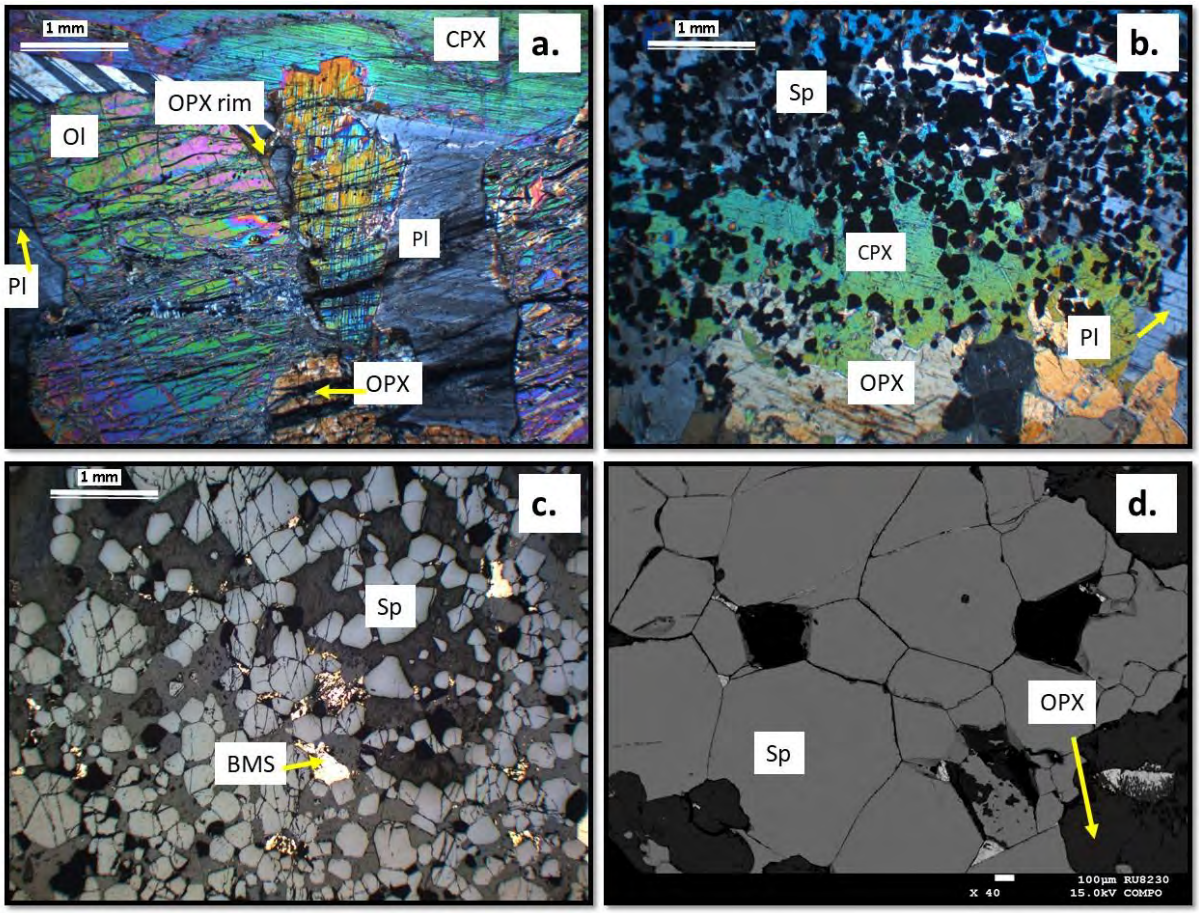

Figure 4-9: Photomicrograph textural relationships present in the olivine gabbronorite and the chromitite. ***a*** *Sample SD-33 showing cumulus olivine, orthopyroxene, clinopyroxene and interstitial plagioclase, with thin orthopyroxene rim in olivine and plagioclase chadacrysts (XPL).* ***b*** *Sample SD-09 heavily disseminated chromite enclosed intercumulus orthopyroxene, clinopyroxene and plagioclase, the clinopyroxene grains show fairly decomposed grain boundaries (XPL).* ***c*** *Sample SD-25 showing heavily disseminated chromite (reflected light).* ***d*** *Sample SD-02 massive chromite that has experienced extensive recrystallization, with 120° triple junction (BSE image).*

(v) Wehrlite

These rock types are made up of olivine (5-45 modal %, pyroxenes (15-30 modal %), plagioclase (<5-10 modal%), chromite (5-45 modal%), sulphides (3-9 modal %) and phlogopite (<5 modal %). Olivine varies in size depending on the proximity to dolomitic xenoliths (now skarn). Proximal to xenoliths, olivine occurs as very coarse-grained (~5 mm) anhedral phases. Towards the centre of the unit, plagioclase occurs as interstitial phases (1 – 5 mm) and enclosed chadacrysts. Interstitial phases are heavily fractured. Olivine and clinopyroxene grains often form a hypidiomorphic (interlocked) texture (Figure 4-10a.). Clinopyroxene (1-4 mm) commonly occurs as subhedral to anhedral coarse poikilitic grains enclosing olivine grains. Clinopyroxene grains in some samples have an anomalously low birefringence (fassaite), almost similar to that of orthopyroxene, but their inclined extinction is used as a diagnostic feature. Orthopyroxene is present as an accessory phase in a few samples as enclosed phases in olivine and/or clinopyroxene (Figure 4-10b & d.). Plagioclase in the wehrlite is interstitial with proportions decreasing towards

the xenolith contact. In a few samples (SD-06 and SD-17) plagioclase is partly resorbed and enclosed in clinopyroxene and olivine (Figure 4-10d.). Phlogopite (0.3-3 mm) is found in varying proportions, often associated with green spinels (Figure 4-10b)

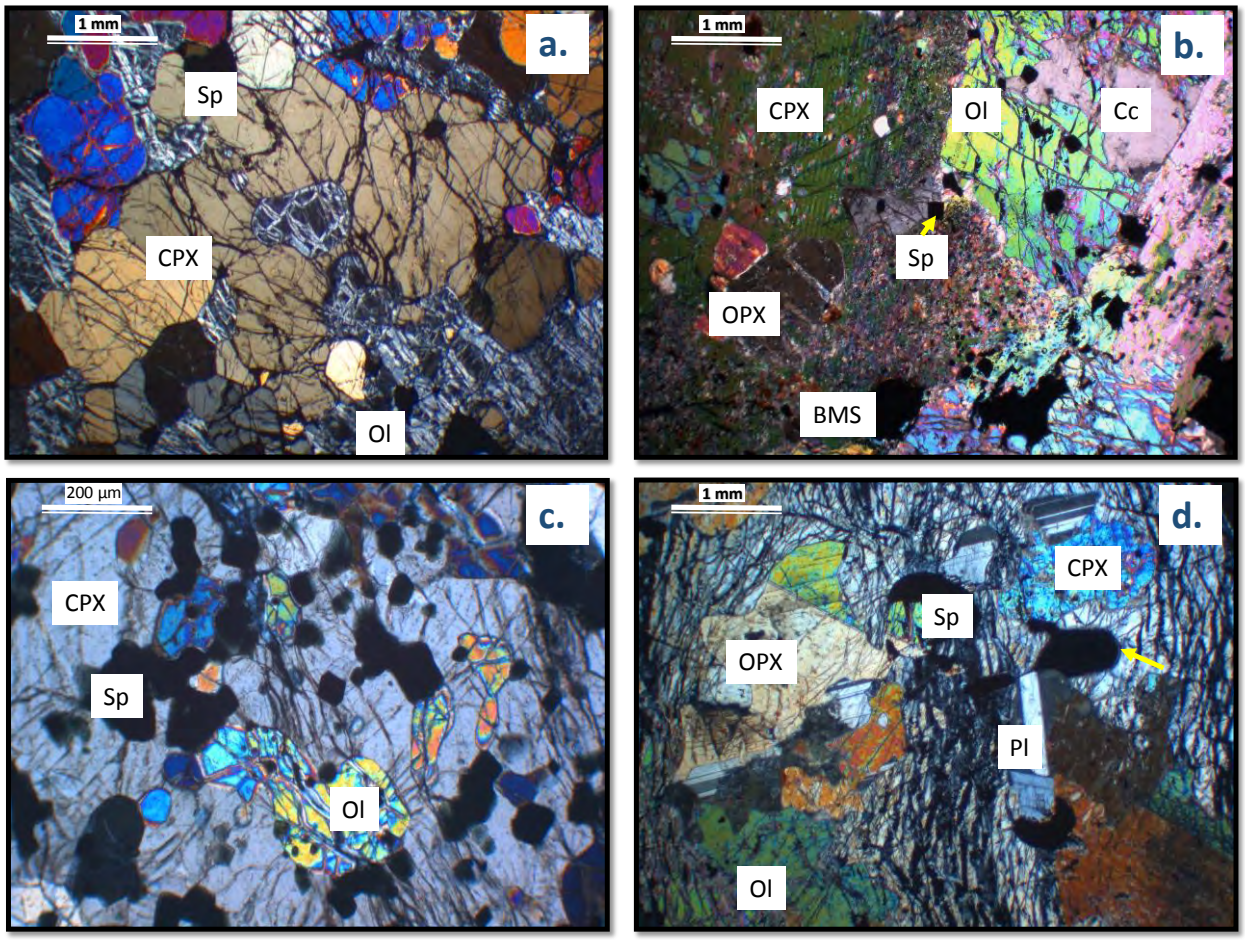

Figure 4-10: Photomicrograph showing wehrlite units from UMT-335 and UMT-094 sections. ***a*** *Sample SD-57 showing interlobate texture in low birefringence clinopyroxene (fassaite) with anhedral highly serpentinized olivine.* ***b*** *Sample SD-06 showing clinopyroxene oikocrysts enclosing orthopyroxene, olivine and minor grains of spinels, cumulus olivine encloses calcite and disseminated spinels.* ***c*** *Sample SD-54 showing a clinopyroxene oikocryst enclosing olivine and spinel grains.* ***d*** *Sample SD-15 showing a coarse-grained olivine crystal enclosing partly consumed plagioclase, orthopyroxene, clinopyroxene and spinel grains. All micrographs are taken under XPL.*

Spinels in this unit have varying modal proportions from 5 to 65 %. They can be present as either disseminated inclusions in silicate grains or they can be interstitial. The former type is often hosted by silicates, and range between opaque and reddish-brown. Chain-textured strings of spinels are found enclosed in clinopyroxene and along the margins of olivine (Figure 4-11c). Interstitial spinels are often subhedral to anhedral green (Al-rich) to opaque spinel (Cr-rich) and may contain inclusions of silicate phases. Green spinels found in feldspathic samples, showing a poikilitic texture hosting silicate, carbonate and minor sulphide phases. Spinels enclosed by interstitial phlogopite is green (pleonaste) and shows minor corrosion along the margins (Figure 4-11a.). In contrast, opaque spinels present in all wehrlite samples in varying proportions.

Spinels present in some samples exhibit exsolution textures of an Fe-rich phase (magnetite). These exsolution textures are defined by two different types. Type 1exsolution lamellae are well-formed and orientated, forming a network-like texture with two perpendicular orientations. These lamellae are sometimes present in completely exsolved spinel grains. Type 2 exsolutions are present in a few samples are occur as irregular blebs and are mostly found along the rims and cores of coarse-grained spinel. The two types of lamellae can be found together and the contact between the two exsolution is normally irregular (Figure 4-11 d.).

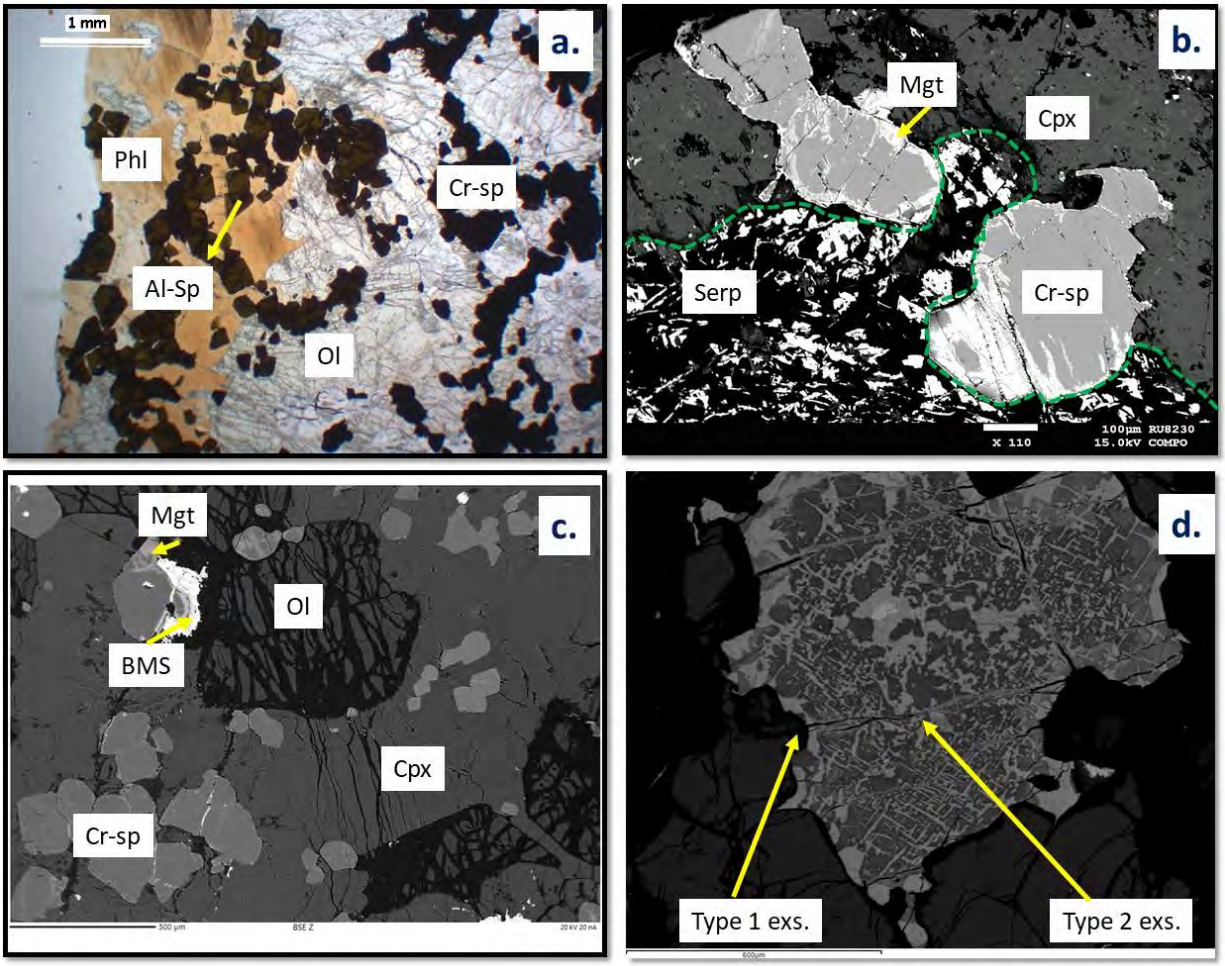

Figure 4-11: Textural relationships in spinels from the wehrlite unit. ***a*** *Sample SD-56 showing phlogopite replacement of cr-spinel to Al-spinel (Al-Sp) (transmitted XPL).* ***b*** *sample SD-14 partly resorbed spinels with ferrit chromite rims occurring between serpentinized olivine and clinopyroxene (BSE image).* ***c*** *Sample SD-56 clinopyroxene-enclosed spinels with a chain-texture.* ***d*** *sample SD-57 showing a BSE image of clinopyroxene-enclosed spinel with type 1 orientated exsolutions and type 2 irregular bleb-like exsolutions.*

Olivine is the most altered phase, affected by serpentinization. Proximal to xenoliths, only pseudomorphic olivine is present, completely replaced by talc, magnesite and magnetite within fractures (Figure 4-12b). Pyroxenes are partly replaced by actinolite within the whole unit. The intensity of alteration in plagioclase varies from sample to sample. In some cases, minor saussuritization affects these grains, while some samples are affected by prehnitization coupled with epidotization. Magnetite is found in fractures of olivine as unformed aggregates. It is

commonly found as thick and patchy rims in interstitial chromite, more especially chromite in contact with serpentinized olivine. Some chromites enclosed in olivines with a high proportion of magnetite have thin rims of magnetite along the margins of the grains. Magnetite can sometimes occur as alteration productions within the fractures of olivine (Figure 4-12b.).

(vi) Serpentinites

Serpentinites are mainly made up of serpentine (~70 modal %), pyroxene (~10 modal %), magnetite (<5 modal %) and minor olivine (5 modal %), spinel (5-30 modal %) and sulphides. Serpentine forms pseudomorphs after olivine, with a poikilitic texture, enclosing subhedral grains of clinopyroxene and sometimes spinels. The serpentine grains display a mesh and hour-glass texture. Magnetite is often found as veins within small relict olivine fractures and as continuous aggregates within fractures (Figure 4-12 a & d). Chromites are found as both anhedral interstitial grains and as angular grains enclosed in pyroxene. Interstitial chromite is mostly atoll-like and skeletal, forming around the boundaries of olivine (Figure 4-12c). Interestingly, some grains of chromite are porous-to-spongy in texture, enclosing significant amounts of silicate phases and sulphide phases (Figure 4-12c-d).

Uralitization is the predominant alteration process occurring in pyroxene, which is mostly present in oikocrystic grains, while enclosed grains display less degree of alteration. Serpentinization of olivines is sometimes associated with thin magnesite veins and halos of associated lizardite (Figure 4-12a-b). Talc is also a dominant alteration by-product within relict olivine grains

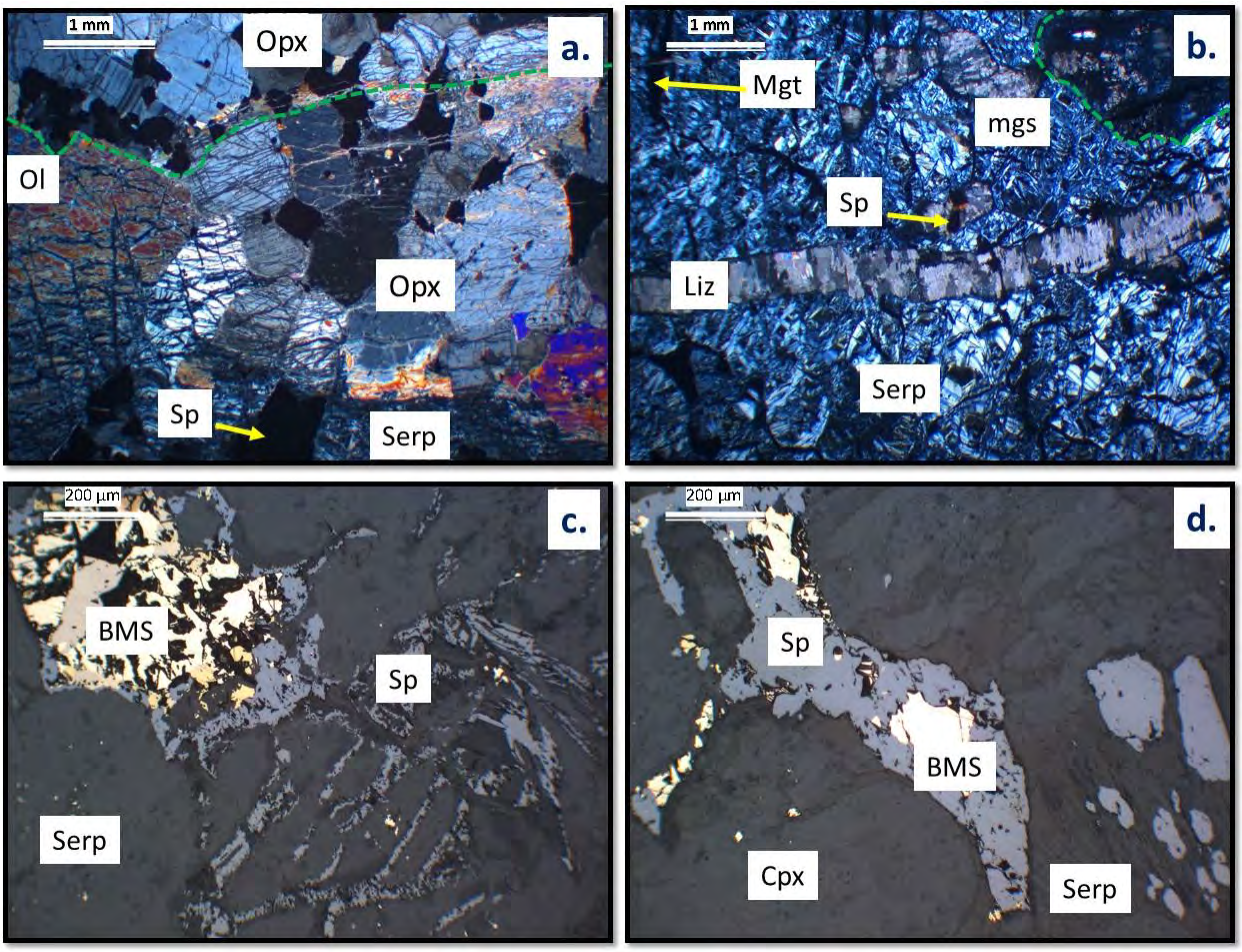

*Figure 4-12: Photomicrograph showing serpentinite unit. **a** shows olivine pseudomorph that has been completely replaced by serpentine (mainly antigorite), with crosscutting lizardite (Liz) vein and magnetite filling in the fractures (transmitted light). **b** mesh-like texture of antigorite serpentine crosscut by magnesite (Mgs) and lizardite halos and clinopyroxene altered to basitite (lizardite and antigorite) (transmitted light). **c** interstitial skeletal chromite spinel enclosing sulphide phases within clinopyroxene and serpentine (reflected light). **d** shows anhedral chromite spinel enclosing sulphide phases and carbonates (Carb. incl) and magnetite aggregated forming alone the fractures of serpentinized olivine (reflected light).*

(vii) Calc-silicate

Calc-silicate rocks differ in mineral assemblage from core to core. Predominantly phases include clinopyroxene, olivine, periclase, with accessory vesuvianite, akermanite, periclase, calcite, phlogopite, prehnite, sphene, calcite, periclase, some oxides and sulphides. Peak metamorphic assemblages are defined by a granoblastic-polygonal texture of clinopyroxene, olivine and vesuvianite. Retrograde metamorphic assemblages are often found as symplectite reactions of akermanite, spinel, calcite, phlogopite and forsterite along the margins of peak phases, and also as inclusions in poikiloblasts.

Drill core UMT-335 comprises predominantly of clinopyroxene that is mostly anhedral, often forming lobate boundaries with surrounding minerals. The clinopyroxene is diopside, with a poikiloblastic texture that hosts accessory phases of calcite, akermanite and sphene, phlogopite, forsterite etc. In samples closer to cumulus rocks in UMT-094, periclase is present in high

proportions associated with forsterite, diopside, vesuvianite and wollastonite. The periclase usually forms idioblastic grains associated with olivine in a matrix of calcite. Vesuvianite is predominantly associated with wollastonite and calcite, often exhibiting zonation textures (Figure 4-13 b). Sulphide phases in these rocks occur as haloes that are ~3 mm in size, associated with olivine and vesuvianite. The sulphide phases present in the calc-silicate units occur in a matrix of calcite as Mn-sulphides (alabandite) and Fe-sulphides as shown in Figure 4-13 d.

Akermanite is mainly found along the boundaries of clinopyroxene and olivine. It is xenoblastic, often containing inclusions of calcite, and sometimes enclosed in clinopyroxene and vesuvianite grains. Olivine varies from idioblastic enclosed grains to interstitial grains. Corona textures of pyroxene in olivines are observed in a few samples. Prehnite mainly found in UMT-335 either as well-formed grains, replacement products in plagioclase or as thin veins in olivine and pyroxene. Serpentine phases occasionally replace interstitial olivine or partly replace remnants of olivine enclosed in clinopyroxene. The intensity of alteration increases from 60 to >90 % closer to cumulus units. Periclase grains are partly altered to brucite along veins. Phlogopite is often found as inclusions in poikiloblastic clinopyroxene, and in symplectitic intergrowths with akermanite, forsterite, calcite and clinopyroxene (Figure 4-13). Chlorite is the retrograde phase, often replacing phlogopite, clinopyroxene and vesuvianite.

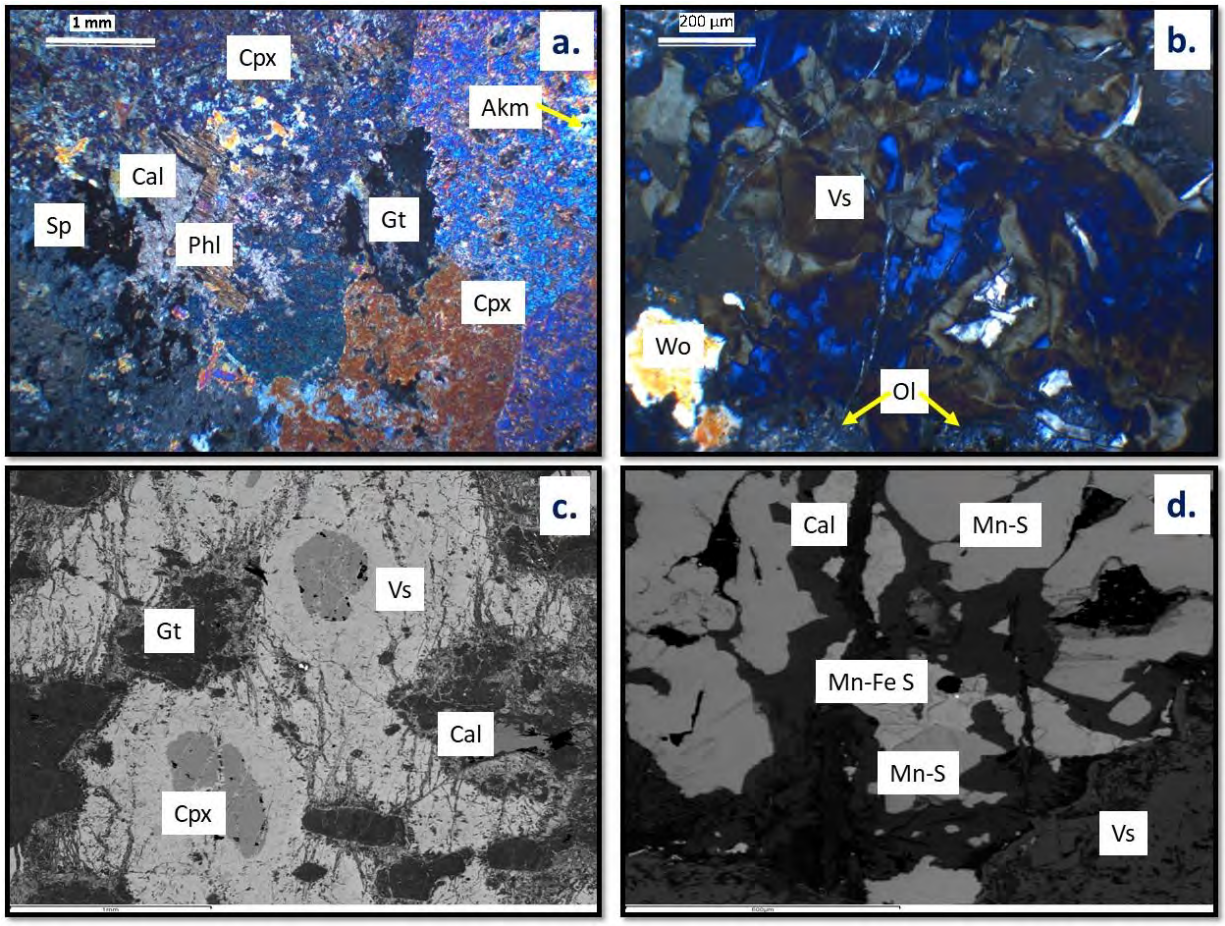

Figure 4-13: Photomicrograph showing calc-silicate assemblage and textures. ***a*** *Sample SD-18 showing a granoblastic-polygonal texture of poikiloblastic clinopyroxene with some grains showing a symplectite texture of phlogopite, calcite, akermanite and spinel.* ***b*** *Sample SD-61 showing wollastonite (Wo) rare vesuvianite (Vs) in a matrix of serpentinized olivine.* ***c*** *shows a BSE image of sample SD-58 with pockets of garnet in vesuvianite with clinopyroxene-rich cores.* ***d*** *a BSE image of sample SD-58 showing a halo of alabandite (Mn-S), Mn-rich sulphide (Mn-Fe S) and calcite; enclosed by vesuvianite.*

(viii) Para-pyroxenite

This rock type is predominantly diopside (~70 %) and plagioclase (~25 %), with minor phlogopite, vesuvianite, sulphides, magnetite and olivine. Diopside occurs as subhedral grains of about 2 mm in size (Figure 4-14 a and b). These grains show extensive recrystallization with 120° triple junctions along the grain boundaries. They also have interlobate to embayed grain-boundaries. Plagioclase grains form interstitially to diopside grains. Phlogopite grains are xenoblastic, showing no well-formed cleavages. They can either form along the boundaries of plagioclase and diopside or within diopside phenocrysts. Phlogopite enclosed in plagioclase varies in size between 0.5 - 2 mm, while in diopside it is less than 0.5 mm. Smaller phlogopite grains are dispersed as replacement products, rather than as flakey aggregates.

Saussuritization of plagioclase is the most predominant alteration product within the para-pyroxenite. It gives off a dirty look in plagioclase so much that the feldspar is largely unrecognizable. Minor prehnite aggregates are sometimes present as replacement products in

plagioclase, associated with calcite. Actinolite is an alteration product of diopside, where some thin sections are more highly altered than others. Calcite is mostly found as a replacement product of vesuvianite, diopside and melilite. Calcite can either be present as well-formed grains or aggregates enclosed by diopside and within the fractures of melilite. Olivine is variably serpentinized.

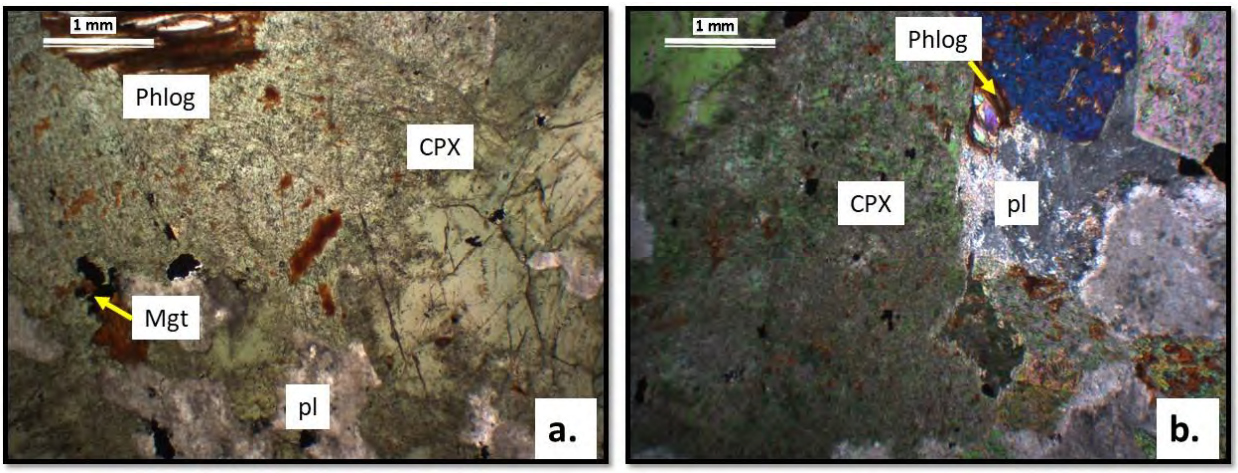

Figure 4-14: Photomicrograph showing parapyroxenite rock with predominant clinopyroxene and minor amounts of plagioclase, phlogopite and magnetite

4.2 Mineral Chemistry

4.2.1 UMT-345

Drill core UMT—345 is the least contaminated drill core, with low variability in lithologies. It mostly made up of feldspathic pyroxenite (85 %), olivine gabbronorite, serpentinite and chromitite seams. EPMA analysed thin sections were only selected from the olivine gabbronorite and the chromitite seam, and these data are shown in Appendix B.

(i) Olivine

Olivine in the olivine-bearing gabbronorite is found as cumulus grains that enclose chrome-spinels. They are partially fractured and altered into serpentine and magnetite tends to grow within fractures of these olivines. Compositions of these olivines are illustrated in Figure 4-15. Olivines from this unit have variable forsterite contents [Molar ×100 $Mg/(Mg+Fe^{2+})$] ranging between Fo_{78} and Fo_{79}. Olivine in olivine gabbronorite shows a subtle negative correlation of NiO with Fo, which varies between 0.22-0.27 wt. %. On the other hand, Cr_2O_3 and CaO do not show a systematic variation with Fo content, ranging between 0-0.03 wt. % and 63 to 490 ppm, respectively.

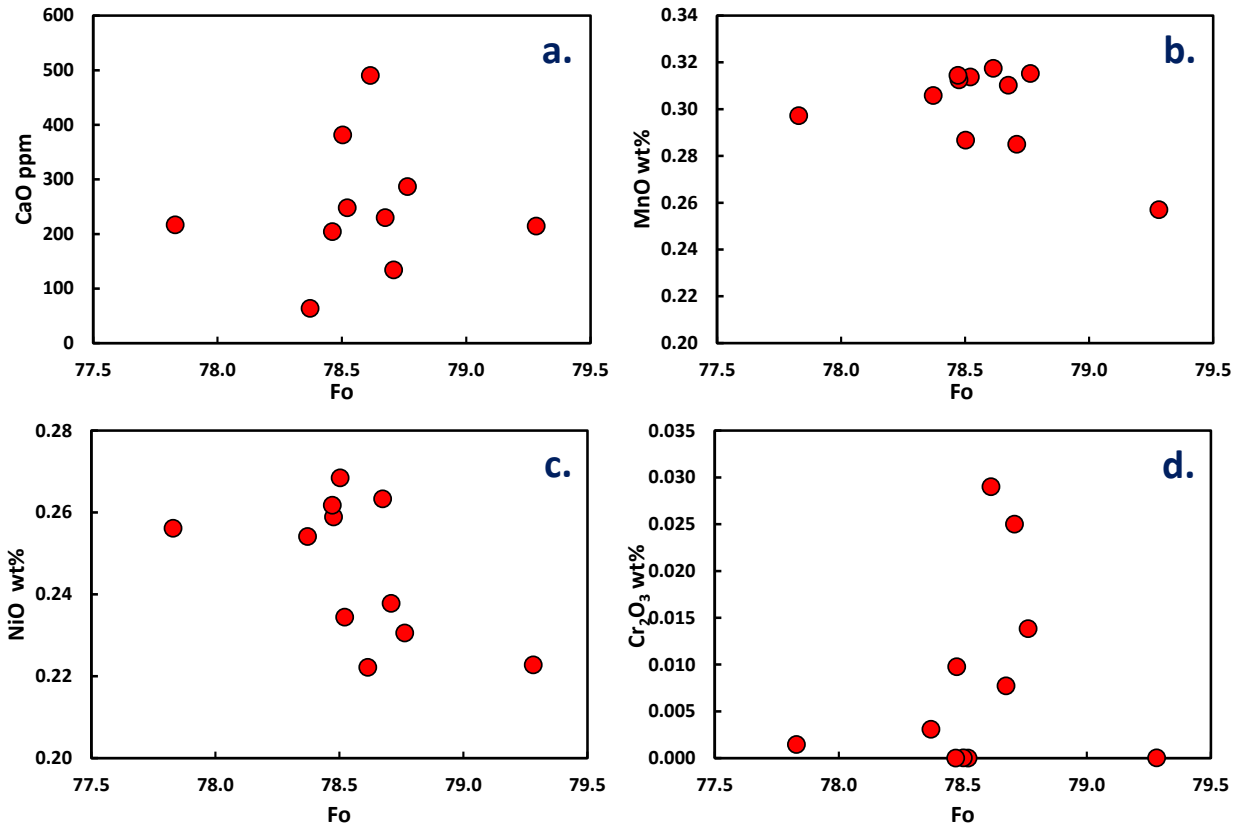

Figure 4-15: Olivine compositions in the olivine gabbronorite from drill core UMT—345. ***a.*** *CaO in ppm,* ***b.*** *MnO in wt.%,* ***c.*** *NiO in wt.%, and* ***d.*** *Cr_2O_3 in wt.%.*

(ii) Pyroxene

Pyroxene compositions in this drill core were obtained from the massive chromitite seam and the olivine gabbronorite. Compositional variations of the pyroxenes are illustrated in Figure 4-16 and Figure 4-17

Orthopyroxene in the chromitite is enstatitic, characterized by Wo_{1-2} En_{86-91} Fs_{9-12} (Figure 4-16), with an Mg# varying between 84 and 85 (Figure 4-17d-f). Concentrations of MnO oxide are very low and show limited correlation with Mg#, ranging between 0.05 and 0.1 wt. %. Al_2O_3 content of orthopyroxene in this unit shows a bit of variation, wherein a few grains show an average of 1.3 wt. % and one grain is enriched, with up to 3.3 wt. % Al_2O_3. The concentration of Cr_2O_3 has a limited variation with Mg#, ranging between 0.4 and 0.7 wt. %. Clinopyroxene in this unit is characterised by Wo_{29-50} En_{49-67} Fs_{0-8} exhibiting compositions from diopside to augite. Cr_2O_3 contents are more heterogeneous than those of orthopyroxene, varying between 0.4 and 1.1 wt. %. Calculated Ca-Tschermak activities of these clinopyroxenes are low, with compositions ranging between 4 and 11 %. Fe^{3+} apfu of clinopyroxene was calculated by stoichiometry. The Fe^{3+}/Fe^{total} ratio of clinopyroxenes from the chromitite ranges between 0.17 and 0.21.

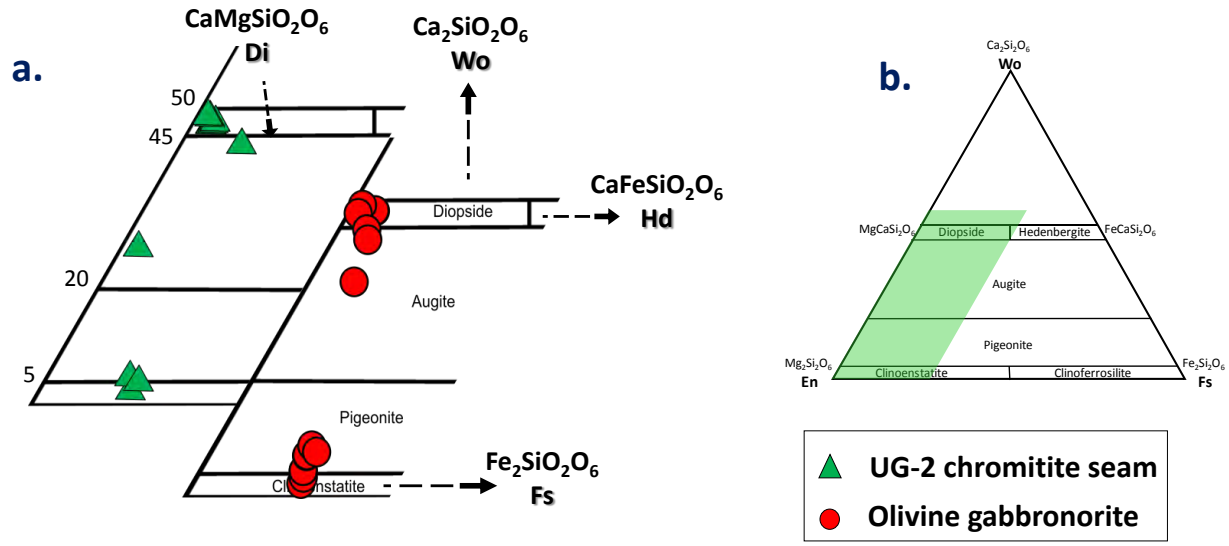

Figure 4-16: Wo-En-Fs quadrilateral representation of pyroxene compositions from drill core UMT-345. ***a.*** *a close-up figure into the enstatite-diopside section of the quadrilateral showing samples from the UG-2 chromitite and olivine gabbronorite.* ***b.*** *Pyroxene quadrilateral plot showing the zoomed area.*

Orthopyroxene within the olivine gabbronorite is present as enstatite with a composition of $Wo_{1.6-7.2}$ En_{77-82} Fs_{16-18} and relatively lower Mg# varying between 80 and 81. Their MnO and Cr_2O_3 oxide composition have limited variations, between 0.1-3.6, 27-29, 0.3-0.5 wt. % respectively. Al_2O_3 content is equal to that of the chromitite grains, ranging between 1.4 and 1.8 wt. %. In this unit, clinopyroxene is characterised by a composition of Wo_{35-48} En_{47-56} Fs_{4-9}, falling under the diopside and augite end-members (Figure 4-16), with Mg# falling between 81

and 85. The composition of Cr_2O_3 in clinopyroxenes of the olivine gabbronorite has a lower average, varying between 0.4 and 0.7 wt. %. Calculated Ca-Tschermak activity of these pyroxenes is low, varying between 6 and 9.8 mol.%. The Fe^{3+}/Fe^{total} ratios of clinopyroxene in the olivine gabbronorite are low, ranging between 0.04 and 0.11.

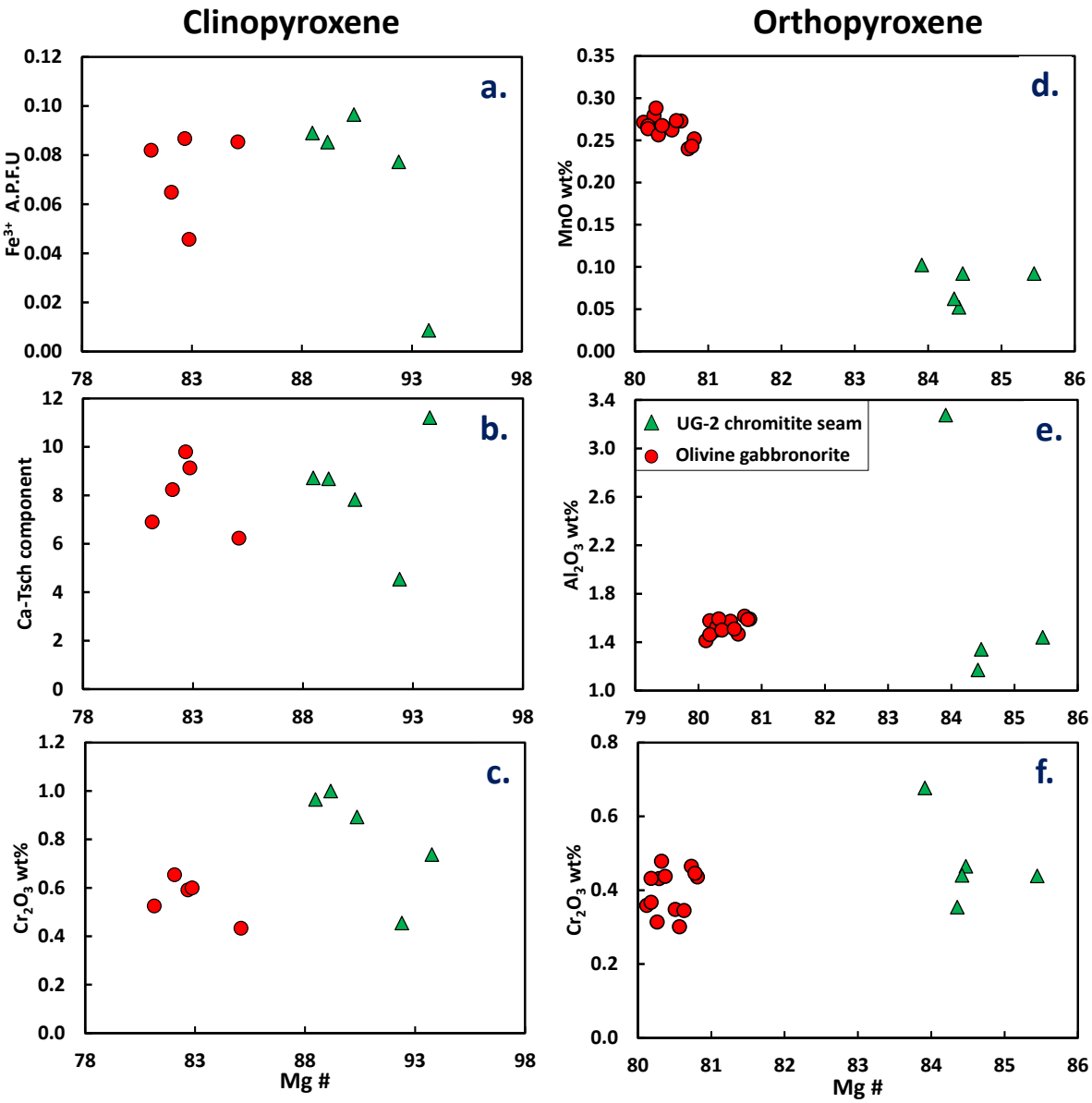

Figure 4-17: Compositions of clinopyroxene and orthopyroxene from the UG-2 chromitite seam and olivine gabbronorite in drill core UMT-345. Clinopyroxene components include ***a.*** *Fe^{3+} cation in apfu,* ***b.*** *Ca-Tschermak component,* ***c.*** *Cr_3O_3. Orthopyroxene components include;* ***d.*** *MnO,* ***e.*** *Al_2O_3,* ***f.*** *Cr_3O_3.*

(iii) Plagioclase

Within this drill core, plagioclase is present as an interstitial phase in the chromitite seam, while both interstitial and olivine-hosted plagioclase phases are found in the olivine gabbronorite. Representative compositions of these lithological units are illustrated in Figure 4-18. Plagioclase in the UG-2 chromitite is labradorite, with an anorthite content varying between An_{58} and An_{64}.

Oxide compositions of Na_2O, K_2O Al_2O_3 and CaO range between 3.82-4.5, 0.01-0.37, 28.5-30 and 11.7-3.5 wt. % respectively.

Plagioclase in the olivine gabbronorite shows slightly more calcic compositions than that of the chromitite seam. In the olivine gabbronorite, plagioclase is present as a bytownite with an An content ranging between An_{70} and An_{77}, more calcic than those grains from the UG-2 chromitite. Their oxide compositions of Na_2O, K_2O, Al_2O_3 and CaO range between 2.5-3.2, 0.09-0.34, 30.3-31.5 and 14.5—15.88 wt. %, respectively. Enclosed plagioclase grains display a reverse chemical zonation from a sodic (An_{70}) core to a more calcic (An_{76-77}) rim. The latter range is similar to the chemical composition observed within the interstitial grains.

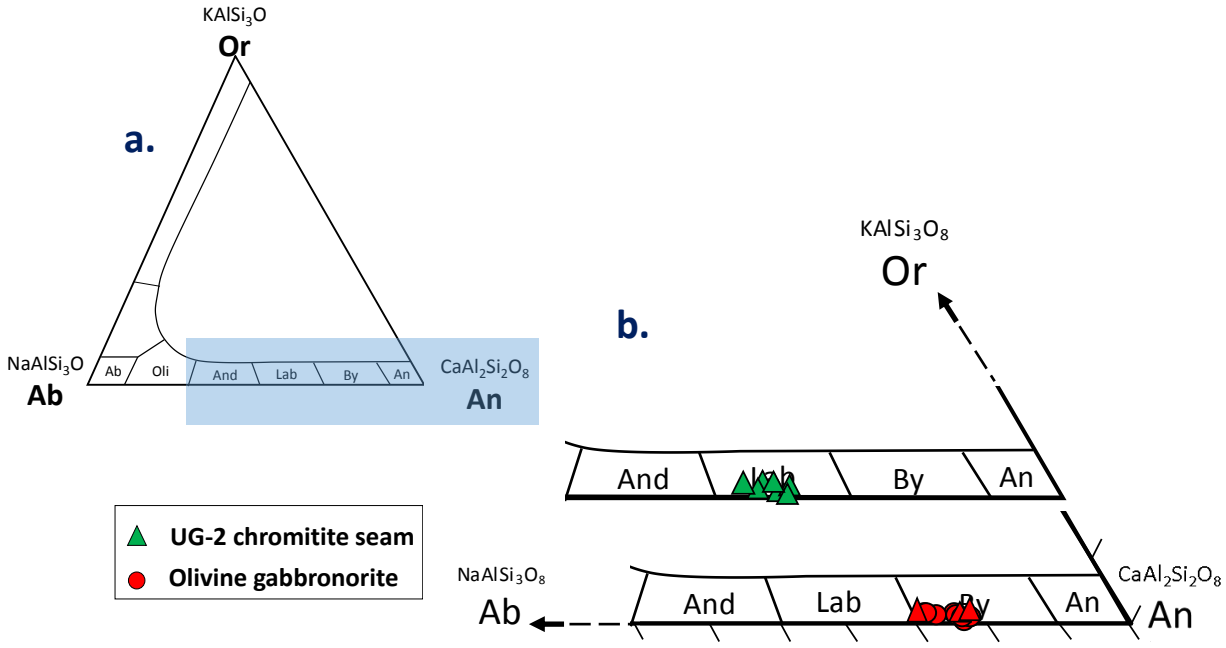

*Figure 4-18: Ternary Ab-Or-An diagram in **a.** showing the zoomed in section. plagioclase compositions from the chromitites seam and olivine gabbronorite in UMT—345. For the olivine gabbronorite, ▲ represents enclosed grains and ● represents interstitial grains.*

(iv) Spinel-group minerals

Spinels from this drill core were obtained from the two different lithological units; chromitite seam and olivine gabbronorite. Within the chromitite, spinels occur as cumulus grains often exhibiting annealed textures. Spinels within the olivine gabbronorite occur as enclosed grains in olivine and pyroxene grains. These different types of spinel follow characteristic trend based on their mineral chemistry (Figure 4-19 and Figure 4-20).

Spinels in the UG-2 chromitite display homogeneous composition, with Mg# ranging between 52 and 56. Al_2O_3 and Cr_2O_3 contents are clustered at averages of ~16 and 40 wt.% respectively (Figure 4-19a and b). Similarly, contents of TiO_2 and V_2O_3 cluster at values of ~0.9 and 0.3 wt.%

respectively (Figure 4-19c and d). Based on the Cr-Fe-Al ternary classification plot in Figure 4-20a, the UG-2 chromitite displays values clustered at ~$Cr_{53}Al_{32}Fe^{3+}_{15}$, subtly following an Fe-Ti trend.

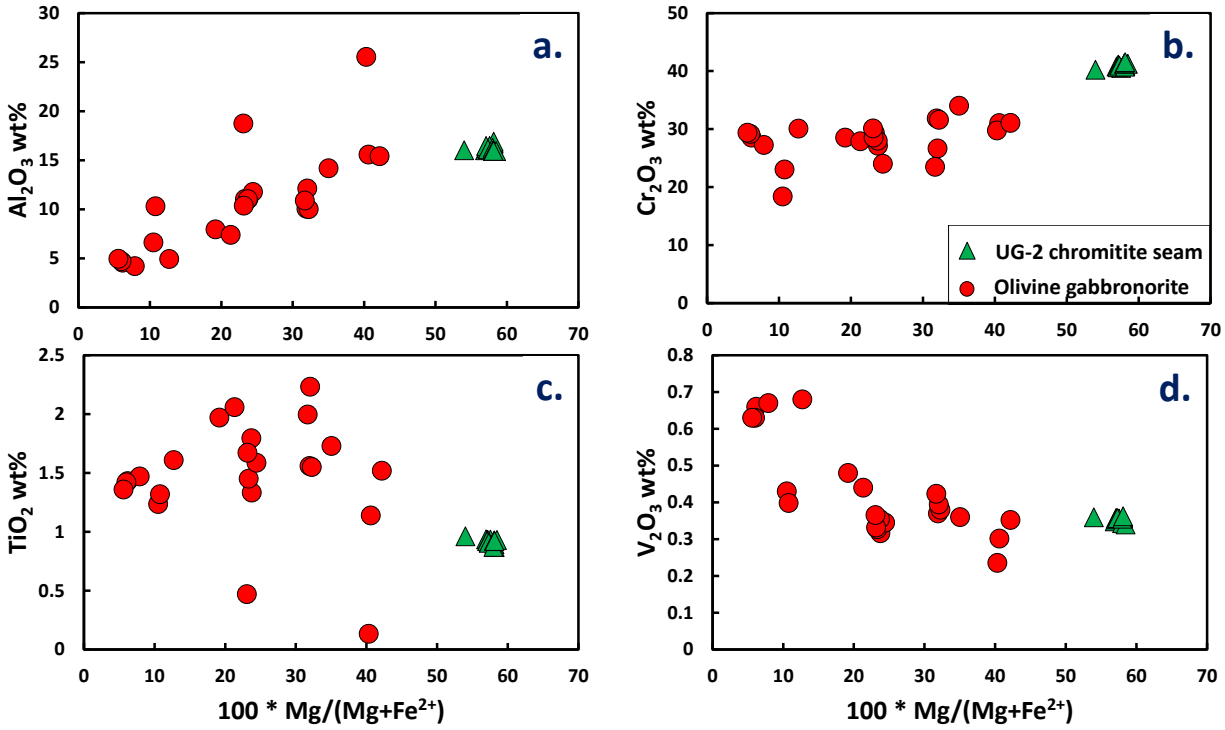

*Figure 4-19: Spinel compositional variations of **a.** Al_2O_3, **b.** Cr_2O_3, **c.** TiO_2 and **d.** V_2O_3 with progressive decreasing Mg# (100 * molar Mg/(Mg+Fe^{2+})) from the UG-2 chromitite and olivine gabbronorite.*

In contrast, spinels from the olivine gabbronorite show heterogeneous mineral compositions, with Mg# ranging between 6 and 42 (Figure 4-19). There is an observed positive correlation in Al_2O_3 and Cr_2O_3 with Mg#, with values decreasing from 25 to 5 and 34 to 18 wt.% respectively. Contents of TiO_2 of Cr-spinels in the olivine gabbronorite are slightly variable and higher than that of the UG-2 chromitite, ranging between 0.1 and 2.2 wt.%. Contents of V_2O_3 increase with decreasing Mg# from 0.2 to 0.7 wt.%. Based on the ternary Cr-Al-Fe^{3+} plot in Figure 4-20a, most Cr-spinels in the olivine gabbronorite follow the Fe-Ti trend, with values increasing towards the Fe^{3+} apex.

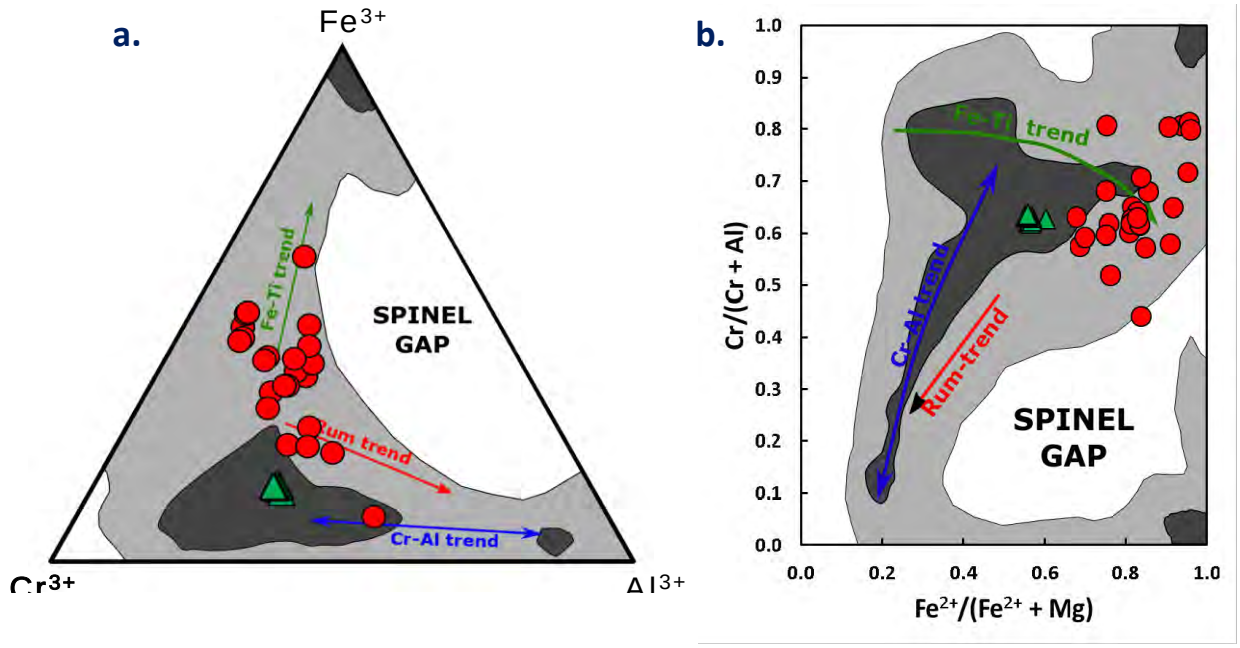

Figure 4-20: Distribution of trivalent cations (Cr-Fe-Al) and variation in Cr/(Cr+Al) vs $Fe^{2+}/(Fe^{2+}+Mg)$ in spinels from UMT-345 sections for the olivine gabbronorite and UG-2 chromitite. Fields for 90% (dark grey) and 50% (light grey) data are adapted from Barnes and Roeder (2001).

4.2.2 UMT-335

From this drill core, six samples from three different lithologies were analysed, including the UG-2 chromitite, chromitite and wehrlite. Minerals analysed include olivine, pyroxene, plagioclase and spinel.

(i) Olivine

Olivine in the wehrlite can occur as relatively large anhedral grain enclosing silicates, and as fine grains in a massive texture associated with interstitial plagioclase and clinopyroxene. In these wehrlites, olivines show a bimodal chemical distribution. The forsterite content of most olivines ranges between Fo_{73} and Fo_{78} as shown in Figure 4-21. MnO shows a negative trend with Mg#, ranging from 0.3 to 0.5 wt. %. Conversely, a positive correlation is observed for NiO, varying between 0.3 and 0.05 wt. %. No clear systematic trend is observed for CaO and Cr_2O_3 with Mg#, such that the two oxides range between 0.015-0.059 wt. % and 0-0.12 wt. %, respectively.

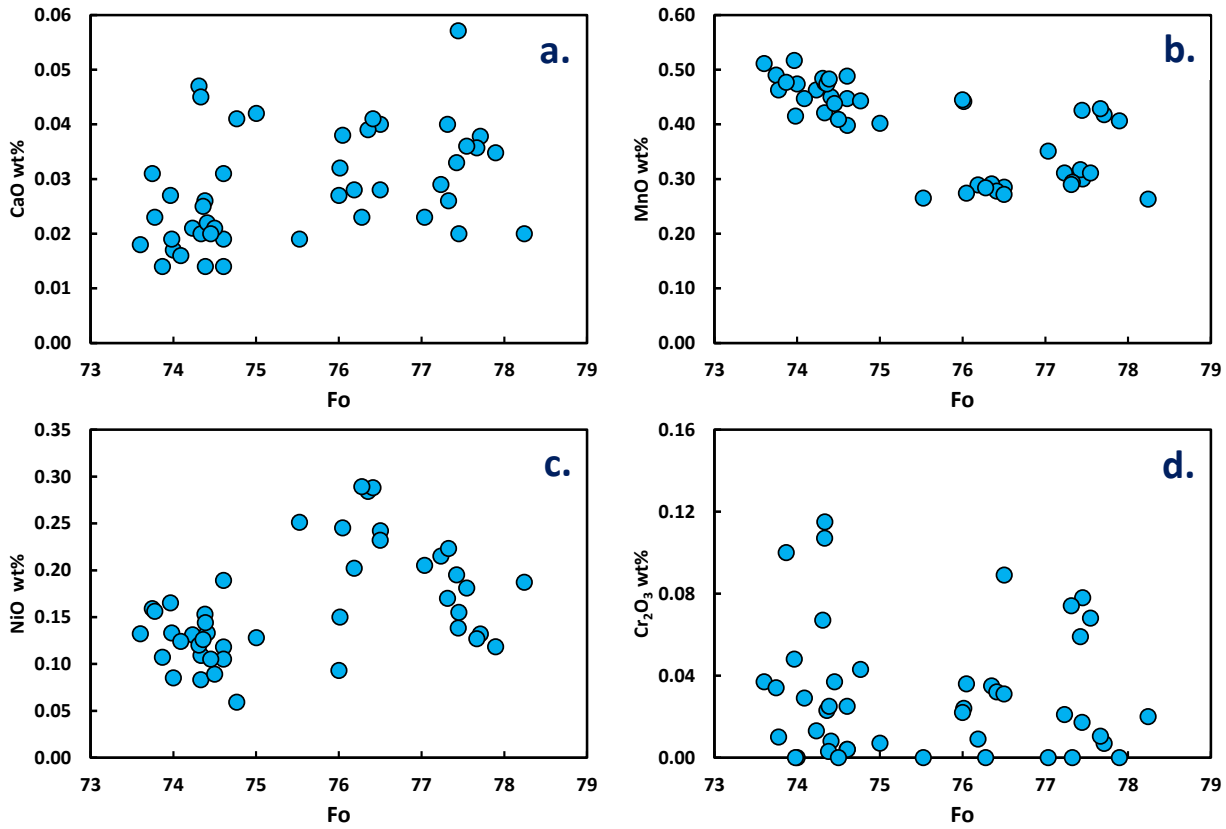

*Figure 4-21: Olivine mineral chemistry ternary plot showing data from the wehrlite. Compositions of **a.** CaO, **b.** MnO, **c.** MnO, **d.** Cr_2O_3 are plotted against forsterite (Fo).*

(ii) Pyroxene

Pyroxene was analysed in three different lithologies in this drill core, in the UG-2 chromitite, lower chromitite seam and wehrlites. In the lower chromitite seam, pyroxene is found as both cumulus orthopyroxene and oikocrystic clinopyroxene, whereas in the selected UG-2 chromitite section, clinopyroxene was rarely found, hence never analysed. Representative pyroxene compositions are illustrated in Figure 4-22 and Figure 4-23.

In the UG-2 chromitite, pyroxene is present exclusively as enstatite with a composition of $Wo_{1.2-4.2}$ $En_{79.4-83}$ $Fs_{14.8-17.2}$, while the Mg# is ranging from 82 to 85. With decreasing Mg#, MnO shows a subtle inversely correlated trend, increasing from 0.17 to 0.29 wt.%. The contents of Al_2O_3 and Cr_3O_3 show a subtle negative correlation with Mg#, increasing from 0.8 to 1.5 wt.% and 0.28 to 0.57 wt.%, respectively.

Orthopyroxene in the chromitite is present as enstatite with a composition of $Wo_{1,8-8.7}$ En_{82-84} Fs_{12-16} and an Mg# ranging between 84 and 88. MnO, Al_2O_3 and Cr_2O_3 in this unit also have limited variations with compositions ranges of 0.22-0.24 wt.%, 1.35-1.46 wt.% and 0.4-0.51 wt. %, respectively. Oikocrystic clinopyroxene present in this unit is between augite and diopside, with a composition of Wo_{46-49} En_{47-51} Fs_{2-4}. The Mg# (87-89) shows little variation with

Fe^{3+}(~0.075-0.086). Contents of Al_2O_3 (not shown) and Ca-Tschermak have subtle but negative correlations with Mg#, with values ranging between 2.0-2.4 wt.% and 7.7-9.0 mol%.

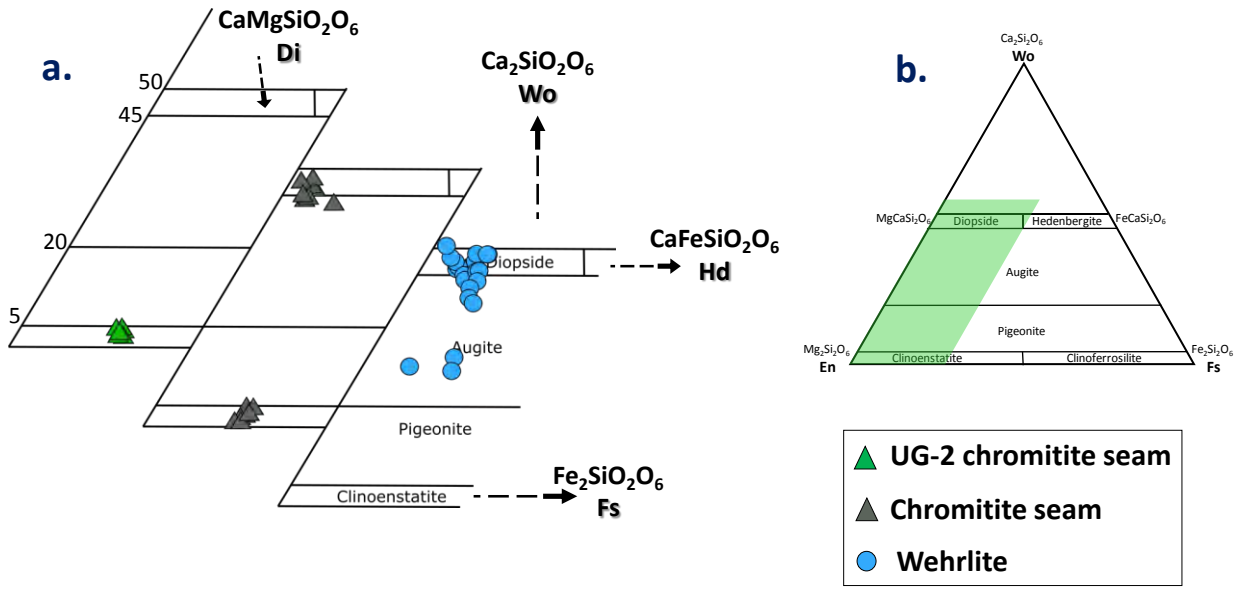

Figure 4-22: Wo-En-Fs quadrilateral representation of pyroxene compositions from drill core UMT-335. ***a.*** *a close-up figure into the enstatite-diopside section of the quadrilateral showing samples from the UG-2 chromitite seam, lower chromitite seam and wehrlite.* ***b.*** *Pyroxene quadrilateral plot showing the zoomed area.*

In the wehrlite, orthopyroxene is only found as grains enclosed within olivine grains. Three well-preserved grains were analysed from this unit (not shown in Figure 22). These pyroxenes are, interestingly, more Fe-rich, having a composition of $Wo_{0-2}\ En_{81-82}\ Fs_{17-19}$, with an Mg# of 79-80 that slightly lower than that of the lower chromitite seam and UG-2 chromitite. The grains are devoid of Cr_2O_3. MnO is slightly higher, with an average of 0.3 wt. %, whereas Al_2O_3 compositions are lower than those of the chromitite orthopyroxene (<0.4 wt. %).

Clinopyroxene within the wehrlite is often found as an interstitial phase enclosing spinel grains and olivine grains in some thin sections. In this unit clinopyroxene is present as diopside and augite, displaying a compositional range of $Wo_{27-50}\ En_{41-58}\ Fs_{6-15}$, and an Mg# range of 91-80 (Figure 4-22 and Figure 4-23). Fe^{3+} contents display a negative correlation with Mg#, with values increasing from 0.01 to 0.04 apfu (Figure 4-23a). Calculated contents of Ca-Tschermak activity displays a negative correlation with Mg# and is found to be low in those sections selected just above the xenolith (SD-06 and SD-17) with a range between 0.7 and 9.7 mol %. In comparison, clinopyroxene from most of the wehrlites display higher contents of Ca-Tschermak activity, ranging between 11 and 18.9 mol%. Compared with those of the chromitite, Cr_2O_3 in these clinopyroxenes have a steep negative correlation with Mg#, increasing from 0 to 1.1 wt.%.

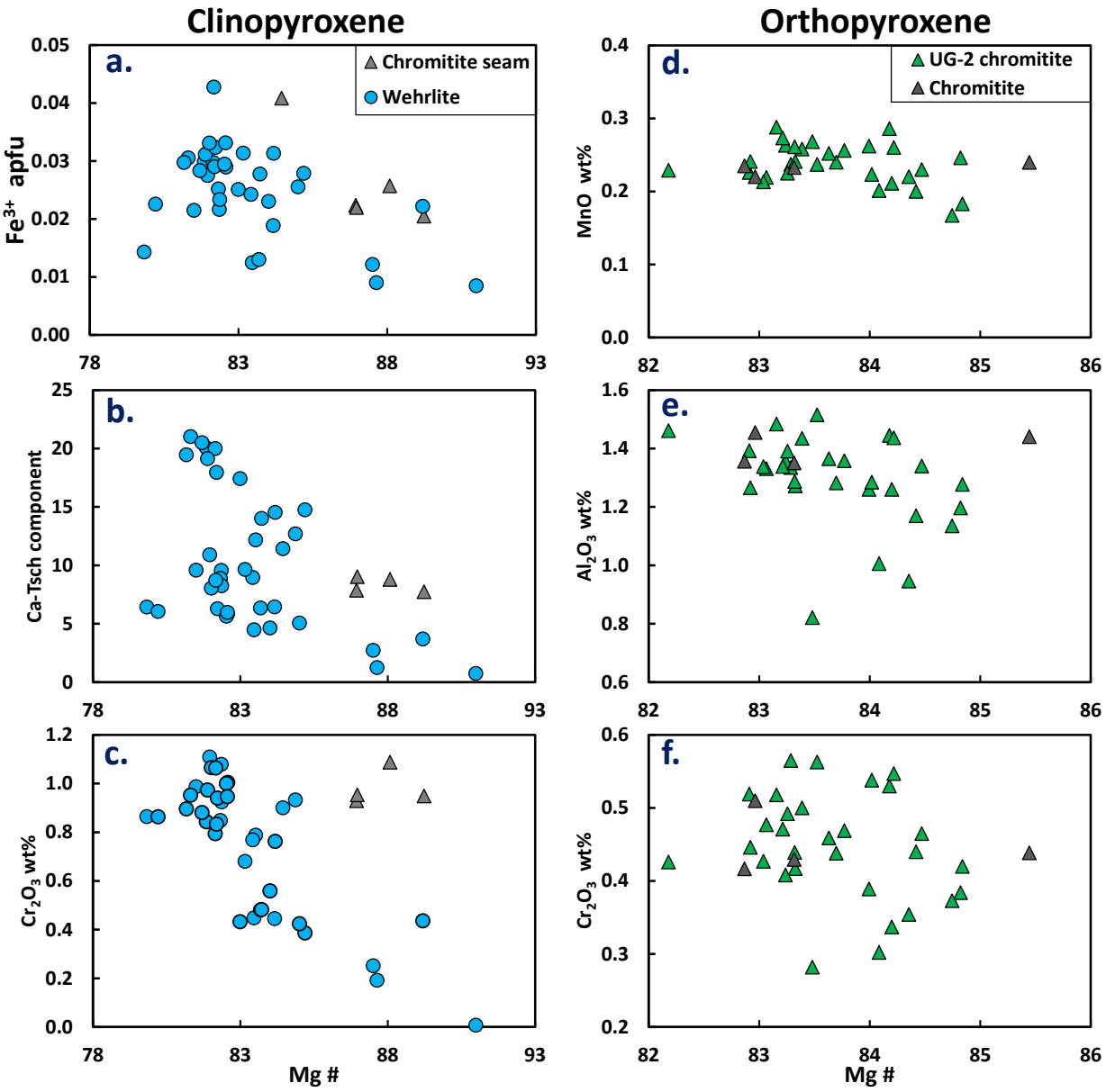

Figure 4-23: Compositions of clinopyroxene from the wehrlite and lower chromitite seam, and of orthopyroxene from the UG-2 chromitite seam and lower chromitite seam in drill core UMT-335. Clinopyroxene components include ***a.*** *Fe^{3+} cation in a.p.f.u,* ***b.*** *Ca-Tschermak component,* ***c.*** *Cr_3O_3. Orthopyroxene components include:* ***d.*** *MnO,* ***e.*** *Al_2O_3,* ***f.*** *Cr_3O_3.*

(iii) Plagioclase

Plagioclase compositions were analysed from three different lithologies in drill core UMT-335, including the UG-2 chromitite, lower chromitite seam and wehrlites. In the former two lithologies, plagioclase is present solely as an interstitial phase, while in the wehrlite plagioclase is present as both interstitial and olivine-enclosed phases. Representative composition of plagioclase are shown in Figure 4-24.

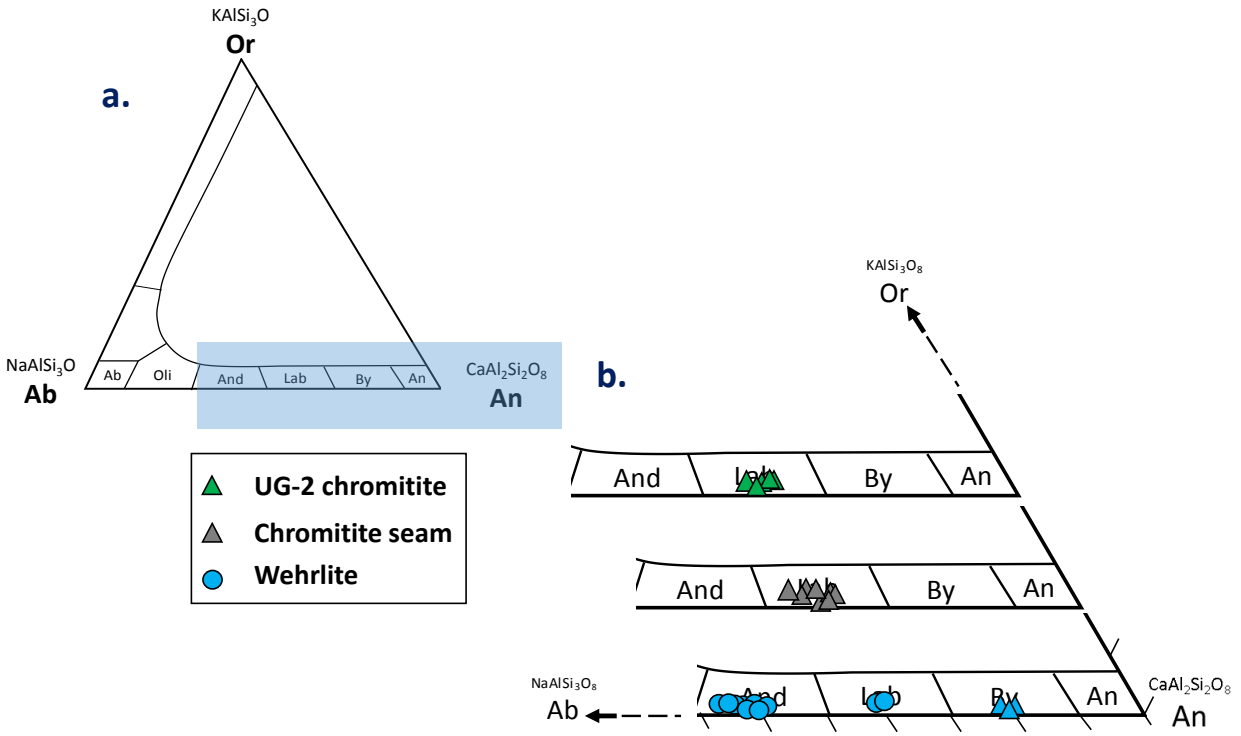

*Figure 4-24: Ternary Ab-Or-An diagram in **a.** showing the zoomed in section. plagioclase compositions from the UG-2 chromitite, lower chromitite seam and wehrlite in UMT—335. ▲ represents enclosed grains and ● represents interstitial grains.*

Plagioclase compositions in the UG-2 chromitite and chromitite are relatively homogeneous. The compositions of these feldspars are labradorite, with an An content range of An_{58-62}. The Na_2O, K_2O Al_2O_3 and CaO compositions are also evidently similar, ranging from 3.8 to 4.4, 0.18 to 0.37, 28.5 to 30 and 11.7 to 13 wt. %, respectively.

In the wehrlite, interstitial plagioclase shows a bimodal distribution of An composition. Plagioclase grains obtained higher in the stratigraphic section (SD-06) are relatively more calcic, with an An compositional range of An_{56-57}. Their Na_2O, K_2O Al_2O_3 and CaO compositions range between 4.5-4.6, 0.34-0.48, 27.7-29, 11.35-11.46 wt. % respectively. While those grains obtained lower in the stratigraphy (SD-17) have more sodic compositions with an An range of An_{31-39}. The Na_2O, K_2O Al_2O_3 and CaO oxide composition in this section vary between 6.7-77, 0.2-0.4, 24-26, and 6.5-7.9 wt. % respectively. Interestingly, enclosed plagioclase grains in this unit have more calcic compositions, with an average An content of 76, and Na_2O, K_2O Al_2O_3 and CaO oxide concentrations of 2.7, 0.01, 31 and 22.9 wt. % respectively.

(iv) Spinel-group minerals

As shown in Figure 4-25, spinels from this drill core occur as cumulus phases in the UG-2 chromitite and chromitite seam, while the spinels in the wehrlite units are disseminated. The spinels show a wide range of chemical variations with regards to major mineral compositions such

that three different spinel populations have been identified. Representative data of spinel from this drill core is shown in APPENDIX C.

Spinels from the UG-2 chromitite and lower chromitite units display more homogenous compositions than spinels in the wehrlite; these spinels have been categorized as type 1. The type 1 spinels comprise limited compositional variation with decreasing Mg#, with Mg# varying between 42 and 63. Contents of Al_2O_3 and Cr_2O_3 show positive correlations with Mg#. TiO_2 is slightly higher in the UG-2 chromitite (~1.5 wt) than in the chromitite seam (~0.9 wt.%). On the contrary, contents of V_2O_3 are higher in the chromitite seam compared with the UG-2 chromitite, with average values of 0.35 and 0.16 wt.% respectively. Based on the Cr-Fe-Al ternary classification plot in Figure 4-25a., Type 1 spinels show little compositional evolution from $Cr_{49}Fe^{3+}_{21}Al_{30}$ to $Cr_{46}Fe^{3+}_{28}Al_{26}$, demonstrating Cr—$Fe^{3+}$ exchange with little effect on Al, which follows the Fe-Ti trend. Similarly, the plot in Figure 4-25b shows a fairly constant Cr/(Cr+Al) ratio at ~0.63, while Fe^{2+}/(Fe^{2+}+Mg) increases from 0.38 to 0.54, following the Fe-Ti trend as well.

The population of accessory spinels found in the wehrlite are homogeneous chadacrysts enclosed in olivine and pyroxene and inhomogeneous textured spinel types. Homogenous spinels are categorized as type 2; they show systematically low Mg#, decreasing with decreasing Al_2O_3 (14.9 to 1.4 wt.%) and increasing TiO_2 (0.4 to 4.5 wt.%) contents. The contents of Cr_2O_3 and V_2O_3 show limited variability with Mg#, with values ranging between 30.9-42.4 wt.% and 0.24-0.54 wt.% respectively. In the Cr-Al-Fe ternary diagram in Figure 4-25a, these spinels follow the Fe-Ti trend where Fe^{3+} dramatically increases at the expense of Cr, while there is a subtle decrease in Al. In the variation plot of Cr/(Cr+Al) vs Fe^{2+}/(Fe^{2+}+Mg) in Figure 4-25b, these chadacrysts spinels exhibit subtle negative correlations, with ratios ranging between 0.58-0.73 and 0.76-0.93 respectively.

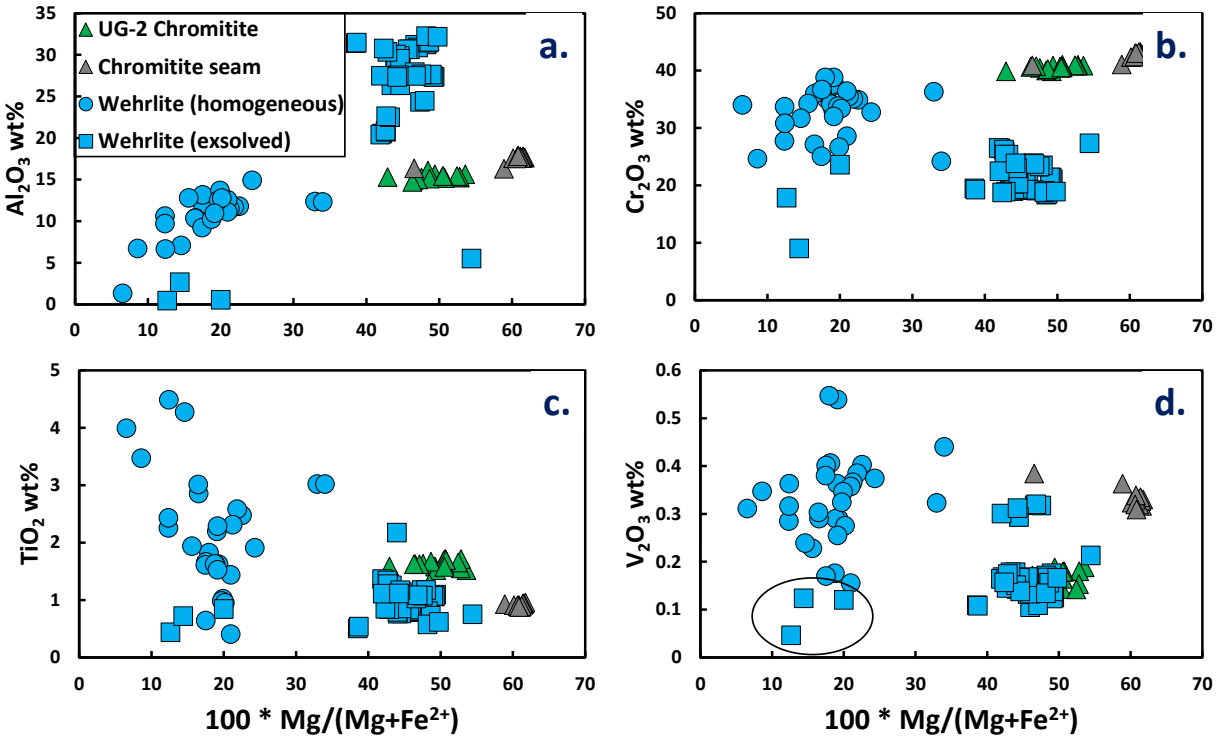

*Figure 4-25: Spinel geochemical variations of **a.** Al_2O_3, **b.** Cr_2O_3, **c.** TiO_2 and **d.** V_2O_3 potted against molar ratios of $Mg/(Mg+Fe^{2+})$ from the UG-2 chromitite, chromitite seam and wehrlite units. The points in the circle represent grains completely replaced by magnetite.*

Inhomogeneous spinels make up the type 3 spinel population. These spinels are characterised by relatively homogeneous Mg# and oxide compositions. Mg# slightly overlaps spinels from the chromitite seams, ranging between 38.6 and 54.4 (Figure 4-25). The Al_2O_3 content of these grains increases with increasing Mg#, while Cr_2O_3 and TiO_2 content show a subtle but negative correlation with Mg#, with values respectively varying between 21-32 wt.%, 18.4-26.5 wt.% and 0.6-2.2 wt.%. In Figure 4-26, inhomogeneous spinels follow the Rum trend, with the strongest Al enrichment towards the Al-apex compared with Cr and Fe^{3+}. Similarly, Cr/(Cr+Al) dramatically decreases with a subtle decrease in $Fe^{2+}/(Fe^{2+}+Mg)$. Grains that have experienced magnetite replacement show the lowest contents of Al_2O_3 (0.47-2.86 wt.%), Cr_2O_3 (9.03-23.63 wt.%), TiO_2 (0.44-0.84 w%) and V_2O_3 (0.05-0.12 wt.%), and the highest Cr/(Cr+Al) and $Fe^{2+}/(Fe^{2+}+Mg)$ ratios, with values of ~0.96 and 0.87 respectively.

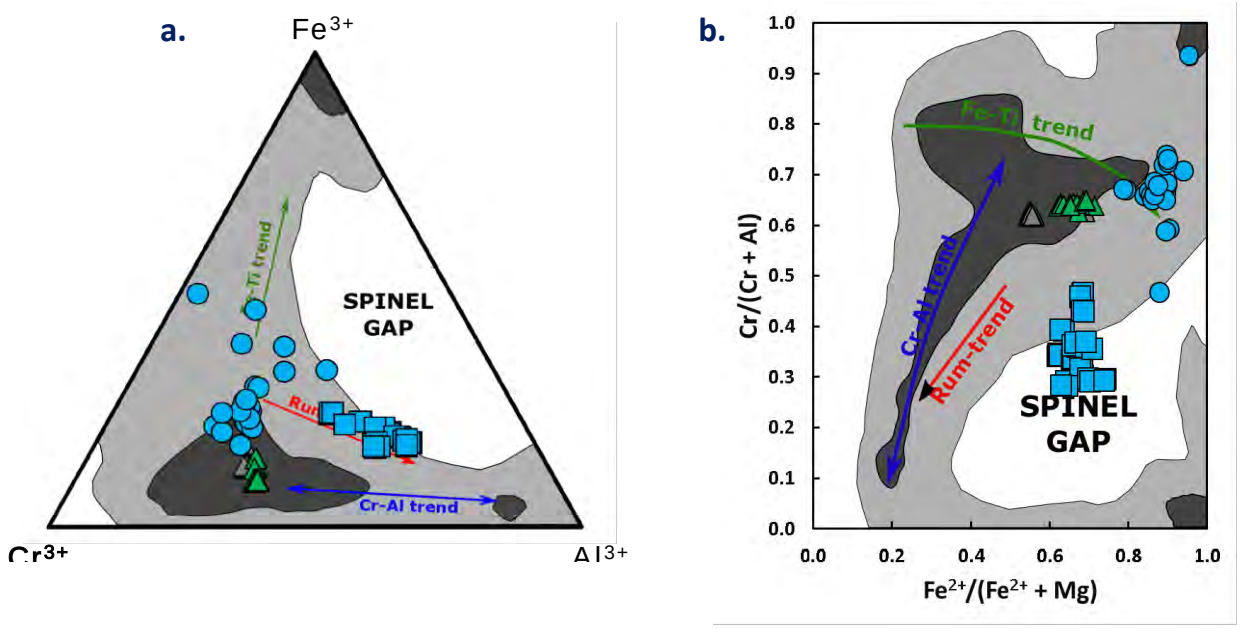

Figure 4-26: Solid solution chemical classification diagram for spinels from the feldspathic pyroxenite, chromitite seam and wehrlite within drill core UMT—335. Key for lithologies is the same as in Figure 4-25.

To evaluate compositional core-rim variations in spinels from the inhomogeneous grains, element distribution from core to the rim were determined. The grain shown in Figure 4-27 comprises an Al-rich core, which transitions into a Cr-Fe-rich zone (ferrit chromite) and then into a thin Cr-magnetite rim. The transition from the core to the ferrit chromite zone is more gradual in most oxide components, except for Al_2O_3 that shows a dramatic drop towards the rim. The core of the grain is enriched in Al_2O_3, FeO, Cr_2O_3, Fe_2O_3 with minor contents of MgO and TiO_2, MnO and V_2O_3 (less than 10 wt.%). There is a progressive enrichment in FeO and Fe_2O_3 towards the magnetite-rich rim, with values increasing from 26-55 wt.% and 14-29 wt.% respectively. MgO decreases from 7.2 wt.% to 0.3 wt.% towards rims, accompanied by a decrease in TiO_2 towards the magnetite rim. Contents of Cr_2O_3 show little variability from the core to the rim, a trend replicated by V_2O_3. Contents of MnO in the core are low compared to that of TiO_2, which subsequently increase at the ferrit chromite-core boundary then display a trend similar to that of TiO_2.

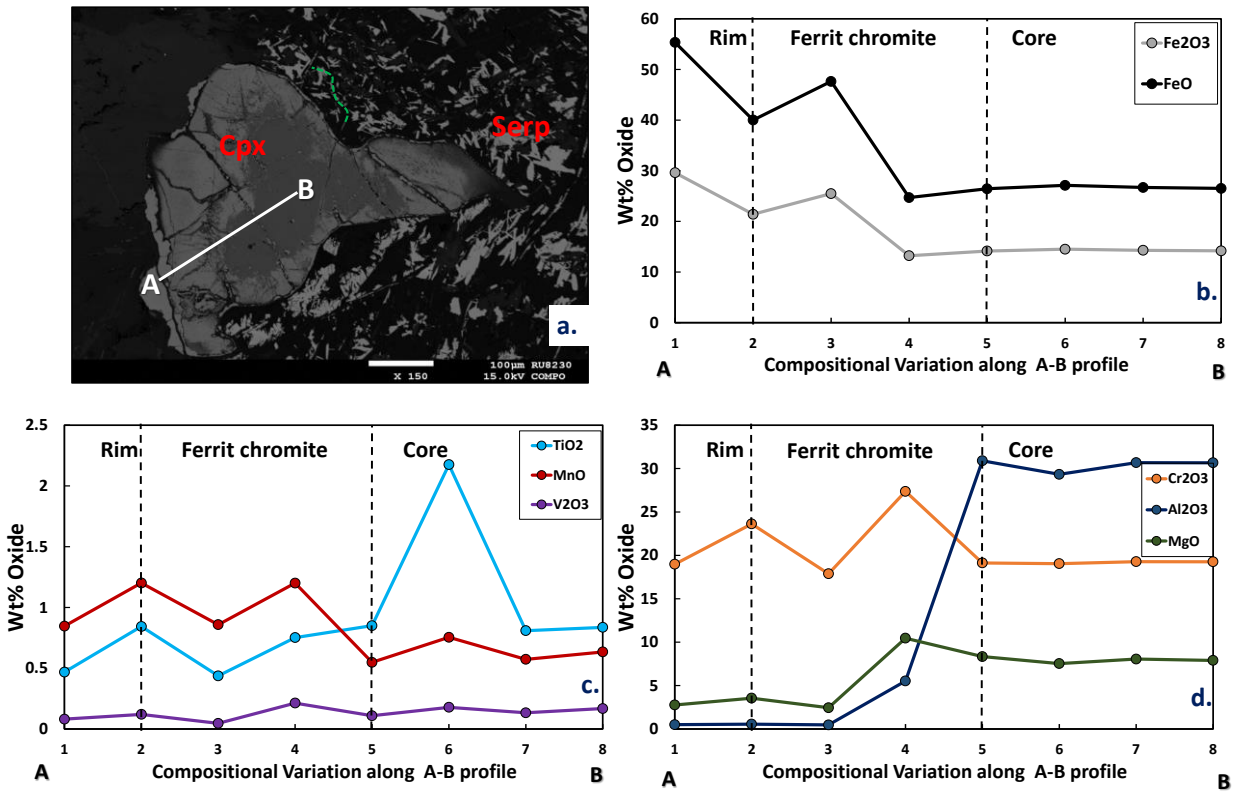

Figure 4-27: Quantitative microprobe core-to-rim profile of ***a.*** *spinel grain in sample SD-14* ***b.*** *Fe^{3+}, Fe^{2+},* ***c.*** *Ti, Mn, V* ***d.*** *Cr, Al, and Mg.*

4.2.3 UMT-094

Four sections were selected for mineral chemistry analyses in the most contaminated drill core, UMT-094. One section was obtained from the pyroxene-bearing troctolite, and three from the wehrlite. This drill core was analysed for olivine, pyroxene, plagioclase and spinel.

(i) Olivine

Olivine is in this drill core present as both anhedral (0.5-5 mm) grains and as subhedral grains enclosed in pyroxene. Mineral compositions of both olivines are illustrated in Figure 4-28. Within the troctolite, the compositions of olivines show limited variations between interstitial and enclosed grains. Their forsterite contents vary between Fo_{78} and Fo_{79}. There seems to be no systematic variation of oxides when plotted against Fo contents. Instead, contents of NiO form clusters of values between 0.22 and 0.26 wt.%. CaO, MnO and Cr_2O_3 contents are on average lower than those of olivine in the wehrlite, varying between 0.01-0.07, 0.28-0.32, and 0-0.015 wt. %, respectively.

Within the wehrlite, olivine compositions are relatively higher than that of the troctolite. Forsterite contents of interstitial phases vary between Fo_{84} and Fo_{86}. CaO and MnO slightly similar to those of the troctolite, ranging between 0.02-0.09 and 0.27-0.36 wt. %, respectively. NiO contents are much lower than those of the troctolite, forming a cluster between 0.03 and 0.1 wt.%. Meanwhile,

Cr_2O_3 shows an interesting distribution in contrast to that of the troctolite, by having many grains having no detectable Cr-content, while in a few grains, Cr_2O_3 ranges between 0.01 and 0.02 wt. %.

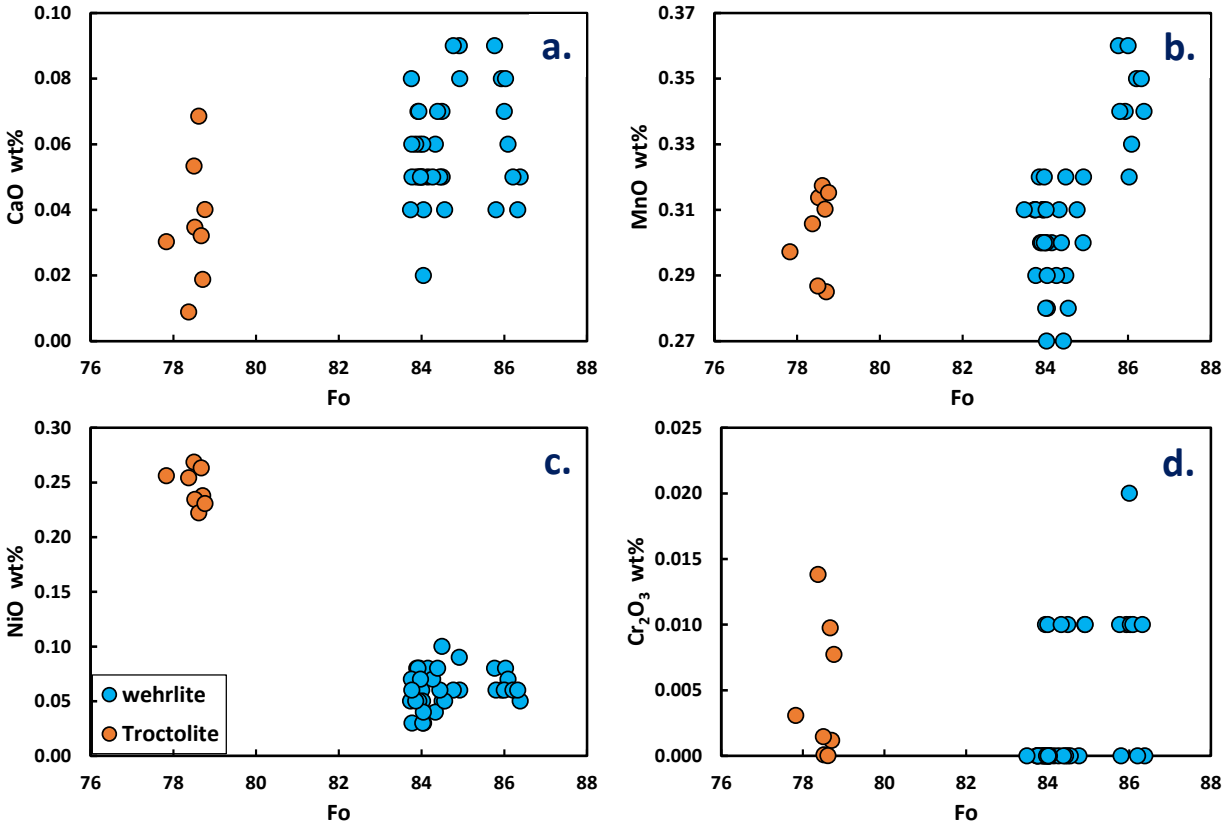

Figure 4-28: Olivine compositions from troctolite and wehrlite unitswithin the UMT—094 drill core.

(ii) Pyroxene

In this drill core, pyroxene is mostly found as cumulus clinopyroxene grains that tend to enclose minor grains of olivine and spinel. Orthopyroxene grains are only found as chadacrysts enclosed in olivine. The least altered grains were chosen for EPMA analyses in both lithological units, and only three grains of orthopyroxene were found and analysed. Representative mineral composition from both lithologies are illustrated in Figure 4-29 and Figure 4-30.

Those orthopyroxene grains enclosed in olivine are enstatite (not shown), with compositions of $Wo_{1.9-2.2}$ $En_{80-80.4}$ Fs_{17-18} and Mg# ranging between 82.0 and 82.2. Their oxide components of MnO, Al_2O_3 and Cr_2O_3 have limited variations, with compositions of 0.1-0.3, 0-0.1 and 0-0.3 wt. % respectively.

Clinopyroxene in the troctolite and wehrlite units are present as augite and diopside. In the troctolite, clinopyroxene displays a composition of Wo_{24-49} En_{43-62} Fs_{8-13} (Figure 4-29), with a relatively high Mg# ranging between 87 and 82. The Cr_2O_3 in these grains shows no systematic variation with Mg# with a range of 0.4-1.9 wt. %. Al_2O_3 shows a nearly linear correlation with

Mg#, varying between 1.6 and 3 wt. %. Similarly, the constrained Ca-Tschermak component of these clinopyroxenes is low compared with those of the wehrlite, ranging between 4 and 9.2 mol.%. The Fe^{3+}/Fe^{total} ratio in these clinopyroxene has a range between 0.02 and 0.3.

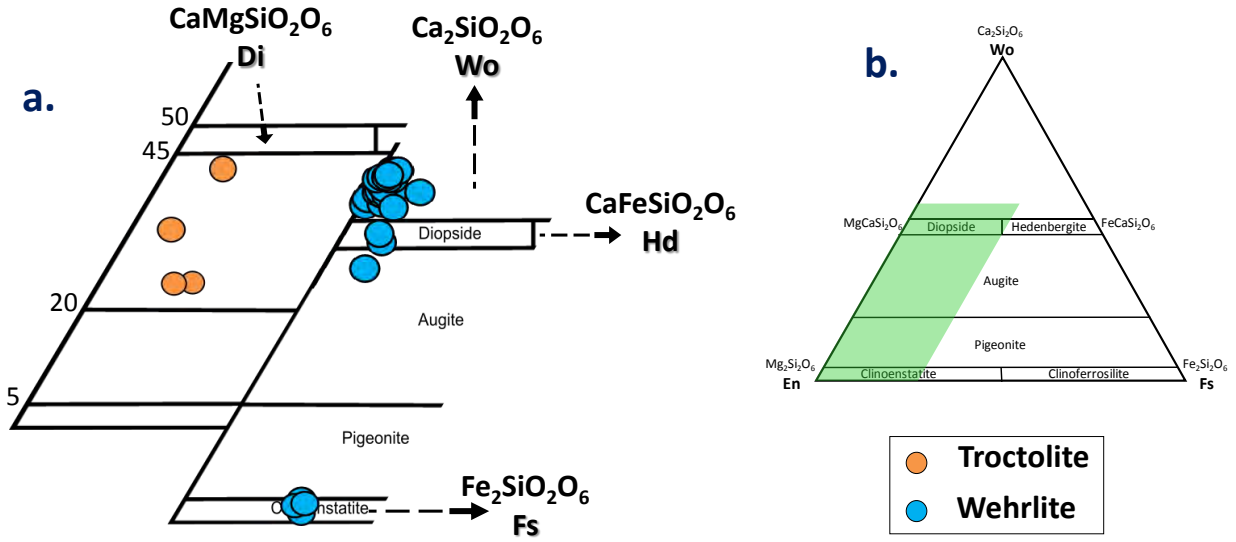

Figure 4-29: Wo-En-Fs quadrilateral representation of pyroxene compositions from drill core UMT-345. ***a.*** *a close-up figure into the enstatite-diopside section of the quadrilateral showing samples from the UG-2 chromitite and olivine gabbronorite.* ***b.*** *Pyroxene quadrilateral plot showing the zoomed area.*

Clinopyroxenes in the wehrlite, in comparison, are more Ca-rich. Their compositions average around $Wo_{42-53}\ En_{31-41}\ Fs_{3-9}$. These clinopyroxenes exhibit more Mg# variation, ranging between 80 and 92. Contents of Al_2O_3 show negative trends with Mg#, increasing from 0.7 to 9.6 wt. % . While the Cr-content shows no obvious trend with changing Mg#. Interestingly, a few grains of clinopyroxene in the wehrlite are devoid of Cr_2O_3, while in most grains the Cr-content ranges between 0.5 and 1.2 wt. %. Ca-Tschermak activity constrained for clinopyroxene is more variable, with values ranging between 2.2-33.1 mol%, with the highest values in samples proximal to the calc-silicate. A slightly negative trend can be observed for Fe^{3+}/Fe^{total} ratio, with values varying between 0 and 1.3, which are higher and more variable than those of the troctolite.

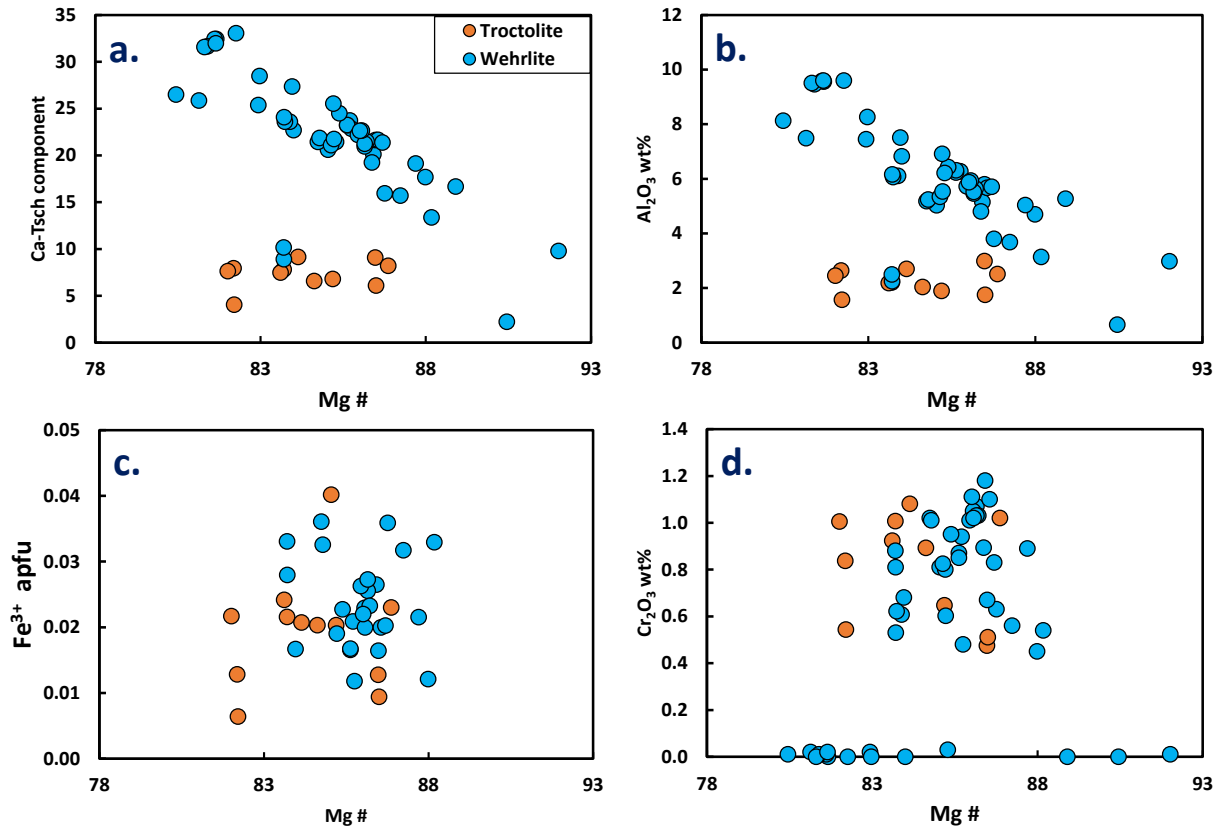

Figure 4-30: Clinopyroxene composition showing selected oxides (Al_2O_3 and Cr_3O_3), Ca-Tschermak component and Fe^{3+}apfu plotted against Mg# from the wehrlite and troctolite in UMT-094.

(iii) Plagioclase

Well-preserved plagioclase crystals are only present in the troctolite, mostly as grains enclosed in olivine, and a few as interstitial grains. Almost all the analysed grains in the wehrlite section are partially altered to clinozoisite. Representative mineral compositions of these grains are illustrated in Figure 4-31. Both enclosed and interstitial grains show limited variations in their mineral chemistry. The An content of the enclosed grains varies between An_{70-71}, classified as bytownite. Oxide compositions for Na_2O, K_2O Al_2O_3 and CaO range between 3.2-3.3, 0.2-0.3, 30.4-30.6, and 14.6-14.7 wt. % respectively. The An content of the interstitial grains ranges between An_{65} and An_{72}, with Na_2O, K_2O, Al_2O_3 and CaO ranging between 3.0-3.8, 0.2-0.3, 29.9-30.9, and 13.5-14.9 wt. % respectively.

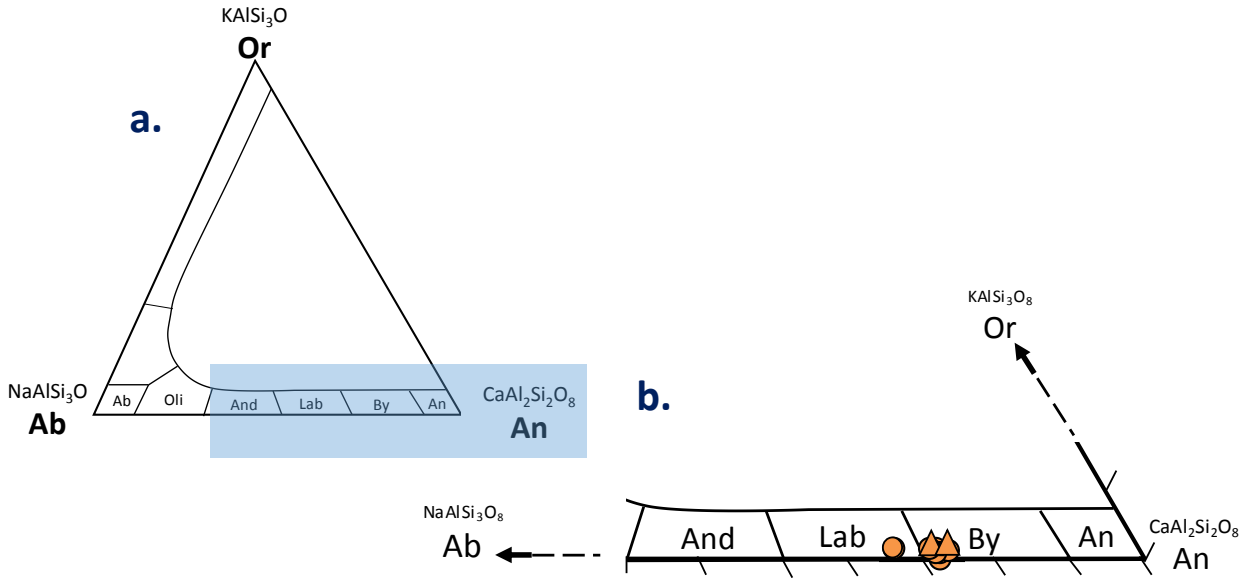

*Figure 4-31: Ternary Ab-Or-An diagram in **a.** showing the zoomed in section. plagioclase compositions from the troctolite in UMT-094. The ▲ represents enclosed grains, while ● represents interstitial phases.*

(iv) Spinel group minerals

In drill core UMT-094, spinels from the wehrlite and troctolite were analysed for mineral chemistry and are shown in Figure 4-32. Spinels in the troctolite have relatively low Mg# (24-29) and oxides with a limited compositional variation that are characterised by values of Cr_2O_3 (11.6-32.5 wt. %), TiO_2 (0.2-1.9 wt. %) and V_2O_3 (0.1-0.5 wt. %), and low Al_2O_3 (13.1-48.2 wt. %). In Figure 4-32a, these spinels are defined by a slight increase towards the Fe^{3+} apex following the diagram's Fe-Ti trend. The ratios of Cr/(Cr+Al) and Fe^{2+}/(Fe^{2+}+Mg) from this unit are relatively high, with values of ~0.63 and 0.73, respectively.

Most spinels that were analysed in the wehrlite in UMT-094 are opaque grains that are enclosed in clinopyroxene, together with just a few interstitial green spinels in a few samples. Spinels in the wehrlite, generally, display a wide range in Mg# that increases from 22 to 70 (Figure 4-32). A marked positive trend is observed for Al_2O_3 in both spinel types, increasing from 13 to 61 wt.%. In comparison, compositions of Cr_2O_3, TiO_2 and V_2O_3 display negative trends when plotted against Mg# decreasing from 32.1 to 0.1 wt.%, 1.9 to 0 wt.% and 0.4 to 0.01 wt.% respectively. Based on the ternary Cr-Fe^{3+}-Al diagram Figure 4-33a, these spinels show increasing contents towards the Al-apex following the Rum trend. This trend indicates an enrichment of Al in spinel at the expense of Cr and Fe^{3+}. Similarly, Cr/(Cr+Al) and Fe^{2+}/(Fe^{2+}+Mg) ratios of these spinels suggest the removal of Fe^{2+} and Cr in the spinel structure (Figure 4-33b.), which is balanced by the Al and Mg components.

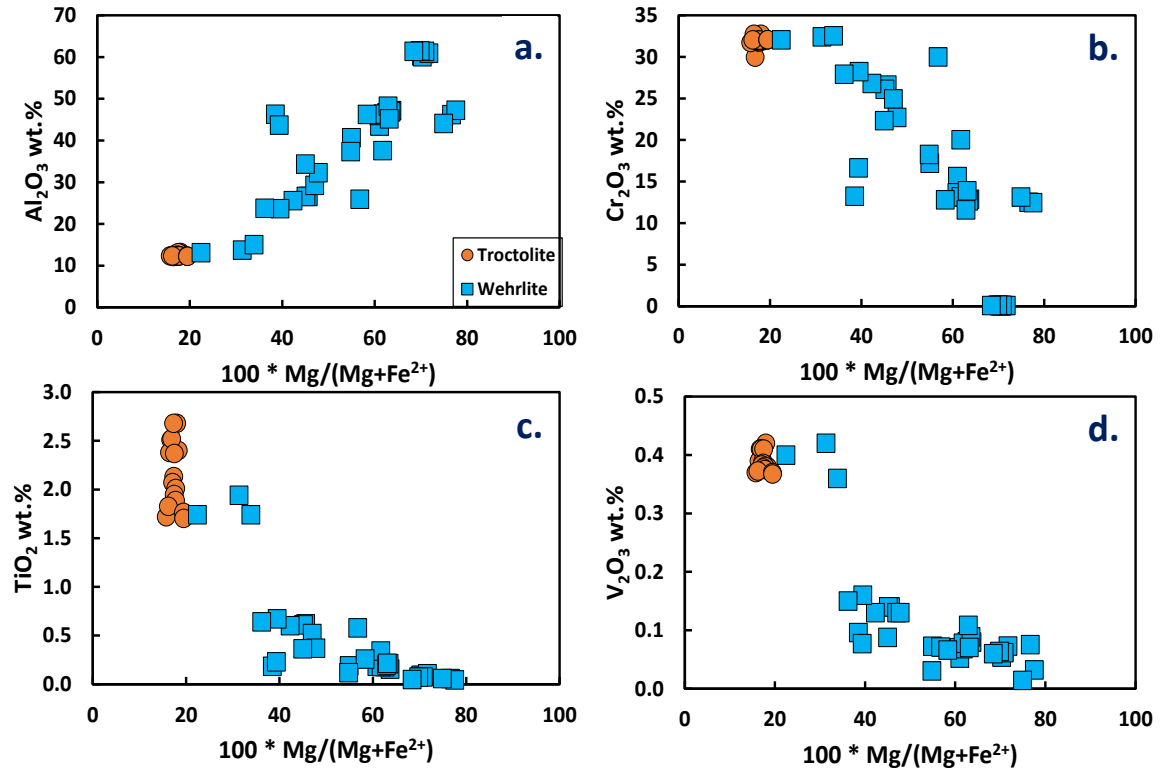

Figure 4-32: Spinel variations in ***a.*** *Al_2O_3,* ***b.*** *Cr_2O_3,* ***c.*** *TiO_2 and* ***d.*** *V_2O_3 potted against molar proportions of $Mg/(Mg+Fe^{2+})$ from both troctolite and wehrlite units.*

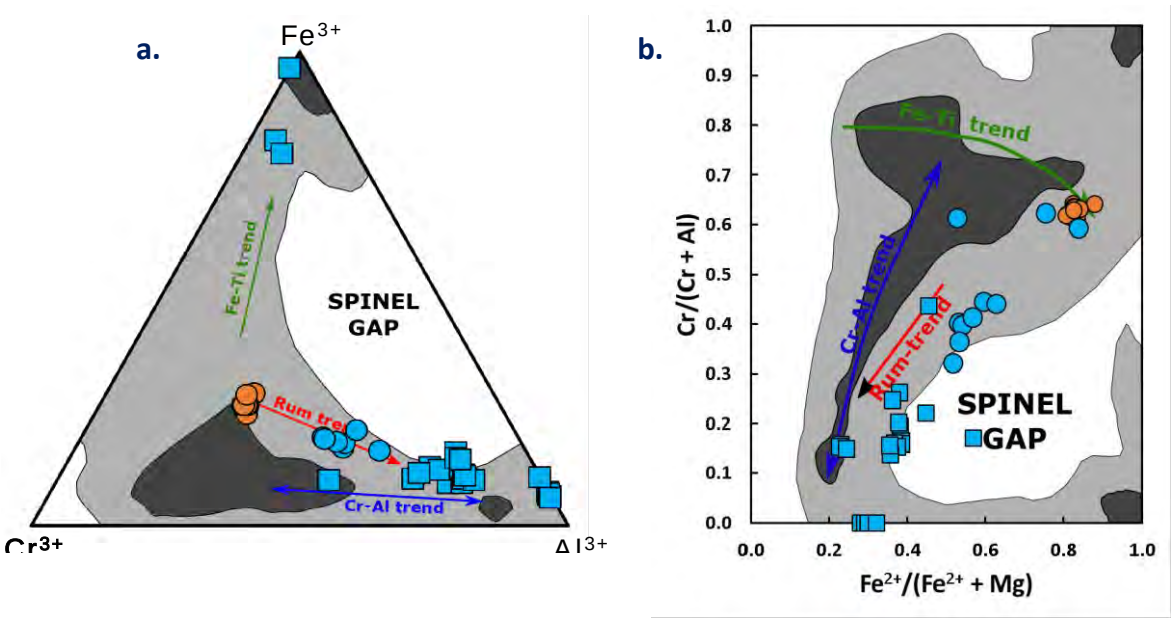

Figure 4-33: Spinel mineral compositions from the wehrlite and the troctolite. Symbols as in Figure 4-32 and grey field as in Figure 4-20

Exsolved spinel grains in the wehrlite are mainly found in sample SD-57, which is in contact with the dolomitic footwall (Figure 4-34). The spinels are exsolved into a Fe-rich phase (magnetite) and an Al-rich phase (spinel). The compositions of lamellae and bleb-like Fe-rich phase are enriched

in TiO_2 (0.97-1.11 wt.%) and depleted in MgO (2.7-4.9 wt.%), V_2O_3 (0.1-0.3 wt.%) and Al_2O_3 (2.6-3.1 wt.%). In comparison, the Al-rich phase has higher contents of MgO (up to 19 wt.%) and V_2O_3 (up to 0.6 wt.%) and depleted in TiO_2 (~up to 0.5 wt.%). There is a limited difference in Cr_2O_3 contents between the Al-phase and Fe-phase, as it varies between 11 and 13 wt.%, respectively. In the ternary Cr-Al-Fe^{3+} plot, the exsolved spinel fall within the miscibility gap for calculated spinels that coexist with olivine (Fo_{95}) at 600 ºC (Sack and Ghiorso, 1991).

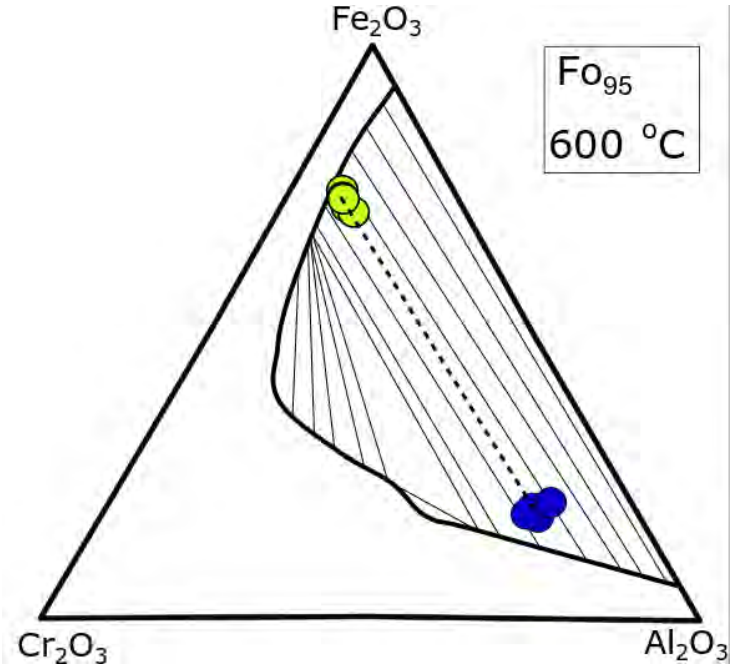

Figure 4-34: Ternary Cr-Al-Fe^{3+} plot showing compositional variation of exsolved Al (blue circles) and Fe (green circle) phase in spinels from SD-57. The fields for the solvus curve and its tie-lines are calculated for spinels that coexist with olivine Fo_{95} at 600 ºC (Sack and Ghiorso, 1991).

4.2.4 Summary of spinel morphology and chemistry

In summary, spinels examined in this study are categorised into three types based on morphology and mineral chemistry, as shown in Table 3. The categories include chromites found in the lower chromitite seam, UG-2 and the lower chromitite as type 1 spinels. These chromian spinels are found as cumulus phases in semi-massive to massive UG-2 chromitites as well as in the heavily disseminated chromitite seam. UG-2 chromites are often recrystallized, forming annealing texture characterised by triple-junction angles. Generally, type 1 chromian spinels comprise the most homogenous compositions as observed from Cr#, Mg# and Fe^{3+}/Fe^{total} ratios (Table 3)

Cr-spinels categorized as type 2 occur in the Footwall Assimilation Zone, mostly in its olivine gabbronorite, pegmatoidal troctolite and a few wehrlite units. Type 2 spinels are ferrian chromites that occur as enclosed chadacrysts in silicates, mostly olivine and orthopyroxene, and they are characterised by the lowest Mg# and highest Cr# ratios (Table 3).

Lastly, type 3 spinels are exclusive to units that experienced significant degrees of contamination (wehrlite) and vary from opaque picotite to green-coloured pleonaste and hercynite. These spinels comprise low contents of Cr, Ti, V and Mn and are enriched in Al and Mg. There is no marked systematic variation in Fe^{3+}/Fe^{total} ratios amongst the different types of spinels, except for a few type 3 spinels being enriched in Fe^{3+}.

Table 3: Summary of the morphology and the occurrence of spinel from the Flatreef

	Type 1	Type 2	Type 3
Host rock	Chromitite seam	Olivine gabbronorite, wehrlite, troctolite	Restricted to the wehrlite
Occurrence	Cumulus phase associated with interstitial orthopyroxene, clinopyroxene and plagioclase	Enclosed chadacrysts in olivine and orthopyroxene	Some are poikilitically enclosed in clinopyroxene and some are interstitial
Morphology	Euhedral to subhedral, polygonal chromites exhibit 120^{o} grain boundaries	Sometimes euhedral, but mostly subhedral, with smoothed grain boundaries	Anhedral, comprise resorbed grain interface
Rim	No rims	Zonation in grains associated with sulphides	Ferrit chromite, Cr magnetite
Exsolution	No exsolution	No exsolution	Thin magnetite veinlets, Al- Fe-orientated lamellae and bleb-like irregular exsolution
Mg#	31-45	4-30	29-70
Cr#	62-64	47-93	0-44
$Fe^{3+}/\sum Fe$	0.25-0.33	0.28-0.57	0.27-0.82

4.3 Whole-rock geochemistry

4.3.1 UMT-345

(a) Major element profiles

Major element variations across stratigraphic profiles for this core are plotted in Figure 4-35. Major elements generally show minor variation with stratigraphic depth but mainly depend on the rock-type. Whole-rock major and trace element concentration are presented in APPENDIX C.

The proportion of major elements generally show little variations between feldspathic pyroxenite units at the base and the top of the drill core, suggesting little variation. Abrupt changes can only be noted within the gabbronorite, calc-silicate, serpentinite and UG-2 chromitite. In the feldspathic pyroxenite, MgO, Fe_2O_3, CaO and MnO all show consistent patterns with changing stratigraphic depth. Cr_2O_3, Al_2O_3, TiO_2 and total alkalis display a more erratic pattern with changing height in the feldspathic pyroxenite. These patterns are disturbed by large anomalies at a depth of 1587 m, characterized by low MgO and Cr_2O_3, and high concentrations of CaO, Al_2O_3 and total alkalis. LOI (loss on ignition), reflecting mineral bound volatile contents of the samples, is generally low within the lower feldspathic pyroxenite, except at a depth of 1587 m where the LOI shows a minor positive anomaly.

Concentrations of MgO, Fe_2O_3 and MnO remain fairly constant in the olivine gabbronorite, showing average of 22, 12 and 0.2 wt.%, respectively. Concentrations of Cr_2O_3 and TiO_2 are erratic within this unit, similar to the feldspathic pyroxenite, ranging between 0.35-0.56 and 0.09-0.17 wt.%, respectively. Contents of CaO show a subtle but increasing trend within the gabbronorite, from 5 wt % closer to the pyroxenite contact to 10 wt.% st the calc-silicate contact. Concentrations of Al_2O_3 show a subtle concave up trend with changing stratigraphic depth, ranging between 3 and 6 wt.%.

Within the calc-silicate unit, the lowest concentrations of MgO (6 wt.%), Fe_2O_3 (8 wt.%), Cr_2O_3 (0.04 wt.%) and TiO_2 (0.08 wt.%) were noted. These compositions are accompanied by high values of Al_2O_3 (21 wt.%), CaO (16 wt.%), MnO (0.6 wt.%), total alkalis (1.4 wt.%) and moderately high LOI (3.2 wt.%). The transition from the calc-silicate to the serpentinites is defined by high concentrations of MgO and Fe_2O_3, respectively varying between 25-30 wt.% and 12-13 wt.%. Concentrations of Cr_2O_3 and TiO_2 are subtly increasing from the lower contact to the upper serpentinite contact, with values ranging between 0.05-0.2 wt.% and 0.04-0.1 wt.%.

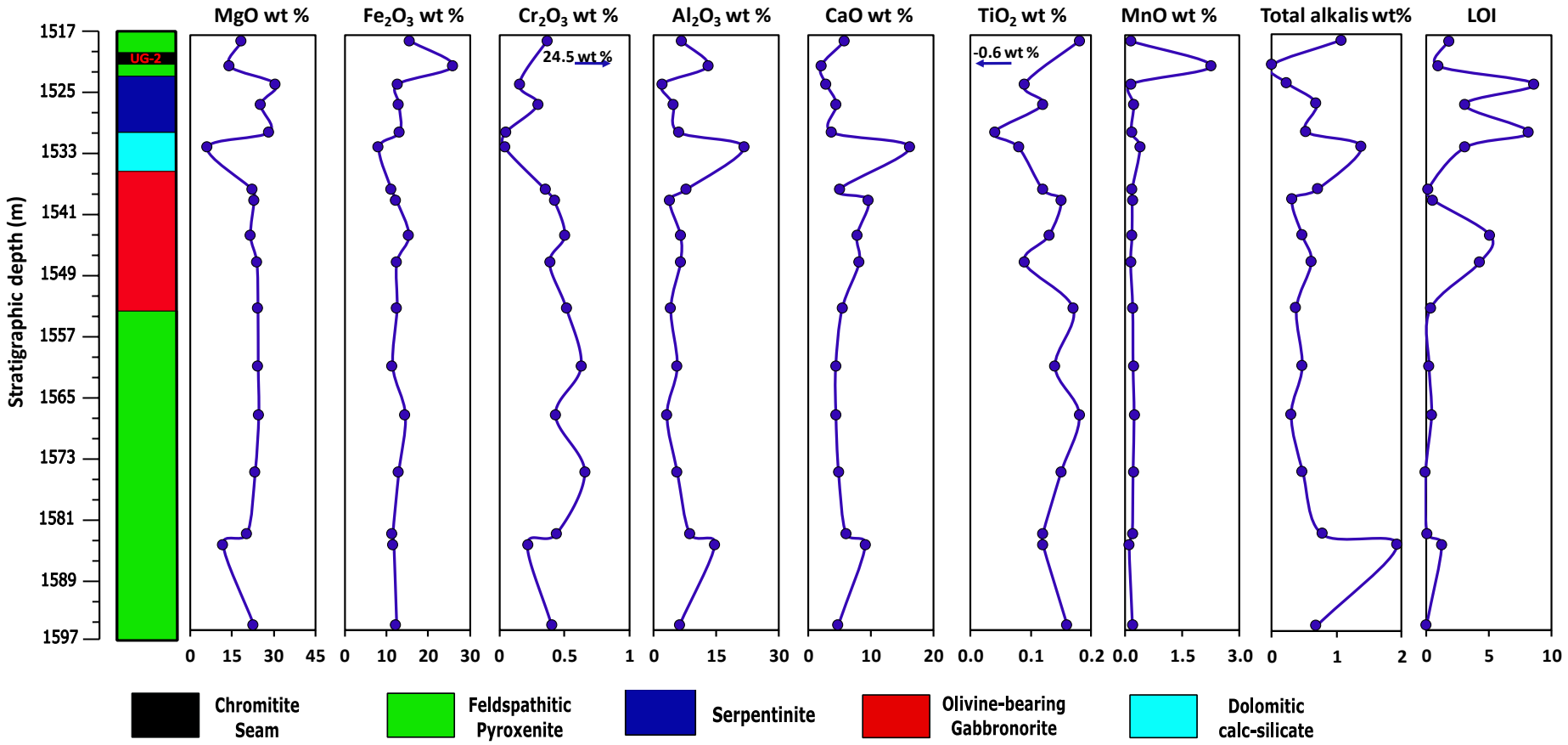

Figure 4-35: Selected major element variations across stratigraphic profiles from drill core UMT-094. The major elements presented here are MgO, Fe_2O_3 (as total iron), Cr_2O_3, Al_2O_3, CaO, MnO, TiO_2, total alkalis (K_2O + Na_2O) and LOI (loss on ignition). Variations within these elements are controlled by both changes in lithology and stratigraphic height.

Trends of decreasing abundance from the lower contact to the upper contact have been noted for Al_2O_3, CaO and total alkalis, varying between 6-2 wt.%, 4-2 wt and 0.6-0.2 wt.%, respectively.

Compositions within the UG-2 chromitite are characterized by relatively low concentrations of MgO, CaO, TiO_2, total alkalis and LOI, ranging between 14 wt.%, 2 wt.%, below detection levels of -0.6 wt.%, 0 wt.% and 1 wt.%, respectively. These compositions are accompanied by high contents of Fe_2O_3, Cr_2O_3, Al_2O_3 and MnO, with values varying between 26 wt, 25 wt.%, 13 wt.% and 2.3 wt.%, respectively. The feldspathic pyroxenite at the top of the drill core is characterised by low contents of MgO (18 wt.%), Fe_2O_3 (16 wt.%), Al_2O_3 (7 wt.%) and CaO (6 wt.%), with higher contents of TiO_2 (0.2 wt.%), total alkalis (1 wt.%) and LOI (1.8 wt.%).

(b) Trace element profiles

Transition metals

Figure 4-36 shows transition element profiles (V, Ni, Ti, Co, Cu) across the stratigraphic section of drill core UMT-345. Concentrations of V and Ti are largely controlled by the abundance of Cr-spinels within the entire drill core. V and Ti elements show relatively consistent concentrations in the feldspathic pyroxenite; gabbronorite, calc-silicate and serpentinite, with concentrations, mostly ranging between 28-137 ppm and 294-988 ppm respectively. Concentrations of V and Ti within the UG-2 chromitite are high, with values at 370 and 3808 ppm respectively. Contents of Ni, Co and Cu show similar trends, which are largely controlled by sulphides. The values of Ni, Co and Cu subtly increase towards the top of the stratigraphic section, ranging between 443-4100 ppm, 34-187 ppm, 103-2900 ppm. The abovementioned trends display a major anomaly at a depth of 1584 m, characterized by high contents of Ni, Co and Cu, with values at 4100 ppm, 187 ppm and 2041 ppm, respectively. This anomaly corresponds to an abundance of sulphides at this depth.

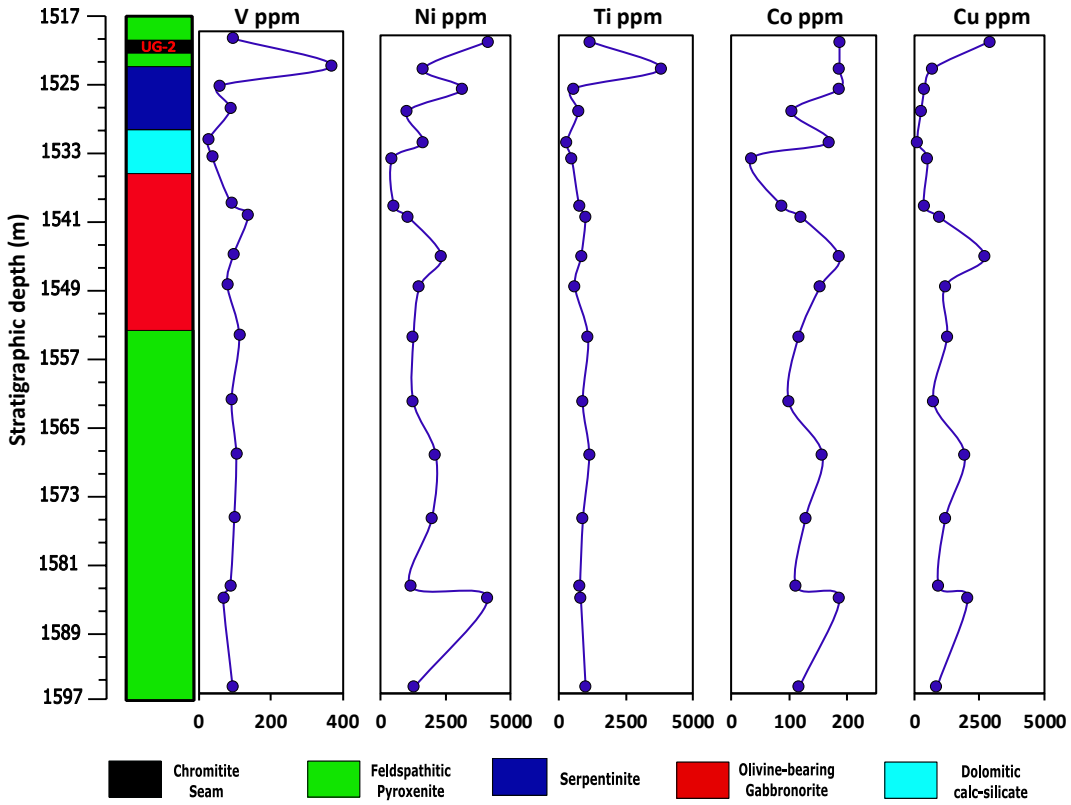

Figure 4-36: Selected transition elements of V, Ni, Ti Co and Cu from drill core UMT-345 plotted across stratigraphic depth.

Large Ion Lithophile Elements (LILE)

Large ion lithophile elements Sr, Rb, Ba, Cs and Pb, shown in Figure 4-37, display similar trends with stratigraphic depth. All LILE in the feldspathic pyroxenite show generally low concentrations of Sr (30-101 ppm), Rb (0.28-1.9 ppm), Ba (13-31 ppm), Cs (0.0-0.2 ppm), and Pb (0.0-0.1 ppm). At a depth of 1584 m, a positive anomaly has been noted, characterized by high concentrations of Sr (286 ppm), Rb (2.3 ppm), Ba (96 ppm) and Pb (29 ppm).

LILE in the gabbronorite are similar to those of the feldspathic pyroxenite, showing concentrations of Sr (43-95 ppm), Rb (0.8-2.5 ppm), Ba (14-36 ppm), Cs (0.1-0.7 ppm) and Pb (0.1-0.5 ppm). The calc-silicate displays the highest enrichment in Sr, Ba and Pb compared to adjacent units, with concentrations of 417, 142 and 22 ppm respectively. Concentrations of Rb (11 ppm) and Cs (2 ppm) are also enriched compared to the underlying gabbronorite. The serpentinite is enriched in Ba (2.5-21 ppm) and Cs (1.4-3.7 ppm). Concentrations of Sr, Rb and Pb are generally low, with concentrations varying between 62-10 ppm, 2.8-41 ppm and 5.7-9.2 ppm, respectively.

The UG-2 chromitite is depleted in Sr, Rb, Ba and Pb, with concentrations at 26 ppm, 2.1 ppm, 5.6 ppm and 4.2 ppm respectively. Cs is enriched compared to the feldspathic pyroxenite, with a composition of 1.6 ppm. Hanging wall feldspathic pyroxenite displays enrichment in LILE, with concentrations at Sr (79 ppm), Rb (12 ppm), Ba (42 ppm), Cs (0.9 ppm) and Pb (9 ppm).

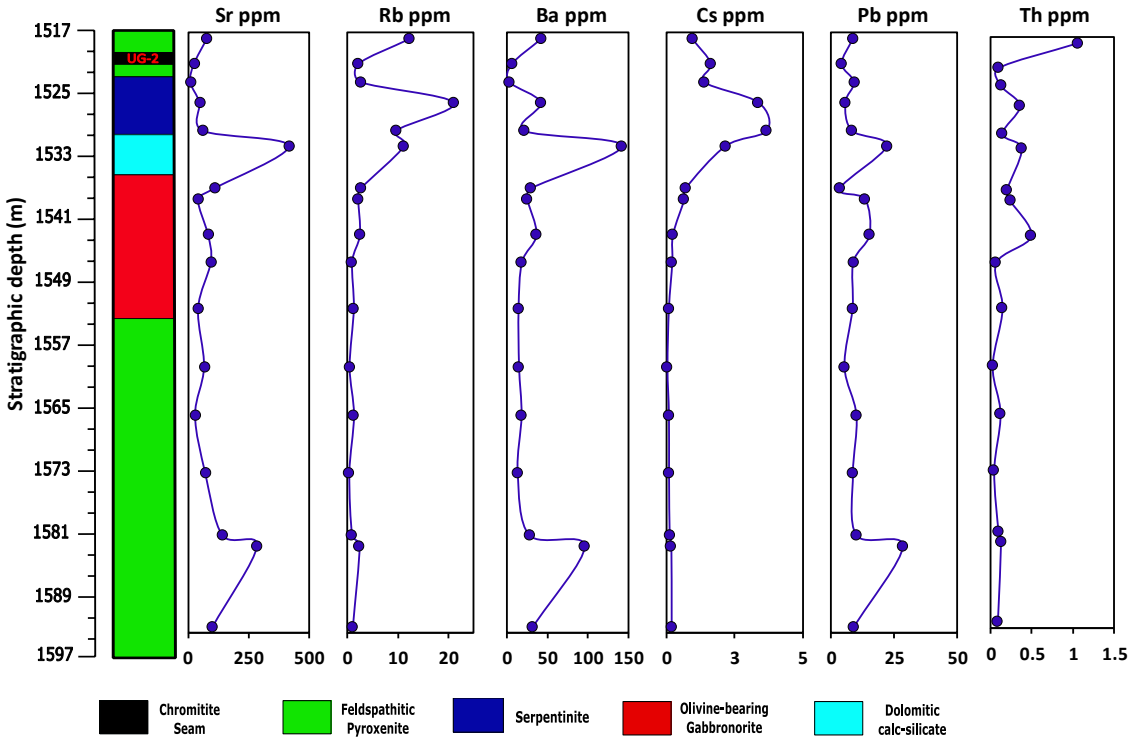

Figure 4-37: Selected large ion lithophile elements of Sr, Rb, Ba, Cs and Pb plotted across stratigraphic depth from drill core UMT-345.

High field strength elements (HFSE)

Figure 4-38 represents selected Zr, Hf, Nb, Ta, Y and Sc (HFSE) variations across stratigraphy. These elements show generally increasing trends with decreasing stratigraphic depth. Within the feldspathic pyroxenite HFSE show variations of Zr (6.2-8.2 ppm), Hf (0.14-0.26 ppm), Nb (0.1-0.3 ppm), Ta (0.007-0.013 ppm), Y (2.7-4.5 ppm) and Sc (20-30 ppm). The gabbronorite and calc-silicate unit show more HFSE enrichment with varying concentrations of Zr (6-13 ppm), Hf (0.2-0.4 ppm), Nb (0.1-0.7 ppm), Ta (0-0.04 ppm), Y (2.4-5.8 ppm) and Sc (24-42 ppm). The HFSE within the serpentinite show increasing trends towards the UG-2 chromitite hanging wall, with concentrations of Zr, Hf, Nb, Ta, Y and Sc ranging between 6-14 ppm, 0.1-0.4 ppm, 0.2-1.3 ppm, 0.01-0.1 ppm, 1.2-5.5 ppm and 9-27 ppm, respectively

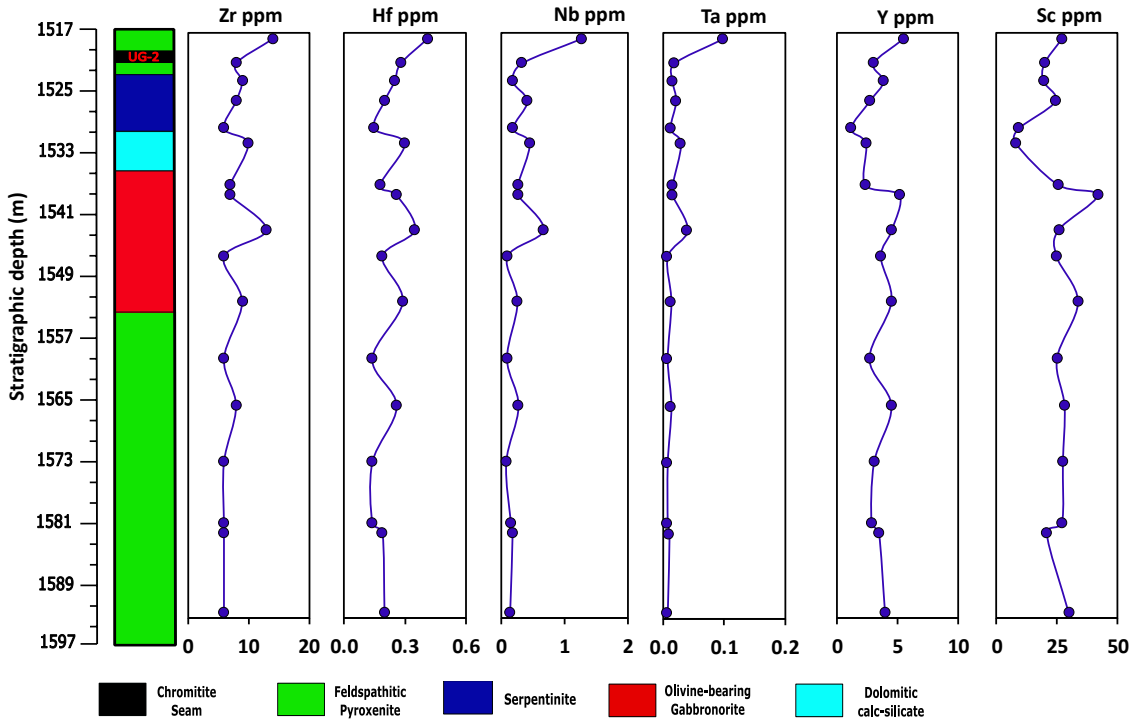

Figure 4-38: Variation of high field strength elements (Zr, Hf, Nb, Ta, Y and Sc) through drill core UMT-345.

(c) Primitive-mantle normalised element spidergram

Primitive-mantle normalized incompatible element plots from various lithologies from section UMT-345 are shown in Figure 4-39. When compared with the primitive-mantle, concentrations of Th, U, Pb and Sr are enriched, characterised by positive spikes, while Nb, Ta and P are depleted with negative spikes in all lithologies.

Feldspathic pyroxenite and olivine gabbronorite samples are slightly less enriched in incompatible trace elements than UG-2 chromitite, calc-silicate and serpentinite units. The observed positive Sr anomaly is more pronounced in the feldspathic pyroxenite compared to the olivine gabbronorite. One sample (UG-2 chromitite hangingwall) in the feldspathic pyroxenite shows slight enrichment of incompatible elements. This sample, comparable with the UG-2 chromitite, lacks both Rb and Sr anomalies, has a marked negative Ba anomaly and shows U enrichment relative to Th. The Nb-Ta anomaly observed in the UG-2 chromitite is not as pronounced as that of the feldspathic pyroxenite and olivine gabbronorite. Lack of Sr and Rb anomalies indicate low proportions to absence of evolved. A marked positive Ti anomaly is only observed in the UG-2 chromitite, consistent with the high proportion of chromite.

There is little to distinguish between the serpentinite and calc-silicate samples, except for a positive Ba spike in the calc-silicate and a Ba trough with varying amplitudes in the serpentine unit. The Sr spike in the calc-silicate is more pronounced than that of the serpentinites, and both lithologies lack Rb anomalies. The Sr anomaly in these units can be attributed to an abundance of carbonate-bearing phases (e.g. calcite). A negative Ti anomaly is observed in both units, accompanied by subtle negative Zr anomalies relative to the primitive mantle.

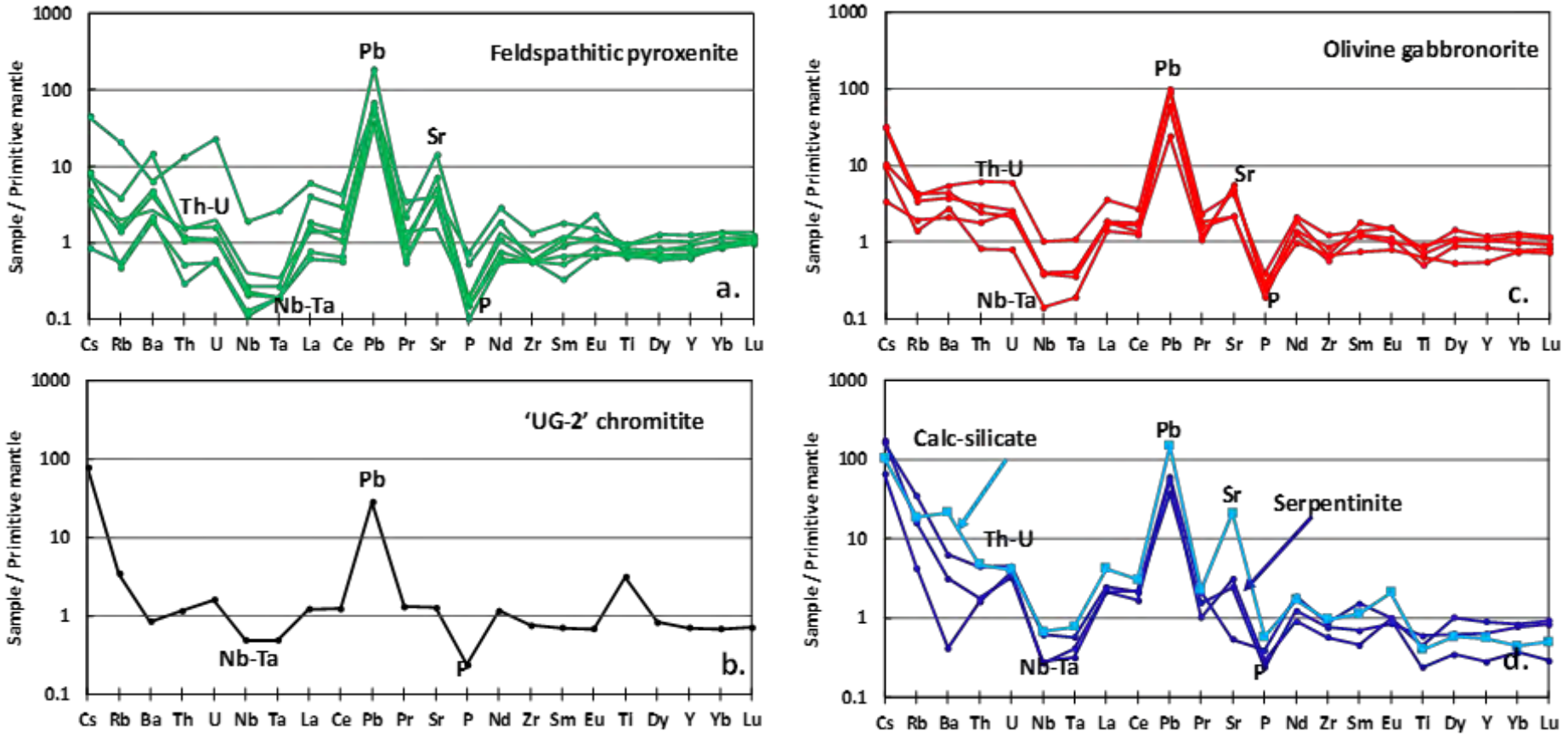

*Figure 4-39: Primitive-mantle normalized trace elements from selected lithological units of (**a**) feldspathic pyroxenite, (**b**) UG-2 chromitite, (**c**) olivine gabbronorite, (**d**) calc-silicate and serpentine. The normalization values are obtained from (McDonough and Sun, 1995)*

(d) Rare earth elements

Chondrite-normalized rare earth element (REE) plots for individual lithologies from UMT-345 are shown in Figure 4-40. Generally, all the lithologies show enrichment of light rare earth elements (LREE) and a flat heavy rare earth element (HREE) profile.

The REE distribution pattern for feldspathic pyroxenite samples is variable, with LREE varying amongst the samples while HREE are more consistent. Generally, the feldspathic pyroxenites show low REE abundance [$(La/Yb)_N$ = 0.8 – 4.6]. Most samples in the feldspathic pyroxenite display a positive Eu anomaly [$Eu/Eu^* = Eu_N/\sqrt{(Sm_N * Gd_N)}$] varying between 1.4 – 2.4, while a few samples lack an anomaly. The positive anomaly reflects high modal plagioclase content within the pyroxenites. The sample from the UG-2 chromitite exhibits a moderately enriched LREE and a flat HREE pattern, accompanied by the low ratio of $(La/Yb)_N$ = 1.8. The UG-2 chromitite profile is accompanied by a subtle negative Eu anomaly, with a Eu/Eu* ratio of 0.8.

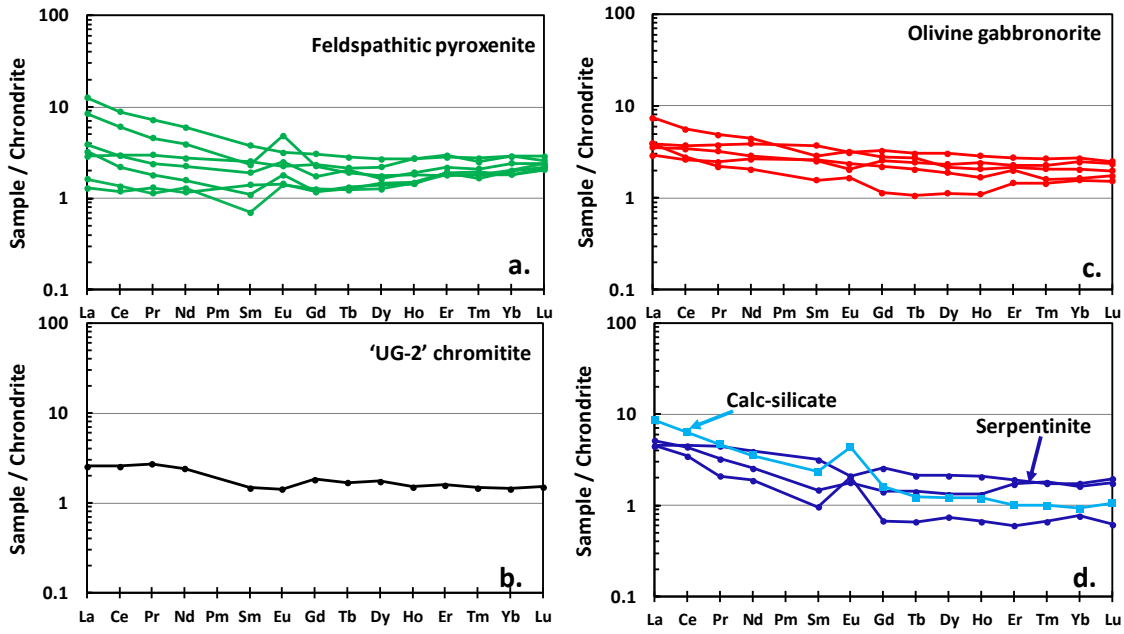

*Figure 4-40: Chondrite-normalized REE patterns from UMT-345 showing selected samples the (**a**) feldspathic pyroxenite, (**b**) UG-2 chromitite, (**c**) olivine gabbronorite, (**d**) calc-silicate and serpentinite. Normalization values from Boynton (1984).*

Olivine gabbronorites are characterised by a gently-sloping REE distribution pattern, with slight LREE-enrichment and near-flat HREE profile. Some of the samples in this unit do not show any Eu anomaly, while one sample shows a negative Eu anomaly and another a positive Eu anomaly. The serpentinite unit is characterised by LREE-enrichment and a flat

HREE pattern. Two samples show positive Eu anomalies with different amplitudes and one sample has a negative Eu anomaly. The calc-silicate sample shows a steeper LREE-enriched profile compared to serpentinites, with a flat HREE profile and a positive Eu anomaly (Eu/Eu* = 2.25).

4.3.2 UMT-335

(a) Major element profiles

Figure 4-41 illustrates the major element and LOI profiles with stratigraphic depth. This drill core has been affected by a substantial amount of contamination, which has resulted in more variable compositional distributions with stratigraphic depth. The feldspathic pyroxenite at the base of the section is characterised by high concentrations of MgO (21 wt.%), Fe_2O_3 (14 wt.%) and low Al_2O_3 (6.5 wt.%), CaO (4.2 wt.%) and total alkalis (1 wt.%). MgO and Fe_2O_3 decrease towards the para-pyroxenite and calc-silicate unit, with concentrations ranging between 7-9 wt.% and 7-11 wt.% respectively. Concentrations of Al_2O_3 and CaO are higher in the para-pyroxenite and calc-silicate unit, with concentrations of 11-15 wt.% and 20-22 wt.%, respectively. The following wehrlite unit is bound by two dolomitic xenoliths. This unit displays a concave trend of major elemental concentrations of MgO, Fe_2O_3, alkalis and MnO, characterised by concentrations varying between 19-24 wt.%, 14-16 wt.%, 0.3-0.8 wt.% and 0.21-0.26 wt.%, respectively. Concentrations of Al_2O_3, CaO and TiO_2 have decreasing values towards the centre of the section, with concentrations ranging between 2-9 wt.%, 8-14 wt.% and 0.1-0.4 wt.% respectively. LOI concentration is high in the wehrlite, calc-silicate and para-pyroxenite units.

The middle section of the stratigraphy is characterized by concentrations of MgO, Fe_2O_3, Cr_2O_3 and MnO that increase from the calc-silicate xenolith at 1745.5 m towards the UG-2 chromitite hanging wall at 1715 m, with concentrations ranging between 6.2-24.1 wt.%, 8.9-13.5 wt.%, 0-3.9 wt.% and 0.15-0.2 w%, respectively. Concentrations of Al_2O_3, CaO and alkalis are more antipathetic, decreasing from the calc-silicate to the chromitite seam, mostly ranging between 5.7-22.2 wt.%, 3.2-17.9 wt.% and 0.1-2.4 wt.%, respectively. The chromitite seam at 1734.6 m shows the highest enrichment in MgO (24.1 wt.%), Fe_2O_3 (13.5 wt.%), Cr_2O_3 (3.8 wt.%) and MnO (0.2wt.%), with the low contents of Al_2O_3 (5.7 wt.%), CaO (3.2 wt.%), TiO_2 (0.2 wt.%), alkalis (0.5 wt.%) and LOI.

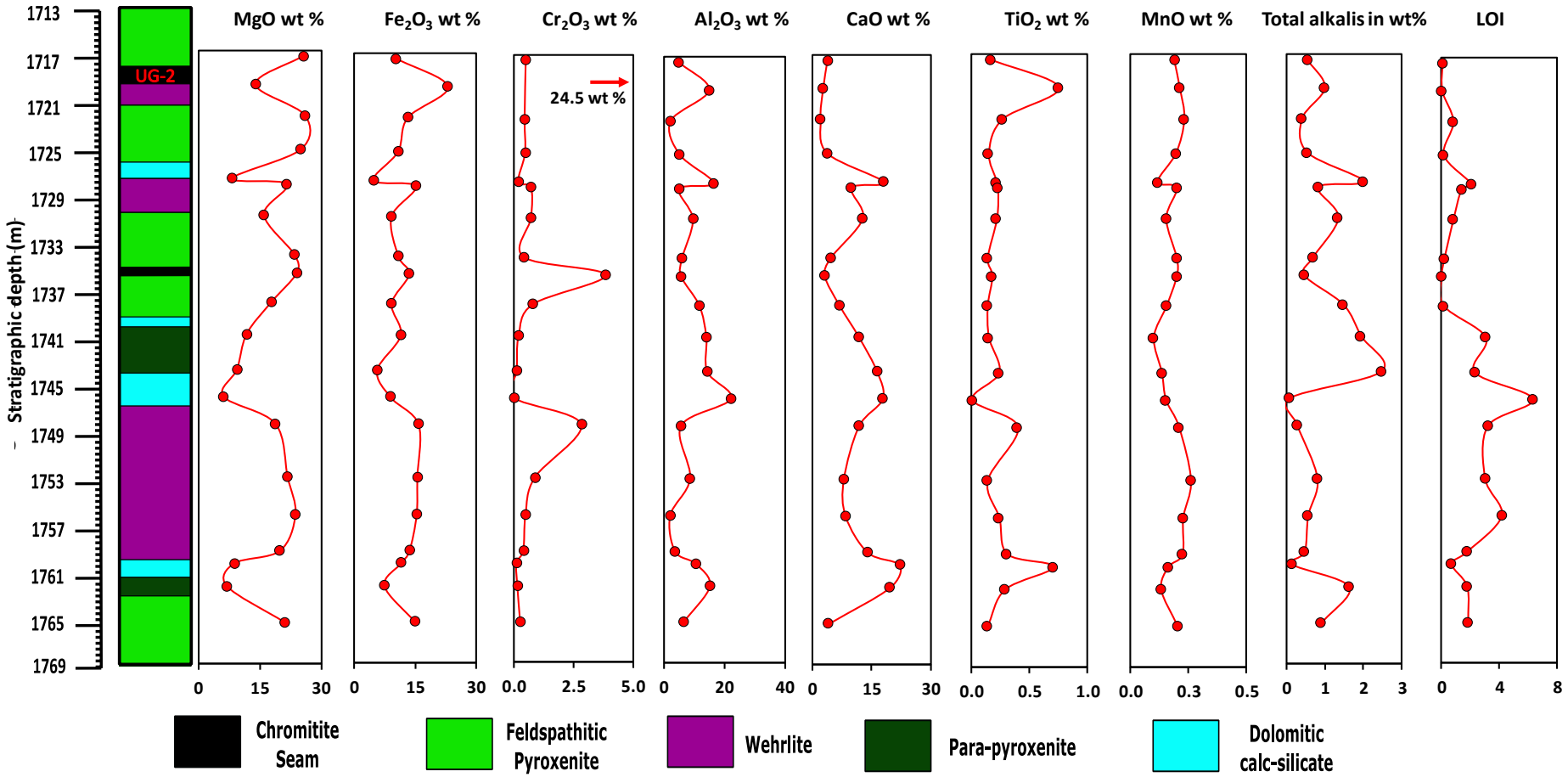

Figure 4-41: Selected major elements MgO, Fe_2O_3, Cr_2O_3, Al_2O_3, CaO, TiO_2, MnO, total alkalis and LOI through UMT-335 stratigraphic section

From the chromitite seam hangingwall (1733 m) to the UG-2 hangingwall (1715.5 m) a generally increasing trend is observed in MgO (23.5-26.7 wt.%), Fe_2O_3 (10.8-10.2 wt.%), TiO_2 (0.1-0.2 wt.%) and slight increasing in Cr_2O_3 (0.4-0.5 wt.%). A decreasing trend is also observed for Al_2O_3 (6.0-4.9 wt.%), CaO (4.8-3.9 wt.%) and total alkalis (0.7-0.5 wt.%). LOI is generally at its lowest within the pyroxenite unit and is only higher within the calc-silicate and contaminated unit, thus producing concave trend. The observed trends are disturbed by anomalies resulting from the calc-silicate unit, defined by low contents of MgO (8.3 wt.%), Fe_2O_3 (4.7 wt.%) and Cr_2O_3 (0.2 wt.%), as well as high Al_2O_3 (16.6 wt.%), CaO (18.2 wt.%) total alkalis (2.0 wt.%) and LOI.

The UG-2 chromitite seam at a depth of 1718 m is defined by peaks for Fe_2O_3, Cr_2O_3, Al_2O_3 and TiO_2, with concentrations of 23.0 wt.%, 24.5 wt.%, 15.0 wt.% and 0.8 t% respectively. A negative anomaly is only observed in MgO, showing a concentration of 14.0 wt.%.

(b) Trace element profiles

Transition metals

Transition metals in the UMT-094 drill core are mostly controlled by the variable occurrence of sulphides and chromite (Figure 4-42). Despite the presence of various spikes, transition metals show subtle decreasing profile with stratigraphic depth. Composition of the feldspathic pyroxenite at the base of the section is marked by low contents of V (87 ppm), Ti (889 ppm) and Cu (603 ppm) accompanied by low contents of Ni (1395.9 ppm) and Cu (144.6 ppm), relative to the hangingwall. These compositions show increasing trends into the hangingwall para-pyroxenite and calc-silicate. Interestingly, the latter unit shows the maximum values of V (208.3 ppm), Ni (1979.6 ppm), Ti (4477 ppm), Co (112.8 ppm), and Cu (1952.4 ppm) in the calc-silicate.

The thick wehrlite succession at the bottom of the section shows a little compositional variation in Ni, Co and Cu with stratigraphic depth. The average Ni, Co and Cu concentrations are recorded to be 1316.5 ppm, 135.5 ppm and 945.5 ppm, respectively. By contrast, concentrations of V and Ti are highly enriched at the depth of 1747.9 m, with maximum values of 358.1 ppm and 2456 ppm, respectively. Compared with the wehrlite unit, the overlying calc-silicate is depleted in all transition metals. Above the calc-silicate, the para-pyroxenite unit displays V, Ti and Cu concentrations equal to those of the

feldspathic pyroxenite. While one sample of the para-pyroxenite shows a slight positive spike in Ni and Co, indicative of abundance of sulphide phases.

The feldspathic pyroxenite at the top of the section (between 1737.2 and 1715.5 m) exhibits fairly consistent transition metals, only showing marked spikes arising from interlayered lower chromitites seam and calc-silicates. Average concentrations of V, Ni, Ti, Co, and Cu in the feldspathic pyroxenite have respective values of 108.7 ppm, 573.8pp, 1083 ppm, 88.4 ppm and 162.0 ppm. The chromitite seam and UG-2 chromitite at depths of 1734.6 m and 1718.0 m display pronounced enrichment spikes in all transition metals. In contrast, the calc-silicate only shows local enrichment in Ni (3413 ppm), Co (187 ppm), and Cu (1701 ppm).

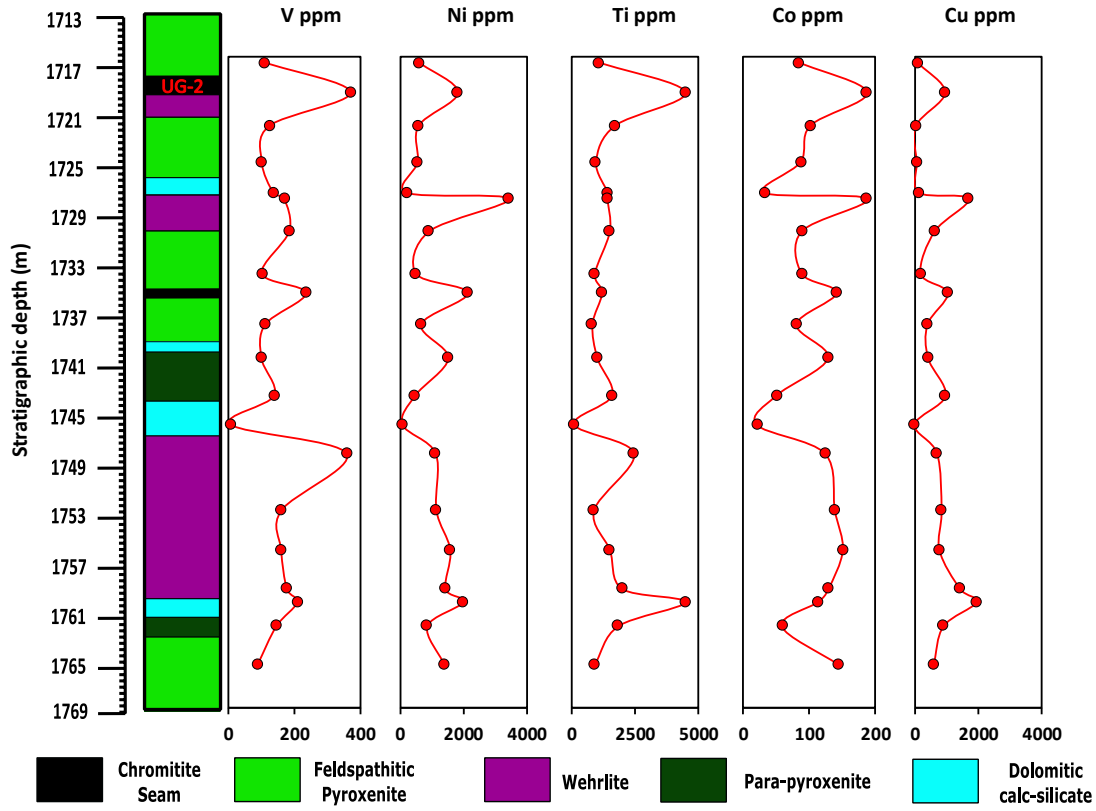

Figure 4-42: Selected transition metals of V, Ni, Ti, Co and Cu from various lithologies with UMT-335 drill core.

Large ion lithophile elements

Large ion lithophile element (Sr, Rb, Ba Cs and Pb) profiles plotted against stratigraphic depth are displayed in Figure 4-43. Except for various anomalies, all LIL elements behave the same across stratigraphic depth. Generally, the feldspathic pyroxenite is characterised by low concentrations of LILE, including chromitite layers. There is a trend of decreasing

LILE in feldspathic pyroxenites with decreasing stratigraphic depth, with significant concentration ranges for Sr (149.3-69.9 ppm), Rb (10.9-2.3 ppm), Ba (97.8-24.3 ppm), Cs (7.1.-1.2 ppm), and Pb (10.8-2.3 ppm).

The feldspathic pyroxenite between the depths of 1737.2 m and 1715.9 m comprises interlayered units of chromitite, minor wehrlite and calc-silicates. Generally, LILE compositions show trends of subtly decreasing concentration towards the top of the section; Sr (188.6 to 65.9 ppm), Rb (4.8 to 2.3 ppm), Ba (76.3 to 24.3 ppm) and Cs (1.0 to 1.2 ppm). A pronounced enrichment spike is observed within the calc-silicate for Sr, Rb and Ba, with values of 348.6 ppm, 75.0 ppm and 439.9 ppm, respectively.

Concentrations of LILE in the wehrlite unit between the depth of 1759.1 – 1747.9 m have an erratic pattern. Sr and Ba display similar patterns with low concentration ranges of 155.6–54.1 ppm and 22.4–57.3 ppm, respectively. A positive spike is present in sample SD-15 (at 1752.6 m) of Sr (434.0 ppm) and Ba (165.1 ppm). Compositional trends of Rb (2.8-10.6 ppm), Cs (1.3–4.5 ppm) and Pb (2.8–10.6 ppm) are similar in the wehrlite. These are marked by a positive spike in sample SD-16 (at 1755.9 m) relative to Sr and Ba.

Para-pyroxenite units at the depth of 1762.2, 1742.6 and 1740 m show high concentrations of LILE relative to calc-silicates, with regards to contents of Sr (333.5-463.7 ppm), Rb (63.8-85.7 ppm), Ba (257.5-636.5 ppm), and Cs (2.4-2.9 ppm). In contrast, an associated dolomitic xenolith at the depth of 1745.4 m is depleted in all LILE and contain values of 28.0 ppm Sr, 0.53 ppm Rb, 7.5 ppm Ba and 0.05 ppm Cs. In comparison, the para-pyroxenite units are characterised by high concentrations of LILE. Sr, Rb, Ba and Cs range between 453.7-429.2 ppm, 63.8-19.9 ppm, 257.5-186.0 ppm and 2.4-2.8 ppm, respectively.

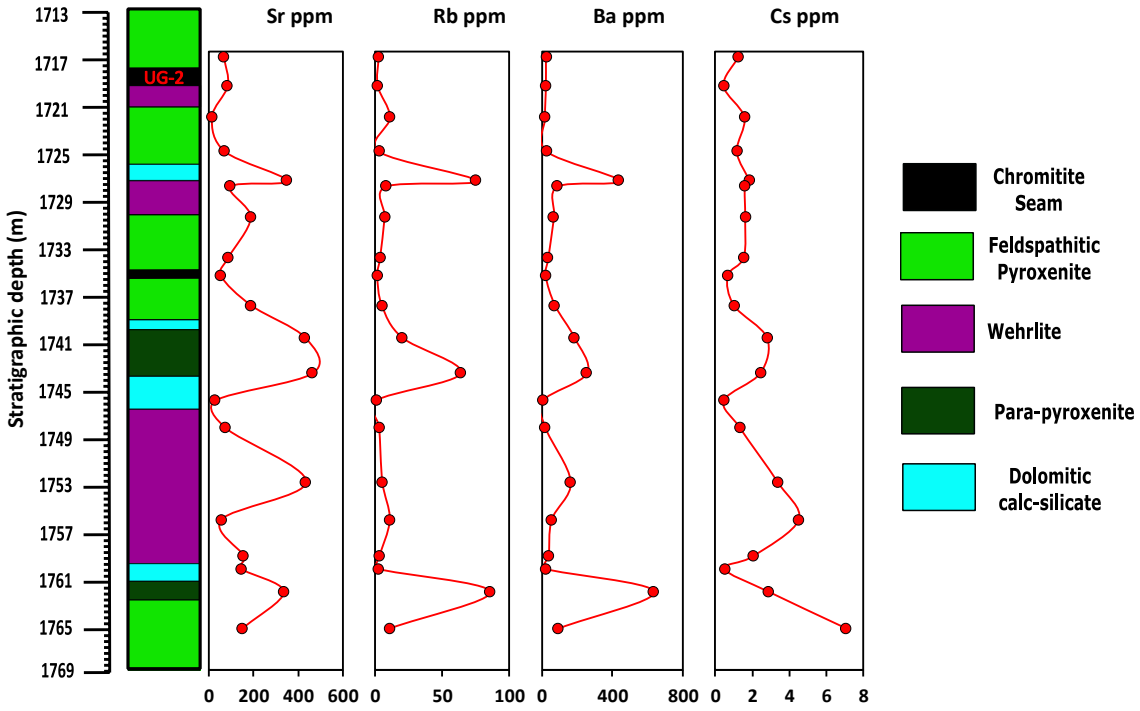

Figure 4-43: Large ion lithophile elements of Sr, Rb, Ba and Cs from various lithologies plotted against stratigraphic height from drill core UMT-35.

High field strength elements (HFSE)

High field strength element profiles from selected lithologies of UMT-335 are illustrated in Figure 4-44. These profiles exhibit trends of subtly decreasing concentration towards the top of the stratigraphic section, as was also described for the LILE. Feldspathic pyroxenite at the base of the section is characterised by low concentrations of HFS elements, such as Zr (6 ppm), Hf (0.14 ppm), Nb (0.19 ppm), Ta (0.01 ppm), Y (3.5 ppm), and Sc (21.6 ppm). The overlying para-pyroxenite is defined by a pronounced positive spike in most HFSE, with enriched concentrations of Zr (86 ppm), Hf (3.2 ppm), Nb (0.7 ppm), Ta (0.1 ppm) and Sc (62.2 ppm). Y is not seemingly following the same trend as other HFSE, as it is marked by a negative anomaly with a concentration of 5.4 ppm.

Wehrlite samples mostly show consistent compositions with stratigraphic depth, excluding sample SD-15 that shows a marked HFSE depletion. The wehrlite HFSE concentrations range between Zr (25-32 ppm), Hf (0.6-0.9 ppm), Nb (0.8-1.2 ppm), Ta (0.07-0.1 ppm), Y (10.1-116 ppm) and Sc (34-40 ppm). The only calc-silicate in this drill core that is depleted in HFSE is the calc-silicate at a depth of 1745.5 m. Its concentrations are Zr (6.0 ppm), Hf (0.14 ppm), Nb (0.47 ppm), Ta (0.01 ppm), Y (4.61 ppm), and Sc (1.1 ppm). The para-

pyroxenite above the calc-silicate shows minor enrichment of HFS elements, with values at Zr (79 ppm), Hf (0.7 ppm), Nb (0.9 ppm), Ta (0.1 ppm), Y (11 ppm), and Sc (27 ppm).

The lower chromitite seam at the base of this pyroxenite has depleted HFS elements. In comparison, the wehrlite and calc-silicate show similar compositions to those of the wehrlite between the depth of 1759 and 1747.9 m. The footwall to the UG-2 is characterised by increased HFSE concentrations, similar to that of depth 1747.9 m (SD-14), with contents of Zr (64 ppm), Hf (1.11 ppm), Nb (1.64 ppm), Ta (0.10 ppm), Y (0.71 ppm) and Sc (7.6 ppm).

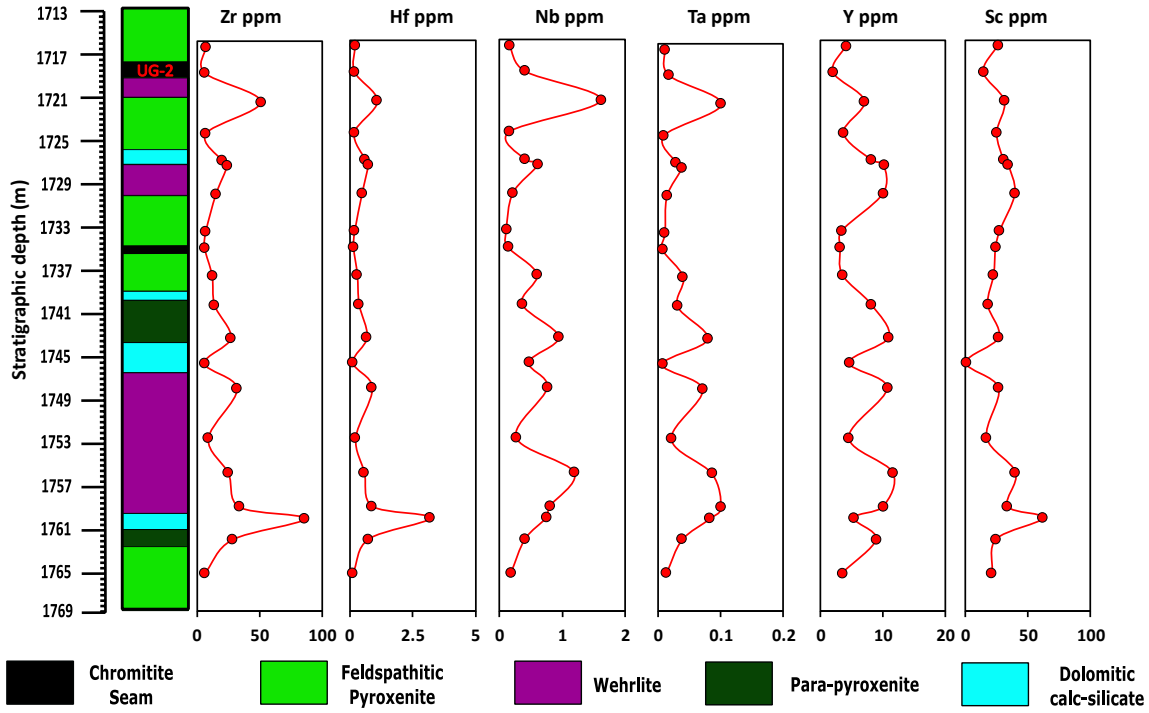

Figure 4-44: Selected high field strength elements of Zr, Hf, Nb, Ta, Y and Sc selected from various lithologies present in the section UMT-335

(c) Primitive-mantle normalised trace element spidergrams

Primitive mantle normalized element variation plots of different lithologies from drill core UMT-345 are illustrated in Figure 4-45. All these plots show relatively similar trends and anomalies, with negative Nb-Ta, P and positive Th-U, and Pb anomalies. The element patterns are relatively steep with enriched HFS elements, which then generally flattens out from Nd to Lu.

All feldspathic pyroxenite and wehrlite samples show near-similar patterns (Figure 4-45 a and c.). The Sr peaks are subtle and not greater than 10 times the primitive mantle (PM)

in the feldspathic pyroxenite. Within the wehrlites, one sample shows a subtle Ba peak, pronounced depleted Th, U, Nb and Ta anomalies and an enriched Sr peak. The Sr anomaly in the wehrlites is nearly absent in most samples and is only enriched in one sample with a value ~20 x PM. A subtle Zr and Ti trough is present in both lithologies.

The chromitite seams (Figure 4-45 b) show generally similar trace element patterns, which are Ba-enriched relative to Rb and subtly Ta depleted relative to Nb. Both seams lack an anomaly for Zr. A marked Ti enrichment is present in the UG-2 chromitite, while that of the lower-lying chromitite is subtler.

The analysed four calc-silicate samples all show slightly variable trace element patterns (Figure 4-45 d). Only two samples show enrichment in LILE (Cs, Rb and Ba). All calc-silicate samples maintain the observed positive Th-U and negative Nb-Ta anomalies, while only one sample lacks the marked positive Pb, Sr and negative P anomaly that were noted in the cumulate rocks. Most calc-silicate samples maintain the observed negative Zr and Ti anomaly of the cumulate rocks, only one sample has positive Zr and Ti anomalies. Both analysed para-pyroxenite samples show similar profiles to two calc-silicate samples. They are LILE-enriched, similar to one calc-silicate sample. These maintain the negative Zr and Ti anomaly observed in the cumulate rocks.

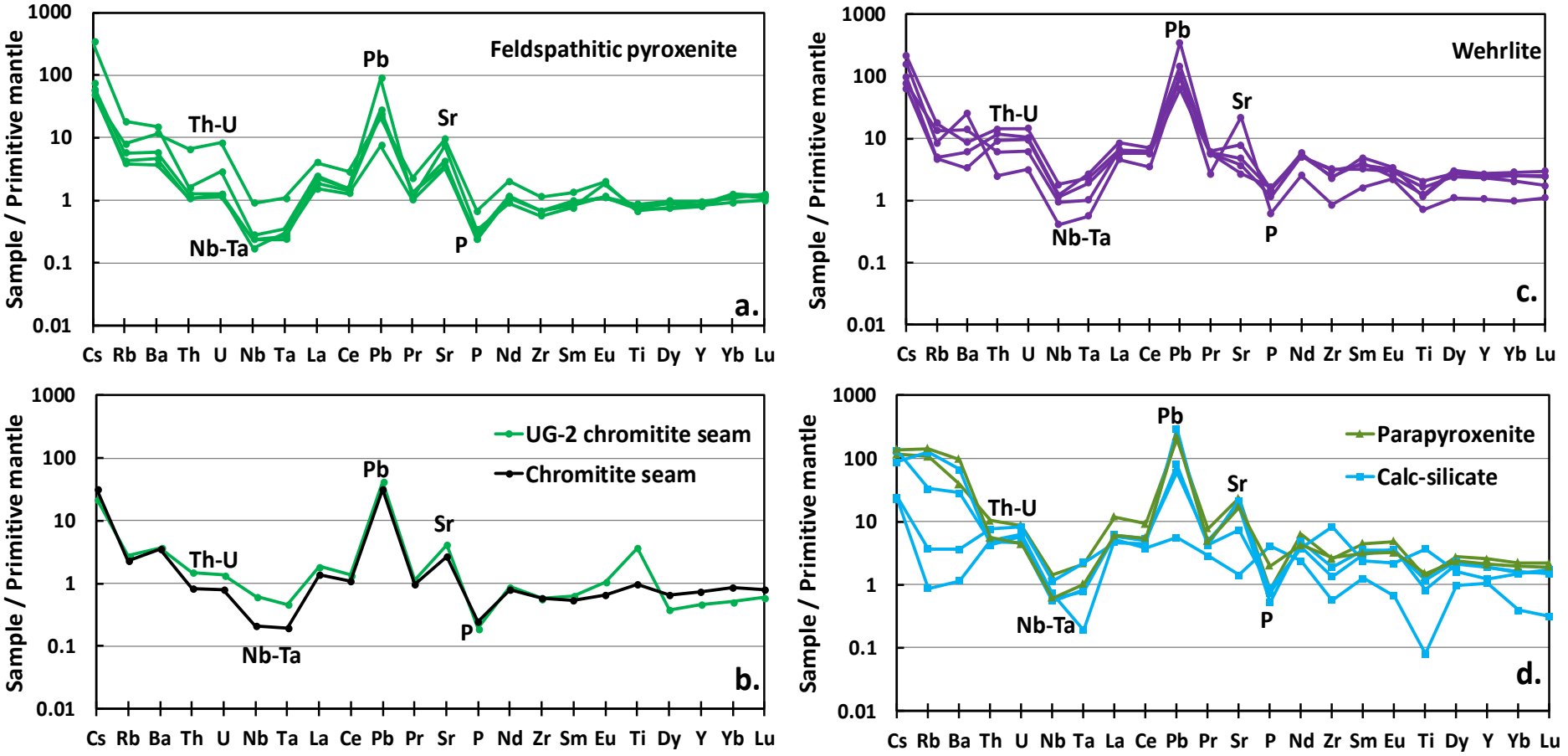

*Figure 4-45: Primitive mantle-normalized trace elements from selected samples of the feldspathic pyroxenite, (**b**) UG-2 chromitite and lower chromitite seam, (**c**) wehrlite, (**d**)calc-silicate and para-pyroxenite lithologies in drill core UMT-345. Normalization data from McDonough and Sun (1995).*

(d) Rare earth elements

Chondrite-normalized REE patterns for individual lithologies from UMT-335 are plotted in Figure 4-46. The chondrite normalized lithologies are LREE enriched and have flat HREE-depleted pattern. Most feldspathic pyroxenite and chromitite lithologies have trough-like patterns that are depleted in middle rare earth elements (MREE) and have flat HREE. Wehrlites, para-pyroxenites and calc-silicate all show relative enrichments in LREE about 10 times chondrite.

The feldspathic pyroxenite samples are have relatively flat REE patterns, as shown by low $(La/Yb)_N$ ratios ranging between 1.5 and 4.3. There is a relative enrichment in total REE in a few samples. A positive Eu anomaly with varying amplitudes (Eu/Eu* = 1.3-2.7) is present in most samples, while one sample shows a marked negative Eu anomaly (Eu/Eu* = 0.4). The feldspathic pyroxenite samples display a slight enrichment in the $(Ga/Lu)_N$ ratio, with values ranging between 0.5 to 0.8, displaying concave-up patterns.

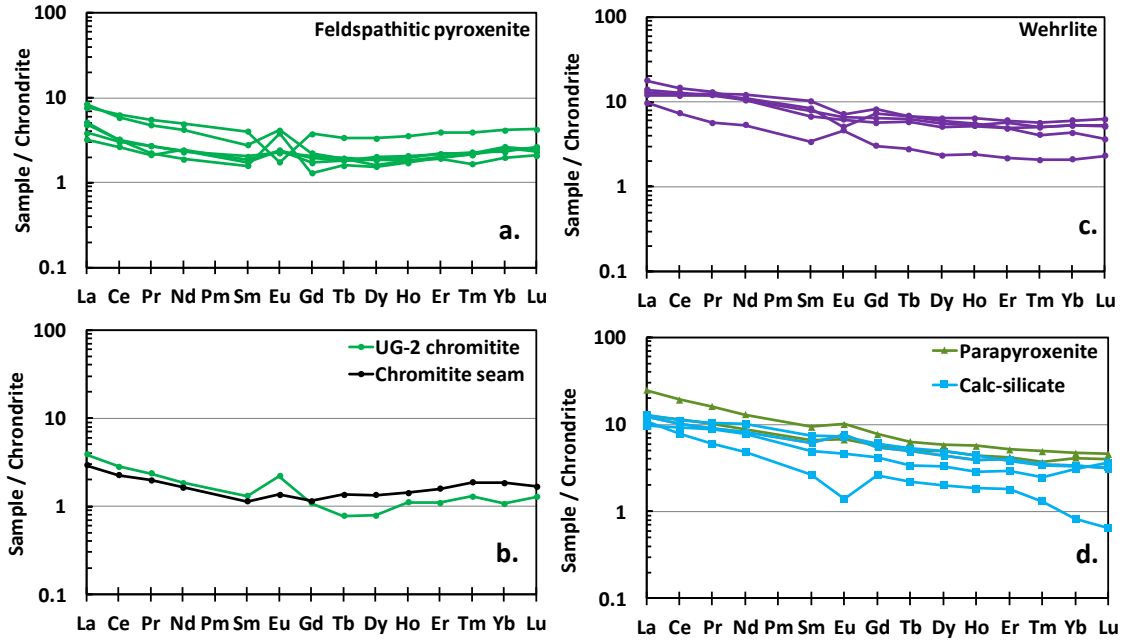

Figure 4-46: Chondrite-normalized rare earth elements profiles for selected samples in feldspathic pyroxenite, chromitite seams, wehrlite, parapyroxenite and hornfels lithological units. Normalization values from Boynton (1984).

Both chromitite seam profiles (Figure 4-46 b.) show distribution patterns that are characterised by a slightly steep LREE (La ~4 x chondrite) and flat HREE profiles. Their $(La/Yb)_N$ ratio varies between 1.6 and 3.6. A positive Eu anomaly is present in both samples, with a Eu/Eu* range of 1.6-1.9. Interestingly, the HREE pattern of the chromitite

seam pattern is more elevated than that of the UG-2 chromitite. The $(Gd/Yb)_N$ ratio of the UG-2 chromitite and lower chromitite seam is 0.9 and 0.7 respectively, showing a concave-up pattern.

Wehrlite samples in Figure 4-46 c show patterns that are enriched in REE with one sample that is, in comparison, slightly depleted in REE. The samples in this unit have gentle-sloping patterns, with a $(La/Yb)_N$ ratio of 2.2-4.46. Some samples have negative Eu anomalies (Eu/Eu* = 0.7-0.8), while some lack an anomaly. Only one sample is characterised by a positive Eu anomaly (Eu/Eu* = 1.4).

The calc-silicates samples (Figure 4-46 d.) display patterns characterised by enriched LREE and depleted HREE, also shown by the high ratios of $(La/Yb)_N$ that vary between 3.9 and 13.3. Only one sample has a negative Eu, quantified by an Eu/Eu* ratio of 0.5. This sample is also characterised by marked depletion of Yb and Lu relative to other calc-silicates. Para-pyroxenite samples shows patterns similar to calc-silicates, with LREE enrichment (~10 x chondrite) and HREE depletion. A low enrichment of REE from this unit is defined by the $(La/Yb)_N$ ratio range of 3.1-5.3. The para-pyroxenite samples are characterised by less marked positive Eu anomalies with Eu/Eu* range of 1.1 and 1.3.

4.3.3 UMT-094

(a) Major element profiles

Major element profiles in UMT-094, from base to top, are of the footwall calc-silicates, wehrlite units, troctolite and feldspathic pyroxenite, as shown in Figure 4-47. The footwall calc-silicates display inconsistent major element profiles, with MgO generally decreasing towards the wehrlite contact, from 30 to 15 wt. %. This trend is opposite to most major elements that gradually increase towards the wehrlite contact. This trend is, however, interrupted by an anomaly at 1415.4 m depth, with higher contents of MgO (~25 wt. %) and low contents of TiO_2 (0.25 wt.), CaO (12 wt. %) and MnO (0.38 wt. %).

The concentrations of volatiles are generally low in less/uncontaminated rock units, such that a trend of decreasing LOI concentration from the dolomitic footwall to the feldspathic pyroxenite is present. In the dolomitic footwall, there is a marked decrease of LOI towards the wehrlite contact from 13.4 to 2.5 wt.%. The wehrlite is composed of high proportions of olivine that are locally altered (serpentinised) and thereby result in an anomalous distribution of LOI. The LOI concentrations in the wehrlite decrease from the dolomitic

contact (8.7 wt.%) to the troctolite footwall (2.3 wt.%). One troctolite sample displays high LOI content of 6.4 wt.%, influenced by the high degree of alteration in olivine. Feldspathic pyroxenite at the top of the section has the lowest LOI contents (<~1 wt.%).

The lower wehrlite contact is marked by an abundance of clinopyroxene, serpentinized olivine and absence of plagioclase, with plagioclase increasing in abundance upwards. These minerals control the trends observed in major elements. At the contact, the wehrlite is characterised by high contents of MgO (30 wt. %) and Fe_2O_3 (22 wt. %), and generally depleted in Cr_2O_3 (<0.1 wt. %), Al_2O_3 (1.9 wt. %), CaO (5 wt. %), TiO_2 (0.2 wt. %) and alkalis. A subtle increase in MgO is observed above the contact, from 18 to 24 wt.% towards the top of the unit. Fe_2O_3 shows a generally parallel trend to MgO towards the top of the contact, as well as does Cr_2O_3, except for two high anomalies encountered in between. Conversely, Al_2O_3, CaO, TiO_2 and alkalis do not show any consistent trend with stratigraphic depth. These trends can rather be ascribed to changing proportions of minerals. One interesting anomaly is observed at a depth of 1385 m, characterised by a slight increase in MgO and low concentrations of CaO (6 wt.%) and TiO_2 (<0.01 wt. %). These latter mentioned traits do not correspond to any significant changes in mineralogy.

The chromitite unit at 1365 m is characterised by high Cr_2O_3 (4 wt.%), accompanied by minor increases in Fe_2O_3 and Al_2O_3, and depletion in MgO and TiO_2 compared to the hanging and footwall of the seam. Abrupt changes in these major elements occur from the troctolite unit, and remain fairly consistent upwards into the feldspathic pyroxenite (Figure 4-47). The compositions within these units are characterised by subtly decreasing contents of MgO and Fe_2O_3 from 17 to 12 wt.% and 26 to 22 wt.%, respectively. This trend is accompanied by concentrations of Al_2O_3, CaO, MnO, total alkalis and TiO_2 that are inversely increasing towards the top of the stratigraphic section.

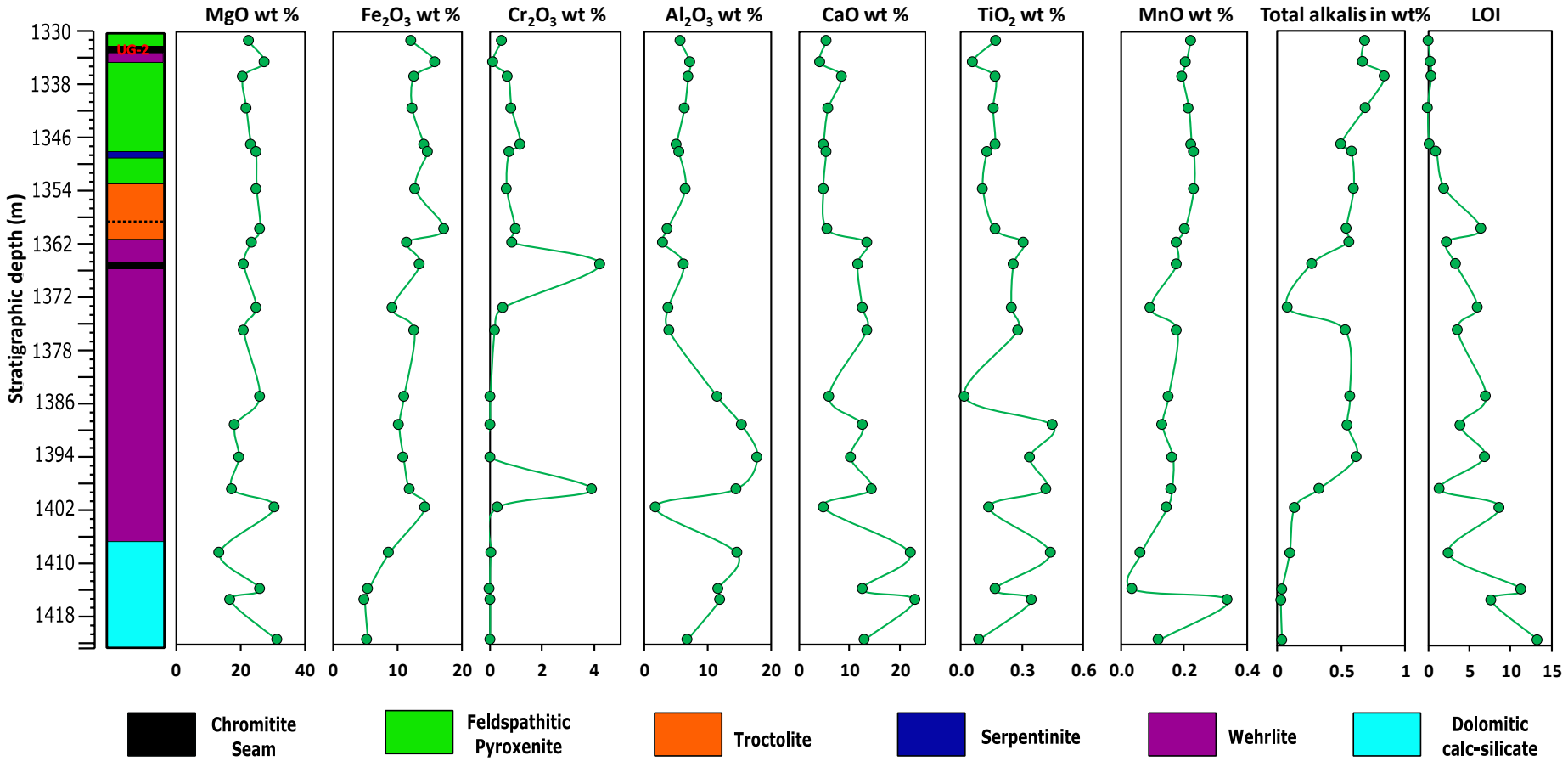

Figure 4-47: Variations of major element (MgO, Fe_2O_3, Cr_3O_3, Al_2O_3, CaO, TiO_2, MnO, total alkalis and LOI) abundances through the UMT-094 section. Total alkalis = Na_2O + K_2O; LOI = loss on ignition

(b) Trace element profiles

Trace element profiles are presented as two categories; compatible elements and incompatible elements. Selected compatible elements presented in this section are transition metals, V, Ni, Ti, Co and Cu. As before, incompatible elements are subdivided into LIL and HFS elements. Selected LIL elements are Sr, Rb, Ba, Cs and Pb, while selected HFS elements are Zr, Hf, Nb, Ta, Y and Sc.

Transition metals

In Figure 4-48, transitional metals in dolomite have low concentrations, except at 1409.9 m depth, in which all transition metals are enriched. This enrichment can be associated with the high abundance of oxides and BMS in this unit. Concentrations of V, Ti and Cu are depleted at the wehrlite contact, while Ni and Co are enriched. Above this contact, Ni, Co and Cu increase to the top contact of the wehrlite. Ti shows an inconsistent, but generally decreasing trend towards the top contact. The inconsistent presence of spinels across the profile greatly affects V concentrations, such that it displays an erratic distribution that is generally less than 250 ppm. Ti and V trends are greatly depleted at a depth of 1385 m, but none of the other elements show corresponding anomalies at this depth. Only V is highly enriched within the chromitite, at 1365 m.

Within the troctolite unit, all the transition elements are relatively enriched, except for Ti. These anomalies can be associated with the high abundance of olivine and BMS in the troctolite. From the base of the feldspathic pyroxenite to the UG-2 hanging wall, all transition metals show an upward increase, with minor erratic anomalies. At 1334.7 m depth V and Ti have the lowest concentrations, while Ni, Co and Co are most enriched relative to adjacent samples.

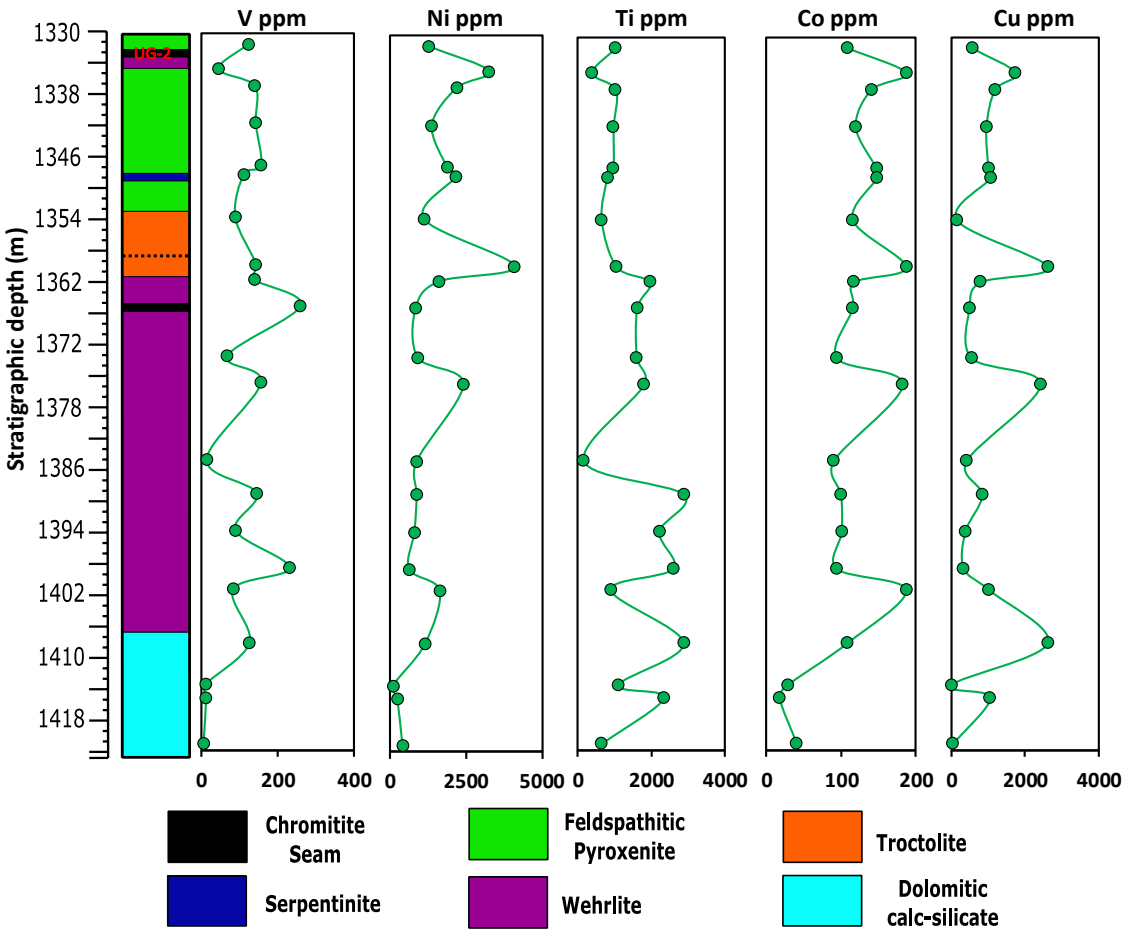

Figure 4-48: Stratigraphic variation of compatible transition metals (V, Ni, Ti Co and Cu) though drill core UMT-094.

Large ion lithophile elements (LILE)

Variations of selected large ion lithophile elements Sr, Rb, Ba, Cs and Pb are shown in Figure 4-49. Generally, LIL elements increase towards the feldspathic pyroxenite at the top of the section, except a pronounced enrichment in the centre of the wehrlite unit. The dolomitic footwall has the lowest concentrations of LILE, except for enrichments in Sr (2.6-67.1 ppm) and Pb (2.2-17.3 ppm). Within the overlying wehrlite, Sr, Cs, Rb, Ba and Pb are most enriched in samples between 1395.2 – 1375.8 m, resulting an almost concave pattern. At a depth of 1334.7 m, there is an enriched anomaly of Sr and Pb, while Rb, Ba and Cs are more depleted relative to the adjacent samples.

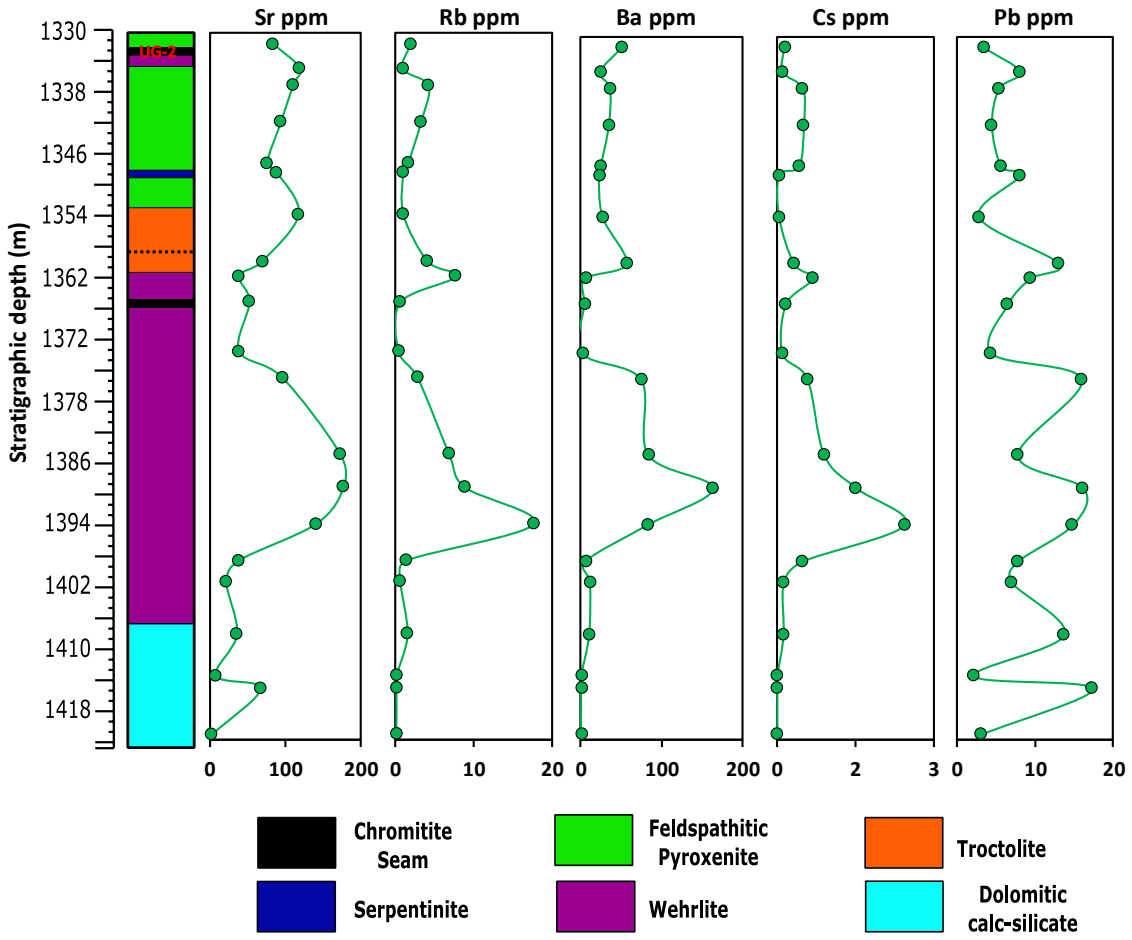

Figure 4-49: Stratigraphic variation in incompatible and mobile large ion lithophile elements of Sr, Rb, Ba Cs and Pb from section UMT-094.

High field strength elements (HFSE)

High field strength element profiles of Zr, Hf, Nb, Ta and Y are shown in Figure 4-50. Their profiles generally show decreasing trends from the dolomitic footwall and up towards the feldspathic pyroxenite. The dolomitic unit shows anomalous distribution of HFSE, with highest concentrations in the wehrlite contact. Within the wehrlite, the lowest concentrations are recorded for SD-53 with less than 10 ppm Zr and less than 1 ppm Hf, Nb, Ta and Y. Above 1375.8 m, HFS elements are increasing, with a subtle depletion within the chromitite seam (1365.7 m).

The base of the troctolite is marked by low HFSE contents, which remain fairly constant up through the feldspathic pyroxenite, with compositional ranges of Zr (12-10 ppm), Hf (0.3-0.2 ppm), Nb (0.4-0.3 ppm), Ta (0.12-0.10 ppm) and Y (4.7-4.3 ppm). A pronounced depletion, similar to that of SD-53, is observed in SD-42 (1334.7 m), characterised by the lowest HFS element concentrations.

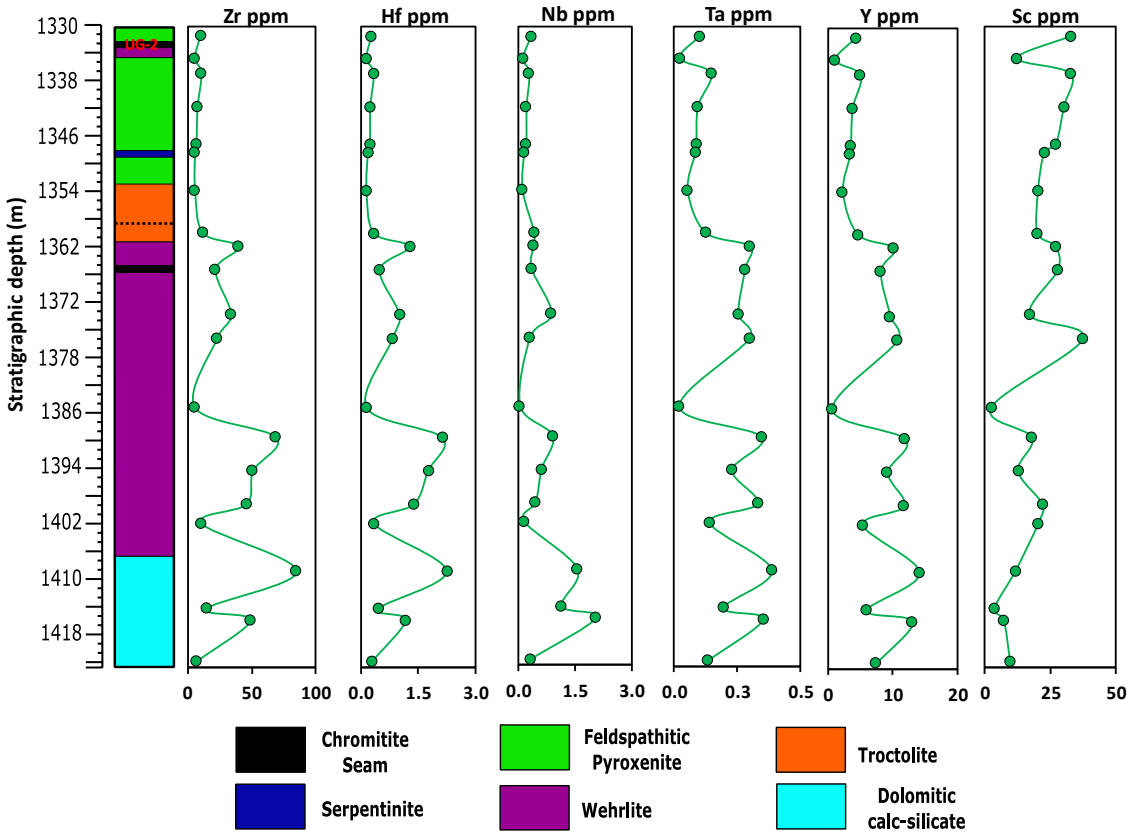

Figure 4-50: High field strength elemental profiles for samples in section UMT-094 showing Zr, Hf, Nb, Ta, Y and Sc.

(c) Primitive-mantle normalised trace elements

Primitive-mantle normalised element patterns from various lithologies in UMT-094 are illustrated in Figure 4-51a-d. All cumulate rocks show similar gently-sloping profiles, characterised by slightly enriched LILE and LREE and a flat profile from Nd to Lu. The cumulus rocks maintain the preserved anomalies observed in previous drill cores, the negative Nb-Ta, P slightly marked Zr and Ti anomalies, and positive Th-U, Pb and Sr anomalies.

Feldspathic pyroxenite and troctolite samples in Figure 4-51a and b display similar patterns. These units have negative Rb, P, Nb-Ta, positive Ba, Sr and Pb anomalies. These units also maintain subtle negative Zr anomalies observed in other cumulate rocks.

All calc-silicate samples in Figure 4-51d are characterised by a relatively gently-sloping profile, with varying degrees of incompatible element enrichment amongst each other. The samples have a pronounced depletion in LILE (Cs, Rb and Ba), positive Th-U, P and negative Ti anomalies. Moreover, these samples display a marked Nb depletion relative to

an absent Ta anomaly. These samples lack the Sr anomaly observed in the cumulate rocks. One sample lacks a strong negative P anomaly that is common in most lithologies, suggesting the presence of apatite. The pattern from Nd to Lu has a gentle profile marked by negative Zr anomalies, except for one sample (SD-58) that shows a positive Zr anomaly and an enrichment in Y, Yb and Lu.

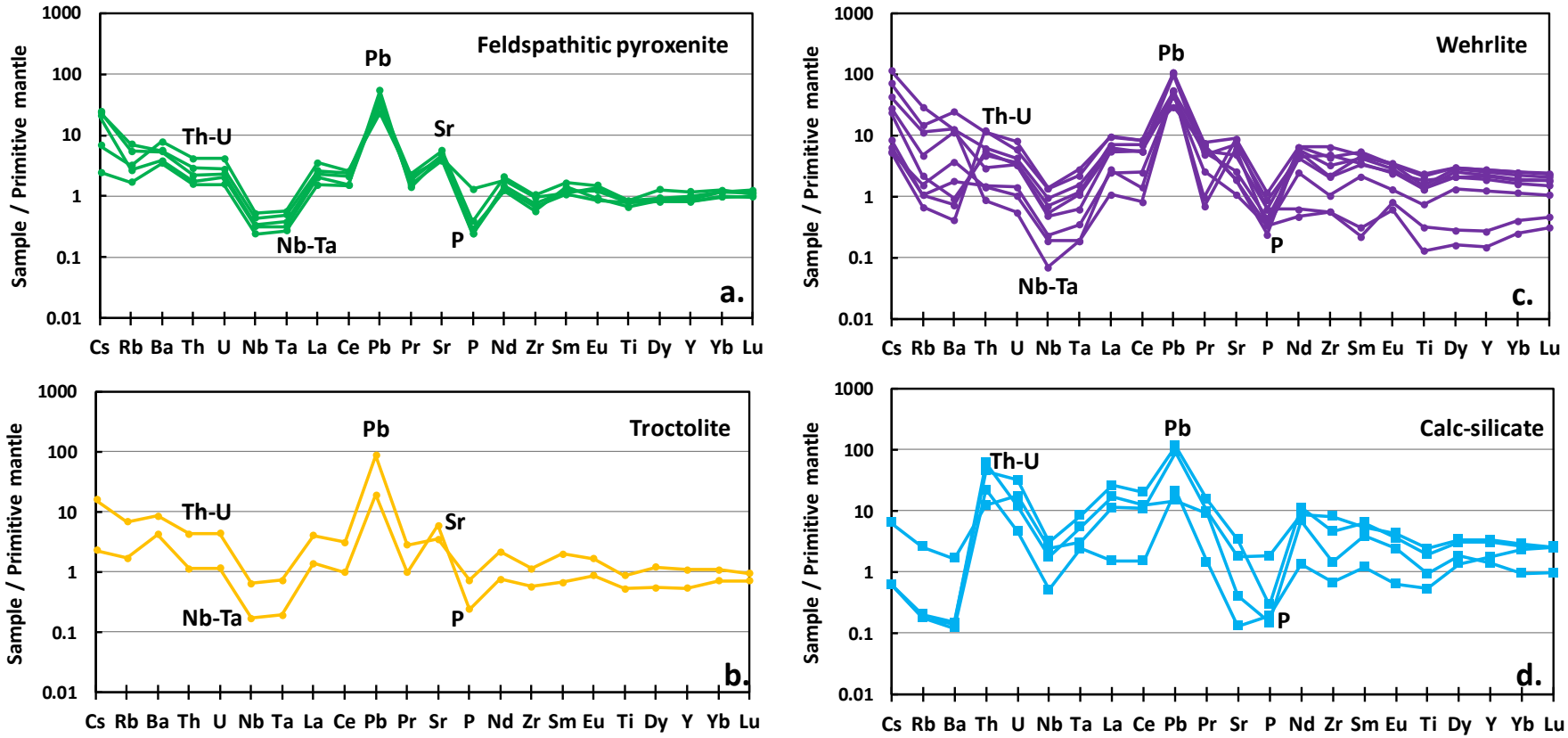

Figure 4-51: Primitive-mantle normalised trace element profiles for a. feldspathic pyroxenite, b. troctolite, c. wehrlite, and d. calc-silicate lithologies obtained from UMT-0. Normalization values from McDonough and Sun (1995).

(d) Rare earth elements

Chondrite-normalized rare earth element profiles by the four main lithologies of UMT-094 are illustrated in Figure 4-52. Generally, cumulate rocks show gently-sloping REE profiles with $(La/Yb)_N$ ratios ranging from 1.5 to 10.9. The feldspathic pyroxenite samples show an almost concave-upward profile, with a slight depletion in the MREE relative to the HREE and LREE. They show both positive (Eu/Eu* = 1.1-1.3) and negative (Eu/Eu* = 0.8) Eu anomalies with various slight amplitudes indicating varying proportions of plagioclase. In comparison, the troctolite samples show two different patterns. One sample is LREE-enriched with a $(La/Yb)_N$ ratio of 3.6 and lack an Eu anomaly. The profile of one sample is similar to those of the feldspathic pyroxenite with a $(La/Yb)_N$ ratio of 1.9 and an Eu anomaly with a Eu/Eu* ratio of 1.5

Samples from the wehrlite display slightly steeper REE patterns with $(La/Yb)_N$ ratios of 2.1-10.9, compared to the feldspathic pyroxenite. Two radically different type patterns are exhibited by the wehrlite unit, such that one pattern is REE-enriched (10 times the chondrite) with a less marked negative Eu anomaly [(Eu/Eu*) = 0.7-0.8], and the other pattern displays a gently-sloping REE pattern with a more pronounced positive Eu anomaly [(Eu/Eu*) = 2.5 -3.2].

The calc-silicates are characterised by two different types of REE patterns. Sample SD-58, SD-59 and SD-60 show steep patterns with $(La/Yb)_N$ ratios ranging between 3.9 and 17.9. Sample SD-61 shows enrichment of HREE [$(Gd/Lu)_N$ = 0.5] relative to LREE [$(La/Sm)_N$ = 1.3]. All calc-silicate samples display negative Eu anomalies with varying amplitudes (Eu/Eu* = 0.5-0.9).

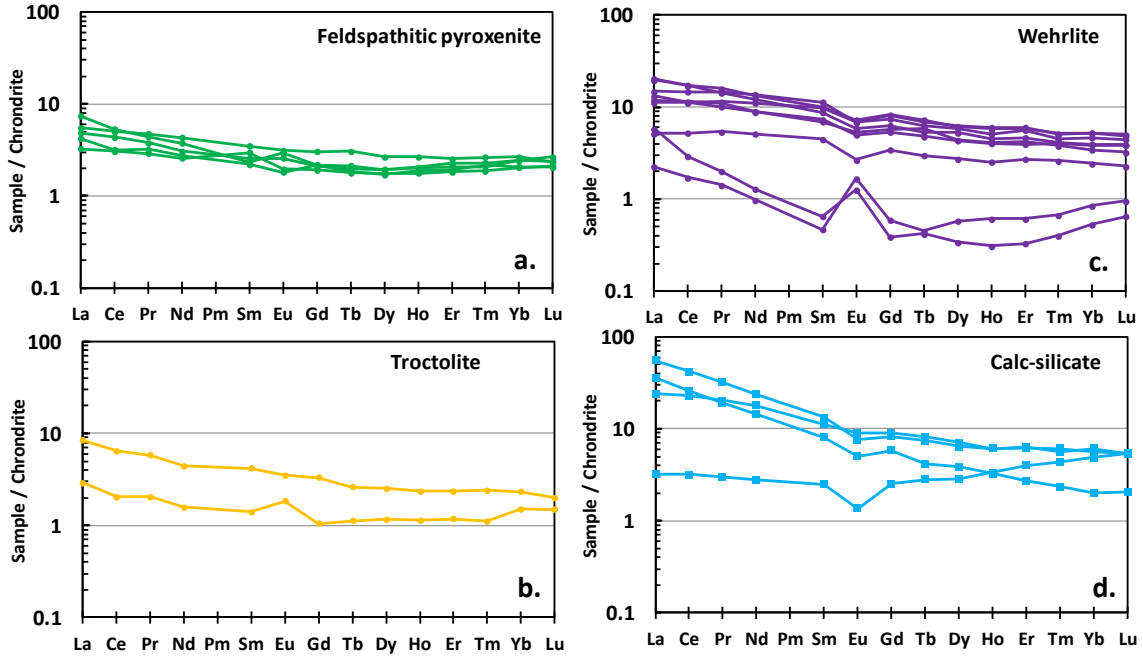

Figure 4-52: Chondrite-normalized rare earth elements of selected sampled from the feldspathic pyroxenite, troctolite, wehrlite and calc-silicate units from UMT-094. Normalization values from Boynton (1984).

Chapter 5. : Discussion

5.1 Local contamination history

5.1.1 Evidence for carbonate assimilation

In the Northern Limb, there is abundant evidence for contamination by country rock, provided by numerous entrained xenoliths of calc-silicates, hornfels and quartzite in the Flatreef, Platreef and Main Zone (Harris and Chaumba, 2001; Grobler et al., 2018). Calc-silicate xenoliths that are observed in the Lower Flatreef preserved evidence for high temperature reactions with the host magma. Mineralogical, textural and geochemical features indicate a dolomitic protolith. The calc-silicate samples comprise metamorphic assemblages such as diopside, calcite, akermanite, forsterite, periclase, vesuvianite. (Figure 4-13) These assemblages are formed at high temperatures during metamorphism, as previously documented in the Eastern Limb (Wallmach et al, 1989).

Local contamination is most significant in units proximal to dolomitic xenoliths leading to the presence of footwall assimilation-influenced rocks such as wehrlite, olivine gabbronorite, and troctolite. These units are major constituents of the footwall assimilation zone and are characterised by the presence of pure carbonate grains that are associated with abundant clinopyroxene and olivine (Figure 4-10b), as well as inclusions in spinels (Figure 4-12d). These units are presumed to have formed from a hybrid melt produced through the mixing of carbonate and magmatic melt. Deegan et al. (2010) suggested that a hybrid melt produced during carbonate assimilation will have a chemically distinct signature and contrasting viscosity from the precursor melt. They also suggest that hybridization of the melt is dependent on both the rate at which CaO will diffuse into the melt and on the ability to mix with a host liquid despite contrasting viscosities (Deegan et al., 2010). Hamann et al. (2018) argued that the inability of the silicate melt and carbonate melt to overcome contrasting viscosities may hinder complete homogenization, producing an immiscible carbonate phase. The presence of carbonate phases enclosed by spinels has also been observed in Volspruit Sulphide Zone in the Northern Limb (Tanner et al., 2019) and the Jacurici intrusion in Brazil (Friedrich et al., 2019), and both studies attributed the carbonate inclusions to rapid crystallization of chromites upon contamination.

The presence of abundant amoeboidal olivine and clinopyroxene proximal to dolomitic rafts, in contrast to the mineralogy and textures found in the associated, less obviously contaminated pyroxenites, provides evidence for local contamination of the magma.

Olivines that are products of carbonate assimilation have been reported to be both more calcic and forsteritic, comprising compositions of up to 0.8 wt.% CaO and Fo_{92}, respectively (e.g. Wenzel et al., 2002; Gaeta et al., 2009). It is noteworthy, however, that olivines in the FAZ are neither highly calcic (~0.1 wt.%) nor highly forsteritic (less than Fo_{86}), despite their apparent link to carbonate-contaminated magmas. However, the abundance of these olivines in units proximal to dolomitic xenoliths is nonetheless attributed to the influence of contamination of the melt.

In addition, the FAZ includes abundant Ca-Tsch-rich clinopyroxene, which has been experimentally shown to reflect assimilation of carbonate material (Iacono-marziano et al., 2008; Conte et al., 2009; Mollo et al., 2010). Clinopyroxene compositions display high Ca contents (up to Wo_{52}) with high Ca-Tschermak components (up to 33 mol.%) compared with mineral compositions from pyroxenites and chromitites, suggesting an interaction of melt with carbonate-derived fluids (Di Rocco, 2012). Furthermore, plagioclase found in the wehrlite is relatively calcic (~An_{76}) compared to those of chromitite (up to An_{65}), indicative of a relatively high CaO-activity of the melt. Reverse zonation of relict plagioclase hosted in olivine is observed in the olivine gabbronorite and pegmatoidal troctolite, and the feldspars have compositions evolving from An_{70} to An_{77} from core to rim, respectively (Figure 4-18 and Figure 4-24). The more calcic rims correspond to the composition of the interstitial plagioclase, indicating disequilibrium of early plagioclase as a result of the addition of a carbonate melt, producing a magma that is becoming progressively Ca-rich. Alternatively, the Ca-rich plagioclase rims could indicate equilibrium with a magma that is becoming progressively wet as a result of infiltration of H_2O-rich fluids (Baker and Black, 1980). Thermodynamic modelling constraints conducted by Howarth and Prevec (2013) showed that the An content of plagioclase increases with increasing water content in the magma without any significant change in the compositions of co-existing silicate phases. Boudreau (2019) also characterised the presence of relict plagioclase as evidence of infiltration of fluids, triggering decomposition of early destabilised phases (plagioclase).

Compared to felspathic pyroxenite, lithostratigraphic element profiles spikes within FAZ units, which also indicate a secondary source of CaO linked to proximity to carbonate xenoliths intersected by the core. This CaO enrichment in the melt can be monitored with CaO/Al_2O_3 ratios (Kinnaird et al., 2005; Conte et al., 2009), where, units of the FAZ exhibit higher CaO/Al_2O_3 ratios than feldspathic pyroxenite units, reflecting the

accumulation of Ca-rich phases (Figure 5-1a). Similarly, CaO addition also affects the CaO/SiO_2 ratio of the melt, such that the CaO/SiO_2 ratio of the FAZ is high (0.3-0.4) compared to the feldspathic pyroxenite (0.09-0.1) (Figure 5-1). Therefore, enhanced CaO/SiO_2 and CaO/Al_2O_3 ratios observed in the FAZ units provides evidence for carbonate incorporation during melt interaction with footwall dolomite. This is in agreement with the investigations carried out on skarn-bearing lithologies (Wenzel et al., 2002; Barnes et al., 2005; Spandler et al., 2012; Di Rocco et al., 2012), demonstrating that partial melting of carbonate wall-rocks produces high amounts of CaO and volatile fluids, which mix with a melt and trigger crystallization of Ca-rich phases. Ihlenfeld and Keays (2011) ascribed the enrichment of CaO, coupled with MgO, to the digestion of carbonates in drill cores intersecting dolomite rafts at Sandsloot and Tweefontein in the Platreef.

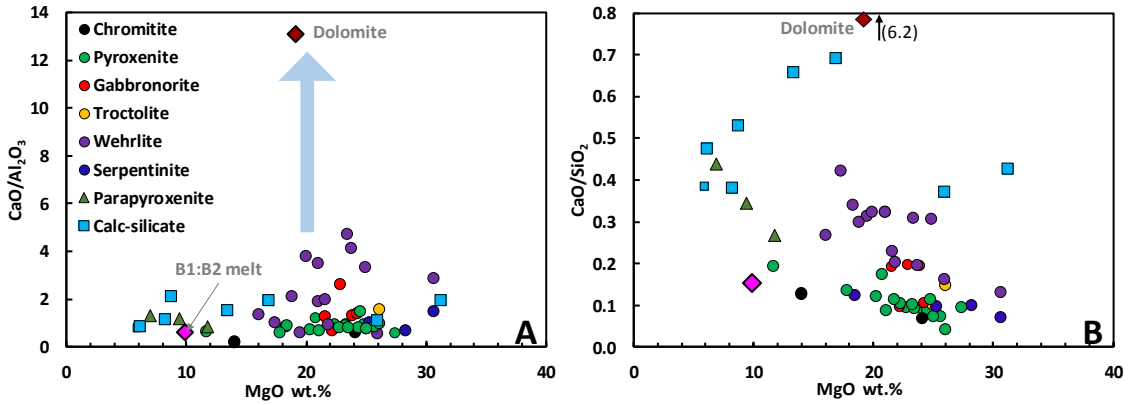

Figure 5-1: Whole-rock ratios of CaO/Al_2O_3 and CaO/SiO_2 with respect to MgO content comparing the Flatreef rocks to the unaffected dolomite(Clay, 1981).

Evidence for melt-rock interaction in the Flatreef is also indicated by enrichment of LILE, HFSE and REE in the FAZ units relative to the pyroxenites and chromitites (Figure 4-39, Figure 4-45 and Figure 4-51). This is reflected by the enrichment of LREE, Zr, Hf, Nb, Ta, and Y in the wehrlite compared to the feldspathic pyroxenite, which were probably elevated during contamination. The Malmani dolomite displays high concentrations of REE (Stephenson, 2018), and because REEs are typically immobile in aqueous fluid phases, the hybrid lithologies that would be generated from dolomite-melt hybrids will retain slightly elevated REE concentrations. This is most prominent in wehrlite lithologies (Figure 4-46 and Figure 4-52), where the REE concentrations are higher than that of the feldspathic pyroxenites, signifying a larger influence of dolomite. The olivine gabbronorite lithology comprises REE concentrations that are in close similarity to the feldspathic pyroxenite (Figure 4-40), suggesting a minor influence of dolomite during

5.1.2 Modelling carbonate assimilation

The potential effect of dolomite assimilation on the melt and mineral composition was investigated based on magmatic crystallization modelling using the software programmes PELE (Boudreau, 1999) and rhyolite-MELTS (Gualda et al., 2012). The C_UZ has been proposed to have crystallized from a mixture of B1 and B2 liquids at a ratio of 60% and 40%, respectively. The Flatreef has been proposed to have formed correspondingly and correlated to C_UZ of the Bushveld, thus the B1:B2 mixture was used as the starting composition for the modelling (McDonald et al., 2005; Barnes et al., 2010). Two modelling constraints have been imposed. The first involved a simple incremental 1 wt.% addition of CaO-melt to the magma up to 5 wt.%, before the onset of crystallization. The second constraint attempted assimilation-fractional crystallization modelling involving assimilating 10%, 20% and 30% dolomite into the C_UZ melt. Modelling was performed under H_2O-bearing conditions (0.5 wt.%), based on the conclusions by Wyllie and Tuttle (1960) that $CaCO_3$ will completely dissolve under high temperatures in the presence of water.

Model 1: CaO addition in the melt

The main aim of this model was to investigate the minimum content of CaO required to potentially change the composition of the magma and crystallizing phases. The modelling program used for this investigation was MELTS, and the results are shown in Figure 5-2. The Upper Reef pyroxenite of the Flatreef is proposed to have crystallized from mixing of a residual liquid and a Cr and PGE-poor primitive melt (Yudovskaya et al., 2017). Therefore, the least contaminated pyroxenite encountered in drill core is assumed to have crystallized from the B1:B2 melt mixture. Quantitative MELTS simulations for the uncontaminated magma predict crystallization of orthopyroxene as the first liquidus phase that is then followed by spinel at slightly lower temperatures (1215 ^oC). Progressive crystallization stabilizes clinopyroxene and orthopyroxene at lower temperatures.

Decarbonation reactions occurring during assimilation of dolomite release CaO and CO_2 fluids into the host melt, thus changing the phase equilibria of the melt (Wenzel et al., 2001; Iacono-marziano et al., 2008; Gaeta et al., 2009). Only CaO was introduced to the parental melt in these MELTS simulations, assuming that CaO will impose the most significant influence on the composition of the melt over CO_2, because of the very low solubility of CO_2 (Wenzel et al., 2002; Ganino et al., 2013). Results show that adition of minor contents of CaO (1-2 wt.%) in the melt only affects the stability temperature of

orthopyroxene over spinel as the melt becomes progressively CaO-richer. The stability of spinel does not change with increasing CaO it just becomes progressively Cr-rich (from ~37 to 40 wt.% Cr_2O_3) as orthopyroxene becomes less stable. The similar lower crystallization temperatures for plagioclase and clinopyroxene show no apparent change in saturation temperatures with adding up to 3 wt.% of low contents of CaO.

The mineral crystallization sequence changes more radically after addition of slightly higher CaO (~3-5 wt.%) contents, evolving from orthopyroxene-dominated assemblages towards spinel+olivine+clinopyroxene dominated assemblages. This model shows that it would require a minimum of 4 wt.% assimilation of CaO to completely destabilize or suppress orthopyroxene in favour of olivine, subsequently promoting early crystallization of Cr-rich spinel. Moreover, the stability of olivine is restricted to CaO contents of 3-5 wt.%; while contents higher than 5.6 wt.% completely destabilize olivine in favour of clinopyroxene.

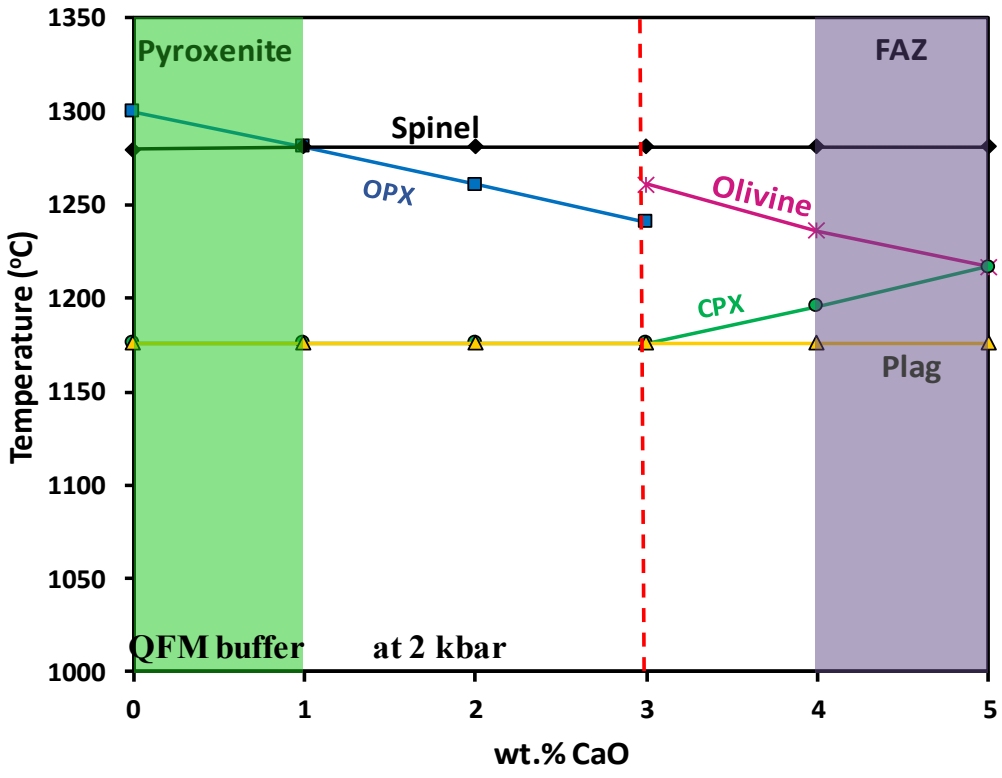

Figure 5-2: The effects of adding CaO to a 60:40 B1:B2 melt mixture plotted agianst temperature to show the appearance of orthopyroxene (opx), spinel, olivine, clinopyroxene (cpx) and plagioclase (plag) at increments of 1 wt.%. Calculated using the rhyolite-MELTS program (Gualda et al., 2012).

Model 2: Assimilation-fractional crystallization (AFC) modelling

Modelling simulations were performed using PELE to constrain the influence of dolomite assimilation on the mineral paragenesis and composition. The AFC model was performed at 2 Kbar and fO_2 = QFM. Assimilation of dolomite into the parental liquid has a major impact on the liquid line of descent compared to the uncontaminated liquid (Figure 5-3). The results of the model also showed that up to about 9 wt.% CO_2 is generated.

The model shows that spinels will crystallize much earlier followed by olivine and co-precipitate to lower temperatures. The forsterite content of olivine increases from 84, 85 to 86 with proportions proportion of 10%, 20%, and 30% added into the melt respectively. Clinopyroxene and plagioclase appear on the liquidus at slightly higher temperatures in the contaminated melt than the normal melt. The Di content in clinopyroxene and An content of plagioclase increases slightly with increasing amount of dolomite. The uncontaminated melt has a higher proportion of plagioclase than clinopyroxene. The addition of dolomite favours clinopyroxene crystallization over plagioclase, thus producing clinopyroxene-dominated assemblages.

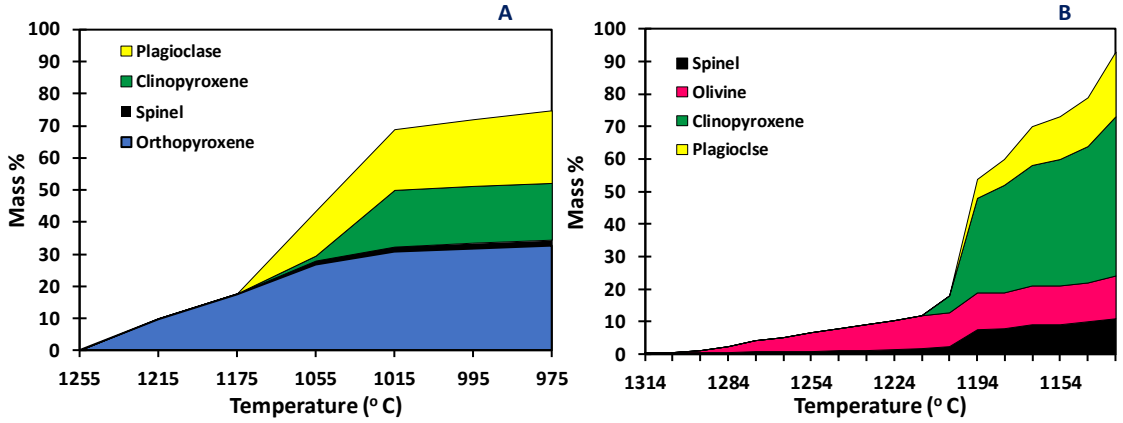

*Figure 5-3: Results of PELE modelling showing proportions of crystallizing phases as a function of temperature in the magma. **A.** simulation of a dolomite-free B1:B2 parental melt showing abundant orthopyroxene and a minor proportion of spinel. **B** predicted liquid line of descent of a melt assimilating 30% mass phase of dolomite.*

Implications of modelling on the phase equilibria:

The most prominent effect of carbonate assimilation observed from the modelling is the apparent change in the liquid line of descent with progressive accumulation of CaO_{melt} and dolomite assimilation. These observations are consistent with experimental work on carbonate assimilation (e.g. Iacono-marziano et al., 2008; Conte et al., 2009; Carter and Dasgupta, 2016) and natural skarn-bearing magmas (e.g. Chadwick et al., 2007; Di Rocco

et al., 2012). All these studies, including this one, report that enrichment of CaO in the melt will enhance clinopyroxene and olivine stability over orthopyroxene (reaction 3), and are accompanied by a reduction in SiO_2. Joesten (1977) proposed that accumulation of CaO would potentially reduce the content of SiO_2 in the melt, subsequently lowering the silica activity, a process termed 'desilicification'. Later, Morse (1980) envisaged that a reduced SiO_2 activity results in the decomposition of crystallizing orthopyroxene in favour of olivine; thus releasing excess SiO_2 in the residue melt which will stabilize clinopyroxene. Incomplete decomposition of early orthopyroxene will result in preservation of partially resorbed grains in the melt (Patkó et al., 2020). In the FAZ, preserved orthopyroxene chadacrysts are most prevalent in units proximal to dolomitic xenoliths.

$$CaMg(CO_3)_2^{solid} + 4MgSiO_3^{melt} \rightarrow 2Mg_2SiO_4 + CaMgSi_2O_6 + 2CO_2 \quad (3)$$

5.1.3 Implication of carbonate assimilation on the formation of the FAZ

The FAZ originates from a melt that assimilated dolomite material, as evidenced by the occurrence of extensively contaminated rocks and the presence of metamorphosed dolomite xenoliths. The assimilation of dolomite produced mineral assemblages that are distinctive from those of uncontaminated units. The FAZ is mainly dominated by clinopyroxene, olivine, spinel, and plagioclase in varying proportions. Orthopyroxene is rarely observed in the most contaminated sections, and where observed occurs as relict grains enclosed in olivine and clinopyroxene. The scarcity of orthopyroxene in the FAZ indicates progressive silica depletion with an increasing degree of carbonate contamination as modelled above. The formation of these units with respect to increasing influence of dolomite assimilated will be discussed based textural and geochemical observations from FAZ samples in combination with the observed modelling constraints.

Drill core UMT-094 comprises an ~8 m thick pegmatoidal troctolite dominated mainly by coarse amoeboidal olivine (Fo_{78}), plagioclase (An_{70}) and occasional chromitite stringers (Figure 4-5, Figure 4-28 and Figure 4-31). Clinopyroxene is present in minor proportions and has compositions ($Mg\#_{82\text{-}87}$ and Ca-Tschermak of ~7 mol.%) that are considerably overlapping those of the cpx in the olivine gabbronorite, suggesting a minor influence of dolomite contamination. Maier et al. (2020) invoked recrystallization in the presence of fluids as a mechanism to produce pegmatoidal lithologies in the Flatreef. This mechanism was previously proposed by Nicholson and Mathez (1991), and later Mathez and Kinzler

(2017), for the origin of Merensky Reef pegmatoidal lithologies, suggesting that infiltration of H_2O-rich fluids would induce decomposition of orthopyroxene in favor of olivine, and theoretically, promote chromite crystallization. Dissolution of orthopyroxene will saturate the melt in Cr, Mg, and Si, subsequently promoting crystallization of chromitiferous spinel and olivine (Bédard and Hebert, 1998; Mathez and Kinzler, 2017; Boudreau, 2019; Patkó et al., 2020).

The olivine-bearing gabbronorite was only observed in UMT-345, situated below a dolomite xenolith. This unit is dominated by orthopyroxene, olivine, clinopyroxene, and plagioclase. Whole-rock compositions of the olivine gabbronorite show significant overlap with the feldspathic pyroxenite, with an exception of slight enrichment in LOI (Figure 4-35 and Figure 4-39). This indicates that contamination was not as significant as in the wehrlite units. Modelling simulations (Model 1; Figure 5-2) indicate that the olivine gabbronorite assemblages are produced by infiltration of about 3 wt.% CaO into the parental liquid. The model indicates that with CaO addition, the silica content of the melt will be lowered, including the crystallization temperature of orthopyroxene, in favour of early spinel, olivine, clinopyroxene, and plagioclase.

However, the olivine gabbronorite consists of early relict grains of orthopyroxene and plagioclase enclosed in olivine (Figure 4-9), which cannot be reproduced by the simulations. The relict orthopyroxene grains enclosed in olivine can be explained by phase disequilibrium with a melt becoming progressively more Si-undersaturated as it mixes with CaO_{melt} (Patkó et al., 2020; Maier et al., 2021). This mechanism is supported by nearly similar compositions of relict (~En_{81}) and cumulus orthopyroxene (~En_{78}); suggesting that cumulus orthopyroxene crystallized from a slightly differentiated melt rather than from an influx of primitive melt. Plagioclase, on the other hand, becomes progressively more An-rich with CaO infiltration. This is evident by the reverse zonation observed in plagioclase relicts, with the An content increasing from core (An_{70}) to rim (An_{76}) (Figure 4-18) suggestive of an increasing CaO content of the liquid during fractionation prior to cessation of early phases.

The wehrlite (occasionally plagioclase-bearing) unit is dominated by a high abundance of clinopyroxene, olivine, with variably disseminated spinel and minor plagioclase, sulphides, and phlogopite. Relict orthopyroxene and plagioclase are occasionally preserved in olivine, suggesting that the precursor melt of the wehrlite was initially noritic,

and orthopyroxene decomposed upon infiltration of carbonate fluids as in reaction (3). The AFC model in Figure 5-3 reproduces the petrography and thereby argues for the influence of a dolomite-derived carbonate melt in the mineral paragenesis of the wehrlite. In the presence of carbonate material, the liquid line of descent shifts from orthopyroxene-dominated assemblages to olivine-clinopyroxene dominated assemblages (Figure 5-3). The crystallization sequence obtained from the AFC model is summarized in a Fo-Di-An phase diagram in figure 5-4. The diagram shows that the stability fields of spinel, olivine and diopside expand in the presence of aqueous fluids at the expense of plagioclase (Boudreau, 1999; Ford et al, 1972). From the diagram, sole crystallization of spinel is followed by cotectic olivine, and once the melt reaches a eutectic with clinopyroxene the stability field of spinel contracts in favour of plagioclase. This contraction in spinel is mainly due to the high partition coefficient of Cr in pyroxene (3.8 in clinopyroxene; Hart and Dunn, 1993). Once spinel ceases to crystalize, an Al-bearing component will become stable, thus permitting crystallization of plagioclase.

Results obtained from model 1 simulation in Figure 5-2 show that the assemblages and composition observed in the wehrlite samples correspond to the mixing of about 4-5 wt.% CaO_{melt} with a B1: B2 parental liquid. Such high amounts of CaO are supported by results from the AFC model; which show that the most contaminated wehrlites are produced by up to 30% dolomitic assimilation. These proportions are in close agreement with values reported by Iacono-marziano et al. (2008) and Carter and Dasgupta (2016). Increasing degrees of contamination from the simulation is manifested by the increasing Fo content in olivine and an increasing amount of crystallizing clinopyroxene relative to plagioclase. The forsterite content of olivine in the wehrlite is highest (~Fo_{86}; Figure 4-28) in drill core UMT-094 proximal to the dolomite contact and decreases with distance from the dolomite, suggesting higher degrees of contamination with proximity to the dolomite. This argument is supported by a high Ca-Tschermak component and Wo in clinopyroxene associated with forsterite olivine. These observations also suggest that assimilation was localized around the xenoliths, around the magma-carbonate interface.

The CaO content of olivines from the wehrlites is lower (<0.1 wt.%) than that predicted by the CaO-addition model (up to 0.4 wt.%). The CaO content in olivine reflects the CaO content of the melt from which olivine crystallizes, this was demonstrated using the Ca partitioning in olivine by Libourel (1999) and Gavrilenko et al. (2016). Extrapolation from the Ca partitioning in olivine model by Gavrilenko et al. (2016) suggest that olivines (0.05

to 0.08 wt.%) in the wehrlite would have crystallized from a melt with a CaO content of about 5-8 wt.%, which is close to the proposed parental liquid (~8 wt.%; Barnes et al, 2010). Gavrilenko et al. (2016) argue that crystallization of Ca-rich pyroxene can lower the partition coefficient of Ca in olivine, thus crystallizing olivine with lower CaO content. Similarly, Wenzel et al. (2002) proposed that the CaO content of coexisting olivine could be lowered by an influx of fresh magma, which would dilute a CaO-contaminated melt and thereby crystallize olivine with a lower CaO and higher NiO content. The latter argument seems more viable as olivines in the wehrlite with a higher CaO content also have lower NiO content (Figure 4-28), while those olivines with lower CaO contents have slightly higher NiO contents (Figure 4-21).

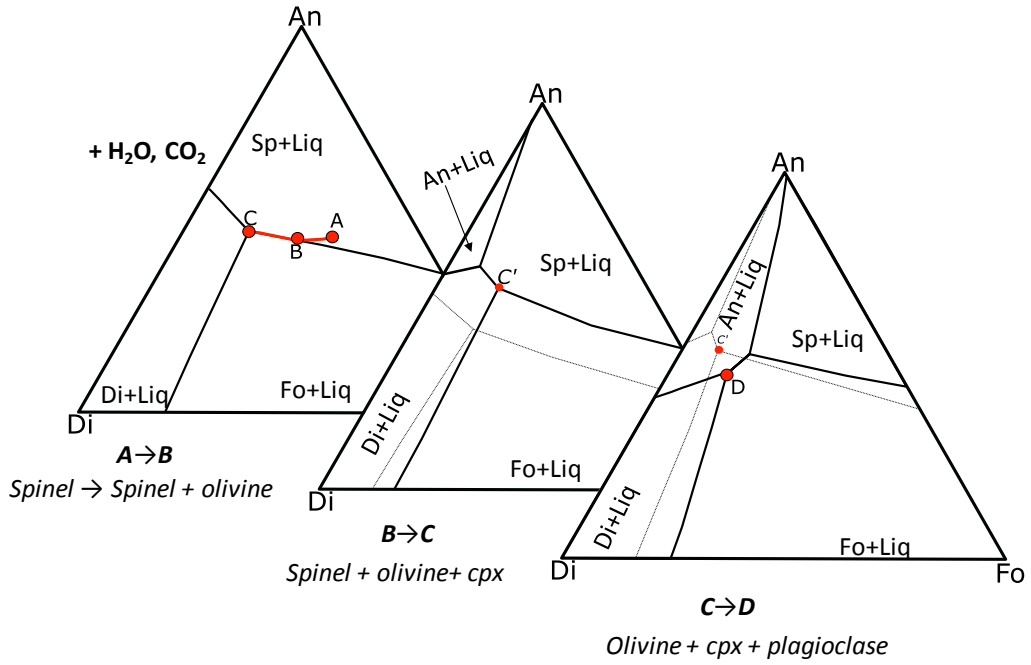

Figure 5-4: A poorly constrained phase diagram for anorthite (An)-diopside (Di)-forsterite (Fo) showing the crystallization path for phases present in the Flatreef wehrlite units. The crystallization sequence of the wehrlite assemblages is extrapolated from PELE modelling results. The melt first temporarily crystallized sole Cr-spinel at 'A', cotectic fractional begins at 'B' as olivine appears on the liquidus. At point C clinopyroxene appears on the liquidus and destabilizes spinel and, subsequently, plagioclase crystallizes at the expense of spinel. The stability diagram is modified after Morse (1980) and Bédard and Hebert (1998).

5.2 Influence of carbonate assimilation on spinels of the FAZ

5.2.1 Correlation of carbonate influence to spinel formation

The occurrence of abundant contaminated units in the Lower Flatreef is proposed to have influenced the formation of spinels. This is mainly observed from the widespread geochemical and textural variation amongst Flatreef spinels, including chromites. Spinels formed within or proximal to contaminated units have mineral compositions that differ

from spinel from uncontaminated units, mainly due to the influence of contamination on the melt. These distinctions lead to the categorization of spinels into three main types, based on texture and composition (Table 3).

Type 1 spinels are those chromites from the UG-2 chromitite seams in UMT-345 and UMT-335, and chromites from the lower chromitite seam in UMT-335. The UG-2 chromitite in UMT-335 is in direct contact with a contaminated (FAZ) footwall (Figure 4-3d), while the other chromitite samples are not associated with a contaminated unit (Figure 4-1). These type 1 spinels are representative of the near-primary compositions as they have relatively homogenous mineral compositions, with limited Mg#, Cr#, and low Fe^{3+}# ratios (Figure 5-7). Higher concentrations of Fe^{3+}#, Fe^{2+}#, and TiO_2 with lower Cr# and Mg# in type 1 spinels are indicative of primary melt differentiation (Hulbert and Von Gruenewaldt, 1985). A slight difference in compositions of spinels is observed between those of the UG-2 chromitite seam in UMT-335 (with a FAZ footwall) and those of the UG-2 in UMT-345 and lower chromitite seam in UMT-335. The former chromites contain slightly elevated TiO_2 and lower Mg# contents compared to chromites from the UG-2 in UMT-345 and the lower chromitite seam in UMT-335.

The contents of Al_2O_3 and TiO_2 in spinels are often used to monitor the composition of the melt (Kamenetsky, 2001). These components in spinels are controlled by the composition of the melt from which they crystallized. Therefore, employing the method of Rollinson (2008), the Al_2O_3 and TiO_2 contents of the melt from which the spinels crystallized were constrained using the following equations:

$$Al_2O_{3\,(melt)} = 5.2181 \times \ln Al_2O_{3\,(spinel)} - 1.0505$$

$$TiO_{2(melt)} = 1.0963 \times TiO_2{}^{0.7863}{}_{(spinel)}$$

Results from the above calculations are shown in Figure 5-5, indicating that type 1 spinels from the UG-2 chromitite and the lower chromitite seam show compositions of having crystallized from an undifferentiated melt with an average of 13 wt.% Al_2O_3, correlating with that of the parental liquid of the B_1:B_2 melt mixture of the C_UZ (Barnes et al., 2010). These results suggest that type 1 spinels were not affected by extensive sub-solidus or post cumulus modifications. However, these spinels comprise relatively high contents of TiO_2 (0.9 – 1.7 wt.%) compared to spinels in the FAZ (type 1 and 2). Calculations show that type 1 spinels crystallized from a melt with a TiO_2 content range of 1-1.5 wt.% (Figure 5-5); these values are higher than that of the C_UZ parental liquid (0.47 wt.%). Similar high

TiO_2 contents in spinels were found in chromites from the Platreef of the Northern Limb and the Uitkomst Complex and were attributed to the influence of dolomite assimilation (Yudovskaya and Kinnaird, 2010; Yudovskaya et al, 2015). The enrichment of Ti is accompanied by increasing Fe^{3+} in type 1 spinels, and this trend could have been facilitated by an increase in oxygen fugacity as a consequence of *in situ* contamination, thus increasing their partitioning into chromites (Yudovskaya et al, 2015).

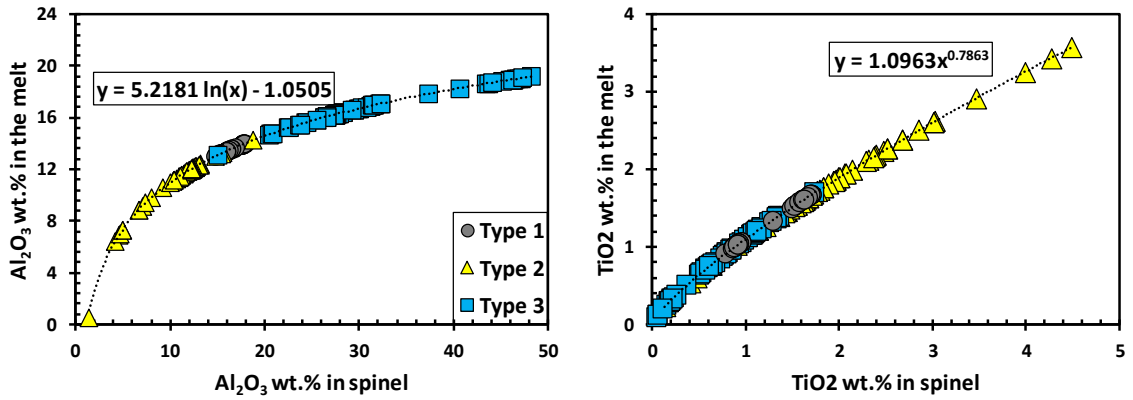

Figure 5-5: Constrained Al_2O_3 and TiO_2 contents of the melt with the aid of spinel chemistry, following Rollinson (2008).

Since type 2 spinels from the troctolite, wehrlite, and olivine gabbronorite are enclosed in cumulates and, for this reason, are expected to be the most primitive and most primary. However, the reaction of these type 2 spinels with an interstitial melt accompanied by olivine-spinel diffusive exchange under sub-solidus conditions may have resulted in the observed heterogeneous compositions. For instance, these spinels have variable but high $Fe^{3+}/(Cr+Fe^{3+}+Al)$, and TiO_2 (Figure 5-6), which follows the Fe-Ti trend postulated by Barnes and Roeder (2001). It is difficult to relate this trend the influence of sub-solidus re-equilibration, crystallization from an evolved melt, and crystallization from a contaminated liquid in these spinels, because these processes tend to change composition in a similar way (Hill and Roeder, 1974; Roeder and Campbell, 1985; Barnes and Roeder, 2001; Leuthold et al., 2015a).

However, the Fe-Ti trend in type 2 spinels can be assumed to reflect sub-solidus re-equilibration as a result of reaction with an interstitial melt (Barnes and Roeder, 2001). Reaction with an evolved and oxidized interstitial liquid would be responsible for the enrichment in Fe^{3+}, Ti, and Cr# of type 2 spinels (Henderson, 1975; Barnes, 1986; Scowen et al., 1991). It is noteworthy that type 2 spinels occasionally coexist with calcite grains in rocks affected by extensive dolomite contamination (Figure 4-10b), thus it seems viable

to propose that the interstitial melt that re-equilibrated with spinels was highly oxidizing and was thereby able to increase the overall Fe^{3+}/Fe^{total} ratio.

Type 3 spinels are exclusively found in the wehrlite units, and these comprise compositions with high Al, low Ti-V-$Fe^{3+,}$ and low ratios of Cr# and Fe^{3+} # (Figure 5-7). Compositions of these spinels follow the so-called 'Rum-trend', which is defined by increasing Al/Cr ratios with decreasing Fe^{total} content. The Rum trend has been interpreted to result from many factors, such as the reaction of spinels with an interstitial melt or olivine and plagioclase; reaction with a Ca-Tschermak clinopyroxene, reaction with a hybrid Al-rich melt of picrite and troctolite composition, and post-cumulus metamorphic reactions (e.g., Henderson, 1975; Bédard and Hebert, 1998; Barnes and Roeder, 2001; Gaeta et al., 2009; Leuthold et al., 2015).

An argument could be made that the overall enrichment towards the Al-apex in type 3 spinels (Figure 5-6) corresponds with the removal of Cr^{3+} and Fe^{3+} in the spinel structure upon reaction with an interstitial liquid that is Al-rich (Barnes and Roeder, 2001), as evident by the wehrlite's interstitial clinopyroxene and plagioclase. Resorption textures with thin magnetite rims along the interface, indicating disequilibrium between spinels and the melt, in a few spinels samples, provide evidence such reaction of spinels with a melt (Figure 4-11b). Hill and Roeder (1974) suggested that spinel co-existing with early olivine will be partially resorbed by the melt when clinopyroxene starts to crystallize, and spinels will reach equilibrium with the melt by forming thin magnetite rims to hinder complete resorption. However, the absence of such disequilibrium textures in spinels from a few samples (SD-15, SD-56, and SD-54) argues against sub-solidus reaction, unless these spinels and the melt had similar fO_2 at the time of crystallization (Hill and Roeder, 1974).

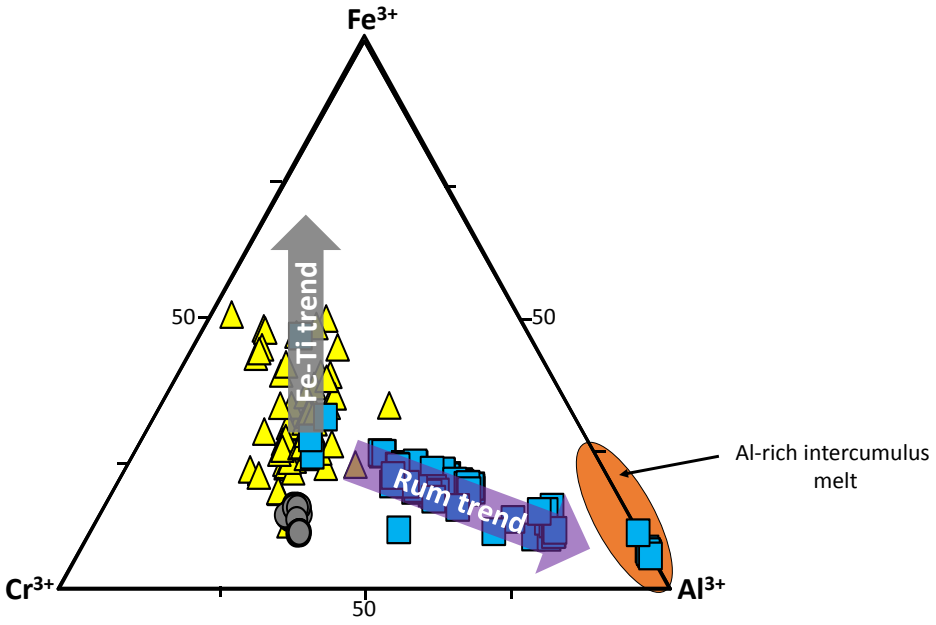

Figure 5-6: A Cr-Fe^{3+}-Al ternary plot showing the chemical evolution of spinel from various lithologies. The purple arrows (including the pink) spinel chemical towards the Al-apex, while the grey arrow shows Fe^{3+} enrichment. The shaded circle (orange) shows presumed plagioclase and clinopyroxene-rich interstitial liquid field. Clinopyroxene and plagioclase positions are based on the average interstitial compositions from the EPMA analysed minerals

An alternative explanation to the observed trend in type 3 spinels is the influence of carbonate addition on the melt and crystallizing phases. Based on Figure 5-5, type 3 spinels crystallized from a melt with high contents of Al_2O_3 of up to 19 wt.%. These concentrations are significantly higher than those of the suggested Upper Critical Zone parental melt (~13 wt.% in Barnes et al. (2010)). Experimental work conducted on carbonate assimilation processes by Conte et al. (2009) and Carter and Dasgupta (2016) show the presence of Al-rich spinels associated with a high Ca-Tschermak component in clinopyroxene. Carter and Dasgupta (2016) found that the Al content of the melt increases with increasing CaO addition, thus promoting the crystallization of Al-bearing phases. These observations concur with my results from the AFC modelling, which revealed that the Al-spinel solid-solution increases with increasing Al content of the melt during fractionation. This high Al_2O_3 content in type 3 spinels is accompanied by significantly low contents of TiO_2, ~ 0.6 wt.%, on average. Mineral compositions of type 3 spinels indicate that these were generated from a magma that was significantly carbonate-contaminated compared to the magma from which crystallized type 1 and type 2 spinels.

5.2.1 Linking carbonate to oxidation

Partial melting of dolomite contributes to liberation of large quantities of CO_2-rich fluids into the host melt (Ganino, 2008). Carbonate melts that are generated during assimilation are highly mobile due to relatively low viscosities and densities, which enables migration through the magma (Wenzel et al., 2002; Deegan et al., 2010). Wenzel et al., (2002) found that CO_2 fluids can have a highly oxidative capacity in the melt, high enough to induce spinel stability. The FAZ in some units, especially proximal to skarns, comprises pure carbonate phases, indicating the presence of fluids in the melt (e.g. Figure 4-10b), thus contributing to changes in oxygen fugacity.

Oxygen fugacity was constrained using the vanadium oxygen barometer calibrated by Mallmann and O'Neill (2009). The vanadium oxygen barometer is based on the partition coefficient of vanadium in spinel ($D_V^{sp/melt}$). The vanadium oxybarometer is most advantageous over other Fe proxies because V is immobile under post-cumulus and metamorphic conditions, and therefore reserves magmatic V^{3+}/V^{total} ratios and the redox conditions (Canil, 2002). The V oxybarometer is also advantageous in older rocks that have been influenced by alteration and metamorphism compared to other Fe proxies, as Fe is highly redox-sensitive. However, this oxygen barometer also has its limits. Its accuracy depends on the parental melt concentration of V that is determined independent of oxygen fugacity. The concentrations of V in parental magmas of the Bushveld Complex and Uitkomst Complex were calculated from the average olivine and chromite mineral compositions (Harmer and Shape, 1985; De Waal et al, 2001), thus independent of oxidation variations. Moreover, Mallmann and O'Neill (2009) calibrated the V oxybarometer at lower pressures (1 atm), thus can be insensitive for these Flatreef chromites that crystallized at depth. To ensure precision of the fO_2, values obtained from Mallman and O'Neill (2009) were compared to those obtained from the calibrations of Canil (1999). The precision was about 1-2% for chromites (type 1 and type 2 spinels) and 5% for type 3 spinels.

Type 1 spinels (from chromitite seams) are defined by homogenous compositions but show a bimodal distribution of oxygen fugacity values. Chromites from the UG-2 in UMT-335 have calculated fO_2 values that are at NNO+0.8, indicating equilibrium with a more oxidizing liquid than chromites from the lower chromitite in UMT-335 and UG-2 in UMT-345 (Figure 5-7). These high fO_2 values are accompanied by high TiO_2 contents, further suggesting an oxidized melt. In comparison, other type 1 spinels from the lower chromitite

and UG-2 in UMT-345 display fO_2 values that are slightly less oxidized (NNO+0.4), suggesting that contamination was less significant. The overall higher fO_2 values of the Flatreef suggest mobilization of fluids during the formation of chromitites, consistent with high amounts of carbonate xenoliths that are proximally located to these type 1chromites with higher calculated fO_2 values.

In comparison, chromites from the lower chromitite seam and UG-2 in UMT-345 display fO_2 values that are slightly less oxidized (NNO+0.3), suggesting that contamination was less significant in these units. The overall higher fO_2 values of the Flatreef suggest mobilization of fluids during the formation of chromitites, consistent with high amounts of carbonate xenoliths

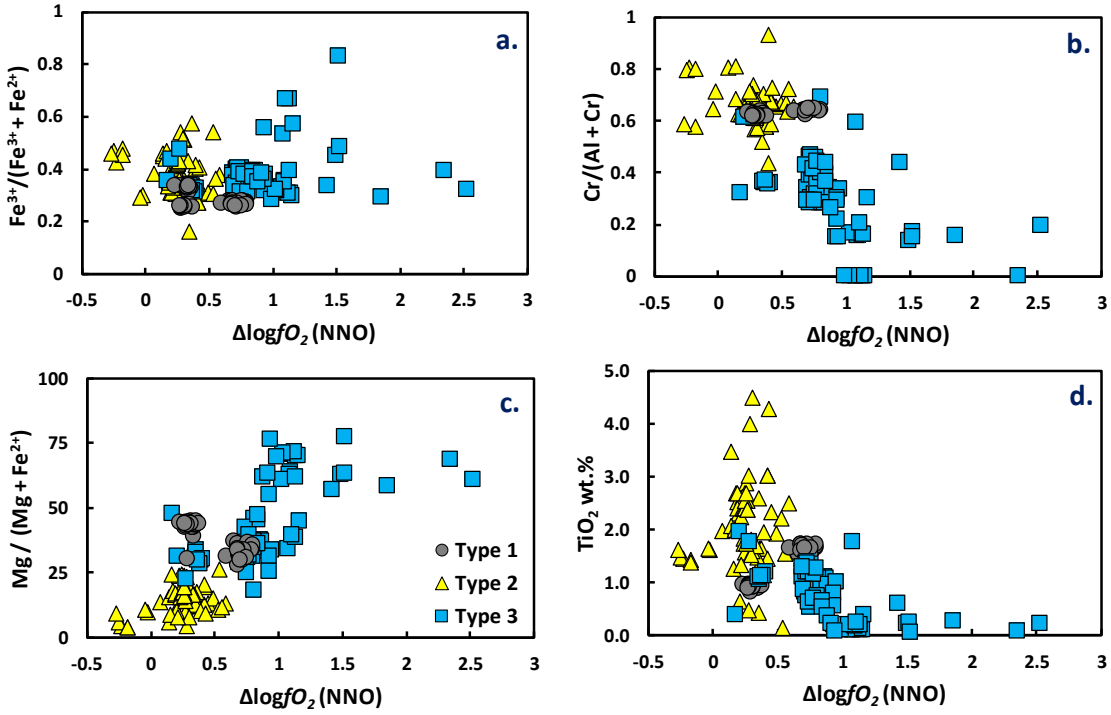

Figure 5-7: Calculated oxygen fugacity of different types of spinels from the Flatreef. Plotted against ***a*** *Fe^{3+}/Fe^{total};* ***b*** *Cr#;* ***c*** *Mg#; and* ***d*** *TiO_2 (wt.%).*

Oxygen fugacity constrained for Cr-spinels in the FAZ increases from spinel chadacrysts hosted in olivine (type 2) to spinels co-existing with olivine and clinopyroxene (type 3). Redox estimates in type 2 spinels range between NNO-0.3 to NNO+0.5 (Figure 5-7), indicating a less oxidized environment compared with type 1 and 3 spinels. In combination with lower fO_2conditions, these type 2 spinels show increasing Fe^{3+} ratio and TiO_2 (Figure 5-7a and d). The fO_2 values in type 2 spinels broadly overlap spinels from the feldspathic pyroxenite of the Platreef (Yudovskaya and Kinnaird, 2010; Jones, 2013), which are the

least contaminated (Figure 5-7). The overlap indicates that type 2 spinel crystallized from a melt that was initially not contaminated and was similar to the Platreef melt. Oxygen fugacity probably increased after the crystallization of spinels, consequently creating a melt with high Fe^{3+} and TiO_2 concentrations.

The most oxidized population in the Flatreef is Type 3 spinels from the FAZ, with fO_2 increasing from NNO+0.2 to NNO+1.5 (-7.9 to -4.8 log units), reflecting an oxidizing melt. Type 3 spinels are only found with the magma-carbonate hybrid zone, often coexisting with carbonate grains. These spinels also comprise lower TiO_2, Cr# and higher Fe^{3+}/Fe^{total}. Higher fO_2 and Fe^{3+}/Fe^{total} in these spinels, compared to type 2 and type 1, are suggest that they were crystallized in melts that interacted with greater amounts of CO_2 (Figure 5-7). An increase in fO_2 in the melt in the hybrid zone is accompanied by a shift of the bulk liquid composition into the spinel stability field, thus triggering the saturation and precipitation of abundant spinels.

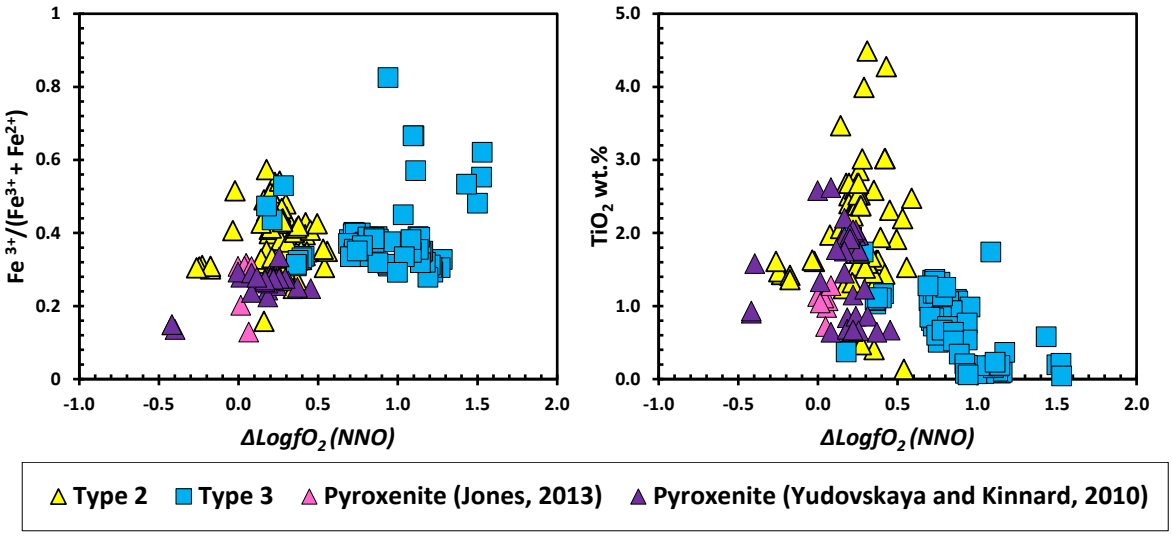

Figure 5-8: Plots of fO_2 vs Fe^{3+}/Fe^{total} and TiO_2 (wt.%) comparing the Flatreef FAZ spinels with spinels from the Platreef feldspathic pyroxenite reported by Jones (2013) and Yudovskaya and Kinnaird (2010).

5.3 Comparison of UG-2 chromitite of Flatreef with the UG-2 of the Bushveld and chromitites of the Platreef and Uitkomst Complex

Redox conditions constrained for the Flatreef chromites were compared with data from various studies from the Northern, Eastern, and Western Limbs, and also from the contemporaneous Uitkomst Complex, shown in Figure 5-9. Generally, all of the chromite data show a positive correlation between Fe^{3+}/Fe^{total} ratio and oxygen fugacity, calculated based on vanadium partitioning in spinels. The Eastern and Western Limbs display variable V content in chromite consistent with a relatively lower fO_2 (NNO+0.4 to NNO-2.4). The Eastern Limb data from the UG-2 analysed by Adetunji et al. (2013) show closely overlapping fO_2 values with the Northern Limb chromitites, indicating a slightly more oxidized magma. Adetunji et al. (2013) attribute these high values to mixing of magmas with different redox conditions. In contrast, UG-2 chromites from the Eastern Limb Booysendal mine (McCall, 2016) record lower fO_2 conditions (~NNO-0.2), indicating equilibration with a relatively reduced melt.

Chromites from the Western Limb reported by Veksler et al. (2014) recorded slightly lower fO_2 values (at ~NNO+0). In contrast, chromite data from the Western Limb from Zondereinde Mine (McCall 2016), interestingly, shows a marked enrichment of V contents of from ~2000 to 5000 ppm without major changes in Cr, Fe^{3+} or Ti (Figure 5-9). This corresponds to a shift in fO_2 values from NNO-0.1 down to NNO-2.4 as a response to increasing $D_V^{spinel/melt}$, attributed to a major increase in the V^{3+}/V^{4+} ratio in the melt (Canil, 1999; Naldrett et al., 2012). Low fO_2 conditions of the melt reduce the solubility of V^{3+}, while increasing the solubility of Cr^{3+} and Fe^{3+} (Barnes, 1986; Roeder and Reynolds, 1991; Papike et al., 2013). At lower fO_2, the competition for the spinel's octahedral site is more prevalent for V^{3+} compared to Cr^{3+} and Fe^{3+} (Canil, 1999), hence, the observed dramatic enrichment of V compared to Cr and Fe^{3+} in the Zondereinde chromites (Figure 5-9a and b). Therefore, it is argued that the recorded shifts in fO_2 of Western Limb chromites represent equilibration with a reducing magma.

Chromites from the 'carbonate-infused' Northern Limb and Uitkomst Complex record more elevated oxygen fugacity values compared to the Eastern and Western Limbs. The Platreef chromites are consistent with fO_2 conditions at ~NNO+0.3, overlapping with semi-massive and disseminated chromites from the Flatreef chromites of this study. Overlapping fO_2 values, including relative overlap in Fe^{3+} ratios and TiO_2, of these chromites, suggest crystallization from a similar magma affected by crustal contamination

to varying degrees (Yudovskaya and Kinnaird, 2010). Pronost et al. (2008) proposed that devolatilization of significant proportions of dolomite contributed to an elevation of CO_2 released into the melt of the Platreef. CO_2-fluids are considered oxidizing agents in melt (Ganino et al., 2008), thus would induce elevated fO_2 values constrained for the northern limb chromites. Such CO_2-fluid addition would probably have been most significant proximal to entrained xenoliths, as indicated by more elevated fO_2, up to NNO+ 1.2, of the massive chromites in contact with a contaminated footwall (Figure 4-3) or hanging wall (Langa et al., 2020).

Chromites from the Uitkomst Complex also recorded elevated fO_2 values at ~NNO+0.5, TiO_2 and Fe^{3+} ratios similar to those of the Northern Limb Platreef and Flatreef. The observed similarity in fO_2 values of the Platreef and Uitkomst Complex are, in both cases, proposed to have resulted from dolomite contamination. Maier et al. (2018) proposed that the Uitkomst Complex melt was contaminated by approximately 20 % Transvaal sediments, consistent with the ~18 % dolomite in the Platreef (Harris and Chaumba, 2001) and Flatreef (Abernethy, 2019).

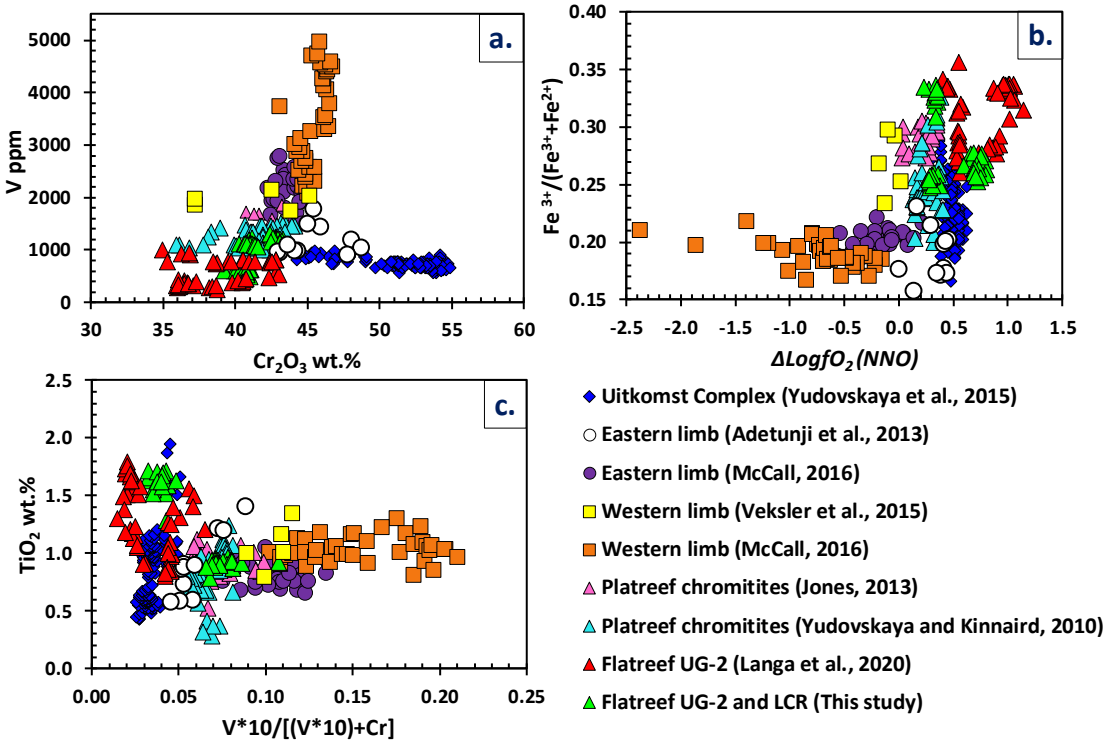

*Figure 5-9: Comparison of **a.** V vs Cr_2O_3, **b.** Fe^{3+}/Fe^{total} vs fO_2 and **c.** TiO_2 vs V/(V+Cr) of chromites from the UG-2 seam in the Bushveld Complex, harzburgite in the Uitkomst Complex, the chromitite ores in the Platreef, and the UG-2 and LCR seams in the Flatreef. LCR is the lower chromitite seam in UMT-335.*

5.4 Implications for the formation of Flatreef chromitites

Dolomite contamination in the Northern Limb is proposed to have taken place upon magma emplacement (e.g. Harris and Chaumba, 2001), resulting in dissolution reactions and partial melting of dolomite. Previous experiments on carbonate contamination and work on natural skarn-bearing lithologies have reported the occurrence of abundant Fe-Ti-V oxides (Chadwick et al., 2007; Ganino et al., 2008; Carter and Dasgupta, 2016; Liao et al., 2016; Gil et al., 2019). In addition, reports from the Volspruit Sulphide Zone in the northern limb (Tanner et al., 2019) and the Jacurici Complex in Brazil (Friedrich et al., 2019) provide evidence of an increase in fO_2 as a consequence of carbonate contamination. Both these studies argue that the liberation of volatile fluids into the melt triggered an earlier saturation of chromite.

Likewise, equally high oxygen fugacity values of chromitites in the Bushveld's Northern Limb and the Uitkomst Complex are also explained by the local infusion of Malmani dolomite. Emplacement of magma onto the carbonate platform triggered substantial production of CO_2-rich volatiles (Ganino et al., 2008; Maier et al., 2018). In magmatic systems, the CO_2 species is regarded as an oxidizing agent. Ganino et al. (2008) suggested that addition of about 10 wt.% CO_2 is enough to increase fO_2 of the magma by an order of magnitude relative to the QFM-buffer. The AFC-model presented above showed that the most contaminated FAZ wehrlite corresponds to liberations of up to 9 wt.% CO_2. Thus, the amounts of the liberated CO_2 would be greater, and have a more oxidizing effect, within the hybrid melt, and will decrease away from the reaction site into the host magma.

The model presented here implies that the Eastern and Western Limbs represent a relatively uncontaminated 'normal' Bushveld magmatic environment. The 'normal' magma crystallized chromites at fO_2 of, on average, NNO-0.5. Emplacement of this 'normal' Bushveld magma onto a carbonate platform can potentially produce magmas and that are chemically distinct, thus crystallize chromites that are also chemically distinct. This is mainly observed in the Northern Limb, where the limb was emplaced onto the Malmani dolomite (Harris and Chaumba, 2001). The magma interacted with larger quantities of liberated CO_2, thus crystallizing chromites at higher fO_2 (NNO+0.3 to NNO+1.3) conditions. Flatreef massive UG-2 chromitites reflect a parental melt that experienced greater interaction with volatile components due to its proximity to the FAZ units. These chromites have distinct redox conditions (up to NNO+1.3) and mineral chemistry (higher Ti, Fe^{3+}/Fe^{total}, lower Cr) compared to other chromites found in the

Flatreef (~NNO+0.3, lower Ti, Fe^{3+}/Fe^{total}, and higher Cr). These distinctions are mainly attributed to the high amounts of CO_2 with highly oxidizing effects that are liberated proximal to hybrid zones in the melt. Papike et al. (2015) showed that increasing fO_2 in the melt will transition the spinel structure from a normal structure to that of an inverse structure. This will allow for the accomdation of Fe^{3+} and tetravalent Ti^{4+}. Hence the high Fe^{3+} and Ti in the chromites most proximla to the FAZ.

The most widely recognized model for the formation of chromitite ores in the northern limb is magma mixing (e.g. Hulbert and Von Gruenewaldt, 1985; McDonald et al., 2005; Yudovskaya et al., 2017). Yudovskaya et al. (2017) propose that the chromitite layers in the Faltreef were mainly triggered by mixing of compositionally similar magmas and, thus, induced crystallization of only minor amounts of chromites. There are no objections to this model for chromites of the lower chromitite seam in UMT-345 and UG-2 seam in UMT-345. However, the chemically distinct chromites of the UG-2 seam that occur proximal to the FAZ are proposed to have been triggered by assimilation of dolomite.

The Flatreef is also characterized by extensive PGE-mineralization. Large quantities of oxidizing fluids in the Northern Limb may have also played a major role in promoting the PGE-rich mineralization. The assimilation of carbonate material could have triggered the saturation of sulphides in the melt as a result of a decrease in the Fe^{2+}/Fe^{3+} ratio with increasing fO_2 (De Waal, 1975; Gauert, 2001). The emplacement of a melt close to sulphide saturation (Hutchinson and Kinnaird, 2005) onto a carbonate footwall, and a subsequent decrease in the S solubility as fO_2 increases, would have promoted sulphide saturation. A similar mechanism for sulphide saturation is proposed for the development of the Volspruit Sulphide Zone in the Grasvally (Tanner et al., 2019).

Conclusions

The chief aim of this study was to examine the influence of carbonate assimilation on precipitation of spinels from the Flatreef. Petrogenetic examination of the drill cores from the Flatreef provides substantial evidence for having been influenced by crustal contamination. Evidence for magma-floor rock interaction is mainly presented by a high abundance of high-temperature skarn xenoliths entrained in the mafic units. High temperature reactions of country rock material with the magma produced highly contaminated hybrid lithologies. Carbonate-contaminated lithologies are dominated by CaO- and MgO-rich assemblages, are consistent with contamination for the partial melting of dolomite. Hybrid lithologies comprise clinopyroxene, olivine, Cr-spinel, and variable proportions of plagioclase. Partial melting of dolomite material mobilized Ca-rich melts, producing silica-undersaturated hybrid magmas that is reflected by correspondingly higher concentrations of fluid-mobile elements (LILE), compared to lesser contaminated silica-rich feldspathic pyroxenite with a low concentration of LILE.

The primary effects for magma-carbonate interaction, as observed from PELE modelling constraints, are (1) the increased stability of earlier crystallization of heavily disseminated Cr-rich spinels, (2) the enhanced stability of early olivine that indicates enhanced MgO concentration in the melt, (3) crystallization of large proportions of clinopyroxene with increasing contents of Al_2O_3 and CaO in the melt, (4) stability of clinopyroxene with enhanced Wo contents, (5) degassing of large quantities of CO_2-fluids, up to 9 wt.%.

PELE modelling results reproduced the mineral assemblage of the most contaminated wehrlite unit in the FAZ. Such as early-formed spinels with a high Al_2O_3 content, amoeboidal olivine with high Fo contents (~86), clinopyroxene with a high calculated Ca-Tschermak component (~33%), and plagioclase with high An contents (An_{77}). Thus, their link to partial decomposition of dolomite is supported.

The highly contaminated lithologies comprise a high modal abundance of spinels. Spinels within moderately contaminated lithologies preserved evidence for having experienced extensive sub-solidus re-equilibration. However, the influence of contamination on these spinels is not clear, as they recorded slightly low overall redox conditions, similar to the feldspathic pyroxenite, in spite of their occurrence within hybrids lithologies. In contrast, spinels that are restricted to highly contaminated wehrlite lithologies indicate a different magma composition, and also recorded highly oxidizing conditions. The formation of

these spinels was clearly promoted by carbonate assimilation, which shifted the liquid line of descent of the primary magma from that of the pyroxenite to that of the spinel-rich wehrlite rocks.

Carbonate assimilation also, theoreticaly, generated high quantities of CO_2-rich fluids, with a total oxidative capacity that decreases from the hybrid zone into the interior of the magma. Consequently, creating an oxidizing environment favourable for the formation of chromitite layers. Chromitites proximal to the contaminated footwall comprise chromites with elevated redox conditions, which suggests an influence of carbonate assimilation on the stability of spinels. These chromites also have mineral compositions that indicate an influence of contamination, such as high TiO_2 and Fe^{3+} ratios. Evidence provided here argues for the extensive influence of country rock assimilation on the saturation of chromites.

Correlation of chromitites from Flatreef with those of the Eastern and Western Limbs, the Platreef and the Uitkomst Complex suggest that the Flatreef chromitites show closest similarity to the Flatreef and Uitkomst Complex. This is attributed to the emplacement of the Northern Limb and the Uitkomst Complex onto the Malmani dolomite carbonate platform. Interaction of the of the magma with greater amounts of carbonate-generated fluids promoted a highly oxidizing environment, thus crystallizing chromites with higher fO_2 values, higher Fe^{3+}/Fe^{total}, TiO_2 and lower Cr_2O_3 contents. These effects were noted to be most pronounced in chromites proximal to contaminated FAZ units. Suggesting that the greater the amount of CO_2 interacting with the melt, the higher the fO_2 and the lower the Cr content in in chromites. Thus, the proposal is for carbonate assimilation as a trigger for chromites solely within close distance to the FAZ.

References

Abernethy, K.E.L. 2019. Assimilation of Dolomite by Bushveld Magmas in the Flatreef; Implications for the Origin of Ni- Cu-PGE Mineralization and the Precambrian Atmosphere (Unpublised PhD thesis). Cardiff University, 332pp.

Adetunji, J., Everitt, S. and Rollinson, H. 2013. New Mössbauer measurements of $Fe^{3+}/\Sigma Fe$ ratios in chromites from the early Proterozoic Bushveld Complex, South Africa. Precambrian Research, 228, 194–205.

Appiah-nimoh, F. 2004. A Geological Study of the Platreef at Potgietersrus Platinum Mine with Emphasis on the Magmatic Processes , Contamination and Metasomatism. Masters Thesis. Rand Afrikaans University, 1–65pp.

Ballhaus, C. 1993. Redox states of lithospheric and asthenospheric upper mantle. Contributions to Mineralogy and Petrology, 114, 331–348.

Ballhaus, C., Berry, R. and Green, D. 1991. High pressure experimental calibration of the olivine-orthopyroxene- spinel oxygen geobarometer: implications for the oxidation state of the upper mantle. Contributions to Mineralogy and Petrology, 104, 27–40.

Barnes, S.J. 1986. The distribution of chromium among orthopyroxene, spinel and silicate liquid at atmospheric pressure. Geochimica et Cosmochimica Acta, 50, 1889–1909.

Barnes, S.J. and Maier, W.D. 2002. Platinum-group elements and microstructures of normal Merensky Reef from Impala Platinum mines, Bushveld Complex. Journal of Petrology, 43, 103–128.

Barnes, S.-J., Maier, W.D. and Curl, E.A. 2010. Composition of the Marginal Rocks and Sills of the Rustenburg Layered Suite, Bushveld Complex, South Africa: Implications for the Formation of the Platinum-Group Element Deposits. Economic Geology, 105, 1491–1511.

Barnes, C.G., Prestvik, T., Sundvoll, B. and Surratt, D. 2005. Pervasive assimilation of carbonate and silicate rocks in the Hortavær igneous complex, north-central Norway. Lithos, 80, 179–199.

Barnes, S.J. and Roeder, P.L. 2001. The range of spinel composition in terrestrial mafic and ultramafic rocks. Journal of Petrology, 42, 2279–2302.

Bédard, J.H. and Hebert, R. 1998. Formation of chromitites by assimilation of crustal pyroxenites and gabbros into peridotitic intrusions: North Arm Mountain massif, Bay of Islands ophiolite, Newfoundland, Canada. Journal of Geophysical Research-Solid Earth, 103, 5165–5184.

Boudreau, A.. 1999. PELE—a version of the MELTS software program for the PC platform. Computers & Geosciences, 25, 201–203.

Boudreau, A.E. 2016. The Stillwater Complex, Montana – Overview and the significance of volatiles. Mineralogical Magazine, 80, 585–637.

Boudreau, A. 2019. The Effects of Volatiles on Mineral Stability and Volatile Fluxing. In: Hydromagmatic Processes and Platinum-Group Element Deposits in Layered Intrusions. Cambridge University Press, 140–155.

Boynton, W. V 1984. Cosmochemistry of the Rare Earth Elements: Meteorite Studies. In: Rare Earth Element Geochemistry. Amsterdam, Elsevier B.V., 63–114.

Buchanan, D.L. and Nolan, J. 1979. Solubility of sulfur and sulfide immiscibility in synthetic tholeiitic melts and their relevance to Bushveld-Complex rocks. Canadian Mineralogist, 17, 483–494.

Buchanan, D.L., Nolan, J., Suddaby, P., Rouse, J.E., Viljoen, M.J. and Davenport, J.W.J. 1981. The genesis of sulfide mineralization in a portion of the Potgietersrus limb of the Bushveld complex. Economic Geology, 76, 568–579.

Button, A. 1975. Geochemistry of the Malmani Dolomite of the Transvaal Supergroup in the northeastern Transvaal. Economic geology Research Unit, 1–21.

Button, A. and Cawthorn, R.G. 2015. Distribution of mafic sills in the Transvaal Supergroup , northeastern South Africa. Journal of Geological Society.

Cameron, E.N. 1977. Chromite in the central sector of the Eastern Bushveld Comples, South Africa. American Mineralogist, 62, 1082–1096.

Cameron, E.N. 1978. The Lower Zone of the eastern Bushveld Complex in the Oliphants River Trough. Journal of Petrology, 19, 437–462.

Cameron, E.N. and Desborough, G.A. 1969. Occurence and characteristics of chromite deposits - eastern Bushveld Complex. Economic Geology Monograph, 4, 23–40.

Canil, D. 1999. Vanadium partitioning between orthopyroxene, spinel and silicate melt and the redox states of mantle source regions for primary magmas. Geochimica et Cosmochimica Acta, 63, 557–572.

Carter, L.B. and Dasgupta, R. 2016. Effect of melt composition on crustal carbonate assimilation: Implications for the transition from calcite consumption to skarnification and associated CO2degassing. Geochemistry, Geophysics, Geosystems, 17, 3893–3916.

Cawthorn, R.G. 2015. The Bushveld Complex, South Africa. In: Layered Intrusions. 517–587.

Chadwick, J.P., Troll, V.R., Ginibre, C., Morgan, D., Gertisser, R., Waight, T.E. and Davidson, J.P. 2007. Carbonate Assimilation at Merapi Volcano, Java, Indonesia: Insights from Crystal Isotope Stratigraphy. Journal of Petrology, 48, 1793–1812.

Charlier, B., Namur, O., Latypov, R. and Tegner, C. 2015. Layered Intrusions. Dordrecht, Springer Netherlands

Clay, A.N. 1981. The geology of the Malmani Dolomite Sub-Group in the Carletonville area, Transvaal. Unpublished Masters Thesis. University of the Witwatersrand, 338pp.

Conte, A.M., Dolfi, D., Gaeta, M., Misiti, V., Mollo, S. and Perinelli, C. 2009. Experimental constraints on evolution of leucite-basanite magma at 1 and 10^{-4} GPa: implications for parental compositions of Roman high-potassium magmas. European Journal of Mineralogy, 21, 763–782.

Crowson, P. 2001. Minerals Handbook 2000-2001. Edenbridge, Mining Journal Books Ltd., 486pp.

Deegan, F.M., Troll, V.R., Freda, C., Misiti, V., Chadwick, J.P., McLeod, C.L. and Davidson, J.P. 2010. Magma–Carbonate Interaction Processes and Associated CO2 Release at Merapi Volcano, Indonesia: Insights from Experimental Petrology. Journal of Petrology, 51, 1027–1051.

Deer, W.A., Howie, R.A. and Zussman, J. 1992. An introduction to rock-forming minerals. England, Longman Group Ltd, 363pp.

De Waal, S. 1975. Carbon dioxide and water from metamorphic reactions as agents for sulfide and spinel precipitation in mafic magmas. Trans. Geol. Soc. S. Afr., 80, 193–196.

De Waal, S.A., Maier, W.D., Armstrong, R.A. and Gauert, C.D.K. 2001. Parental magma and emplacement of the stratiform Uitkomst Complex, South Africa. Canadian Mineralogist, 39, 557–571.

Di Rocco, T., Freda, C., Gaeta, M., Mollo, S. and Dallai, L. 2012. Magma Chambers Emplaced in Carbonate Substrate: Petrogenesis of Skarn and Cumulate Rocks and Implications for CO2 Degassing in Volcanic Areas. Journal of Petrology, 53, 2307–2332.

Eales, H.V. and Cawthorn, R.G. 1996. The Bushveld Complex. In: Layered Intrusions. 181–229.

Filho, C.F.F. and Araujo, S.M. 2009. Review of Brazilian chromite deposits associated with

layered intrusions : geological and petrological constraints for the origin of stratiform chromitites. 118.

Fomin, I., Nikolaev, G. and Ariskin, A. 2013. Estimates of Redox Conditions and Temperatures of Closure of the Olivine-Spinel System in Cumulate Rocks of the Ioko-Dovyren Layered Intrusion. Proceedings of 12th SGA Biennial Meeting "Mineral deposit research for a high-tech world", 3, 982–984.

Friedrich, B.M., Marques, J.C., Olivo, G.R., Frantz, J.C. and Joy, B. 2019. Petrogenesis of the massive chromitite layer from the Jacurici Complex , Brazil : evidence from inclusions in chromite. Mineralium Deposita, 55, 1105–1126.

Gaeta, M., Di Rocco, T. and Freda, C. 2009. Carbonate Assimilation in Open Magmatic Systems: the Role of Melt-bearing Skarns and Cumulate-forming Processes. Journal of Petrology, 50, 361–385.

Gain, S.B. and Mostert, A.B. 1982. The geological setting of the platinoid and base metal sulfide mineralization in the Platreef of the Bushveld Complex in Drenthe, North of Potgietersrus. Economic Geology, 77, 1395–1404.

Ganino, C., Arndt, N.T., Zhou, M.-F., Gaillard, F. and Chauvel, C. 2008. Interaction of magma with sedimentary wall rock and magnetite ore genesis in the Panzhihua mafic intrusion, SW China. Mineralium Deposita, 43, 677–694.

Gauert, C. 2001. Sulphide and oxide mineralisation in the Uitkomst Complex, South Africa: origin in a magma conduit. Journal of African Earth Sciences, 32, 149–161.

Gauert, C.D.K., De Waal, S.A. and Wallmach, T. 1995. Geology of the ultrabasic to basic Uitkomst complex, eastern Transvaal, South Africa: an overview. Journal of African Earth Sciences, 21, 553–570.

Gavrilenko, M., Herzberg, C. and Vidito, C. 2016. A Calcium-in-Olivine Geohygrometer and its Application to Subduction Zone A Calcium-in-Olivine Geohygrometer and its Application to Subduction Zone Magmatism. Journal of Petrology, 57, 1811–1832.

Gil, G., Gunia, P., Barnes, J.D., Szymański, M., Jokubauskas, P., Kalbarczyk-Gil, A. and Bagiński, B. 2019. Origin of Talc and Fe-Ti-V Mineralization in the Kletno Deposit (the Śnieżnik Massif, SW Poland). Minerals, 10, 13.

Grobler, D.F., Brits, J.A.N., Maier, W.D. and Crossingham, A. 2018. Litho- and chemostratigraphy of the Flatreef PGE deposit, northern Bushveld Complex. Mineralium Deposita, 5–8.

Gualda, G.A.R., Ghiorso, M.S., Lemons, R. V. and Carley, T.L. 2012. Rhyolite-MELTS: a Modified Calibration of MELTS Optimized for Silica-rich, Fluid-bearing Magmatic Systems. Journal of Petrology, 53, 875–890.

Hamann, C., Bläsing, S., Hecht, L., Schäffer, S., Deutsch, A., Osterholz, J. and Lexow, B. 2018. The reaction of carbonates in contact with laser-generated, superheated silicate melts: Constraining impact metamorphism of carbonate-bearing target rocks. Meteoritics and Planetary Science, 53, 1644–1686.

Harmer, R.E and Sharpe, M. R., 1985. Field relations and strontium isotope systematics of the marginal rocks of the eastern Busveld complex. Economic Geology, 80, 813-837.

Harris, C. and Chaumba, J.B. 2001. Crustal Contamination and Fluid–Rock Interaction during the Formation of the Platreef, Northern Limb of the Bushveld Complex, South Africa. Journal of Petrology, 42, 1321–1347.

Harris, C., Pronost, J.J.M., Ashwal, L.D. and Cawthorn, R.G. 2005. Oxygen and hydrogen isotope stratigraphy of the Rustenburg Layered Suite, Bushveld Complex: Constraints on crustal contamination. Journal of Petrology, 46, 579–601.

Hart, S.R. and Dunn, T. 1993. Experimental cpx / melt partitioning of 24 trace elements.

Contributions to Mineralogy and Petrology, 113, 1–8.

Henderson, P. 1975. Reaction trends shown by chrome-spinels of the Rhum layered intrusion. Geochimica et Cosmochimica Acta, 39, 1035-2–44.

Herd, C.D.K. 2006. Insights into the redox history of the NWA 1068/1110 martian basalt from mineral equilibria and vanadium oxybarometry. American Mineralogist, 91, 1616–1627.

Hill, R. and Roeder, P. 1974. The Crystallization of Spinel from Basaltic Liquid as a Function of Oxygen Fugacity. The Journal of Geology, 82, 709–729.

Howarth, G.H. and Prevec, S.A. 2013. Hydration vs . oxidation : Modelling implications for Fe-Ti oxide crystallisation in mafic intrusions , with specifi c reference to the Panzhihua intrusion , SW China. Geoscience Frontiers, 4, 555–569.

Hulbert, L.J. and Von Gruenewaldt, G. 1985. Textural and compositional features of chromite in the lower and critical zones of the Bushveld complex south of Potgietersrus. Economic Geology, 80, 872–895.

Hulley, V. 2005. Reactions between Country Rock Xenoliths and the Magma of the Uitkomst Complex , with Implications for the Origin of the Sulphide Mineralisation (Unpublished Masters thesis)., 168pp.

Hutchinson, D. and Kinnaird, J. a. 2005. Complex multistage genesis for the Ni–Cu–PGE mineralisation in the southern region of the Platreef, Bushveld Complex, South Africa. Applied Earth Science : IMM Transactions section B, 114, 208–224.

Iacono-marziano, G., Gaillard, F., Pichavant, M., Iacono-marziano, G., Gaillard, F. and Pichavant, M. 2008. Limestone assimilation by basaltic magmas : an experimental re-assessment and application to Italian volcanoes To cite this version : HAL Id : insu-00194400.

Ihlenfeld, C. and Keays, R.R. 2011. Crustal contamination and PGE mineralization in the Platreef, Bushveld Complex, South Africa: Evidence for multiple contamination events and transport of magmatic sulfides. Mineralium Deposita.

Irvine, T.N. 1975. Crystallization sequences in the Muskox intrusion and other layered Origin of chromitite layers and similar deposits of other magmatic ores. Geochimica et Cosmochimica Actamica et Cos, 39, 991–1020.

Irvine, T.N. 1977. Origin of chromitite layers in the Muskox intrusion and other stratiform intrusions: A new interpretation. Geology, 5, 273–277.

Joesten, R. 1977. Mineralogical and chemical evolution of contaminated igneous rocks at a gabbro-limestone contact, Christmas Mountains, Big Bend region, Texas. Geological Society of America Bulletin, 88, 1515.

Kamenetsky, V.S. 2001. Factors Controlling Chemistry of Magmatic Spinel: an Empirical Study of Associated Olivine, Cr-spinel and Melt Inclusions from Primitive Rocks. Journal of Petrology, 42, 655–671.

Kinnaird, J.A., Hutchinson, D., Schurmann, L., Nex, P.A.M. and de Lange, R. 2005. Petrology and mineralisation of the southern Platreef: northern limb of the Bushveld Complex, South Africa. Mineralium Deposita, 40, 576–597.

Kinnaird, J.A., Kruger, F.J., Nex, P.A.M. and Cawthorn, R.G. 2002. Chromitite formation — a key to understanding processes of platinum enrichment.

Kress, V.C. and Carmichael, I.S.E. 1991. The compressibility of silicate liquids containing Fe2O3 and the effect of composition, temperature, oxygen fugacity and pressure on their redox states. Contributions to Mineralogy and Petrology, 108, 82–92.

Kruger, F.J. 2005. Filling the Bushveld Complex magma chamber : lateral expansion , roof and floor interaction , magmatic unconformities , and the formation of giant chromitite , PGE and Ti-V-magnetitite deposits. 451–472.

Langa, M.M., Jugo, P.J., Leybourne, M.I., Grobler, D.F., Adetunji, J., Adetunji, J. and Skogby, H. 2020. Chromite chemistry of a massive chromitite seam in the northern limb of the Bushveld Igneous Complex , South Africa : correlation with the UG-2 in the eastern and western limbs and evidence of variable assimilation of footwall rocks. Mineralium Deposita.

Latypov, R., Chistyakova, S. and Mukherjee, R. 2017. A Novel Hypothesis for Origin of Massive Chromitites in the Bushveld Igneous Complex. Journal of Petrology, 58, 1899–1940.

Latypov, R., Costin, G., Chistyakova, S., Hunt, E.J., Mukherjee, R. and Naldrett, T. 2018. Platinum-bearing chromite layers are caused by pressure reduction during magma ascent. Nature Communications, 9, 462.

Lee, C.T.A., Leeman, W.P., Canil, D. and Li, Z.X.A. 2005. Similar V/Sc systematics in MORB and arc basalts: Implications for the oxygen fugacities of their mantle source regions. Journal of Petrology, 46, 2313–2336.

Lesher, C.M., Carson, H.J.E. and Houlé, M.G. 2019. Genesis of chromite deposits by dynamic upgrading of Fe ± Ti oxide xenocrysts. Geology, 47, 207–210.

Leuthold, J., Blundy, J.D. and Brooker, R.A. 2015a. Experimental petrology constraints on the recycling of mafic cumulate : a focus on Cr ‑ spinel from the Rum Eastern Layered Intrusion , Scotland. Contributions to Mineralogy and Petrology, 170, 1–27.

Leuthold, J., Blundy, J.D. and Brooker, R.A. 2015b. Experimental petrology constraints on the recycling of mafic cumulate: a focus on Cr-spinel from the Rum Eastern Layered Intrusion, Scotland. Contributions to Mineralogy and Petrology, 170.

Liao, M., Tao, Y., Song, X., Li, Y. and Xiong, F. 2016. Study of oxygen fugacity during magma evolution and ore genesis in the Hongge mafic–ultramafic intrusion, the Panxi region, SW China. Acta Geochimica.

Libourel, G. 1999. Systematics of calcium partitioning between olivine and silicate melt : implications for melt structure and calcium content of magmatic olivines. Contributions to Mineralogy and Petrology, 136, 63–80.

Lipin, B.R. 1993. Pressure Increases , the Formation of Chromite Seams , and the Development of the Ultramafic Series in the Stillwater Complex , Montana. 34, 955–976.

Maier, W.D., Abernethy, K.E.L., Grobler, D.F. and Moorhead, G. 2021. Formation of the Flatreef deposit, northern Bushveld, by hydrodynamic and hydromagmatic processes. Mineralium Deposita, 56, 11–30.

Maier, W.D., Barnes, S.-J. and Groves, D.I. 2013. The Bushveld Complex, South Africa: formation of platinum–palladium, chrome- and vanadium-rich layers via hydrodynamic sorting of a mobilized cumulate slurry in a large, relatively slowly cooling, subsiding magma chamber. Mineralium Deposita, 48, 1–56.

Maier, W.D., Barnes, S.-J. and Li, C. 2002. A Re-Evaluation of the Role of Crustal Contamination in the Formation of Magmatic Sulfides in the Bushveld Complex. In: 9th International Platinum Symposium. 1–3.

Maier, W.D., Prevec, S.A., Scoates, J.S., Wall, C.J., Barnes, S.-J. and Gomwe, T. 2018. The Uitkomst intrusion and Nkomati Ni-Cu-Cr-PGE deposit, South Africa: trace element geochemistry, Nd isotopes and high-precision geochronology. Mineralium Deposita, 53, 67–88.

Mallmann, G. and O'Neill, H.S.C. 2009. The crystal/melt partitioning of V during mantle melting as a function of oxygen fugacity compared with some other elements (Al, P, Ca, Sc, Ti, Cr, Fe, Ga, Y, Zr and Nb). Journal of Petrology, 50, 1765–1794.

Mathez, E.A. and Kinzler, R.J. 2017. Metasomatic chromitite seams in the bushveld and rum layered intrusions. Elements, 13, 397–402.

McCall, M.-J. 2016. Mineralogical and geochemical variations in the UG2 reef at Booysendal and Zondereinde mines , with implications for beneficiation of PGM. (MSc Thesis). Stellenbosch University, 140pp.

McDonald, I., Holwell, D.A. and Armitage, P.E.B. 2005. Geochemistry and mineralogy of the Platreef and 'Critical Zone' of the northern lobe of the Bushveld Complex, South Africa: Implications for Bushveld stratigraphy and the development of PGE mineralisation. Mineralium Deposita, 40, 526–549.

McDonough, W.F. and Sun, S. 1995. The composition of the Earth. Chemical Geology, 2541, 223–253.

Mollo, S., Gaeta, M., Freda, C., Di Rocco, T., Misiti, V. and Scarlato, P. 2010. Carbonate assimilation in magmas: A reappraisal based on experimental petrology. Lithos, 114, 503–514.

Molyneux, T. 1970. The geology of the area in the vicinity of Magnet Heights, eastern Transvaal, with special reference to the magmatic iron ore. Geological society of South Africa: Special publication, 1, 228–241.

Mondal, S.K. and Mathez, E.A. 2007. Origin of the UG2 chromitite layer , Bushveld Complex. 48, 495–510.

Morse, S.A. 1980. Basalts and Phase Diagrams. New York, NY, Springer New York, 1–495pp.

Murck, B.W. and Campbell, I.H. 1986. The effects of temperature, oxygen fugacity and melt composition on the behaviour of chromium in basic and ultrabasic melts. Geochimica et Cosmochimica Acta, 50, 1871–1887.

Naldrett, A.J., Wilson, A., Kinnaird, J., Yudovskaya, M. and Chunnett, G. 2012. The origin of chromitites and related PGE mineralization in the Bushveld Complex: new mineralogical and petrological constraints. Mineralium Deposita, 47, 209–232.

Nex, P.A.M., Cawthorn, R.G. and Kinnaird, J.A. 2002. Geochemical effect of magma addition: compositional reversals and decoupling of trends in the Main Zone of the western Bushveld Complex. Mineralogical magazine, 66, 833–856.

Nicholson, D.M. and Mathez, E.A. 1991. Petrogenesis of the Merensky Reef in the Rustenburg section of the Bushveld Complex. Contributions to Mineralogy and Petrology, 107, 293–309.

Nikolaev, G.S., Ariskin, A.A., Barmina, G.S., Nazarov, M.A. and Almeev, R.R. 2016. Test of the Ballhaus–Berry–Green Ol–Opx–Sp oxybarometer and calibration of a new equation for estimating the redox state of melts saturated with olivine and spinel. Geochemistry International, 54, 301–320.

O'Neill, H.S.C. and Wall, V.J. 1987. The Olivine-Orthopyroxene-Spinel Oxygen Geobarometer , the Nickel Precipitation Curve , and the Oxygen Fugacity of the Earth ' s Upper Mantle. Journal of Petrology, 28, 1169.

Pang, K.-N., Zhou, M.-F., Lindsley, D., Zhao, D. and Malpas, J. 2007. Origin of Fe-Ti Oxide Ores in Mafic Intrusions: Evidence from the Panzhihua Intrusion, SW China. Journal of Petrology, 49, 295–313.

Pang, K.N., Zhou, M.F., Lindsley, D., Zhao, D. and Malpas, J. 2008. Origin of Fe-Ti oxide ores in mafic intrusions: Evidence from the Panzhihua intrusion, SW China. Journal of Petrology, 49, 295–313.

Papike, J.J., Burger, P. V., Bell, A.S., Le, L., Shearer, C.K., Sutton, S.R., Jones, J. and Newville, M. 2013. Developing vanadium valence state oxybarometers (spinel-melt, olivine-melt, spinel-olivine) and V/(Cr+Al) partitioning (spinel-melt) for martian olivine-phyric basalts. American Mineralogist, 287–301.

Papike, J.J., Burger, P. V., Bell, A.S., Shearer, C.K., Le, L. and Jones, J. 2015. Normal to inverse

transition in martian spinel: Understanding the interplay between chromium, vanadium, and iron valence state partitioning through a crystal-chemical lens. American Mineralogist, 100, 2018–2025.

Patkó, L., Liptai, N., Aradi, L.E., Klebesz, R., Sendula, E., Bodnar, R.J., Kovács, I.J., Cesare, B., Novák, A., Trásy, B. and Szabo, C. 2020. Metasomatism-induced wehrlite formation in the upper mantle beneath the Nógrád-Gömör Volcanic Field (Northern Pannonian Basin): Evidence from xenoliths. Geoscience Frontiers, 11, 943–964.

Pecher, A., Arndt, N., Jean, A., Bauville, A., Ganino, C. and Athurion, C. 2010. Structure of the Panzhihua Fe - Ti - V Deposit , China. Geoscience Frontiers, 4, 571–581.

Pronost, J., Harris, C. and Pin, C. 2008. Relationship between footwall composition, crustal contamination, and fluid–rock interaction in the Platreef, Bushveld Complex, South Africa. Mineralium Deposita, 43, 825–848.

Roeder, P.L. and Campbell, I.A.N.H. 1985. The Effect of Postcumulus Reactions on Composition of Chrome-spinels from the Jimberlana Intrusion. 26, 763–786.

Roeder, P.L. and Reynolds, I. 1991. Crystallization of chromite and chromium solubility in basaltic melts. Journal of Petrology, 32, 909–934.

Rollinson, H. 2008. The geochemistry of mantle chromitites from the northern part of the Oman ophiolite : inferred parental melt compositions. Contrib Mineral Petrol, 156, 273–288.

Sack, R.O. and Ghiorso, M.S. 1991. Chromian spinels as petrogenetic indicators: thermodynamics and petrological applications. American Mineralogist, 76, 827–847.

Sato, M. 1978. Oxygen fugacity of basaltic magmas and the role of gas-forming elements. Geophysical Research Letters, 5, 447–449.

Sato, M. and Valenza, M. 1980. Oxygen fugacities of the Layered Series of the Skaergaard Intrusion, East Greenland. American Journal of Science, 280, 134–158.

Scoates, J.S. and Friedman, R.M. 2008. Precise age of the platiniferous Merensky Reef, Bushveld Complex, South Africa, by the U–Pb zircon chemical abrasion ID-TIMS technique. Economic Geology, 103, 465–471.

Scowen, P.A.H., Roeder, P.L. and Helz, R.T. 1991. Reequilibration of chromite within Kilauea Iki lava lake, Hawaii. Contributions to Mineralogy and Petrology, 107, 8–20.

Sharpe, R. 1981. The chronology of magma influxes to the eastern compartment of the Bushveld Complex as exemplified by marginal border groups. Journal of Geological Society, 138, 307–326.

Snethlage, R. and Gruenewaldt, G.V.O.N. 1977. Oxygen Fugacity and Its Bearing on the Origin Chromitite Layers in the Bushveld Complex. In: D.D. Klemm and H.H. Schneider (Editors) Time- and Strata Bound Ore Deposits. Berlin, Germany, Springer Verlag, 352–370.

Spandler, C., Martin, L.H.J. and Pettke, T. 2012. Lithos Carbonate assimilation during magma evolution at Nisyros (Greece), South Aegean Arc : Evidence from clinopyroxenite xenoliths. LITHOS, 146–147, 18–33.

Steenkamp, N.C. 2012. Alteration assemblage in the lower units of the Uitkomst Complex, Mpumalanga Province, South Africa. Doctoral Thesis. Universty of Pretoria, 1–303pp.

Stephenson, G. 2018. The Platreef magma event at the world-class Turfspruit Ni-Cu-PGE deposit: implications for mineralisation processes and the Bushveld Complex stratigraphy (Unpublished PhD thesis).

Tanner, D., McDonald, I., Harmer, R.E.J., Muir, D.D. and Hughes, H.S.R. 2019. A record of assimilation preserved by exotic minerals in the lowermost platinum-group element deposit of the Bushveld Complex: The Volspruit Sulphide Zone. Lithos, 324–325, 584–608.

Teigler, B. and Eales, H.V. 1996. The Lower and Critical Zone of the western Limb of the Bushveld Complex as intersected by the Nooitgedacht boreholes. Geological Survey of South African Bulletin, 11, 126.

Toplis, M.J. and Corgne, A. 2002. An experimental study of element partitioning between magnetite, clinopyroxene and iron-bearing silicate liquids with particular emphasis on vanadium. Contributions to Mineralogy and Petrology, 144, 22–37.

Ulmer, G.C. 1969. Experimental Investigations of Chromite Spinels. In: Magmatic ore deposits, a symposium. 114–131.

Van Der Merwe, M.J. 1976. The Layered sequence of the potgietersrus limb of the Bushveld complex. Economic Geology, 71, 1337–1351.

Veksler, I. V, Reid, D.L., Dulski, P., Keiding, J.K., Schannor, M., Hecht, L. and Trumbull, R.B. 2014. Electrochemical processes in a crystal mush: Cyclic units in the upper critical zone of the bushveld complex, South Africa. Journal of Petrology, 56, 1229–1250.

Von Gruenewaldt, G. 1971. A petrographical and mineralogical investigation of the rocks of the Bushveld Igneous Complex in the Tauteshoogte-Roossenekal area of the eastern Transvaal. Unpublished Ph.D. thesis, University of Pretoria, Pretoria, South Africa. 233 pp.

Wenzel, T., Baumgartner, L.P., Brugmann, G.E., Konnikov, E.G., Kislov, E. V. and Orsoev, D.A. 2001. Contamination of mafic magma by partial melting of dolomitic xenoliths. Terra Nova, 13, 197–202.

Wenzel, T., Baumgartner, L.P., Konnikov, E.G., Bru, G.E. and Kislov, E. V 2002. Partial Melting and Assimilation of Dolomitic Xenoliths by Mafic Magma : the Ioko-Dovyren Intrusion (North Baikal Region , Russia). Journal of Petrology, 43, 2049–2074.

Wilson, A.H. 2015. The Earliest Stages of Emplacement of the Eastern Bushveld Complex : Development of the Lower Zone , Marginal Zone and Basal Ultramafic Sequence. Journal of Petrology, 56, 347–388.

Wyllie, P.J. and Tuttle, F. 1960. The System CaO-CO_2 -H_2O and the Origin of Carbonatites. Journal of Petrology, 1, 1–46.

Xing, C.M., Wang, C.Y. and Zhang, M.J. 2012. Volatile and C-H-O isotopic compositions of giant Fe-Ti-V oxide deposits in the Panxi region and their implications for the sources of volatiles and the origin of Fe-Ti oxide ores. Science China Earth Sciences, 55, 1782–1795.

Yudovskaya, M.A. and Kinnaird, J.A. 2010. Chromite in the Platreef (Bushveld Complex, South Africa): Occurrence and evolution of its chemical composition. Mineralium Deposita, 45, 369–391.

Yudovskaya, M.A., Kinnaird, J.A., Grobler, D.F., Costin, G., Abramova, V.D., Dunnett, T. and Barnes, S.J. 2017. Zonation of Merensky-style platinum-group element mineralization in turfspruit thick reef facies (Northern limb of the Bushveld complex). Economic Geology, 112, 1333–1365.

Yudovskaya, M., Kinnaird, J., Naldrett, A.J., Mokhov, A. V., McDonald, I. and Reinke, C. 2011. Facies variation in PGE mineralization in the central Platreef of the Bushveld Complex, South Africa. The Canadian Mineralogist, 49, 1349–1384.

Yudovskaya, M.A., Kinnaird, J.A., Sobolev, A. V., Kuzmin, D. V., McDonald, I. and Wilson, A.H. 2013. Petrogenesis of the lower zone olivine-rich cumulates beneath the platreef and their correlation with recognized occurrences in the bushveld complex. In: Economic Geology.

Zhou, M.-F., Robinson, P.T, Lesher, C.M., Keays, R.R., Zhang, C.J. and Malpas, J. 2005. Geochemistry, petrogenesis and metallogenesis of the Panzhihua layered intrusions and associated Fe-Ti-V deposits, Sichuan Province, Sw China. Journal of Petrology, 46, 2253–2280.

Appendix A: Mineralogy

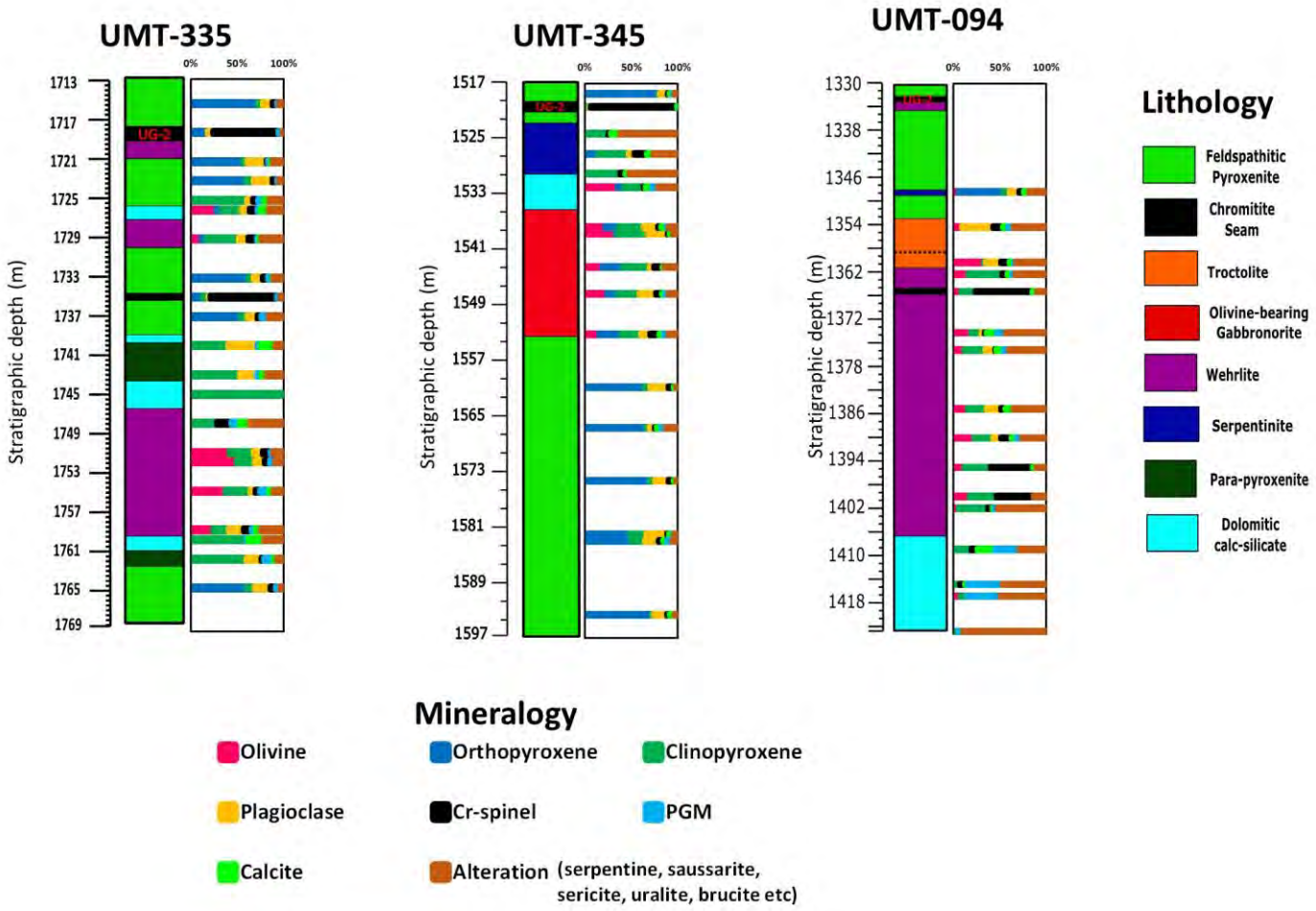

Mineral modal abundnace accros stratigraphic depth of each drill core from the Flatreef. Mineral assemblased are tabulated below

SAMPLES	*LITHOLOGY*	*DEPTH (M)*	*MAIN PHASES*	*PRIMARY ASSEMBLAGES*						*ACCESSORY ASSMBLAGE*					*ALTERATION ASSEMBLAGE*				
UMT-335				**Ol**	**OPX**	**Cpx**	**Pl**	**Spl**	**PGM**	**Phl**	**Cal**	**Mag**	**Ves**	**Prh**	**Brc/Per**	**Akermanite**	**Srp**	**Uralite**	**Sericite, Saussrite, talc, epidote**
SD-01	Feldsplathic pyroxenite	1715.5	Opx+cpx+pl	0	55	10	20	5	2	3	0	0	0		0	0	0	5	0
SD-02	UG-2 Chromitite	1718	spl+opx+pl	0	18	0	5	66	4	5	0	0	0		0	0	0	2	0
SD-03	Feldsplathic pyroxenite	1720.75	Opx+cpx+pl	0	55	5	20	1	3	2	2	0	0		0	0	0	5	7
SD-04	Feldsplathic pyroxenite	1723.75	Opx+cpx+pl	0	35	20	30	5	2	3	0	0	0		0	0	0	5	0
SD-05	Calc-silicate	1725	Cpx+prh+Ca	0	0	50	5	5	5	2	5	0	0	15	0	5	0	5	3
SD-06	Werhlite	1726.5	Ol+cpx+pl	25	5	20	8	8	3	4	8	5	0		0	0	5	5	5
SD-07	Werhlite	1729.5	Cpx+ol+pl±spl	10	5	32	10	8	3	3	2	5	0		2	0	8	10	2
SD-08	Feldsplathic pyroxenite	1733	Opx+cpx+pl	0	60	5	10	5	5	3	1	0	0		1	0	0	5	5
SD-09	Lower chromitite seam	1734.6	spl+opx+pl±cpx	0	13	5	2	70	3	3	0	0	0		0	0	0	0	4
SD-10	Feldsplathic pyroxenite	1737.2	Opx+cpx+pl	0	51	7	10	4	7	5	0	0	0		0	0	0	6	10
SD-11	Parapyroxenite	1740	Cpx+pl+cal	0	0	38	30	0	3	5	15	0	0		0	0	0	2	7
SD-12	Parapyroxenite	1743.1		0	0	50	17	0	5	5	5	0	0		0	0	0	10	8
SD-13	Calc-silicate	1745.5	Cpx+prh	2	0	60	0	0	0	0	0	0	8	30	0	0	0	0	0
SD-14	Werhlite	1747.9	Cpx+spl	0	0	25	0	14	8	5	10	5	0		5	0	20	8	0
SD-15	Werhlite	1751	Ol+cpx+pl±spl	40	0	25	10	8	3	3	0	0	0		0	0	10	0	1
SD-15	Werhlite	1752.6	Ol+cpx+pl±spl	45	0	18	10	5	5	5	0	3	0		0	0	5	0	4
SD-16	Werhlite	1755.9	Ol+cpx+	35	0	25	5	5	9	2	5	5	0		0	0	5	2	3
SD-17	Werhlite	1759.1		22	0	15	15	8	4	3	5	5	0		2	0	8	10	3
SD-18	Calc-silicate skarn	1760.2	Cpx+cal+ak	0	0	55	0	0	2	0	15	0	0	8	0	13	0	5	2
SD-19	Parapyroxenite	1762.2		0	0	55	15	2	10	8	3	0	0		0	0	0	5	2
SD-20	Feldsplathic pyroxenite	1765.4	Opx+cpx+pl	0	57	8	20	5	5	1	0	0	0		0	0	0	4	0

Ol, olivine; opx, orthopyroxene; cpx, clinopyroxene; pl, plagioclase

SAMPLES	*LITHOLOGY*	*DEPTH (M)*	*MAIN PHASES*	*PRIMARY ASSEMBLAGES*						*ACCESSORY ASSMBLAGE*					*ALTERATION ASSEMBLAGE*				
UMT-345				**Ol**	**OPX**	**Cpx**	**Pl**	**Spl**	**PGM**	**Phl**	**Cal**	**Mag**	**Ves**	**Prh**	**Brc /Per**	**Akermanite**	**Srp**	**Uralite**	**Sericite, Saussrite, talc, epidote**
SD-24	Feldspathic pyroxenite	1517.8	Opx+cpx+pl	-	35	10	20	2	8	5	-	-	-	-	-	-	-	10	10
SD-25	UG-2 chromitite	1521.1	Spl+opx+pl+cpx	-	2	2	2	90	1	-	3	-	-	-	-	-	-	-	-
SD-26	Serpentinite	1523.5	Serp+cpx+spl	-	-	20	-	2	8	-	-	15	5	-	-	-	45	5	-
SD-27	Serpentinite	1526.2	Serp+cpx+cal+spl	-	10	25	5	10	5	-	15	5	5	-	-	-	5	15	-
SD-28	Serpentinite	1529.9	Serp+	2	-	30	-	5	3	-	5	10	-	-	-	-	40	3	2
SD-29	Calc-silicate skarn	1531.9	Ol+cpx+cal	20	-	15	-	2	5	5	20	-	8	-	-	-	10	-	15
SD-30	Olivine gabbronorite	1537.5	Opx+ol+cpx±pl±spl	20	20	25	15	3	5	2	6	-	-	-	-	-	-	10	-
SD-31	Olivine gabbronorite	1538.9	Opx+ol+cpx±pl±spl	30	2	30	20	2	3	-	2	8	-	-	-	-	5	-	-
SD-32	Olivine gabbronorite	1543.6	Opx+ol+cpx±pl±spl	15	20	25	5	10	2	-	-	10	-	-	-	-	10	-	3
SD-33	Olivine gabbronorite	1547.2	Opx+ol+cpx±pl±spl	20	10	20	15	5	3	3	10	5	-	-	-	-	-	2	7
SD-34	Olivine gabbronorite	1553.3	Opx+ol+cpx±pl±spl	-	25	35	10	10	5	5	-	-	-	-	-	-	-	5	5
SD-35	Feldspathic pyroxenite	1561	Opx+cpx+pl	-	20	30	35	10	3	-	-	-	-	-	-	-	-	2	-
SD-36	Feldspathic pyroxenite	1567.4	Opx+cpx+pl	-	25	35	15	2	5	5	-	-	-	-	-	-	-	8	5
SD-37	Feldspathic pyroxenite	1575	Opx+cpx+pl	-	45	15	30	5	3	-	-	-	-	-	-	-	-	2	-
SD-38	Feldspathic pyroxenite	1583.2	Opx+cpx+pl	-	35	22	28	3	5	2	-	-	-	-	-	-	-	5	-
SD-39	Feldspathic pyroxenite	1584.6	Opx+cpx+pl	-	48	13	14	5	4	5	-	5	-	-	-	-	1	0	5

SAMPLES	*LITHOLOGY*	*DEPTH (M)*	*MAIN PHASES*	*PRIMARY ASSEMBLAGES*						*ACCESSORY ASSMBLAGE*							*ALTERATION ASSEMBLAGE*		
UMT-345				**Ol**	**OPX**	**Cpx**	**Pl**	**Spl**	**PGM**	**Phl**	**Cal**	**Mag**	**Ves**	**Prh**	**Brc /Per**	**Ak**	**Srp**	**Uralite**	**Sericite, Saussrite, talc, epidote**
SD-46	Feldspathic pyroxenite	1348.5	Opx+chr+Pl	15	25	15	12	5	5	2	-	3	-	-	-	-	10	5	3
SD-47	Troctolite	1354.1	Pl+ol+chr	8	-	-	30	10	5	5	5	5	-	-	-	-	22	5	5
SD-48	Clinopyroxene troctolite	1360.3	Ol+Pl	30	-	2	15	8	5	5	2	3	-	-	-	-	23	2	5
SD-49	Werhlite	1362.3	Ol+cpx	15	-	35	-	5	5	5	3	-	-	-	-	-	25	-	7
SD-50	Lower chromitite seam	1365.7	Spl+cpx+ol	6	2	15	-	60	5	2	-	-	-	-	-	-	5	5	-
SD-51	Werhlite	1372.3	Ol+cpx+	17	-	10	3	2	10	5	8	5	-	-	-	-	30	5	5
SD-52	Werhlite	1375.8	Ol+cpx+	10	-	20	10	1	7	6	5	5	-	-	-	-	20	10	6
SD-53	Werhlite	1385.9	Ol+cpx+pl	15	-	20	15	5	8	0	-	2	-	-	-	-	30	5	-
SD-54	Werhlite	1390.3	Ol+cpx+spl	20	-	18	8	10	5	5	5	5	-	-	-	-	10	5	9
SD-55	Werhlite	1395.2	Ol+cpx+spl	10	-	25	-	40	3	2	-	10	-	-	-	-	5	5	-
SD-56	Werhlite	1400.1	Ol+cpx+spl	15	-	25	-	35	-	8	-	5	-	-	-	-	10	2	-
SD-57	Werhlite	1402.9	Ol+cpx+	5	-	30	-	5	2	5	3	0	-	-	-	-	50	-	-
SD-58	Calc-silicate skarn	1409.9	Cal+ves+cpx+pgm	-	-	15	-	5	15	-	20	5	25	-	5	-	8	-	10
SD-59	Calc-silicate skarn	1415.4	Per+ves+cal+serp	-	-	5	-	5	2	-	30	5	15	-	25	-	13	-	-
SD-60	Calc-silicate skarn	1417.1	Per+srp	5	-	5	-	-	-	2	25	10	18	-	25	-	10	-	-
SD-61	marble	1423.2	Per+srp	-	-	5	-	-	-	-	5	-	-	-	60	-	30	-	-

Appendix B: Mineral Chemistry

Mineral	Cr-SPINEL																		
Drill core	UMT-335																		
Lithology	UG-2 Chromitite																		
Sample	SD-02-1	SD-02-2	SD-02-3	SD-02-4	SD-02-5	SD-02-6	SD-02-7	SD-02-8	SD-02-9	SD-02-10	SD-02-11	SD-02-12	SD-02-13	SD-02-14	SD-02-15	SD-02-16	SD-02-17	SD-02-18	SD-02-19
SiO_2	0.0	0.0	0.0	0.0	0.0	0.0	0.0	0.0	0.0	0.0	0.0	0.0	0.0	0.0	0.0	0.0	0.0	0.0	0.0
TiO_2	1.6	1.6	1.5	1.7	1.5	1.7	1.6	1.6	1.5	1.7	1.6	1.7	1.7	1.7	1.3	1.7	1.6	1.6	1.6
Al_2O_3	15.3	15.3	15.6	15.2	15.4	15.4	15.3	15.3	15.6	15.2	15.0	15.2	15.4	15.2	16.1	15.1	15.4	15.0	14.7
Cr_2O_3	39.9	40.5	40.9	41.0	40.8	41.0	39.9	40.5	40.9	41.0	40.7	40.7	40.6	40.6	40.0	40.3	40.6	40.8	40.7
Fe_2O_3	22.6	22.8	22.0	22.3	22.2	22.1	22.6	22.8	22.0	22.3	23.4	22.8	22.8	22.5	23.0	23.1	22.5	23.4	23.5
V_2O_3	0.2	0.1	0.2	0.2	0.2	0.1	0.2	0.1	0.2	0.2	0.2	0.2	0.2	0.2	0.2	0.2	0.2	0.2	0.2
FeO	12.6	12.7	12.3	12.4	12.4	12.3	12.6	12.7	12.3	12.4	13.1	12.8	12.7	12.6	12.9	12.9	12.6	13.1	13.1
MnO	0.4	0.4	0.4	0.3	0.4	0.4	0.4	0.4	0.4	0.3	0.4	0.3	0.3	0.4	0.3	0.4	0.3	0.3	0.4
MgO	6.9	7.3	8.0	7.8	7.8	7.6	6.9	7.3	8.0	7.8	6.4	7.3	7.3	7.3	6.8	6.9	7.2	6.5	6.4
NiO	0.2	0.1	0.1	0.1	0.1	0.2	0.2	0.1	0.1	0.1	0.1	0.1	0.1	0.2	0.1	0.1	0.1	0.1	0.1
Total	99.6	100.8	101.0	101.1	100.8	100.8	99.6	100.8	101.0	101.1	100.9	101.1	101.3	100.6	100.7	100.6	100.5	101.0	100.7
O=4																			
Si	0.0	0.0	0.0	0.0	0.0	0.0	0.0	0.0	0.0	0.0	0.0	0.0	0.0	0.0	0.0	0.0	0.0	0.0	0.0
Ti	0.0	0.0	0.0	0.0	0.0	0.0	0.0	0.0	0.0	0.0	0.0	0.0	0.0	0.0	0.0	0.0	0.0	0.0	0.0
Al	0.6	0.6	0.6	0.6	0.6	0.6	0.6	0.6	0.6	0.6	0.6	0.6	0.6	0.6	0.6	0.6	0.6	0.6	0.6
Cr	1.0	1.0	1.0	1.0	1.0	1.0	1.0	1.0	1.0	1.0	1.0	1.0	1.0	1.0	1.0	1.0	1.0	1.0	1.0
V	0.0	0.0	0.0	0.0	0.0	0.0	0.0	0.0	0.0	0.0	0.0	0.0	0.0	0.0	0.0	0.0	0.0	0.0	0.0
Mn	0.0	0.0	0.0	0.0	0.0	0.0	0.0	0.0	0.0	0.0	0.0	0.0	0.0	0.0	0.0	0.0	0.0	0.0	0.0
Mg	0.3	0.3	0.4	0.4	0.4	0.4	0.3	0.3	0.3	0.3	0.3	0.3	0.3	0.3	0.3	0.3	0.3	0.3	0.3
Ni	0.0	0.0	0.0	0.0	0.0	0.0	0.0	0.0	0.0	0.0	0.0	0.0	0.0	0.0	0.0	0.0	0.0	0.0	0.0
Fe^{3+}	0.2	0.3	0.2	0.2	0.2	0.2	0.3	0.3	0.3	0.2	0.2	0.2	0.2	0.2	0.2	0.2	0.2	0.2	0.2
Fe^{2+}	0.7	0.7	0.6	0.7	0.6	0.7	0.7	0.7	0.7	0.7	0.7	0.7	0.7	0.7	0.7	0.7	0.7	0.7	0.7
Total	2.9	2.9	2.9	2.9	2.9	2.9	2.9	2.9	2.9	2.9	2.9	2.9	2.9	2.9	2.9	2.9	2.9	2.9	2.9
Cr#	63.6	64.0	63.7	64.4	64.1	64.0	63.7	63.8	64.4	63.6	64.6	64.2	63.9	64.2	62.5	64.1	63.8	64.6	64.9
Mg#	32.6	33.9	37.1	36.2	36.3	35.5	27.6	31.2	33.1	33.8	29.9	33.8	33.8	34.0	31.9	32.1	33.7	30.5	29.9
$Fe^{3+}/\sum Fe$	0.2	0.2	0.2	0.2	0.2	0.2	0.3	0.2	0.2	0.2	0.2	0.2	0.2	0.2	0.2	0.2	0.2	0.2	0.2
fO_2 (NNO-Buffer)	0.7	0.8	0.7	0.7	0.8	0.8	0.7	0.6	0.8	0.8	0.7	0.7	0.7	0.7	0.7	0.7	0.7	0.8	0.7

Mineral	CR-SPINEL																
Drill core	UMT-335																
Lithology	Lower Chromitite seam																
Sample	SD-09	SD-09	SD-09	SD-09	SD-09	SD-09	SD-09	SD-09	SD-09	SD-09	SD-09	SD-09	SD-09	SD-09	SD-09	SD-09	SD-09
SiO_2	0.01	0.03	0.00	0.03	0.01	0.02	0.02	0.02	0.01	0.01	0.01	0.03	0.02	0.01	0.02	0.04	0.00
TiO_2	0.93	0.93	0.95	0.92	0.92	0.88	0.94	0.94	0.91	0.91	0.79	0.89	0.90	0.91	0.90	0.90	0.88
Al_2O_3	16.30	17.69	17.66	17.64	17.64	17.78	17.80	17.60	17.92	17.72	16.37	17.59	17.76	17.56	17.59	17.56	17.81
Cr_2O_3	41.10	42.44	42.76	43.27	42.68	42.80	42.79	43.07	42.92	42.70	40.93	43.20	43.02	42.37	42.56	42.46	43.08
Fe_2O_3	21.47	19.30	19.30	19.28	19.33	19.48	19.35	19.43	19.49	19.51	23.36	19.45	19.54	19.66	19.55	19.57	19.61
V_2O_3	0.36	0.32	0.33	0.33	0.33	0.33	0.33	0.33	0.32	0.33	0.38	0.32	0.33	0.32	0.34	0.32	0.31
FeO	11.99	10.77	10.77	10.76	10.79	10.88	10.80	10.85	10.88	10.89	13.04	10.86	10.91	10.97	10.92	10.93	10.95
MnO	0.27	0.23	0.24	0.24	0.22	0.22	0.27	0.27	0.24	0.23	0.33	0.25	0.22	0.26	0.24	0.20	0.25
MgO	9.63	9.70	9.76	9.62	9.64	9.59	9.69	9.67	9.49	9.45	6.37	9.62	9.47	9.29	9.47	9.43	9.54
NiO	0.00	0.00	0.00	0.00	0.00	0.00	0.00	0.00	0.00	0.00	0.00	0.00	0.00	0.00	0.00	0.00	0.00
Total	102.05	101.41	101.77	102.09	101.57	101.97	101.99	102.19	102.19	101.75	101.57	102.22	102.17	101.36	101.59	101.40	102.42
O=4																	
Si	0.00	0.00	0.00	0.00	0.00	0.00	0.00	0.00	0.00	0.00	0.00	0.00	0.00	0.00	0.00	0.00	0.00
Ti	0.02	0.02	0.02	0.02	0.02	0.02	0.02	0.02	0.02	0.02	0.02	0.02	0.02	0.02	0.02	0.02	0.02
Al	0.60	0.65	0.64	0.64	0.64	0.65	0.65	0.64	0.65	0.65	0.61	0.64	0.65	0.64	0.64	0.64	0.65
Cr	1.01	1.04	1.05	1.06	1.05	1.05	1.04	1.05	1.05	1.05	1.03	1.05	1.05	1.04	1.04	1.04	1.05
V	0.01	0.01	0.01	0.01	0.01	0.01	0.01	0.01	0.01	0.01	0.01	0.01	0.01	0.01	0.01	0.01	0.01
Mn	0.01	0.01	0.01	0.01	0.01	0.01	0.01	0.01	0.01	0.01	0.01	0.01	0.01	0.01	0.01	0.01	0.01
Mg	0.45	0.45	0.45	0.44	0.45	0.44	0.45	0.44	0.44	0.44	0.30	0.44	0.44	0.43	0.44	0.44	0.44
Ni	0.00	0.00	0.00	0.00	0.00	0.00	0.00	0.00	0.00	0.00	0.00	0.00	0.00	0.00	0.00	0.00	0.00
Fe^{3+}	0.28	0.20	0.19	0.19	0.19	0.19	0.19	0.19	0.19	0.19	0.24	0.19	0.19	0.20	0.20	0.20	0.19
Fe^{2+}	0.56	0.56	0.56	0.56	0.56	0.56	0.56	0.56	0.57	0.57	0.70	0.56	0.57	0.57	0.57	0.57	0.57
Total	2.92	2.90	2.90	2.90	2.90	2.90	2.90	2.90	2.90	2.90	2.88	2.90	2.90	2.90	2.90	2.90	2.90
Cr#	62.84	61.67	61.89	62.20	61.89	61.76	61.73	62.15	61.64	61.78	62.66	62.23	61.90	61.81	61.89	61.87	61.87
Mg#	44.43	44.58	44.69	44.02	44.30	43.92	44.34	44.24	43.35	43.38	30.00	44.04	43.27	42.90	43.58	43.44	43.58
$Fe^{3+}/\sum Fe$	0.24	0.15	0.15	0.14	0.15	0.15	0.15	0.15	0.14	0.15	0.22	0.15	0.14	0.15	0.15	0.15	0.15
fO_2 (NNO-Buffer)	0.35	0.32	0.36	0.38	0.30	0.29	0.28	0.30	0.29	0.29	0.29	0.29	0.31	0.28	0.32	0.29	0.28

Mineral	Cr-SPINEL																
Drill core	UMT-335																
Lithology	Footwall Assimilation Zone (Wehrlite)																
Sample	SD-06	SD-06	SD-06	SD-06	SD-06	SD-06	SD-06	SD-14	SD-14	SD-14	SD-14	SD-14	SD-14	SD-14	SD-14	SD-14	SD-14
SiO_2	0.06	0.03	0.02	0.04	0.05	0.00	0.02	0.00	0.05	0.02	0.01	0.02	0.01	0.06	0.03	0.06	0.02
TiO_2	2.48	1.64	2.58	2.31	1.63	1.62	1.91	1.06	0.95	1.03	1.09	1.07	1.06	1.07	1.17	1.17	1.35
Al_2O_3	11.82	10.68	11.71	11.48	11.17	11.51	14.92	26.35	28.36	28.29	27.37	27.45	27.36	27.63	24.35	24.47	20.54
Cr_2O_3	33.84	33.43	33.74	34.05	32.04	31.73	30.86	22.25	20.43	20.58	21.05	21.16	21.39	21.40	23.26	23.53	26.46
Fe_2O_3	31.95	33.53	31.91	32.28	34.13	34.03	31.86	27.79	27.80	27.70	26.80	26.67	26.88	27.03	27.36	27.57	29.08
V_2O_3	0.32	0.28	0.32	0.31	0.26	0.24	0.36	0.15	0.15	0.15	0.13	0.12	0.14	0.18	0.17	0.16	0.17
FeO	17.84	18.72	17.81	18.02	19.05	19.00	17.79	15.52	15.52	15.47	14.96	14.89	15.01	15.09	15.28	15.39	16.24
MnO	0.39	0.47	0.46	0.44	0.47	0.40	0.42	0.54	0.55	0.54	0.56	0.49	0.49	0.42	0.48	0.51	0.54
MgO	2.91	2.33	2.80	2.73	2.56	2.48	3.21	6.69	7.04	7.03	8.19	8.08	8.16	8.13	7.72	7.98	6.64
NiO	0.17	0.20	0.16	0.12	0.13	0.11	0.19	0.06	0.04	0.13	0.13	0.08	0.08	0.15	0.16	0.11	0.06
Total	101.78	101.29	101.49	101.77	101.48	101.12	101.53	100.40	100.89	100.94	100.27	100.03	100.57	101.16	99.98	100.94	101.11
O=4																	
Si	0.00	0.00	0.00	0.00	0.00	0.00	0.00	0.00	0.00	0.00	0.00	0.00	0.00	0.00	0.00	0.00	0.00
Ti	0.06	0.04	0.06	0.06	0.04	0.04	0.05	0.02	0.02	0.02	0.03	0.02	0.02	0.02	0.03	0.03	0.03
Al	0.46	0.42	0.46	0.45	0.44	0.46	0.57	0.96	1.02	1.02	0.99	0.99	0.98	0.99	0.89	0.89	0.76
Cr	0.88	0.89	0.89	0.89	0.85	0.84	0.80	0.54	0.49	0.50	0.51	0.51	0.52	0.51	0.57	0.57	0.66
V	0.01	0.01	0.01	0.01	0.01	0.01	0.01	0.00	0.00	0.00	0.00	0.00	0.00	0.00	0.00	0.00	0.00
Mn	0.01	0.01	0.01	0.01	0.01	0.01	0.01	0.01	0.01	0.01	0.01	0.01	0.01	0.01	0.01	0.01	0.01
Mg	0.14	0.12	0.14	0.13	0.13	0.12	0.16	0.31	0.32	0.32	0.37	0.37	0.37	0.37	0.36	0.37	0.31
Ni	0.00	0.01	0.00	0.00	0.00	0.00	0.00	0.00	0.00	0.00	0.00	0.00	0.00	0.00	0.00	0.00	0.00
Fe^{3+}	0.56	0.56	0.39	0.39	0.38	0.40	0.39	0.39	0.39	0.38	0.40	0.39	0.40	0.39	0.42	0.43	0.46
Fe^{2+}	0.92	0.89	0.90	0.90	0.89	0.89	0.89	0.69	0.68	0.68	0.63	0.63	0.63	0.64	0.65	0.64	0.70
Total	2.86	2.87	2.86	2.86	2.88	2.88	2.87	2.90	2.90	2.90	2.92	2.91	2.91	2.91	2.91	2.92	2.91
Cr#	65.77	67.73	65.92	66.55	65.82	64.90	58.12	36.16	32.58	32.79	34.03	34.08	34.41	34.18	39.05	39.22	46.36
Mg#	13.43	11.58	13.36	13.09	12.61	12.22	14.94	30.69	31.96	31.84	37.27	36.79	37.00	36.57	35.61	36.47	30.89
$Fe^{3+}/\sum Fe$	0.84	0.80	0.50	0.50	0.48	0.52	0.50	0.42	0.41	0.41	0.41	0.40	0.41	0.41	0.45	0.46	0.53
fO_2 (NNO-Buffer)	0.59	0.28	0.35	0.45	0.37	0.38	0.49	0.77	0.77	0.79	0.87	0.88	0.82	0.70	0.72	0.74	0.72

Mineral	Cr-SPINEL														
Drill core	UMT-335														
Lithology	Footwall Assimilation Zone (Wehrlite)														
Sample	SD-14	SD-14	SD-14	SD-14	SD-14	SD-14	SD-14	SD-14	SD-14	SD-14	SD-14	SD-14	SD-14	SD-14	SD-14
SiO_2	0.07	0.03	0.00	0.04	0.00	0.04	0.04	0.02	0.01	0.04	0.05	0.01	0.03	0.00	0.04
TiO_2	1.36	1.33	1.34	0.99	0.94	1.14	0.81	0.80	0.77	0.76	1.26	1.28	0.64	0.72	0.79
Al_2O_3	20.42	20.75	20.86	27.76	27.82	26.35	31.21	31.27	29.86	30.04	22.52	22.64	31.48	31.58	29.50
Cr_2O_3	26.54	25.96	26.25	20.86	20.96	21.93	19.19	19.09	19.44	19.37	25.38	25.38	18.42	18.53	20.27
Fe_2O_3	29.31	28.91	29.19	27.76	28.00	28.01	26.87	26.82	27.36	27.35	27.95	28.23	26.03	25.89	27.56
V_2O_3	0.16	0.15	0.16	0.11	0.13	0.15	0.16	0.17	0.17	0.14	0.18	0.15	0.17	0.16	0.15
FeO	16.36	16.14	16.30	15.50	15.64	15.64	15.00	14.97	15.27	15.27	15.61	15.76	14.53	14.45	15.39
MnO	0.54	0.57	0.53	0.50	0.51	0.52	0.59	0.54	0.55	0.66	0.57	0.47	0.61	0.55	0.70
MgO	6.63	6.75	6.80	7.40	7.37	7.08	7.37	7.84	6.89	6.75	6.67	6.60	7.66	7.69	6.80
NiO	0.10	0.10	0.13	0.13	0.10	0.05	0.13	0.14	0.07	0.02	0.10	0.10	0.07	0.11	0.12
Total	101.50	100.69	101.57	101.03	101.46	100.90	101.37	101.65	100.38	100.40	100.28	100.61	99.64	99.69	101.31
O=4															
Si	0.00	0.00	0.00	0.00	0.00	0.00	0.00	0.00	0.00	0.00	0.00	0.00	0.00	0.00	0.00
Ti	0.03	0.03	0.03	0.02	0.02	0.03	0.02	0.02	0.02	0.02	0.03	0.03	0.01	0.02	0.02
Al	0.76	0.77	0.77	1.00	1.00	0.95	1.10	1.10	1.07	1.08	0.83	0.84	1.12	1.12	1.05
Cr	0.66	0.65	0.65	0.50	0.50	0.53	0.45	0.45	0.47	0.47	0.63	0.63	0.44	0.44	0.48
V	0.00	0.00	0.00	0.00	0.00	0.00	0.00	0.00	0.00	0.00	0.00	0.00	0.00	0.00	0.00
Mn	0.01	0.02	0.01	0.01	0.01	0.01	0.01	0.01	0.01	0.02	0.02	0.01	0.02	0.01	0.02
Mg	0.31	0.32	0.32	0.34	0.33	0.32	0.33	0.35	0.31	0.31	0.31	0.31	0.35	0.35	0.31
Ni	0.00	0.00	0.00	0.00	0.00	0.00	0.00	0.00	0.00	0.00	0.00	0.00	0.00	0.00	0.00
Fe^{3+}	0.46	0.46	0.46	0.40	0.40	0.40	0.35	0.36	0.37	0.36	0.42	0.41	0.35	0.34	0.37
Fe^{2+}	0.70	0.69	0.69	0.66	0.67	0.68	0.67	0.65	0.68	0.69	0.69	0.70	0.64	0.65	0.69
Total	2.91	2.91	2.91	2.91	2.91	2.90	2.90	2.91	2.90	2.90	2.90	2.90	2.91	2.90	2.90
Cr#	46.58	45.64	45.78	33.51	33.58	35.83	29.20	29.04	30.39	30.20	43.06	42.91	28.18	28.24	31.55
Mg#	30.75	31.55	31.46	33.59	33.33	32.25	33.03	34.92	31.37	30.79	31.09	30.51	34.91	34.84	30.87
$Fe^{3+}/\sum Fe$	0.54	0.53	0.53	0.43	0.43	0.44	0.35	0.36	0.39	0.38	0.46	0.46	0.35	0.33	0.39
fO_2 (NNO-Buffer)	0.73	0.76	0.73	0.95	0.84	0.78	0.75	0.71	0.94	0.73	0.80	0.69	0.80	0.72	0.76

Mineral	CR-SPINEL													
Drill core	UMT-335													
Lithology	Footwall Assimilation Zone (Wehrlite)													
Sample	SD-14	SD-14	SD-14	SD-14	SD-14	SD-14	SD-14	SD-15B	SD-15B	SD-15B	SD-15B	SD-15B	SD-15B	SD-15B
SiO_2	0.00	1.02	1.36	0.01	0.01	0.00	0.02	0.00	0.03	0.00	0.01	0.01	0.03	0.03
TiO_2	0.85	0.58	0.62	0.84	0.85	0.50	0.54	1.03	1.07	1.08	1.17	1.11	1.11	0.72
Al_2O_3	29.54	32.26	32.19	30.35	30.78	31.40	31.48	27.94	27.67	27.46	27.53	27.49	27.35	2.69
Cr_2O_3	20.36	18.86	18.95	18.94	18.79	19.50	19.28	23.92	23.33	23.76	22.98	22.51	23.88	9.03
Fe_2O_3	27.67	26.78	26.24	27.46	27.91	28.12	28.20	26.39	26.25	26.52	26.68	27.35	26.82	54.17
V_2O_3	0.14	0.13	0.17	0.17	0.16	0.11	0.11	0.32	0.32	0.32	0.29	0.30	0.31	0.12
FeO	15.45	14.95	14.65	15.33	15.58	15.70	15.75	14.73	14.66	14.81	14.90	15.27	14.97	30.24
MnO	0.64	0.48	0.55	0.65	0.60	0.62	0.72	0.38	0.40	0.38	0.40	0.42	0.42	0.95
MgO	6.98	7.81	8.15	6.46	6.43	5.53	5.58	7.23	7.46	7.32	6.68	6.21	6.66	2.85
NiO	0.09	0.08	0.08	0.07	0.03	0.06	0.08	0.00	0.00	0.00	0.00	0.00	0.00	0.00
Total	101.71	102.97	102.94	100.28	101.14	101.54	101.75	101.93	101.19	101.65	100.65	100.66	101.57	100.79
O=4														
Si	0.00	0.03	0.04	0.00	0.00	0.00	0.00	0.00	0.00	0.00	0.00	0.00	0.00	0.00
Ti	0.02	0.01	0.01	0.02	0.02	0.01	0.01	0.02	0.02	0.02	0.03	0.03	0.03	0.02
Al	1.05	1.11	1.10	1.09	1.09	1.11	1.11	0.99	0.99	0.98	0.99	0.99	0.98	0.12
Cr	0.48	0.43	0.44	0.45	0.45	0.46	0.46	0.57	0.56	0.57	0.56	0.55	0.57	0.26
V	0.00	0.00	0.00	0.00	0.00	0.00	0.00	0.01	0.01	0.01	0.01	0.01	0.01	0.00
Mn	0.02	0.01	0.01	0.02	0.02	0.02	0.02	0.01	0.01	0.01	0.01	0.01	0.01	0.03
Mg	0.31	0.34	0.35	0.29	0.29	0.25	0.25	0.32	0.34	0.33	0.30	0.28	0.30	0.16
Ni	0.00	0.00	0.00	0.00	0.00	0.00	0.00	0.00	0.00	0.00	0.00	0.00	0.00	0.00
Fe^{3+}	0.37	0.35	0.35	0.35	0.36	0.33	0.34	0.32	0.34	0.34	0.34	0.32	0.32	0.32
Fe^{2+}	0.68	0.65	0.63	0.70	0.71	0.74	0.74	0.68	0.67	0.68	0.71	0.72	0.71	0.71
Total	2.90	2.89	2.89	2.89	2.89	2.88	2.88	2.89	2.90	2.90	2.89	2.89	2.89	3.03
Cr#	31.61	28.17	28.31	29.50	29.04	29.40	29.12	36.48	36.12	36.72	35.90	35.46	36.94	69.30
Mg#	31.47	34.39	35.86	29.41	29.00	25.04	25.28	32.23	33.41	32.68	30.07	28.15	29.89	18.09
$Fe^{3+}/\sum Fe$	0.39	0.35	0.34	0.37	0.38	0.36	0.36	0.32	0.34	0.34	0.36	0.34	0.33	0.33
fO_2 (NNO-Buffer)	0.77	0.82	0.83	0.73	0.70	0.76	0.94	0.36	0.36	0.36	0.41	0.40	0.37	0.81

Mineral	CR-SPINEL																		
Drill core	UMT-335																		
Lithology	Footwall Assimilation Zone (Wehrlite)																		
Sample	SD-17	SD-17	SD-17	SD-17	SD-17	SD-17	SD-17	SD-17	SD-17	SD-17	SD-17	SD-17	SD-17	SD-17	SD-17	SD-17	SD-17	SD-17	SD-17
SiO_2	0.02	0.04	0.04	0.10	0.01	0.03	0.06	0.02	0.05	0.05	0.02	0.04	0.03	0.02	0.02	0.04	0.04	0.04	0.08
TiO_2	2.20	2.29	1.83	1.66	3.02	3.02	2.85	3.01	1.61	1.63	0.64	0.40	3.47	1.44	1.94	3.99	1.53	4.27	4.49
Al_2O_3	11.78	11.64	12.15	12.06	12.37	12.34	10.40	10.36	9.23	10.26	13.18	12.59	6.73	11.13	12.81	1.35	10.97	7.10	6.66
Cr_2O_3	34.93	35.14	35.11	35.54	37.38	37.53	32.76	33.05	38.84	38.82	36.23	36.33	24.22	36.03	27.17	28.59	34.29	27.79	26.69
Fe_2O_3	31.06	31.44	30.94	31.25	27.68	27.62	33.07	33.29	30.27	30.07	30.50	30.80	41.53	31.61	36.39	42.42	32.97	38.22	38.81
V_2O_3	0.40	0.41	0.39	0.37	0.29	0.29	0.37	0.36	0.54	0.55	0.40	0.32	0.44	0.29	0.30	0.36	0.23	0.29	0.35
FeO	17.34	17.55	17.27	17.45	15.45	15.42	18.47	18.59	16.90	16.79	17.03	17.20	23.19	17.65	20.31	23.68	18.41	21.34	21.67
MnO	0.65	0.66	0.60	0.65	0.50	0.47	0.69	0.65	0.56	0.58	0.66	0.57	0.85	0.73	0.63	0.54	0.62	0.67	0.65
MgO	2.30	2.33	2.13	2.09	4.26	4.46	2.05	2.06	2.00	2.18	2.03	2.56	1.23	2.63	2.11	0.93	2.45	2.05	1.72
NiO	0.05	0.07	0.05	0.02	0.06	0.03	0.10	0.08	0.04	0.04	0.09	0.04	0.01	0.04	0.01	0.07	0.07	0.02	0.08
Total	100.72	101.56	100.50	101.17	101.01	101.19	100.82	101.47	100.06	100.95	100.78	100.85	101.68	101.57	101.70	101.97	101.56	101.78	101.19
O=4																			
Si	0.00	0.00	0.00	0.00	0.00	0.00	0.00	0.00	0.00	0.00	0.00	0.00	0.00	0.00	0.00	0.00	0.00	0.00	0.00
Ti	0.06	0.06	0.05	0.04	0.07	0.07	0.07	0.08	0.04	0.04	0.02	0.01	0.09	0.04	0.05	0.11	0.04	0.11	0.12
Al	0.46	0.46	0.48	0.47	0.48	0.48	0.41	0.41	0.37	0.41	0.52	0.49	0.28	0.44	0.50	0.06	0.43	0.29	0.27
Cr	0.92	0.92	0.93	0.94	0.97	0.97	0.87	0.88	1.05	1.03	0.95	0.96	0.66	0.95	0.72	0.80	0.91	0.75	0.73
V	0.01	0.01	0.01	0.01	0.01	0.01	0.01	0.01	0.01	0.01	0.01	0.01	0.01	0.01	0.01	0.01	0.01	0.01	0.01
Mn	0.02	0.02	0.02	0.02	0.01	0.01	0.02	0.02	0.02	0.02	0.02	0.02	0.03	0.02	0.02	0.02	0.02	0.02	0.02
Mg	0.11	0.12	0.11	0.10	0.21	0.22	0.10	0.10	0.10	0.11	0.10	0.13	0.06	0.13	0.10	0.05	0.12	0.10	0.09
Ni	0.00	0.00	0.00	0.00	0.00	0.00	0.00	0.00	0.00	0.00	0.00	0.00	0.00	0.00	0.00	0.00	0.00	0.00	0.00
Fe^{3+}	0.41	0.41	0.40	0.41	0.31	0.31	0.48	0.47	0.40	0.38	0.40	0.44	0.81	0.46	0.61	0.86	0.51	0.67	0.40
Fe^{2+}	0.92	0.93	0.92	0.92	0.85	0.84	0.95	0.96	0.93	0.92	0.90	0.87	1.01	0.88	0.93	1.05	0.90	0.99	1.02
Total	2.85	2.85	2.85	2.85	2.86	2.86	2.86	2.86	2.85	2.85	2.86	2.87	2.89	2.87	2.88	2.89	2.87	2.87	2.87
Cr#	66.55	66.95	65.98	66.41	66.97	67.12	67.89	68.16	73.85	71.74	64.84	65.95	70.72	68.47	58.73	93.45	67.72	72.42	72.91
Mg#	11.00	11.08	10.28	10.08	19.67	20.52	9.77	9.69	9.89	10.57	10.09	12.82	5.91	12.87	10.16	4.49	11.96	9.53	8.00
$Fe^{3+}/\sum Fe$	0.54	0.55	0.54	0.55	0.36	0.36	0.68	0.67	0.52	0.49	0.52	0.58	1.49	0.62	0.95	1.65	0.71	1.12	0.57
fO_2 (NNO-Buffer)	0.53	0.20	0.24	0.27	0.42	0.42	0.26	0.28	-0.02	-0.04	0.21	0.35	0.14	0.42	0.39	0.29	0.56	0.43	0.31

Mineral	Cr-SPINEL												
Drill core	UMT-345												
Lithology	UG-2 Chromitite												
Sample	SD-25	SD-25	SD-25	SD-25	SD-25	SD-25	SD-25	SD-25	SD-25	SD-25	SD-25	SD-25	SD-25
SiO_2	0.04	0.02	0.01	0.02	0.03	0.01	0.02	0.01	0.02	0.03	0.03	0.01	0.01
TiO_2	0.94	0.89	0.96	0.87	0.93	0.93	0.92	0.91	0.87	0.93	0.93	0.92	0.92
Al_2O_3	16.03	16.70	16.02	16.89	16.46	16.23	16.46	16.12	16.26	15.98	15.94	15.96	15.95
Cr_2O_3	40.80	40.96	40.26	40.97	40.57	41.13	40.67	40.95	41.24	40.79	41.28	41.33	41.56
Fe_2O_3	22.09	21.56	22.76	21.19	21.88	21.90	22.06	21.78	21.66	21.68	21.58	21.55	21.72
V_2O_3	0.35	0.36	0.36	0.35	0.36	0.36	0.35	0.36	0.34	0.36	0.34	0.36	0.36
FeO	12.34	12.03	12.70	11.83	12.22	12.23	12.31	12.16	12.10	12.11	12.05	12.03	12.12
MnO	0.31	0.27	0.31	0.28	0.26	0.29	0.28	0.28	0.26	0.26	0.26	0.29	0.25
MgO	9.15	9.38	8.37	9.23	9.30	9.15	9.19	9.17	9.37	9.42	9.52	9.34	9.44
NiO	0.00	0.00	0.00	0.00	0.00	0.00	0.00	0.00	0.00	0.00	0.00	0.00	0.00
Total	102.05	102.17	101.74	101.62	102.02	102.23	102.27	101.73	102.13	101.56	101.92	101.79	102.35
O=4													
Si	0.00	0.00	0.00	0.00	0.00	0.00	0.00	0.00	0.00	0.00	0.00	0.00	0.00
Ti	0.02	0.02	0.02	0.02	0.02	0.02	0.02	0.02	0.02	0.02	0.02	0.02	0.02
Al	0.59	0.61	0.59	0.62	0.61	0.60	0.60	0.60	0.60	0.59	0.59	0.59	0.59
Cr	1.01	1.01	1.00	1.01	1.00	1.02	1.00	1.02	1.02	1.01	1.02	1.02	1.03
V	0.01	0.01	0.01	0.01	0.01	0.01	0.01	0.01	0.01	0.01	0.01	0.01	0.01
Mn	0.01	0.01	0.01	0.01	0.01	0.01	0.01	0.01	0.01	0.01	0.01	0.01	0.01
Mg	0.43	0.44	0.39	0.43	0.43	0.43	0.43	0.43	0.44	0.44	0.44	0.44	0.44
Ni	0.00	0.00	0.00	0.00	0.00	0.00	0.00	0.00	0.00	0.00	0.00	0.00	0.00
Fe^{3+}	0.29	0.27	0.29	0.26	0.28	0.28	0.28	0.28	0.28	0.29	0.28	0.28	0.28
Fe^{2+}	0.58	0.57	0.61	0.58	0.58	0.58	0.58	0.58	0.57	0.57	0.56	0.57	0.57
Total	2.91	2.91	2.90	2.91	2.91	2.91	2.91	2.91	2.91	2.91	2.91	2.91	2.91
Cr#	63.07	62.21	62.76	61.94	62.33	62.96	62.37	63.02	62.98	63.12	63.47	63.47	63.62
Mg#	42.43	43.23	38.99	42.76	42.93	42.30	42.40	42.57	43.30	43.75	44.08	43.33	43.54
$Fe^{3+}/\sum Fe$	0.25	0.23	0.26	0.21	0.24	0.24	0.25	0.24	0.24	0.25	0.24	0.24	0.24
fO_2 (NNO-Buffer)	0.28	0.37	0.34	0.34	0.33	0.34	0.34	0.33	0.36	0.34	0.24	0.36	0.34

Mineral	Cr-SPINEL															
Drill core	UMT-345															
Lithology	Olivine Gabbronorite															
Sample	SD-30	SD-30	SD-30	SD-30	SD-30	SD-30	SD-30	SD-30	SD-30	SD-30	SD-32	SD-32	SD-32	SD-32	SD-32	SD-32
SiO_2	0.02	0.04	0.02	0.03	0.03	0.02	0.03	0.00	0.04	0.02	0.00	0.02	0.01	0.04	0.03	2.93
TiO_2	1.56	1.55	1.97	2.06	1.43	1.47	1.42	1.73	1.36	1.61	2.23	1.33	1.45	1.14	1.59	2.00
Al_2O_3	10.06	10.03	7.97	7.39	4.57	4.21	4.70	14.18	4.97	4.94	12.13	11.01	11.06	15.59	11.77	10.90
Cr_2O_3	31.85	31.63	28.54	27.91	28.55	27.30	29.20	34.06	29.41	30.12	26.68	27.15	29.35	31.06	24.06	23.52
Fe_2O_3	33.41	33.31	37.76	37.88	40.95	42.22	40.77	29.51	40.28	39.41	34.82	36.85	35.73	29.89	38.22	34.26
V_2O_3	0.37	0.38	0.48	0.44	0.66	0.67	0.63	0.36	0.63	0.68	0.39	0.32	0.33	0.30	0.35	0.42
FeO	18.65	18.60	21.08	21.15	22.86	23.57	22.76	16.47	22.49	22.00	19.44	20.57	19.95	16.69	21.34	19.13
MnO	0.30	0.30	0.32	0.33	0.45	0.42	0.39	0.34	0.44	0.42	0.33	0.36	0.40	0.28	0.41	1.23
MgO	4.91	4.97	2.81	3.22	0.85	1.14	0.82	4.99	0.75	1.80	5.14	3.60	3.41	6.41	3.87	4.99
NiO	0.00	0.00	0.00	0.00	0.00	0.00	0.00	0.00	0.00	0.00	0.00	0.00	0.00	0.00	0.00	0.00
Total	101.13	100.81	100.95	100.41	100.35	101.02	100.73	101.64	100.37	101.00	101.16	101.21	101.69	101.39	101.64	99.37
O=4																
Si	0.00	0.00	0.00	0.00	0.00	0.00	0.00	0.00	0.00	0.00	0.00	0.00	0.00	0.00	0.00	0.10
Ti	0.04	0.04	0.05	0.05	0.04	0.04	0.04	0.04	0.04	0.04	0.06	0.03	0.04	0.03	0.04	0.05
Al	0.40	0.40	0.32	0.30	0.19	0.18	0.20	0.54	0.21	0.20	0.47	0.44	0.44	0.59	0.47	0.43
Cr	0.84	0.84	0.78	0.77	0.81	0.77	0.82	0.87	0.83	0.84	0.70	0.72	0.78	0.79	0.64	0.62
V	0.01	0.01	0.01	0.01	0.02	0.02	0.02	0.01	0.02	0.02	0.01	0.01	0.01	0.01	0.01	0.01
Mn	0.01	0.01	0.01	0.01	0.01	0.01	0.01	0.01	0.01	0.01	0.01	0.01	0.01	0.01	0.01	0.03
Mg	0.25	0.25	0.14	0.17	0.05	0.06	0.04	0.24	0.04	0.09	0.25	0.18	0.17	0.31	0.19	0.25
Ni	0.00	0.00	0.00	0.00	0.00	0.00	0.00	0.00	0.00	0.00	0.00	0.00	0.00	0.00	0.00	0.00
Fe^{3+}	0.43	0.62	0.55	0.74	0.74	0.86	0.91	0.91	0.82	0.80	0.39	1.13	0.16	0.50	0.87	0.67
Fe^{2+}	0.79	0.78	0.90	0.88	0.99	0.98	0.99	0.79	0.99	0.94	0.80	0.84	0.86	0.71	0.84	0.77
Total	2.91	2.91	2.90	2.91	2.90	2.91	2.90	2.89	2.90	2.90	2.92	2.91	2.90	2.91	2.92	2.89
Cr#	68.00	67.91	70.61	71.70	80.75	81.31	80.66	61.71	79.88	80.37	59.60	62.32	64.04	57.21	57.82	59.15
Mg#	23.72	24.17	13.79	15.85	4.36	5.81	4.19	23.48	3.85	9.08	24.06	17.70	16.45	30.38	18.77	24.38
$Fe^{3+}/\sum Fe$	0.52	0.88	0.80	1.20	1.27	1.57	1.73	1.56	1.48	1.40	0.47	2.23	0.17	0.60	1.48	0.97
fO_2 (NNO-Buffer)	0.26	0.25	0.07	0.14	-0.23	-0.25	-0.18	0.28	-0.18	-0.26	0.22	0.37	0.34	0.39	0.31	0.17

Mineral	CR-SPINEL															
Drill core	UMT-345							UMT-094								
Lithology	Olivine Gabbronorite							Footwall Assimilation Zone (Pegmatoidal troctolite)								
Sample	SD-32	SD-32	SD-32	SD-32	SD-32	SD-32	SD-32	SD-48	SD-48	SD-48	SD-48	SD-48	SD-48	SD-48	SD-48
SiO_2	0.02	0.03	0.04	0.03	0.03	0.02	0.03	0.01	0.01	0.01	0.01	0.03	0.01	0.02	0.03
TiO_2	1.79	1.67	0.47	1.24	0.13	1.52	1.32	2.68	2.51	2.68	2.60	2.40	2.38	2.52	2.68
Al_2O_3	11.03	10.38	18.75	6.63	25.55	15.42	10.31	13.12	12.59	13.12	12.40	12.67	12.18	12.57	12.21
Cr_2O_3	28.03	28.55	30.14	18.42	29.79	31.08	23.05	32.72	29.95	31.50	29.60	31.91	32.72	31.87	32.01
Fe_2O_3	35.98	36.23	30.45	46.29	25.78	29.48	41.16	31.02	32.92	31.02	32.92	32.05	31.67	31.84	31.82
V_2O_3	0.35	0.33	0.37	0.43	0.24	0.35	0.40	0.42	0.41	0.41	0.38	0.38	0.39	0.41	0.37
FeO	20.09	20.23	17.00	25.84	14.39	16.46	22.98	17.32	18.38	17.32	18.38	17.89	17.68	17.78	17.76
MnO	0.35	0.36	0.45	0.38	0.24	0.30	0.33	0.39	0.48	0.39	0.48	0.36	0.38	0.43	0.34
MgO	3.51	3.42	2.87	1.71	5.46	6.74	1.56	3.95	3.47	3.95	3.47	3.58	3.73	3.64	3.70
NiO	0.00	0.00	0.00	0.00	0.00	0.00	0.00	0.00	0.00	0.00	0.00	0.00	0.00	0.00	0.00
Total	101.16	101.20	100.53	100.96	101.61	101.37	101.14	101.62	100.72	100.39	100.24	101.27	101.14	101.08	100.92
O=4															
Si	0.00	0.00	0.00	0.00	0.00	0.00	0.00	0.00	0.00	0.00	0.00	0.00	0.00	0.00	0.00
Ti	0.05	0.04	0.01	0.03	0.00	0.04	0.03	0.07	0.06	0.07	0.06	0.06	0.06	0.06	0.07
Al	0.44	0.41	0.72	0.28	0.92	0.59	0.42	0.51	0.49	0.51	0.49	0.49	0.48	0.49	0.48
Cr	0.75	0.76	0.77	0.52	0.72	0.79	0.63	0.85	0.79	0.85	0.79	0.83	0.86	0.83	0.84
V	0.01	0.01	0.01	0.01	0.01	0.01	0.01	0.01	0.01	0.01	0.01	0.01	0.01	0.01	0.01
Mn	0.01	0.01	0.01	0.01	0.01	0.01	0.01	0.01	0.01	0.01	0.01	0.01	0.01	0.01	0.01
Mg	0.18	0.17	0.14	0.09	0.25	0.32	0.08	0.19	0.17	0.19	0.17	0.18	0.18	0.18	0.18
Ni	0.00	0.00	0.00	0.00	0.00	0.00	0.00	0.00	0.00	0.00	0.00	0.00	0.00	0.00	0.00
Fe^{3+}	0.70	0.64	0.44	0.73	0.83	0.75	0.65	0.43	0.51	0.64	0.56	0.47	0.47	0.47	0.47
Fe^{2+}	0.86	0.86	0.85	0.94	0.70	0.70	0.95	0.86	0.88	0.86	0.86	0.87	0.86	0.87	0.88
Total	2.90	2.90	2.87	2.94	2.87	2.91	2.91	2.87	2.88	2.87	2.88	2.87	2.87	2.87	2.87
Cr#	63.03	64.86	51.89	65.09	43.89	57.49	60.02	62.59	61.48	62.59	61.48	62.83	64.33	62.98	63.75
Mg#	16.96	16.65	13.94	8.77	26.21	31.51	7.77	18.23	16.38	18.30	16.72	16.76	17.54	17.06	17.28
$Fe^{3+}/\sum Fe$	1.08	0.97	0.56	1.22	1.27	1.08	1.04	0.56	0.72	0.96	0.79	0.64	0.62	0.63	0.63
fO_2 (NNO-Buffer)	0.29	0.34	0.27	0.16	0.54	0.30	0.21	0.18	0.19	0.25	0.23	0.19	0.23	0.26	0.19

Mineral	CR-SPINEL																	
Drill core	UMT-094																	
Lithology	Footwall Assimilation Zone (Pegmatoidal troctolite)								Footwall Assimilation Zone (Wehrlite)									
Sample	SD-48	SD-48	SD-48	SD-48	SD-48	SD-48	SD-48	SD-48	SD-50	SD-50	SD-50	SD-50	SD-50	SD-50	SD-50	SD-50	SD-50	SD-50
SiO_2	0.03	0.03	0.01	0.02	0.03	0.03	0.02	0.02	0.03	0.03	0.02	0.03	0.02	0.02	0.03	0.03	0.00	0.03
TiO_2	1.72	2.40	2.38	2.52	2.68	1.72	2.37	2.37	0.62	0.61	0.60	0.67	0.64	0.52	0.37	1.94	1.74	1.74
Al_2O_3	12.33	12.56	12.23	12.30	12.67	12.38	13.08	13.08	26.57	26.56	25.57	23.62	23.75	29.24	32.28	13.74	13.08	15.03
Cr_2O_3	31.72	31.91	32.72	31.87	32.01	31.72	31.78	31.78	26.61	26.09	26.80	28.23	27.90	24.94	22.71	32.39	32.05	32.52
Fe_2O_3	32.92	32.05	31.67	31.84	31.82	32.92	31.34	31.34	24.08	23.84	24.75	25.40	26.24	22.76	22.38	29.97	32.12	28.83
V_2O_3	0.35	0.37	0.42	0.44	0.39	0.38	0.42	0.43	0.14	0.14	0.13	0.16	0.15	0.13	0.13	0.42	0.40	0.36
FeO	18.38	16.89	17.68	17.78	17.76	18.38	17.50	17.50	13.45	13.31	13.82	14.18	14.65	12.71	12.49	16.73	17.93	16.10
MnO	0.40	0.36	0.38	0.43	0.34	0.40	0.36	0.36	0.34	0.34	0.40	0.39	0.39	0.32	0.34	0.30	0.32	0.35
MgO	3.30	3.58	2.50	3.64	3.70	3.30	4.14	4.14	10.06	9.92	9.24	8.56	7.84	10.78	10.89	5.25	3.29	5.95
NiO	0.00	0.00	0.00	0.00	0.00	0.00	0.00	0.00	0.00	0.00	0.00	0.00	0.00	0.00	0.00	0.00	0.00	0.00
Total	101.15	100.15	99.99	100.84	101.40	101.23	101.00	101.01	101.90	100.84	101.34	101.24	101.58	101.42	101.62	100.78	100.93	100.91
O=4																		
Si	0.00	0.00	0.00	0.00	0.00	0.00	0.00	0.00	0.00	0.00	0.00	0.00	0.00	0.00	0.00	0.00	0.00	0.00
Ti	0.04	0.06	0.06	0.06	0.07	0.04	0.06	0.06	0.01	0.01	0.01	0.02	0.01	0.01	0.01	0.05	0.04	0.04
Al	0.48	0.49	0.48	0.49	0.48	0.48	0.51	0.51	0.94	0.95	0.92	0.86	0.86	1.02	1.11	0.53	0.51	0.57
Cr	0.83	0.83	0.86	0.83	0.84	0.83	0.83	0.83	0.63	0.62	0.64	0.69	0.68	0.58	0.52	0.84	0.84	0.83
V	0.01	0.01	0.01	0.01	0.01	0.01	0.01	0.01	0.00	0.00	0.00	0.00	0.00	0.00	0.00	0.01	0.01	0.01
Mn	0.01	0.01	0.01	0.01	0.01	0.01	0.01	0.01	0.01	0.01	0.01	0.01	0.01	0.01	0.01	0.01	0.01	0.01
Mg	0.16	0.18	0.18	0.18	0.18	0.16	0.20	0.20	0.45	0.45	0.42	0.39	0.36	0.48	0.47	0.26	0.16	0.29
Ni	0.00	0.00	0.00	0.00	0.00	0.00	0.00	0.00	0.00	0.00	0.00	0.00	0.00	0.00	0.00	0.00	0.00	0.00
Fe^{3+}	0.52	0.57	0.59	0.60	0.61	0.63	0.47	0.64	0.34	0.35	0.36	0.36	0.39	0.31	0.28	0.43	0.51	0.63
Fe^{2+}	0.87	0.86	0.85	0.85	0.85	0.85	0.85	0.85	0.54	0.54	0.57	0.60	0.63	0.54	0.52	0.56	0.56	0.56
Total	2.88	2.87	2.87	2.87	2.87	2.88	2.88	2.88	2.93	2.93	2.92	2.92	2.91	2.93	2.93	2.89	2.88	2.90
Cr#	63.31	62.83	64.33	62.98	63.75	63.31	61.97	61.97	40.18	39.72	41.29	44.50	44.08	36.40	32.06	61.26	62.18	59.21
Mg#	15.84	17.07	17.74	17.41	17.71	16.17	19.39	19.38	45.60	45.13	42.28	39.49	36.21	46.99	47.78	31.33	22.43	33.87
$Fe^{3+}/\sum Fe$	0.72	0.82	0.85	0.87	0.90	0.92	0.61	0.95	0.30	0.31	0.34	0.35	0.41	0.26	0.22	0.43	0.54	0.75
fO_2 (NNO-Buffer)	0.24	0.24	0.25	0.25	0.26	0.26	0.26	0.27	0.81	0.85	0.75	0.78	0.85	0.85	0.18	0.21	0.28	1.08

Mineral	Cr-SPINEL														
Drill core	UMT-094														
Lithology	Footwall Assimilation Zone (Wehrlite)														
Sample	SD-54	SD-54	SD-54	SD-54	SD-54	SD-54	SD-54	SD-54	SD-56	SD-56	SD-56	SD-56	SD-56	SD-56	SD-56
SiO_2	0.00	0.01	0.02	0.01	0.01	0.01	0.02	0.01	0.02	0.01	0.01	0.02	0.02	0.02	0.03
TiO_2	0.09	0.09	0.08	0.09	0.11	0.08	0.07	0.05	0.21	0.15	0.18	0.18	0.18	0.19	0.36
Al_2O_3	61.03	60.83	60.26	60.04	60.91	61.34	61.45	61.34	43.43	47.14	46.60	45.98	46.33	40.65	34.35
Cr_2O_3	0.07	0.06	0.07	0.07	0.07	0.10	0.12	0.07	15.59	12.86	13.14	13.65	13.15	17.20	22.32
Fe_2O_3	13.12	13.16	13.44	13.66	13.23	12.81	12.63	13.39	17.41	16.13	16.58	16.89	16.62	19.15	20.03
V_2O_3	0.06	0.06	0.05	0.07	0.06	0.06	0.06	0.05	0.08	0.08	0.07	0.07	0.07	0.09	0.10
FeO	7.33	7.35	7.51	7.62	7.39	7.15	7.05	7.48	9.72	9.00	9.26	9.43	9.28	10.69	11.18
MnO	0.15	0.16	0.18	0.14	0.17	0.18	0.16	0.18	0.32	0.26	0.31	0.32	0.30	0.35	0.36
MgO	18.34	18.43	17.99	17.95	18.57	18.48	18.12	18.36	14.54	15.68	15.33	14.76	15.34	13.04	12.24
NiO	0.00	0.00	0.00	0.00	0.00	0.00	0.00	0.00	0.00	0.00	0.00	0.00	0.00	0.00	0.00
Total	100.18	100.14	99.61	99.66	100.52	100.22	99.70	100.93	101.32	101.32	101.48	101.30	101.29	101.38	100.96
Cations (calculated on the basis of 3 cations)															
Si	0.00	0.00	0.00	0.00	0.00	0.00	0.00	0.00	0.00	0.00	0.00	0.00	0.00	0.00	0.00
Ti	0.00	0.00	0.00	0.00	0.00	0.00	0.00	0.00	0.00	0.00	0.00	0.00	0.00	0.00	0.01
Al	1.84	1.83	1.83	1.83	1.83	1.84	1.85	1.84	1.41	1.50	1.49	1.47	1.48	1.34	1.17
Cr	0.00	0.00	0.00	0.00	0.00	0.00	0.00	0.00	0.34	0.27	0.28	0.29	0.28	0.38	0.51
V	0.00	0.00	0.00	0.00	0.00	0.00	0.00	0.00	0.00	0.00	0.00	0.00	0.00	0.00	0.00
Mn	0.00	0.00	0.00	0.00	0.00	0.00	0.00	0.00	0.01	0.01	0.01	0.01	0.01	0.01	0.01
Mg	0.70	0.70	0.69	0.69	0.71	0.70	0.69	0.69	0.60	0.63	0.62	0.60	0.62	0.54	0.53
Ni	0.00	0.00	0.00	0.00	0.00	0.00	0.00	0.00	0.00	0.00	0.00	0.00	0.00	0.00	0.00
Fe^{3+}	0.13	0.14	0.13	0.12	0.12	0.13	0.12	0.21	0.18	0.19	0.20	0.18	0.24	0.25	0.86
Fe^{2+}	0.29	0.29	0.29	0.29	0.28	0.29	0.30	0.32	0.38	0.36	0.37	0.38	0.38	0.45	0.65
Total	2.95	2.95	2.95	2.95	2.95	2.95	2.95	2.95	2.94	2.95	2.94	2.94	2.94	2.93	2.93
Cr#	0.06	0.06	0.06	0.06	0.06	0.10	0.13	0.06	19.40	15.46	15.90	16.60	16.00	22.11	30.35
Mg#	70.50	70.83	70.12	70.26	71.70	70.83	69.81	68.42	61.01	63.70	62.56	60.87	61.77	54.93	44.97
$Fe^{3+}/\sum Fe$	0.06	0.06	0.05	0.05	0.05	0.06	0.05	0.11	0.10	0.11	0.11	0.10	0.15	0.17	1.29
fO_2 (NNO-Buffer)	1.08	1.08	1.15	1.16	1.13	1.04	1.00	2.36	2.53	1.10	1.10	1.03	1.14	0.94	1.17

Mineral	Cr-SPINEL									
Drill core	UMT-094									
Lithology	Footwall Assimilation Zone (Wehrlite)									
Sample	SD-56	SD-56	SD-56	SD-56	SD-56	SD-56	SD-56	SD-56	SD-57	SD-57
SiO_2	0.01	0.02	0.02	0.02	0.01	0.03	0.00	0.02	0.01	0.01
TiO_2	0.18	0.23	0.34	0.21	0.58	0.20	0.26	0.21	0.06	0.04
Al_2O_3	46.29	43.67	37.56	46.87	25.93	48.21	46.24	45.17	46.18	47.24
Cr_2O_3	13.22	16.63	20.02	12.69	29.98	11.59	12.79	13.88	12.50	12.46
Fe_2O_3	16.82	16.65	18.41	15.79	21.58	16.16	16.29	17.08	14.42	12.75
V_2O_3	0.08	0.08	0.09	0.07	0.11	0.07	0.07	0.08	0.03	0.01
FeO	9.39	9.30	10.28	8.82	12.05	9.02	9.10	9.54	8.05	7.12
MnO	0.31	0.28	0.31	0.28	0.38	0.27	0.27	0.34	0.47	0.48
MgO	15.35	15.37	13.97	16.27	11.23	15.80	15.80	14.95	18.50	19.14
NiO	0.00	0.00	0.00	0.00	0.00	0.00	0.00	0.00	0.00	0.00
Total	101.65	102.22	101.01	101.02	101.84	101.34	100.82	101.27	100.22	99.25
Cations (calculated on the basis of 3 cations)										
Si	0.00	0.00	0.00	0.00	0.00	0.00	0.00	0.00	0.00	0.00
Ti	0.00	0.00	0.01	0.00	0.01	0.00	0.01	0.00	0.00	0.00
Al	1.48	1.40	1.25	1.49	0.91	1.53	1.48	1.45	1.48	1.51
Cr	0.28	0.36	0.45	0.27	0.71	0.25	0.27	0.30	0.27	0.27
V	0.00	0.00	0.00	0.00	0.00	0.00	0.00	0.00	0.00	0.00
Mn	0.01	0.01	0.01	0.01	0.01	0.01	0.01	0.01	0.01	0.01
Mg	0.62	0.62	0.59	0.66	0.50	0.63	0.64	0.61	0.75	0.77
Ni	0.00	0.00	0.00	0.00	0.00	0.00	0.00	0.00	0.00	0.00
Fe^{3+}	1.97	1.92	0.19	0.23	0.19	0.31	0.19	1.68	0.28	0.21
Fe^{2+}	0.99	0.96	0.37	0.38	0.38	0.37	0.46	0.36	0.23	0.22
Total	2.94	2.95	2.94	2.95	2.93	2.95	2.95	2.94	2.98	2.98
Cr#	16.08	20.34	26.33	15.36	43.69	13.88	15.64	17.09	15.37	15.03
Mg#	38.48	39.34	61.70	63.48	56.76	62.88	58.35	63.11	76.62	77.51
$Fe^{3+}/\sum Fe$	5.84	5.52	0.11	0.14	0.11	0.21	0.12	3.42	0.14	0.09
fO_2 (NNO-Buffer)	1.14	1.11	0.89	0.92	1.43	1.50	1.86	1.53	0.94	1.53

Mineral	*OLIVINE*															
Drill core	**UMT-335**															
Lithology	**Footwall Assimilation Zone (Wehrlite)**															
Sample	**SD-06**	**SD-06**	**SD-06**	**SD-06**	**SD-06**	**SD-06**	**SD-06**	**SD-06**	**SD-06**	**SD-06**	**SD-06**	**SD-06**	**SD-06**	**SD-06**	**SD-06**	**SD-06**
SiO_2	38.10	38.05	38.23	38.20	38.43	38.16	38.02	38.02	38.00	37.68	38.01	37.85	37.92	37.64	37.92	37.96
TiO_2	0.05	0.01	0.00	0.00	0.00	0.04	0.04	0.06	0.01	0.01	0.00	0.01	0.00	0.00	0.04	0.02
Al_2O_3	0.00	0.00	0.00	0.00	0.02	0.02	0.00	0.03	0.00	0.00	0.00	0.01	0.01	0.00	0.00	0.01
Cr_2O_3	0.08	0.06	0.07	0.02	0.00	0.07	0.00	0.02	0.09	0.04	0.03	0.01	0.00	0.03	0.04	0.00
FeO	20.72	20.85	20.61	20.80	20.82	20.66	20.99	19.89	21.57	21.50	21.42	21.66	21.75	21.46	21.94	22.26
MnO	0.30	0.32	0.31	0.31	0.29	0.29	0.35	0.26	0.29	0.29	0.28	0.29	0.28	0.27	0.27	0.27
MgO	39.92	40.10	39.93	39.58	39.83	39.50	39.50	40.13	39.40	38.94	38.92	38.88	39.23	39.19	39.07	38.54
CaO	0.02	0.03	0.04	0.03	0.03	0.04	0.02	0.02	0.04	0.04	0.04	0.03	0.02	0.03	0.04	0.02
NiO	0.16	0.20	0.18	0.22	0.22	0.17	0.21	0.19	0.24	0.28	0.29	0.20	0.29	0.23	0.25	0.25
Na_2O	0.01	0.00	0.00	0.00	0.00	0.00	0.00	0.02	0.00	0.00	0.01	0.00	0.03	0.00	0.00	0.01
Total	**99.34**	**99.61**	**99.37**	**99.15**	**99.65**	**98.96**	**99.13**	**98.63**	**99.64**	**98.78**	**99.00**	**98.93**	**99.54**	**98.85**	**99.56**	**99.32**
Cations (Calculated on the basis of 3 cations)																
Si	0.99	0.99	0.99	1.00	1.00	1.00	0.99	0.99	0.99	0.99	1.00	0.99	0.99	0.99	0.99	1.00
Ti	0.00	0.00	0.00	0.00	0.00	0.00	0.00	0.00	0.00	0.00	0.00	0.00	0.00	0.00	0.00	0.00
Al	0.00	0.00	0.00	0.00	0.00	0.00	0.00	0.00	0.00	0.00	0.00	0.00	0.00	0.00	0.00	0.00
Cr	0.00	0.00	0.00	0.00	0.00	0.00	0.00	0.00	0.00	0.00	0.00	0.00	0.00	0.00	0.00	0.00
Fe^{2+}	0.45	0.45	0.45	0.45	0.45	0.45	0.46	0.43	0.47	0.47	0.47	0.48	0.48	0.47	0.48	0.49
Mn	0.01	0.01	0.01	0.01	0.01	0.01	0.01	0.01	0.01	0.01	0.01	0.01	0.01	0.01	0.01	0.01
Mg	1.55	1.55	1.55	1.54	1.54	1.54	1.54	1.56	1.53	1.53	1.52	1.52	1.53	1.54	1.52	1.51
Ca	0.00	0.00	0.00	0.00	0.00	0.00	0.00	0.00	0.00	0.00	0.00	0.00	0.00	0.00	0.00	0.00
Ni	0.00	0.00	0.00	0.00	0.00	0.00	0.00	0.00	0.01	0.01	0.01	0.00	0.01	0.00	0.01	0.01
Total	3.01	3.01	3.00	3.00	3.00	3.00	3.01	3.00	3.01	3.01	3.00	3.01	3.01	3.01	3.01	3.00
Fo	77.4	77.4	77.5	77.2	77.3	77.3	77.0	78.2	76.5	76.3	76.4	76.2	76.3	76.5	76.0	75.5
Ca (ppm)	142.9	235.9	257.3	207.3	185.8	285.9	164.4	142.9	285.9	278.7	293.0	200.1	164.4	200.1	271.6	135.8

Mineral	*OLIVINE*													
Drill core	**UMT-335**													
Lithology	**Footwall Assimilation Zone (Wehrlite)**													
Sample	**SD-17**	**SD-17**	**SD-17**	**SD-17**	**SD-17**	**SD-17**	**SD-17**	**SD-17**	**SD-17**	**SD-17**	**SD-17**	**SD-17**	**SD-17**	**SD-17**
SiO_2	37.55	38.16	37.97	37.87	38.31	37.63	37.70	37.74	38.07	37.86	37.88	37.41	38.03	37.86
TiO_2	0.00	0.03	0.01	0.01	0.00	0.00	0.00	0.05	0.00	0.00	0.02	0.00	0.01	0.02
Al_2O_3	0.00	0.00	0.01	0.00	0.00	0.01	0.01	0.03	0.00	0.01	0.01	0.01	0.01	0.01
Cr_2O_3	0.04	0.00	0.01	0.12	0.04	0.00	0.01	0.02	0.02	0.03	0.03	0.00	0.07	0.03
FeO	23.68	22.83	23.26	23.04	22.81	22.91	22.35	21.53	21.76	23.64	22.86	23.50	23.11	23.39
MnO	0.51	0.45	0.46	0.48	0.44	0.40	0.40	0.44	0.45	0.49	0.49	0.42	0.48	0.45
MgO	37.05	37.63	37.60	37.43	37.92	37.76	37.62	38.27	38.66	37.25	37.68	37.49	37.50	37.52
CaO	0.02	0.01	0.02	0.02	0.04	0.03	0.04	0.03	0.03	0.03	0.02	0.02	0.05	0.02
NiO	0.13	0.12	0.13	0.11	0.06	0.19	0.13	0.15	0.09	0.16	0.11	0.13	0.12	0.12
Na_2O	0.00	0.00	0.00	0.00	0.02	0.01	0.00	0.00	0.00	0.00	0.02	0.00	0.00	0.03
Total	**98.98**	**99.23**	**99.48**	**99.07**	**99.66**	**98.94**	**98.25**	**98.26**	**99.07**	**99.48**	**99.12**	**98.98**	**99.37**	**99.44**
Cations (Calculated on the basis of 3 cations)														
Si	1.00	1.00	1.00	1.00	1.00	0.99	1.00	1.00	1.00	1.00	1.00	0.99	1.00	1.00
Ti	0.00	0.00	0.00	0.00	0.00	0.00	0.00	0.00	0.00	0.00	0.00	0.00	0.00	0.00
Al	0.00	0.00	0.00	0.00	0.00	0.00	0.00	0.00	0.00	0.00	0.00	0.00	0.00	0.00
Cr	0.00	0.00	0.00	0.00	0.00	0.00	0.00	0.00	0.00	0.00	0.00	0.00	0.00	0.00
Fe^{2+}	0.53	0.50	0.51	0.51	0.50	0.51	0.50	0.48	0.48	0.52	0.50	0.52	0.51	0.52
Mn	0.01	0.01	0.01	0.01	0.01	0.01	0.01	0.01	0.01	0.01	0.01	0.01	0.01	0.01
Mg	1.47	1.48	1.47	1.47	1.48	1.49	1.49	1.51	1.51	1.46	1.48	1.48	1.47	1.47
Ca	0.00	0.00	0.00	0.00	0.00	0.00	0.00	0.00	0.00	0.00	0.00	0.00	0.00	0.00
Ni	0.00	0.00	0.00	0.00	0.00	0.00	0.00	0.00	0.00	0.00	0.00	0.00	0.00	0.00
Total	3.00	2.99	3.00	3.00	3.00	3.00	3.00	3.00	3.00	3.00	3.00	3.01	3.00	3.00
Fo	73.6	74.6	74.2	74.3	74.7	74.6	75.0	76.0	76.0	73.7	74.6	74.0	74.3	74.1
Ca (ppm)	128.6	100.1	150.1	142.9	293.0	221.6	300.2	228.7	193.0	221.6	135.8	135.8	335.9	114.4

Mineral	*OLIVINE*													
Drill core	**UMT-335**													
Lithology	**Footwall Assimilation Zone (Wehrlite)**													
Sample	**SD-17**	**SD-17**	**SD-17**	**SD-17**	**SD-17**	**SD-17**	**SD-17**	**SD-17**	**SD-17**	**SD-17**	**SD-15B**	**SD-15B**	**SD-15B**	**SD-15B**
SiO_2	37.77	37.75	38.07	37.78	38.10	37.86	38.06	37.91	38.08	38.00	37.99	38.07	38.15	38.34
TiO_2	0.00	0.00	0.00	0.06	0.00	0.03	0.00	0.00	0.03	0.00	0.10	0.10	0.10	0.10
Al_2O_3	0.00	0.03	0.00	0.00	0.01	0.00	0.00	0.01	0.00	0.02	0.00	0.01	0.01	0.00
Cr_2O_3	0.01	0.11	0.01	0.00	0.02	0.00	0.05	0.04	0.03	0.10	0.01	0.00	0.01	0.02
FeO	23.01	23.07	23.77	23.13	23.27	23.18	23.74	23.14	22.96	23.41	20.84	20.59	20.85	20.95
MnO	0.45	0.42	0.46	0.48	0.47	0.41	0.52	0.44	0.48	0.48	0.42	0.41	0.43	0.43
MgO	37.53	37.48	37.52	37.68	37.86	37.98	37.83	37.83	37.40	37.13	40.75	40.71	40.67	40.34
CaO	0.02	0.05	0.02	0.03	0.03	0.02	0.03	0.02	0.01	0.01	0.04	0.03	0.04	0.06
NiO	0.13	0.08	0.16	0.15	0.13	0.09	0.17	0.11	0.14	0.11	0.13	0.12	0.13	0.14
Na_2O	0.02	0.00	0.01	0.00	0.00	0.00	0.00	0.01	0.00	0.00	0.00	0.00	0.00	0.00
Total	**98.94**	**98.99**	**100.02**	**99.32**	**99.89**	**99.57**	**100.39**	**99.50**	**99.13**	**99.25**	**100.27**	**100.04**	**100.37**	**100.37**
Cations (Calculated on the basis of 3 cations)														
Si	1.00	1.00	1.00	1.00	1.00	0.99	0.99	1.00	1.00	1.00	0.98	0.98	0.98	0.99
Ti	0.00	0.00	0.00	0.00	0.00	0.00	0.00	0.00	0.00	0.00	0.00	0.00	0.00	0.00
Al	0.00	0.00	0.00	0.00	0.00	0.00	0.00	0.00	0.00	0.00	0.00	0.00	0.00	0.00
Cr	0.00	0.00	0.00	0.00	0.00	0.00	0.00	0.00	0.00	0.00	0.00	0.00	0.00	0.00
Fe^{2+}	0.51	0.51	0.52	0.51	0.51	0.51	0.52	0.51	0.51	0.52	0.45	0.45	0.45	0.45
Mn	0.01	0.01	0.01	0.01	0.01	0.01	0.01	0.01	0.01	0.01	0.01	0.01	0.01	0.01
Mg	1.48	1.48	1.47	1.48	1.48	1.49	1.47	1.48	1.47	1.46	1.57	1.57	1.56	1.55
Ca	0.00	0.00	0.00	0.00	0.00	0.00	0.00	0.00	0.00	0.00	0.00	0.00	0.00	0.00
Ni	0.00	0.00	0.00	0.00	0.00	0.00	0.00	0.00	0.00	0.00	0.00	0.00	0.00	0.00
Total	3.00	3.00	3.00	3.00	3.00	3.00	3.00	3.00	2.99	3.00	3.02	3.01	3.01	3.01
Fo	74.4	74.3	73.8	74.4	74.3	74.5	73.9	74.4	74.4	73.9	77.7	77.9	77.6	77.4
Ca (ppm)	157.2	321.6	164.4	185.8	178.7	150.1	193.0	142.9	100.1	100.1	270.2	248.7	255.1	408.1

Mineral	*Olivine*																	
Drill core	**UMT-345**										**UMT-094**							
Lithology	**Olivine Gabbronorite**										**Footwall Assimilation Zone (Pegmatoidal Troctolite)**							
Sample	**SD-30**	**SD-30**	**SD-30**	**SD-30**	**SD-30**	**SD-30**	**SD-30**	**SD-30**	**SD-30**	**SD-30**	**SD-48**	**SD-48**	**SD-48**	**SD-48**	**SD-48**	**SD-48**	**SD-48**	**SD-48**
SiO_2	38.71	38.29	38.71	38.62	38.95	38.28	39.44	38.47	38.48	38.83	38.29	38.71	38.62	38.95	38.28	39.44	38.47	38.48
TiO_2	0.02	0.00	0.01	0.02	0.02	0.00	0.01	0.00	0.02	0.01	0.00	0.01	0.02	0.02	0.00	0.01	0.00	0.02
Al_2O_3	0.01	0.02	0.00	0.01	0.00	0.00	0.00	0.00	0.01	0.00	0.02	0.00	0.01	0.00	0.00	0.00	0.00	0.01
Cr_2O_3	0.00	0.03	0.00	0.03	0.00	0.00	0.00	0.01	0.01	0.04	0.00	0.00	0.00	0.00	0.00	0.01	0.01	0.01
FeO	19.58	19.91	20.10	20.01	19.97	20.77	20.15	19.88	20.08	20.23	19.91	20.10	20.01	19.97	20.77	20.15	19.88	20.08
MnO	0.26	0.29	0.31	0.32	0.29	0.30	0.31	0.32	0.31	0.32	0.29	0.31	0.32	0.29	0.30	0.31	0.32	0.31
MgO	42.04	41.29	41.23	41.27	40.91	40.90	40.97	41.37	41.55	41.33	41.29	41.23	41.27	40.91	40.90	40.97	41.37	41.55
CaO	0.03	0.02	0.03	0.07	0.05	0.03	0.01	0.04	0.03	0.03	0.02	0.03	0.07	0.05	0.03	0.01	0.04	0.03
NiO	0.22	0.24	0.23	0.22	0.27	0.26	0.25	0.23	0.26	0.27	0.24	0.23	0.22	0.27	0.26	0.25	0.23	0.26
Na_2O	0.01	0.01	0.01	0.01	0.01	0.01	0.01	0.01	0.01	0.00	0.01	0.00	0.00	0.00	0.01	0.00	0.00	0.01
Total	**100.89**	**100.09**	**100.64**	**100.58**	**100.47**	**100.54**	**101.15**	**100.34**	**100.76**	**101.05**	**100.06**	**100.63**	**100.54**	**100.46**	**100.54**	**101.16**	**100.33**	**100.76**
Cations (Calculated on the basis of 3 cations)																		
Si	0.99	0.99	0.99	0.99	1.00	0.99	1.00	0.99	0.98	0.99	0.99	0.99	0.99	1.00	0.99	1.00	0.99	0.98
Ti	0.00	0.00	0.00	0.00	0.00	0.00	0.00	0.00	0.00	0.00	0.00	0.00	0.00	0.00	0.00	0.00	0.00	0.00
Al	0.00	0.00	0.00	0.00	0.00	0.00	0.00	0.00	0.00	0.00	0.00	0.00	0.00	0.00	0.00	0.00	0.00	0.00
Cr	0.00	0.00	0.00	0.00	0.00	0.00	0.00	0.00	0.00	0.00	0.00	0.00	0.00	0.00	0.00	0.00	0.00	0.00
Fe^{2+}	0.42	0.43	0.43	0.43	0.43	0.45	0.43	0.43	0.43	0.43	0.43	0.43	0.43	0.43	0.45	0.43	0.43	0.43
Mn	0.01	0.01	0.01	0.01	0.01	0.01	0.01	0.01	0.01	0.01	0.01	0.01	0.01	0.01	0.01	0.01	0.01	0.01
Mg	1.60	1.59	1.57	1.58	1.56	1.57	1.55	1.58	1.59	1.57	1.59	1.57	1.58	1.56	1.57	1.55	1.58	1.59
Ca	0.00	0.00	0.00	0.00	0.00	0.00	0.00	0.00	0.00	0.00	0.00	0.00	0.00	0.00	0.00	0.00	0.00	0.00
Ni	0.00	0.00	0.00	0.00	0.01	0.01	0.01	0.00	0.01	0.01	0.00	0.00	0.00	0.01	0.01	0.01	0.00	0.01
Total	3.01	3.01	3.01	3.01	3.00	3.01	3.00	3.01	3.01	3.01	3.01	3.01	3.01	3.00	3.01	3.00	3.01	3.01
Fo	79.2	78.7	78.5	78.5	78.4	77.8	78.4	78.7	78.6	78.4	78.7	78.5	78.5	78.4	77.8	78.4	78.7	78.6
Ca (ppm)	214.4	134.2	248.0	490.1	381.3	216.6	63.4	286.6	229.7	204.1	134.2	248.0	490.1	381.3	216.6	63.4	286.6	229.7

Mineral	*OLIVINE*													
Drill core	**UMT-094**													
Lithology	**Footwall Assimilation Zone (Wehrlite)**													
Sample	**SD-50**	**SD-50**	**SD-50**	**SD-50**	**SD-54**	**SD-54**	**SD-54**	**SD-54**	**SD-54**	**SD-54**	**SD-54**	**SD-54**	**SD-54**	**SD-54**
SiO_2	39.96	39.97	39.84	39.79	40.61	40.39	40.53	40.63	40.36	40.25	40.21	40.58	39.90	40.10
TiO_2					0.00	0.02	0.00	0.01	0.01	0.00	0.00	0.01	0.00	0.01
Al_2O_3	0.01	0.00	0.00	0.00	0.02	0.00	0.01	0.00	0.01	0.01	0.01	0.00	0.01	0.01
Cr_2O_3	0.01	0.01	0.01	0.00	0.01	0.01	0.01	0.00	0.01	0.02	0.01	0.00	0.00	0.01
FeO	14.46	14.41	14.85	14.59	13.46	13.61	13.31	13.56	13.24	13.29	15.38	15.12	15.31	15.24
MnO	0.30	0.32	0.32	0.31	0.34	0.36	0.32	0.34	0.33	0.36	0.31	0.30	0.31	0.30
MgO	45.66	45.54	45.40	45.55	46.13	46.01	45.98	45.98	45.97	45.81	45.13	45.05	44.95	44.90
CaO	0.05	0.06	0.05	0.03	0.09	0.08	0.07	0.09	0.08	0.09	0.08	0.04	0.06	0.07
NiO	0.09	0.10	0.07	0.06	0.09	0.06	0.10	0.06	0.06	0.08	0.08	0.06	0.07	0.06
Na_2O	0.00	0.00	0.01	0.00	0.00	0.00	0.00	0.00	0.00	0.01	0.00	0.02	0.01	0.02
Total	**100.54**	**100.41**	**100.55**	**100.33**	**100.75**	**100.54**	**100.33**	**100.67**	**100.07**	**99.92**	**101.21**	**101.18**	**100.62**	**100.72**
Cations (Calculated on the basis of 3 cations)														
Si	1.00	1.00	0.99	0.99	1.00	1.00	1.01	1.01	1.00	1.00	1.00	1.01	1.00	1.00
Ti	0.00	0.00	0.00	0.00	0.00	0.00	0.00	0.00	0.00	0.00	0.00	0.00	0.00	0.00
Al	0.00	0.00	0.00	0.00	0.00	0.00	0.00	0.00	0.00	0.00	0.00	0.00	0.00	0.00
Cr	0.00	0.00	0.00	0.00	0.00	0.00	0.00	0.00	0.00	0.00	0.00	0.00	0.00	0.00
Fe^{2+}	0.30	0.30	0.31	0.30	0.28	0.28	0.28	0.28	0.28	0.28	0.32	0.31	0.32	0.32
Mn	0.01	0.01	0.01	0.01	0.01	0.01	0.01	0.01	0.01	0.01	0.01	0.01	0.01	0.01
Mg	1.70	1.69	1.69	1.70	1.70	1.70	1.70	1.70	1.70	1.70	1.67	1.66	1.67	1.67
Ca	0.00	0.00	0.00	0.00	0.00	0.00	0.00	0.00	0.00	0.00	0.00	0.00	0.00	0.00
Ni	0.00	0.00	0.00	0.00	0.00	0.00	0.00	0.00	0.00	0.00	0.00	0.00	0.00	0.00
Total	3.00	3.00	3.00	3.01	3.00	3.00	2.99	2.99	3.00	3.00	3.00	2.99	3.00	3.00
Fo	84.9	84.9	84.4	84.7	85.8	85.7	85.9	85.7	86.0	85.9	83.9	84.1	83.9	83.9
Ca (ppm)	357.4	428.8	357.4	214.4	643.2	571.8	500.3	643.2	571.8	643.2	571.8	285.9	428.8	500.3

Mineral	*OLIVINE*												
Drill core	**UMT-094**												
Lithology	**Footwall Assimilation Zone (Wehrlite)**												
Sample	**SD-54**	**SD-54**	**SD-54**	**SD-54**	**SD-54**	**SD-54**	**SD-54**	**SD-54**	**SD-56**	**SD-56**	**SD-56**	**SD-56**	**SD-56**
SiO_2	40.23	40.03	39.88	40.18	40.20	40.49	40.08	40.26	40.63	40.48	40.33	40.41	40.09
TiO_2	0.04	0.01	0.00	0.00	0.02	0.00	0.02	0.03	0.00	0.01	0.01	0.00	0.00
Al_2O_3	0.01	0.01	0.02	0.02	0.00	0.03	0.00	0.00	0.01	0.00	0.00	0.01	0.01
Cr_2O_3	0.00	0.00	0.00	0.00	0.00	0.00	0.00	0.00	0.00	0.00	0.01	0.00	0.01
FeO	15.18	15.18	15.33	15.44	15.24	15.39	15.18	15.31	13.05	13.20	12.99	14.87	15.02
MnO	0.28	0.30	0.30	0.29	0.30	0.31	0.31	0.31	0.34	0.35	0.35	0.29	0.31
MgO	44.88	44.79	44.77	44.71	44.61	44.51	44.50	44.22	46.46	46.29	46.00	45.47	45.36
CaO	0.05	0.05	0.06	0.05	0.04	0.05	0.05	0.05	0.07	0.08	0.07	0.04	0.05
NiO	0.08	0.08	0.05	0.06	0.03	0.05	0.08	0.03	0.08	0.07	0.05	0.05	0.05
Na_2O	0.00	0.00	0.00	0.01	0.00	0.01	0.00	0.00	0.00	0.00	0.00	0.00	0.00
Total	**100.75**	**100.45**	**100.41**	**100.76**	**100.44**	**100.84**	**100.22**	**100.21**	**100.64**	**100.48**	**99.81**	**101.14**	**100.90**
Cations (Calculated on the basis of 3 cations)													
Si	1.00	1.00	1.00	1.00	1.01	1.01	1.00	1.01	1.00	1.00	1.00	1.00	1.00
Ti	0.00	0.00	0.00	0.00	0.00	0.00	0.00	0.00	0.00	0.00	0.00	0.00	0.00
Al	0.00	0.00	0.00	0.00	0.00	0.00	0.00	0.00	0.00	0.00	0.00	0.00	0.00
Cr	0.00	0.00	0.00	0.00	0.00	0.00	0.00	0.00	0.00	0.00	0.00	0.00	0.00
Fe^{2+}	0.32	0.32	0.32	0.32	0.32	0.32	0.32	0.32	0.27	0.27	0.27	0.31	0.31
Mn	0.01	0.01	0.01	0.01	0.01	0.01	0.01	0.01	0.01	0.01	0.01	0.01	0.01
Mg	1.67	1.67	1.67	1.66	1.66	1.65	1.66	1.65	1.71	1.71	1.71	1.68	1.68
Ca	0.00	0.00	0.00	0.00	0.00	0.00	0.00	0.00	0.00	0.00	0.00	0.00	0.00
Ni	0.00	0.00	0.00	0.00	0.00	0.00	0.00	0.00	0.00	0.00	0.00	0.00	0.00
Total	3.00	3.00	3.00	3.00	2.99	2.99	3.00	2.99	3.00	3.00	2.99	3.00	3.00
Fo	84.0	84.0	83.8	83.7	83.9	83.7	83.9	83.7	86.3	86.1	86.2	84.5	84.3
Ca (ppm)	357.4	357.4	428.8	357.4	285.9	357.4	357.4	357.4	500.3	571.8	500.3	285.9	357.4

Mineral	*OLIVINE*												
Drill core	**UMT-094**												
Lithology	**Footwall Assimilation Zone (Wehrlite)**												
Sample	**SD-56**	**SD-56**	**SD-56**	**SD-56**	**SD-56**	**SD-56**	**SD-56**	**SD-56**	**SD-56**	**SD-56**	**SD-56**	**SD-56**	**SD-56**
SiO_2	40.15	40.14	40.10	40.15	40.34	40.10	40.30	40.12	40.21	39.83	40.31	40.42	40.44
TiO_2	0.00	0.00	0.01	0.03	0.01	0.01	0.02	0.00	0.00	0.00	0.00	0.01	0.00
Al_2O_3	0.01	0.01	0.01	0.01	0.00	0.02	0.00	0.01	0.01	0.01	0.00	0.01	0.00
Cr_2O_3	0.00	0.00	0.00	0.00	0.00	0.00	0.00	0.00	0.00	0.00	0.00	0.00	0.00
FeO	14.76	15.34	14.86	15.03	14.89	15.26	15.16	15.35	15.44	15.19	15.70	15.09	15.08
MnO	0.28	0.27	0.27	0.29	0.30	0.30	0.29	0.32	0.31	0.32	0.31	0.31	0.28
MgO	45.34	45.28	45.25	45.17	45.16	44.86	44.80	44.74	44.69	44.66	44.55	44.51	44.46
CaO	0.05	0.04	0.05	0.06	0.04	0.06	0.05	0.05	0.07	0.05	0.02	0.06	0.06
NiO	0.06	0.06	0.05	0.04	0.05	0.03	0.06	0.07	0.08	0.07	0.04	0.05	0.06
Na_2O	0.00	0.00	0.01	0.00	0.01	0.00	0.00	0.00	0.00	0.00	0.01	0.00	0.00
Total	**100.65**	**101.14**	**100.61**	**100.78**	**100.80**	**100.64**	**100.68**	**100.66**	**100.81**	**100.13**	**100.94**	**100.46**	**100.38**
Cations (Calculated on the basis of 3 cations)													
Si	1.00	1.00	1.00	1.00	1.00	1.00	1.00	1.00	1.00	1.00	1.00	1.01	1.01
Ti	0.00	0.00	0.00	0.00	0.00	0.00	0.00	0.00	0.00	0.00	0.00	0.00	0.00
Al	0.00	0.00	0.00	0.00	0.00	0.00	0.00	0.00	0.00	0.00	0.00	0.00	0.00
Cr	0.00	0.00	0.00	0.00	0.00	0.00	0.00	0.00	0.00	0.00	0.00	0.00	0.00
Fe^{2+}	0.31	0.32	0.31	0.31	0.31	0.32	0.32	0.32	0.32	0.32	0.33	0.32	0.32
Mn	0.01	0.01	0.01	0.01	0.01	0.01	0.01	0.01	0.01	0.01	0.01	0.01	0.01
Mg	1.68	1.68	1.68	1.68	1.67	1.67	1.67	1.67	1.66	1.67	1.66	1.66	1.66
Ca	0.00	0.00	0.00	0.00	0.00	0.00	0.00	0.00	0.00	0.00	0.00	0.00	0.00
Ni	0.00	0.00	0.00	0.00	0.00	0.00	0.00	0.00	0.00	0.00	0.00	0.00	0.00
Total	3.00	3.00	3.00	3.00	3.00	3.00	2.99	3.00	3.00	3.00	3.00	2.99	2.99
Fo	84.5	84.0	84.4	84.2	84.3	83.9	84.0	83.8	83.7	83.9	83.5	84.0	83.9
Ca (ppm)	357.4	285.9	357.4	428.8	285.9	428.8	357.4	357.4	500.3	357.4	142.9	428.8	428.8

Mineral	*ORTHOPYROXENE*																			
Drill core	**UMT-335**																			
Lithology	**UG-2 Chromitite**																			
Sample	**SD-02-1**	**SD-02-2**	**SD-02-3**	**SD-02-4**	**SD-02-5**	**SD-02-6**	**SD-02-7**	**SD-02-8**	**SD-02-9**	**SD-02-10**	**SD-02-11**	**SD-02-12**	**SD-02-13**	**SD-02-14**	**SD-02-15**	**SD-02-16**	**SD-02-17**	**SD-02-18**	**SD-02-19**	**SD-02-20**
SiO_2	55.25	55.67	55.27	55.01	55.66	55.76	55.37	56.22	55.94	55.62	55.72	56.05	55.64	55.62	55.82	55.52	55.22	55.43	55.02	55.80
TiO_2	0.07	0.13	0.22	0.10	0.22	0.15	0.19	0.15	0.11	0.17	0.18	0.18	0.13	0.18	0.14	0.17	0.21	0.16	0.18	0.15
Al_2O_3	1.33	1.34	1.48	1.52	1.34	1.17	1.28	0.95	1.01	1.26	1.20	1.14	1.26	1.28	1.36	1.34	1.44	1.37	1.39	1.46
Cr_2O_3	0.48	0.43	0.52	0.56	0.47	0.44	0.44	0.35	0.30	0.34	0.38	0.37	0.39	0.42	0.47	0.57	0.50	0.46	0.52	0.43
MgO	30.68	30.35	30.19	29.79	30.91	30.90	30.61	31.07	31.17	30.97	31.28	30.65	30.81	31.14	30.57	30.15	30.56	30.15	29.68	28.93
MnO	0.22	0.21	0.29	0.24	0.23	0.20	0.24	0.22	0.20	0.21	0.25	0.17	0.26	0.18	0.26	0.24	0.26	0.25	0.23	0.23
FeO	11.15	11.05	10.90	10.47	10.13	10.17	10.63	10.27	10.52	10.36	9.98	9.83	10.47	9.92	10.56	10.79	10.85	10.52	10.90	11.18
CaO	0.80	0.74	1.00	2.19	0.97	1.11	1.10	0.70	0.68	1.03	0.97	1.53	1.01	1.16	0.77	1.15	0.90	1.58	1.98	1.69
Na_2O	0.00	0.01	0.03	0.04	0.00	0.02	0.00	0.04	0.00	0.01	0.00	0.01	0.00	0.00	0.00	0.03	0.02	0.02	0.01	0.03
Total	**99.97**	**99.91**	**99.90**	**99.92**	**99.93**	**99.92**	**99.85**	**99.95**	**99.92**	**99.95**	**99.97**	**99.93**	**99.97**	**99.90**	**99.93**	**99.94**	**99.95**	**99.94**	**99.90**	**99.90**
Cations (Calculated on the basis of 4 cations)																				
Si	1.95	1.97	1.96	1.95	1.96	1.96	1.96	1.98	1.97	1.96	1.96	1.97	1.96	1.96	1.97	1.96	1.95	1.96	1.95	1.98
Ti	0.00	0.00	0.01	0.00	0.01	0.00	0.00	0.00	0.00	0.00	0.00	0.00	0.00	0.00	0.00	0.00	0.01	0.00	0.00	0.00
Al	0.06	0.06	0.06	0.06	0.05	0.05	0.04	0.04	0.05	0.05	0.05	0.05	0.05	0.06	0.06	0.06	0.06	0.06	0.06	0.05
Cr	0.01	0.01	0.01	0.02	0.01	0.01	0.01	0.01	0.01	0.01	0.01	0.01	0.01	0.01	0.01	0.02	0.01	0.01	0.01	0.01
Fe	0.33	0.33	0.32	0.31	0.30	0.30	0.31	0.30	0.31	0.31	0.29	0.29	0.31	0.29	0.31	0.32	0.32	0.31	0.32	0.33
Mn	0.01	0.01	0.01	0.01	0.01	0.01	0.01	0.01	0.01	0.01	0.01	0.00	0.01	0.01	0.01	0.01	0.01	0.01	0.01	0.01
Mg	1.62	1.60	1.59	1.57	1.62	1.62	1.61	1.63	1.64	1.63	1.64	1.61	1.62	1.63	1.61	1.59	1.61	1.59	1.57	1.53
Ca	0.03	0.03	0.04	0.08	0.04	0.04	0.04	0.03	0.03	0.04	0.04	0.06	0.04	0.04	0.03	0.04	0.03	0.06	0.08	0.06
Na	0.00	0.00	0.00	0.00	0.00	0.00	0.00	0.00	0.00	0.00	0.00	0.00	0.00	0.00	0.00	0.00	0.00	0.00	0.00	0.00
Total	4.01	4.00	4.00	4.00	3.99	4.01	3.99	4.00	4.01	4.00	4.00	4.00	4.00	4.01	3.99	4.00	4.00	4.00	4.01	3.98
Cation ratios																				
En	81.79	81.85	81.54	80.00	82.89	82.62	81.92	83.23	83.00	82.55	83.24	82.25	82.37	82.96	82.53	81.43	81.94	81.07	79.75	79.44
Fs	16.67	16.72	16.52	15.78	15.24	15.25	15.96	15.44	15.71	15.49	14.90	14.81	15.70	14.82	15.99	16.34	16.33	15.87	16.44	17.23
Wo	1.54	1.43	1.94	4.23	1.88	2.13	2.12	1.34	1.29	1.96	1.86	2.94	1.93	2.22	1.49	2.23	1.73	3.06	3.82	3.34
Mg#	83.06	83.04	83.16	83.52	84.47	84.42	83.70	84.36	84.09	84.20	84.82	84.75	83.99	84.84	83.77	83.29	83.39	83.63	82.91	82.18

Mineral	*ORTHOPYROXENE*														
Drill core	**UMT-335**														
Lithology	**UG-2 Chromitite**										**Lower chromitite**				**Wehrlite**
Sample	**SD-02-21**	**SD-02-22**	**SD-02-23**	**SD-02-24**	**SD-02-25**	**SD-02-26**	**SD-02-27**	**SD-02-28**	**SD-02-29**	**SD-02-30**	**SD-09-1**	**SD-09-2**	**SD-09-3**	**SD-09-4**	**SD-15B**
SiO_2	55.80	55.23	55.36	55.29	55.24	55.52	55.97	55.26	55.23	55.50	55.34	55.18	54.73	54.91	55.26
TiO_2	0.15	0.14	0.21	0.12	0.16	0.16	0.01	0.13	0.15	0.15	0.13	0.14	0.10	0.12	0.10
Al_2O_3	1.27	1.27	1.36	1.29	1.39	1.34	0.82	1.29	1.45	1.44	1.44	1.35	1.36	1.46	0.42
Cr_2O_3	0.45	0.42	0.41	0.44	0.49	0.47	0.28	0.54	0.53	0.55	0.44	0.43	0.42	0.51	0.00
MgO	29.95	30.40	30.24	30.61	30.41	30.54	30.97	30.89	30.51	30.69	31.66	30.77	30.64	30.02	29.85
MnO	0.24	0.24	0.26	0.26	0.23	0.27	0.27	0.22	0.29	0.26	0.24	0.23	0.23	0.22	0.36
FeO	11.00	10.84	10.85	10.92	10.90	10.98	10.93	10.47	10.22	10.25	9.61	10.98	11.29	10.99	13.77
CaO	1.08	1.34	1.21	0.96	1.08	0.62	0.69	1.07	1.45	1.03	1.16	0.94	1.04	1.36	0.08
Na_2O	0.00	0.02	0.02	0.02	0.01	0.00	0.03	0.01	0.06	0.02	0.02	0.01	0.02	0.03	0.00
Total	**99.92**	**99.90**	**99.92**	**99.90**	**99.92**	**99.91**	**99.97**	**99.87**	**99.88**	**99.89**	**100.04**	**100.04**	**99.84**	**99.62**	**99.86**
Cations (Calculated on the basis of 4 cations)															
Si	1.97	1.96	1.96	1.96	1.95	1.96	1.97	1.95	1.95	1.96	1.97	1.98	1.97	1.98	1.98
Ti	0.00	0.00	0.01	0.00	0.00	0.00	0.00	0.00	0.00	0.00	0.00	0.00	0.00	0.00	0.00
Al	0.05	0.06	0.05	0.06	0.06	0.03	0.05	0.06	0.06	0.06	0.00	0.00	0.00	0.00	0.00
Cr	0.01	0.01	0.01	0.01	0.01	0.01	0.01	0.02	0.01	0.02	0.01	0.01	0.01	0.01	0.00
Fe	0.32	0.32	0.32	0.32	0.32	0.32	0.32	0.31	0.30	0.30	0.29	0.33	0.34	0.33	0.41
Mn	0.01	0.01	0.01	0.01	0.01	0.01	0.01	0.01	0.01	0.01	0.01	0.01	0.01	0.01	0.01
Mg	1.58	1.60	1.59	1.61	1.60	1.61	1.63	1.63	1.61	1.61	1.68	1.64	1.64	1.61	1.60
Ca	0.04	0.05	0.05	0.04	0.04	0.02	0.03	0.04	0.05	0.04	0.04	0.04	0.04	0.05	0.00
Na	0.00	0.00	0.00	0.00	0.00	0.00	0.00	0.00	0.00	0.00	0.00	0.00	0.00	0.00	0.00
Total	3.99	4.01	4.00	4.01	4.00	3.98	4.02	4.02	4.01	4.00	4.02	4.01	4.02	4.01	4.01
Cation ratios															
En	81.18	81.18	81.30	81.79	81.52	82.22	82.38	82.30	81.83	82.55	83.57	81.82	81.23	80.78	79.32
Fs	16.72	16.24	16.37	16.37	16.39	16.59	16.30	15.66	15.38	15.47	14.24	16.38	16.79	16.59	20.53
Wo	2.10	2.57	2.33	1.83	2.09	1.20	1.31	2.04	2.79	1.98	2.20	1.79	1.98	2.64	0.15
Mg#	82.92	83.33	83.24	83.32	83.26	83.21	83.48	84.02	84.18	84.22	85.44	83.32	82.87	82.96	79.44

Mineral	*ORTHOPYROXENE*																			
Drill core	**UMT-345**																		**UMT-094**	
Lithology	**UG-2 Chromitite**					**Olivine Gabbronorite**													**Wehrlite**	
Sample	**SD-25-1**	**SD-25-2**	**SD-25-3**	**SD-25-4**	**SD-25-5**	**SD-30-1**	**SD-30-2**	**SD-30-3**	**SD-30-4**	**SD-30-5**	**SD-30-6**	**SD-30-7**	**SD-30-8**	**SD-30-9**	**SD-30-10**	**SD-30-11**	**SD-30-12**	**SD-30-13**	**SD-50-1**	**SD-50-2**
SiO_2	52.70	55.66	55.76	55.34	56.22	54.53	54.37	54.54	54.13	54.10	54.31	54.19	54.34	54.49	54.28	54.07	54.62	54.95	55.31	54.83
TiO_2	0.02	0.22	0.15	0.13	0.15	0.12	0.12	0.11	0.11	0.10	0.11	0.12	0.11	0.11	0.12	0.12	0.14	0.08		
Al_2O_3	3.27	1.34	1.17	1.44	0.95	1.57	1.41	1.49	1.58	1.53	1.47	1.61	1.46	1.59	1.59	1.59	1.50	1.51	1.18	1.19
Cr_2O_3	0.68	0.47	0.44	0.44	0.35	0.35	0.36	0.31	0.37	0.43	0.34	0.46	0.43	0.44	0.45	0.48	0.44	0.30	0.27	0.30
MgO	31.85	30.91	30.90	31.66	31.07	28.79	29.14	29.28	29.43	29.44	29.70	27.78	28.29	28.41	28.42	28.66	29.10	29.75	29.69	29.42
MnO	0.10	0.09	0.05	0.09	0.06	0.26	0.27	0.28	0.27	0.29	0.27	0.24	0.26	0.25	0.24	0.26	0.27	0.27	0.29	0.28
FeO	10.88	10.13	10.17	9.61	10.27	12.43	12.89	12.83	12.97	12.89	12.72	11.82	12.47	12.03	12.05	12.52	12.67	12.79	12.29	12.50
CaO	0.24	0.97	1.11	1.16	0.70	2.42	1.32	1.11	1.02	1.01	0.82	3.62	2.77	2.58	2.70	2.16	1.81	0.81	0.98	1.11
Na_2O	0.05	0.00	0.02	0.02	0.04	0.03	0.02	0.01	0.01	0.02	0.01	0.05	0.03	0.04	0.03	0.04	0.03	0.01	0.01	0.01
Total	**99.79**	**99.79**	**99.77**	**99.89**	**99.79**	**100.49**	**99.90**	**99.97**	**99.88**	**99.80**	**99.76**	**99.91**	**100.16**	**99.94**	**99.87**	**99.89**	**100.58**	**100.47**	**100.02**	**99.64**
Cations (Calculated on the basis of 4 cations)																				
Si	1.87	1.96	1.97	1.95	1.98	1.97	1.97	1.98	1.97	1.97	1.97	1.97	1.97	1.98	1.97	1.97	1.97	1.98	1.99	1.98
Ti	0.00	0.01	0.00	0.00	0.00	0.00	0.00	0.00	0.00	0.00	0.00	0.00	0.00	0.00	0.00	0.00	0.00	0.00	0.00	0.00
Al	0.14	0.06	0.05	0.06	0.04	0.00	0.00	0.00	0.00	0.00	0.00	0.00	0.00	0.00	0.00	0.00	0.00	0.00	0.00	0.00
Cr	0.02	0.01	0.01	0.01	0.01	0.01	0.01	0.01	0.01	0.01	0.01	0.01	0.01	0.01	0.01	0.01	0.01	0.01	0.01	0.01
Fe	0.32	0.30	0.30	0.28	0.30	0.38	0.39	0.39	0.39	0.39	0.39	0.36	0.38	0.37	0.37	0.38	0.38	0.39	0.37	0.38
Mn	0.00	0.00	0.00	0.00	0.00	0.01	0.01	0.01	0.01	0.01	0.01	0.01	0.01	0.01	0.01	0.01	0.01	0.01	0.01	0.01
Mg	1.69	1.62	1.62	1.66	1.63	1.55	1.58	1.58	1.60	1.60	1.61	1.51	1.53	1.54	1.54	1.56	1.57	1.60	1.59	1.59
Ca	0.01	0.04	0.04	0.04	0.03	0.09	0.05	0.04	0.04	0.04	0.03	0.14	0.11	0.10	0.11	0.08	0.07	0.03	0.04	0.04
Na	0.00	0.00	0.00	0.00	0.00	0.00	0.00	0.00	0.00	0.00	0.00	0.00	0.00	0.00	0.00	0.00	0.00	0.00	0.00	0.00
Total	4.05	4.00	4.00	4.01	3.99	4.02	4.02	4.01	4.02	4.02	4.02	4.02	4.02	4.01	4.02	4.02	4.02	4.01	4.01	4.01
Cation ratios																				
En	83.54	82.89	82.62	83.57	83.23	76.77	78.08	78.54	78.61	78.73	79.36	75.05	75.89	76.77	76.55	76.97	77.58	79.32	79.62	79.02
Fs	16.02	15.24	15.25	14.24	15.44	18.59	19.37	19.31	19.43	19.33	19.07	17.91	18.76	18.23	18.22	18.86	18.95	19.13	18.49	18.84
Wo	0.45	1.88	2.13	2.20	1.34	4.64	2.55	2.15	1.96	1.94	1.58	7.04	5.35	5.01	5.23	4.17	3.47	1.54	1.89	2.14
Mg#	83.91	84.47	84.42	85.44	84.36	80.51	80.12	80.26	80.18	80.29	80.63	80.73	80.18	80.81	80.78	80.32	80.37	80.57	81.15	80.75

Mineral	*CLINOPYROXENE*															
Drill core	**UMT-335**															
Lithology	**Wehrlite**															
Sample	**SD 6-1**	**SD 6-2**	**SD 6-3**	**SD 6-4**	**SD 6-5**	**SD 6-6**	**SD 6-7**	**SD 6-8**	**SD 6-9**	**SD 6-10**	**SD 6-11**	**SD 6-12**	**SD 6-13**	**SD 6-14**	**SD-14- 1**	**SD-14-2**
SiO_2	53.41	52.68	54.78	53.24	52.76	52.68	54.18	54.58	52.86	52.36	52.78	53.61	59.45	53.24	50.72	50.81
TiO_2	0.18	0.37	0.05	0.42	0.43	0.53	0.29	0.06	0.27	0.24	0.35	0.23	0.05	0.40	0.55	0.54
Al_2O_3	2.17	2.56	0.30	2.37	2.67	2.52	1.63	0.64	2.45	2.76	2.65	1.22	0.27	1.96	5.16	5.08
Cr_2O_3	0.86	1.08	0.19	0.85	0.77	0.92	0.45	0.25	0.68	1.11	0.99	0.45	0.01	0.48	0.84	0.79
Fe_2O_3	0.52	0.78	0.33	0.91	0.88	0.84	0.68	0.44	1.13	0.99	0.78	0.45	0.32	0.47	1.07	1.07
FeO	8.78	5.36	3.92	5.15	4.80	5.18	4.60	3.84	4.62	5.15	5.89	5.52	3.83	5.27	4.52	4.38
MnO	0.21	0.15	0.18	0.20	0.22	0.15	0.17	0.18	0.18	0.20	0.19	0.22	0.11	0.20	0.15	0.14
MgO	20.53	15.89	16.75	15.59	15.79	15.56	15.54	16.64	15.62	15.39	16.30	16.79	23.36	16.38	13.88	13.79
CaO	13.12	20.74	23.39	20.82	21.18	21.17	22.13	23.18	21.68	21.42	19.65	21.23	12.45	21.26	22.55	22.85
Na_2O	0.26	0.43	0.14	0.50	0.49	0.52	0.36	0.18	0.53	0.47	0.43	0.21	0.12	0.32	0.62	0.61
Total	100.04	100.03	100.02	100.04	99.99	100.07	100.02	100.01	100.01	100.08	99.99	99.93	99.97	99.97	100.07	100.06
Cations (Calculated on the basis of 4 cations)																
Si	1.94	1.94	2.00	1.95	1.94	1.94	1.98	1.99	1.94	1.93	1.94	1.97	2.08	1.95	1.87	1.87
Ti	0.00	0.01	0.00	0.01	0.01	0.01	0.01	0.00	0.01	0.01	0.01	0.01	0.00	0.01	0.02	0.02
Al^{VI}	0.09	0.11	0.01	0.10	0.12	0.11	0.07	0.03	0.11	0.12	0.11	0.05	0.01	0.08	0.22	0.22
Al^{IV}	0.06	0.06	0.00	0.05	0.06	0.06	0.02	0.01	0.06	0.07	0.06	0.03	0.08	0.05	0.13	0.13
Cr	0.02	0.03	0.01	0.02	0.02	0.03	0.01	0.01	0.02	0.03	0.03	0.01	0.00	0.01	0.02	0.02
Fe^{3+}	0.01	0.02	0.01	0.03	0.02	0.02	0.02	0.01	0.03	0.03	0.02	0.01	0.01	0.01	0.03	0.03
Fe^{2+}	0.27	0.16	0.12	0.16	0.15	0.16	0.14	0.12	0.14	0.16	0.18	0.17	0.11	0.16	0.14	0.14
Mn	0.01	0.00	0.01	0.01	0.01	0.00	0.01	0.01	0.01	0.01	0.01	0.01	0.00	0.01	0.00	0.00
Mg	1.11	0.87	0.91	0.85	0.86	0.85	0.85	0.91	0.86	0.85	0.89	0.92	1.22	0.90	0.76	0.76
Ca	0.51	0.82	0.92	0.82	0.83	0.83	0.87	0.91	0.85	0.85	0.77	0.84	0.47	0.84	0.89	0.90
Na	0.02	0.03	0.01	0.04	0.03	0.04	0.03	0.01	0.04	0.03	0.03	0.01	0.01	0.02	0.04	0.04
Total	4.06	4.06	3.99	4.03	4.06	4.06	4.00	4.00	4.06	4.08	4.06	4.03	4.00	4.04	4.14	4.13
Cation ratios																
Wo	26.83	43.59	46.80	44.14	44.58	44.61	46.28	46.70	45.34	45.05	41.39	43.13	25.85	43.84	48.87	49.45
Ca-Tschermak	6.42	9.56	1.24	8.87	8.96	8.25	6.45	2.72	9.65	10.90	9.58	4.48	0.74	6.35	20.06	20.00
Mg#	79.83	82.36	87.64	82.32	83.42	82.37	84.17	87.51	83.16	81.96	81.50	83.46	90.99	83.68	81.85	82.15
$Fe^{3+}/\sum Fe$	0.05	0.12	0.07	0.14	0.14	0.13	0.12	0.09	0.18	0.15	0.11	0.07	0.07	0.07	0.18	0.18

Mineral	*CLINOPYROXENE*															
Drill core	**UMT-335**															
Lithology	**Wehrlite**															
Sample	**SD-14- 4**	**SD-14- 5**	**SD-14- 6**	**SD-14- 7**	**SD-14- 8**	**SD-14- 9**	**SD-14-10**	**SD-14-11**	**SD-15- 1**	**SD-15- 2**	**SD-15- 3**	**SD-17-1**	**SD-17-2**	**SD-17-3**	**SD-17-4**	**SD-17-5**
SiO_2	51.02	50.62	52.13	55.77	50.82	50.61	52.32	56.49	51.00	50.59	50.18	53.03	53.22	53.22	53.40	53.33
TiO_2	0.48	0.62	0.56	0.35	0.51	0.57	0.42	0.26	0.10	0.10	0.10	0.45	0.40	0.46	0.37	0.37
Al_2O_3	4.58	5.30	3.75	4.33	5.33	5.00	3.48	3.09	2.96	2.97	2.97	1.82	1.76	1.69	1.73	1.82
Cr_2O_3	0.83	0.88	0.39	0.43	0.97	0.90	0.48	0.76	0.79	0.93	1.08	0.86	0.94	1.00	1.00	0.95
Fe_2O_3	1.04	1.02	1.01	0.92	1.12	1.07	1.00	1.15	1.45	1.30	1.14	0.81	1.17	1.05	1.07	1.20
FeO	4.56	4.57	3.68	3.76	4.35	4.74	4.17	3.35	4.09	3.65	3.21	6.56	5.14	5.12	5.10	4.95
MnO	0.15	0.14	0.13	0.10	0.15	0.13	0.15	0.19	0.18	0.13	0.09	0.26	0.25	0.24	0.23	0.20
MgO	14.24	13.75	14.81	12.57	13.59	13.78	14.65	13.09	15.35	15.16	14.98	16.58	16.06	16.12	16.07	16.00
CaO	22.58	22.51	23.00	21.34	22.60	22.67	22.87	21.16	22.61	23.45	24.29	19.19	20.57	20.59	20.58	20.70
Na_2O	0.57	0.62	0.60	0.47	0.63	0.62	0.53	0.53	0.60	0.54	0.48	0.47	0.60	0.58	0.55	0.60
Total	100.05	100.03	100.05	100.04	100.07	100.09	100.07	100.08	99.12	98.82	98.52	100.05	100.08	100.07	100.09	100.10
Cations (Calculated on the basis of 4 cations)																
Si	1.88	1.87	1.91	2.01	1.87	1.87	1.92	2.04	1.90	1.90	1.89	1.95	1.96	1.96	1.96	1.96
Ti	0.01	0.02	0.02	0.01	0.01	0.02	0.01	0.01	0.00	0.00	0.00	0.01	0.01	0.01	0.01	0.01
Al^{VI}	0.20	0.23	0.16	0.18	0.23	0.22	0.15	0.13	0.13	0.13	0.13	0.08	0.08	0.07	0.07	0.08
Al^{IV}	0.12	0.13	0.09	0.01	0.13	0.13	0.08	0.04	0.10	0.10	0.11	0.05	0.04	0.04	0.04	0.04
Cr	0.02	0.03	0.01	0.01	0.03	0.03	0.01	0.02	0.02	0.03	0.03	0.03	0.03	0.03	0.03	0.03
Fe^{3+}	0.03	0.03	0.03	0.03	0.03	0.03	0.03	0.03	0.04	0.04	0.03	0.02	0.03	0.03	0.03	0.03
Fe^{2+}	0.14	0.14	0.11	0.11	0.13	0.15	0.13	0.10	0.13	0.11	0.10	0.20	0.16	0.16	0.16	0.15
Mn	0.00	0.00	0.00	0.00	0.00	0.00	0.00	0.01	0.01	0.00	0.00	0.01	0.01	0.01	0.01	0.01
Mg	0.78	0.76	0.81	0.68	0.75	0.76	0.80	0.70	0.85	0.85	0.84	0.91	0.88	0.88	0.88	0.88
Ca	0.89	0.89	0.90	0.83	0.89	0.90	0.90	0.82	0.90	0.94	0.97	0.76	0.81	0.81	0.81	0.81
Na	0.04	0.04	0.04	0.03	0.04	0.04	0.04	0.04	0.04	0.04	0.03	0.03	0.04	0.04	0.04	0.04
Total	4.13	4.14	4.09	3.91	4.13	4.14	4.08	3.93	4.13	4.14	4.15	4.05	4.05	4.04	4.04	4.04
Cation ratios																
Wo	48.36	49.01	48.75	50.31	49.47	48.97	48.44	49.44	46.93	48.54	50.01	40.01	43.08	43.12	43.16	43.43
Ca-Tschermak	17.96	20.50	14.75	17.42	19.13	19.46	14.01	14.53	11.41	12.17	12.69	6.05	6.28	5.86	5.64	5.98
Mg#	82.19	81.70	85.19	82.99	81.89	81.17	83.72	84.18	83.52	84.87	86.29	80.21	82.23	82.57	82.53	82.56
$Fe^{3+}/\sum Fe$	0.17	0.17	0.20	0.18	0.19	0.17	0.18	0.24	0.24	0.24	0.24	0.10	0.17	0.16	0.16	0.18

Mineral	*CLINOPYROXENE*															
Drill core	**UMT-335**					**UMT-345**					**UMT-094**					
Lithology	**Wehrlite**					**Olivine Gabbronoritel**					**Pegmatoidal Troctolite**					
Sample	**SD-17-6**	**SD-17-7**	**SD-17-8**	**SD-17-9**	**SD-17-10**	**SD-30-1**	**SD-30-2**	**SD-30-3**	**SD-30-4**	**SD-30-5**	**SD-48-1**	**SD-48-2**	**SD-48-3**	**SD-48-4**	**SD-48-5**	**SD-48-6**
SiO_2	53.79	53.11	53.06	54.58	53.88	51.61	51.70	51.87	52.26	52.15	52.12	54.92	52.30	53.87	54.53	54.21
TiO_2	0.40	0.43	0.35	0.06	0.30	0.21	0.24	0.27	0.23	0.19	0.17	0.20	0.26	0.20	0.21	0.37
Al_2O_3	1.33	2.17	2.27	0.86	1.35	2.57	2.61	2.43	2.26	1.63	2.20	1.57	2.99	2.51	2.04	2.64
Cr_2O_3	0.56	1.07	1.06	0.44	0.42	0.59	0.60	0.65	0.52	0.43	1.01	0.54	0.47	1.02	0.89	0.84
Fe_2O_3	0.83	1.20	1.54	0.81	0.93	0.73	0.77	0.55	0.41	0.57	0.78	0.24	0.47	0.85	0.75	0.47
FeO	4.78	4.99	4.60	2.90	4.29	5.24	5.40	6.15	7.64	4.64	5.28	8.27	5.48	4.12	5.12	6.47
MnO	0.24	0.27	0.25	0.19	0.22	0.17	0.15	0.17	0.21	0.14	0.18	0.20	0.31	0.20	0.24	0.26
MgO	16.31	15.54	15.47	16.80	16.28	15.79	16.53	17.06	19.33	16.50	17.24	21.98	21.17	18.11	17.88	17.85
CaO	21.34	20.72	20.81	23.08	21.94	22.48	20.27	20.04	16.83	22.81	20.32	12.04	17.03	19.41	18.32	17.48
Na_2O	0.47	0.61	0.73	0.32	0.47	0.36	0.39	0.32	0.25	0.30	0.36	0.14	0.26	0.41	0.37	0.33
Total	100.05	100.10	100.15	100.04	100.08	100.05	100.03	100.05	100.04	100.07	100.09	100.07	100.08	99.12	98.82	98.52
Cations (Calculated on the basis of 4 cations)																
Si	1.97	1.95	1.95	1.99	1.97	1.91	1.93	1.92	1.92	1.93	1.92	1.98	1.89	1.95	1.97	1.96
Ti	0.01	0.01	0.01	0.00	0.01	0.01	0.01	0.01	0.01	0.01	0.00	0.01	0.01	0.01	0.01	0.01
Al^{VI}	0.06	0.09	0.10	0.04	0.06	0.11	0.11	0.11	0.10	0.07	0.10	0.07	0.13	0.11	0.09	0.11
Al^{IV}	0.03	0.05	0.05	0.01	0.03	0.09	0.07	0.08	0.08	0.07	0.08	0.02	0.11	0.05	0.03	0.04
Cr	0.02	0.03	0.03	0.01	0.01	0.02	0.02	0.02	0.02	0.01	0.03	0.02	0.01	0.03	0.03	0.02
Fe^{3+}	0.02	0.03	0.04	0.02	0.03	0.02	0.02	0.02	0.01	0.02	0.02	0.01	0.01	0.02	0.02	0.01
Fe^{2+}	0.15	0.15	0.14	0.09	0.13	0.16	0.17	0.19	0.23	0.14	0.16	0.25	0.17	0.12	0.16	0.20
Mn	0.01	0.01	0.01	0.01	0.01	0.01	0.00	0.01	0.01	0.00	0.01	0.01	0.01	0.01	0.01	0.01
Mg	0.89	0.85	0.85	0.91	0.89	0.87	0.92	0.94	1.06	0.91	0.95	1.18	1.14	0.97	0.97	0.96
Ca	0.84	0.82	0.82	0.90	0.86	0.89	0.81	0.79	0.66	0.91	0.80	0.46	0.66	0.75	0.71	0.68
Na	0.03	0.04	0.05	0.02	0.03	0.03	0.03	0.02	0.02	0.02	0.03	0.01	0.02	0.03	0.03	0.02
Total	4.02	4.04	4.05	4.01	4.03	4.12	4.09	4.10	4.11	4.09	4.10	4.00	4.15	4.05	4.00	4.02
Cation ratios																
Wo	44.14	44.01	44.27	46.83	45.15	45.83	42.21	40.93	33.68	45.81	41.49	24.46	33.33	40.09	38.39	36.65
Ca-Tschermak	4.63	8.04	8.72	3.70	5.05	9.80	9.13	8.24	6.90	6.23	7.80	4.06	9.08	8.20	6.58	7.93
Mg#	84.01	82.02	82.17	89.19	85.00	82.67	82.86	82.07	81.14	85.09	83.70	82.21	86.48	86.87	84.63	82.19
$Fe^{3+}/\sum Fe$	0.14	0.18	0.23	0.20	0.16	0.11	0.11	0.07	0.05	0.10	0.12	0.03	0.07	0.16	0.12	0.06

Mineral	*CLINOPYROXENE*															
Drill core	**UMT-094**															
Lithology	**Wehrlite**															
Sample	**SD-48-7**	**SD-48-8**	**SD-48-9**	**SD-48-10**	**SD-48-11**	**SD-50-1**	**SD-50-2**	**SD-50-3**	**SD-50-4**	**SD-50-5**	**SD-50-6**	**SD-50-7**	**SD-50-8**	**SD-54-1**	**SD-54-2**	**SD-54-3**
SiO_2	54.50	54.69	54.07	54.67	54.74	50.28	51.65	51.03	49.70	49.40	52.15	51.78	50.85	54.79	52.54	50.75
TiO_2	0.38	0.16	0.35	0.32	0.22									0.10	0.91	0.66
Al_2O_3	2.45	2.18	2.70	1.75	1.89	5.03	3.14	3.80	5.18	5.24	2.25	2.50	3.68	0.66	2.98	4.70
Cr_2O_3	1.01	0.92	1.08	0.51	0.65	0.81	0.54	0.63	1.02	1.01	0.81	0.88	0.56	0.00	0.01	0.45
Fe_2O_3	0.80	0.89	0.76	0.34	0.75	1.44	1.19	1.29	1.29	1.16	1.00	1.19	1.13	0.05	0.78	0.44
FeO	5.98	5.08	4.73	4.16	4.29	3.31	2.68	3.04	3.49	3.59	4.73	4.44	2.97	3.56	3.18	3.22
MnO	0.20	0.22	0.25	0.16	0.07	0.10	0.10	0.11	0.10	0.09	0.16	0.15	0.09	0.13	0.07	0.07
MgO	17.14	16.82	16.13	16.06	16.03	14.71	15.69	15.44	14.49	14.48	16.23	15.88	15.30	18.71	16.04	14.88
CaO	17.88	19.51	20.23	22.26	21.68	23.57	24.18	23.77	23.69	23.86	21.94	22.33	24.13	21.61	25.79	24.85
Na_2O	0.43	0.39	0.43	0.25	0.35	0.56	0.46	0.50	0.50	0.45	0.39	0.46	0.44	0.02	0.05	0.42
Total	100.76	100.86	100.74	100.48	100.67	99.81	99.63	99.61	99.46	99.28	99.66	99.61	99.15	99.63	102.35	100.44
Cations (Calculated on the basis of 4 cations)																
Si	1.97	1.98	1.96	1.98	1.98	1.86	1.91	1.89	1.85	1.84	1.93	1.92	1.89	1.99	1.91	1.86
Ti	0.01	0.00	0.01	0.01	0.01	0.00	0.00	0.00	0.00	0.00	0.00	0.00	0.00	0.00	0.02	0.02
Al^{VI}	0.10	0.09	0.12	0.07	0.08	0.22	0.14	0.17	0.23	0.23	0.10	0.11	0.16	0.03	0.13	0.20
Al^{IV}	0.03	0.02	0.04	0.02	0.02	0.14	0.09	0.11	0.15	0.16	0.07	0.08	0.11	0.01	0.09	0.14
Cr	0.03	0.03	0.03	0.01	0.02	0.02	0.02	0.02	0.03	0.03	0.02	0.03	0.02	0.00	0.00	0.01
Fe^{3+}	0.02	0.02	0.02	0.01	0.02	0.04	0.03	0.04	0.04	0.03	0.03	0.03	0.03	0.00	0.02	0.01
Fe^{2+}	0.18	0.15	0.14	0.13	0.13	0.10	0.08	0.09	0.11	0.11	0.15	0.14	0.09	0.11	0.10	0.10
Mn	0.01	0.01	0.01	0.00	0.00	0.00	0.00	0.00	0.00	0.00	0.01	0.00	0.00	0.00	0.00	0.00
Mg	0.92	0.91	0.87	0.87	0.87	0.81	0.86	0.85	0.80	0.81	0.90	0.88	0.85	1.01	0.87	0.81
Ca	0.69	0.76	0.79	0.86	0.84	0.93	0.96	0.94	0.94	0.95	0.87	0.89	0.96	0.84	1.00	0.98
Na	0.03	0.03	0.03	0.02	0.02	0.04	0.03	0.04	0.04	0.03	0.03	0.03	0.03	0.00	0.00	0.03
Total	4.00	4.00	4.01	3.99	3.99	4.18	4.13	4.15	4.19	4.20	4.09	4.11	4.15	4.00	4.15	4.17
Cation ratios																
Wo	38.07	41.07	43.13	46.28	45.31	49.48	49.41	48.98	49.89	50.10	44.85	45.83	49.72	42.83	50.43	51.37
Ca-Tschermak	7.62	7.48	9.15	6.09	6.81	20.60	13.38	15.94	21.43	21.85	8.90	10.15	15.70	2.21	9.78	17.69
Mg#	82.01	83.61	84.14	86.50	85.19	85.05	88.18	86.76	84.74	84.79	83.71	83.71	87.24	90.24	88.04	87.99
$Fe^{3+}/\sum Fe$	0.11	0.14	0.13	0.07	0.14	0.28	0.28	0.28	0.25	0.23	0.16	0.19	0.26	0.01	0.18	0.11

Mineral	*CLINOPYROXENE*															
Drill core	**UMT-335**															
Lithology	**Wehrlite**															
Sample	**SD-54-4**	**SD-54-5**	**SD-54-6**	**SD-54-7**	**SD-54-8**	**SD-54-9**	**SD-54-10**	**SD-54-11**	**SD-54-12**	**SD-54-13**	**SD-54-14**	**SD-54-15**	**SD-54-16**	**SD-56-1**	**SD-56-2**	**SD-56-3**
SiO_2	50.61	50.28	49.88	50.39	50.02	49.56	49.59	49.71	49.53	49.66	49.19	49.15	48.65	49.51	49.77	50.09
TiO_2	0.56	0.41	0.67	0.44	0.54	0.56	0.54	0.81	0.69	0.70	0.60	0.78	0.73	1.74	0.47	0.65
Al_2O_3	5.04	5.15	5.80	5.46	5.67	6.28	5.91	6.27	6.23	6.31	6.43	6.91	7.51	5.27	5.72	5.71
Cr_2O_3	0.89	1.18	0.67	1.07	1.10	0.94	1.05	0.48	0.87	0.85	0.95	0.80	0.68	0.00	1.01	0.83
Fe_2O_3	0.78	0.96	0.59	0.93	0.72	0.75	0.83	0.43	0.60	0.61	0.82	0.69	0.60	1.51	0.95	0.73
FeO	2.95	3.13	3.43	3.24	3.27	3.50	3.30	3.76	3.64	3.64	3.46	3.64	4.04	4.67	3.30	3.22
MnO	0.09	0.10	0.08	0.09	0.09	0.07	0.08	0.08	0.09	0.08	0.08	0.10	0.11	0.07	0.11	0.07
MgO	14.60	14.24	14.21	14.21	14.16	14.06	13.99	13.98	13.97	13.97	13.77	13.77	13.45	14.88	14.24	14.18
CaO	24.38	24.24	24.31	24.24	24.47	24.26	24.11	24.43	24.32	24.19	24.26	24.33	23.99	25.45	24.20	24.30
Na_2O	0.52	0.53	0.49	0.53	0.49	0.51	0.53	0.48	0.50	0.50	0.55	0.57	0.51	0.09	0.55	0.53
Total	100.42	100.22	100.13	100.59	100.53	100.50	99.92	100.42	100.44	100.50	100.11	100.74	100.27	103.18	100.31	100.31
Cations (Calculated on the basis of 4 cations)																
Si	1.86	1.85	1.84	1.85	1.84	1.82	1.83	1.83	1.82	1.82	1.82	1.80	1.79	1.82	1.83	1.84
Ti	0.02	0.01	0.02	0.01	0.01	0.02	0.02	0.02	0.02	0.02	0.02	0.02	0.02	0.05	0.01	0.02
Al^{VI}	0.22	0.22	0.25	0.24	0.25	0.27	0.26	0.27	0.27	0.27	0.28	0.30	0.33	0.23	0.25	0.25
Al^{IV}	0.14	0.15	0.16	0.15	0.16	0.18	0.17	0.17	0.18	0.18	0.18	0.20	0.21	0.18	0.17	0.16
Cr	0.03	0.03	0.02	0.03	0.03	0.03	0.03	0.01	0.03	0.02	0.03	0.02	0.02	0.00	0.03	0.02
Fe^{3+}	0.02	0.03	0.02	0.03	0.02	0.02	0.02	0.01	0.02	0.02	0.02	0.02	0.02	0.04	0.03	0.02
Fe^{2+}	0.09	0.10	0.11	0.10	0.10	0.11	0.10	0.12	0.11	0.11	0.11	0.11	0.12	0.14	0.10	0.10
Mn	0.00	0.00	0.00	0.00	0.00	0.00	0.00	0.00	0.00	0.00	0.00	0.00	0.00	0.00	0.00	0.00
Mg	0.80	0.78	0.78	0.78	0.78	0.77	0.77	0.77	0.77	0.77	0.76	0.75	0.74	0.81	0.78	0.78
Ca	0.96	0.96	0.96	0.95	0.96	0.96	0.95	0.96	0.96	0.95	0.96	0.96	0.95	1.00	0.96	0.96
Na	0.04	0.04	0.03	0.04	0.03	0.04	0.04	0.03	0.04	0.04	0.04	0.04	0.04	0.01	0.04	0.04
Total	4.17	4.17	4.19	4.18	4.19	4.21	4.19	4.20	4.21	4.20	4.21	4.23	4.24	4.29	4.20	4.18
Cation ratios																
Wo	51.28	51.39	51.53	51.37	51.81	51.52	51.60	51.85	51.72	51.59	51.95	51.97	51.84	50.04	51.21	51.64
Ca-Tschermak	19.14	20.12	21.63	20.96	21.65	23.73	22.56	22.85	23.21	23.23	24.50	25.53	27.36	16.67	22.18	21.38
Mg#	87.70	86.42	86.48	86.16	86.56	85.71	86.06	85.75	85.63	85.63	85.39	85.21	83.96	81.49	85.95	86.69
$Fe^{3+}/\sum Fe$	0.19	0.22	0.13	0.20	0.17	0.16	0.18	0.09	0.13	0.13	0.18	0.15	0.12	0.23	0.21	0.17

Mineral	*CLINOPYROXENE*										
Drill core	**UMT-094**										
Lithology	**Wehrlite**										
Sample	**SD-56-5**	**SD-56-6**	**SD-56-7**	**SD-56-8**	**SD-56-9**	**SD-56-10**	**SD-56-11**	**SD-56-12**	**SD-56-13**	**SD-56-14**	**SD-56-15**
SiO_2	50.11	49.55	49.53	49.49	47.37	47.73	47.29	47.10	48.48	46.55	46.04
TiO_2	0.46	1.20	0.62	0.54	0.90	1.77	1.69	1.39	1.49	1.19	1.56
Al_2O_3	5.52	6.21	5.93	5.87	7.49	6.82	7.45	8.26	8.13	9.60	9.56
Cr_2O_3	1.03	0.03	1.02	1.11	0.02	0.00	0.02	0.00	0.01	0.00	0.00
Fe_2O_3	0.98	0.35	0.72	0.79	0.02	1.28	1.12	0.49	0.69	0.39	0.66
FeO	3.17	4.63	3.40	3.35	5.69	5.77	5.91	5.32	6.19	5.28	5.70
MnO	0.10	0.06	0.08	0.11	0.12	0.08	0.08	0.07	0.07	0.07	0.05
MgO	14.14	14.05	14.04	14.01	13.71	13.61	13.36	13.34	12.86	12.83	12.77
CaO	24.08	24.79	24.43	24.29	22.43	25.01	25.09	24.27	24.30	24.30	24.26
Na_2O	0.56	0.33	0.52	0.51	0.33	0.19	0.22	0.35	0.31	0.31	0.35
Total	100.15	101.20	100.29	100.07	98.08	102.26	102.23	100.59	102.53	100.52	100.95
Cations (Calculated on the basis of 4 cations)											
Si	1.85	1.82	1.83	1.83	1.79	1.77	1.76	1.75	1.78	1.73	1.72
Ti	0.01	0.03	0.02	0.02	0.03	0.05	0.05	0.04	0.04	0.03	0.04
Al^{VI}	0.24	0.27	0.26	0.26	0.33	0.30	0.33	0.36	0.35	0.42	0.42
Al^{IV}	0.15	0.18	0.17	0.17	0.21	0.23	0.24	0.25	0.22	0.27	0.28
Cr	0.03	0.00	0.03	0.03	0.00	0.00	0.00	0.00	0.00	0.00	0.00
Fe^{3+}	0.03	0.01	0.02	0.02	0.00	0.04	0.03	0.01	0.02	0.01	0.02
Fe^{2+}	0.10	0.14	0.10	0.10	0.18	0.18	0.18	0.17	0.19	0.16	0.18
Mn	0.00	0.00	0.00	0.00	0.00	0.00	0.00	0.00	0.00	0.00	0.00
Mg	0.78	0.77	0.77	0.77	0.77	0.75	0.74	0.74	0.70	0.71	0.71
Ca	0.95	0.98	0.96	0.96	0.91	1.00	1.00	0.97	0.95	0.97	0.97
Na	0.04	0.02	0.04	0.04	0.02	0.01	0.02	0.03	0.02	0.02	0.03
Total	4.18	4.22	4.21	4.20	4.25	4.33	4.35	4.32	4.28	4.33	4.36
Cation ratios											
Wo	51.33	51.43	51.84	51.73	48.80	50.68	51.12	51.28	51.15	52.20	51.68
Ca-Tschermak	21.25	21.44	22.65	22.62	25.87	22.68	25.36	28.47	26.49	33.05	32.42
Mg#	86.16	83.50	86.07	86.02	81.07	77.80	77.48	80.51	77.09	80.24	78.34
$Fe^{3+}/\sum Fe$	0.22	0.06	0.16	0.18	0.00	0.17	0.15	0.08	0.09	0.06	0.09

Mineral	*CLINOPYROXENE*									
Drill core	**UMT-094**									
Lithology	**Wehrlite**									
Sample	**SD-56-16**	**SD-56-17**	**SD-56-18**	**SD-56-19**	**SD-57-1**	**SD-57-2**	**SD-57-3**	**SD-57-4**	**SD-57-5**	**SD-57-6**
SiO_2	46.31	46.04	45.75	45.98	48.29	47.83	47.67	47.05	47.51	47.25
TiO_2	1.56	1.78	1.86	1.81	0.40	0.40	0.40	0.40	0.40	0.40
Al_2O_3	9.58	9.46	9.51	9.60	4.80	5.34	5.53	6.11	6.06	6.16
Cr_2O_3	0.01	0.01	0.00	0.02	0.89	0.83	0.60	0.61	0.62	0.53
Fe_2O_3	0.59	0.75	0.93	0.80	0.06	0.09	0.09	0.09	0.10	0.12
FeO	5.63	5.80	5.97	5.73	4.19	4.58	4.55	4.94	4.97	4.94
MnO	0.07	0.07	0.08	0.05	0.06	0.06	0.06	0.06	0.07	0.06
MgO	12.70	12.59	12.52	12.51	14.71	14.46	14.45	14.20	14.09	13.96
CaO	24.38	24.24	24.17	24.28	26.00	26.00	26.00	26.00	26.00	26.00
Na_2O	0.37	0.40	0.36	0.39	0.13	0.11	0.11	0.11	0.11	0.10
Total	101.20	101.14	101.15	101.18	99.54	99.70	99.47	99.58	99.93	99.53
Cations (Calculated on the basis of 4 cations)										
Si	1.72	1.72	1.71	1.71	1.81	1.79	1.79	1.77	1.78	1.78
Ti	0.04	0.05	0.05	0.05	0.01	0.01	0.01	0.01	0.01	0.01
Al^{VI}	0.42	0.42	0.42	0.42	0.21	0.24	0.24	0.27	0.27	0.27
Al^{IV}	0.28	0.28	0.29	0.29	0.19	0.21	0.21	0.23	0.22	0.22
Cr	0.00	0.00	0.00	0.00	0.03	0.02	0.02	0.02	0.02	0.02
Fe^{3+}	0.02	0.02	0.03	0.02	0.00	0.00	0.00	0.00	0.00	0.00
Fe^{2+}	0.17	0.18	0.19	0.18	0.13	0.14	0.14	0.16	0.16	0.16
Mn	0.00	0.00	0.00	0.00	0.00	0.00	0.00	0.00	0.00	0.00
Mg	0.70	0.70	0.70	0.70	0.82	0.81	0.81	0.80	0.79	0.78
Ca	0.97	0.97	0.97	0.97	1.04	1.04	1.05	1.05	1.04	1.05
Na	0.03	0.03	0.03	0.03	0.01	0.01	0.01	0.01	0.01	0.01
Total	4.36	4.37	4.38	4.37	4.26	4.28	4.29	4.31	4.30	4.30
Cation ratios										
Wo	52.03	51.78	51.53	51.96	52.23	52.25	52.29	52.33	52.48	52.68
Ca-Tschermak	32.44	31.64	31.58	31.97	19.25	21.08	21.74	23.59	23.58	24.07
Mg#	78.61	77.60	76.63	77.54	86.07	84.67	84.76	83.43	83.23	83.13
$Fe^{3+}/\sum Fe$	0.09	0.10	0.12	0.11	0.01	0.02	0.02	0.02	0.02	0.02

Mineral	*CLINOPYROXENE*									
Drill core	**UMT-335**					**UMT-345**				
Lithology	**Lower Chromitite seam**					**UG-2 Chromitite**				
Sample	**SD-09-1**	**SD-09-2**	**SD-09-3**	**SD-09-4**	**SD-09-5**	**SD-25-1**	**SD-25-2**	**SD-25-3**	**SD-25-4**	**SD-25-5**
SiO_2	52.21	51.77	51.96	52.26	51.28	51.48	52.93	51.66	51.80	51.79
TiO_2	0.25	0.26	0.23	0.25	0.10	0.12	0.26	0.26	0.22	0.22
Al_2O_3	2.18	2.36	2.29	2.03	2.76	2.58	1.22	2.01	2.28	2.22
Cr_2O_3	0.93	0.95	1.09	0.95	0.90	0.94	0.45	0.89	0.96	1.00
Fe_2O_3	0.81	0.79	0.93	0.74	1.46	1.32	0.59	0.64	0.83	0.84
FeO	3.89	3.63	3.19	2.96	3.78	3.22	2.00	2.64	3.18	2.85
MnO	0.14	0.12	0.13	0.12	0.18	0.16	0.08	0.14	0.14	0.13
MgO	17.25	16.25	16.67	16.85	15.49	15.62	17.26	16.91	16.90	16.64
CaO	21.64	22.86	22.78	23.13	22.78	23.40	24.44	23.45	22.58	23.09
Na_2O	0.41	0.40	0.45	0.38	0.60	0.55	0.33	0.34	0.41	0.41
Total	99.72	99.41	99.71	99.65	99.33	99.40	99.56	98.95	99.31	99.19
Cations (Calculated on the basis of 4 cations)										
Si	1.92	1.92	1.92	1.92	1.91	1.91	1.94	1.92	1.91	1.92
Ti	0.01	0.01	0.01	0.01	0.00	0.00	0.01	0.01	0.01	0.01
Al^{VI}	0.09	0.10	0.10	0.09	0.12	0.11	0.05	0.09	0.10	0.10
Al^{IV}	0.08	0.08	0.08	0.08	0.09	0.09	0.06	0.08	0.09	0.08
Cr	0.03	0.03	0.03	0.03	0.03	0.03	0.01	0.03	0.03	0.03
Fe^{3+}	0.02	0.02	0.03	0.02	0.04	0.04	0.02	0.02	0.02	0.02
Fe^{2+}	0.12	0.11	0.10	0.09	0.12	0.10	0.06	0.08	0.10	0.09
Mn	0.00	0.00	0.00	0.00	0.01	0.00	0.00	0.00	0.00	0.00
Mg	0.95	0.90	0.92	0.92	0.86	0.87	0.94	0.93	0.93	0.92
Ca	0.85	0.91	0.90	0.91	0.91	0.93	0.96	0.93	0.89	0.92
Na	0.03	0.03	0.03	0.03	0.04	0.04	0.02	0.02	0.03	0.03
Total	4.10	4.11	4.11	4.10	4.13	4.12	4.08	4.12	4.11	4.11
Cation ratios										
Wo	43.94	46.80	46.38	46.82	47.16	48.17	48.46	47.39	45.93	47.06
Ca-Tschermak	7.88	9.03	8.80	7.74	11.22	4.54	4.54	7.83	8.73	8.68
Mg#	86.94	86.96	88.08	89.23	84.44	86.33	92.39	90.36	88.47	89.16
$Fe^{3+}/\sum Fe$	0.16	0.16	0.21	0.18	0.26	0.27	0.21	0.18	0.19	0.21

Mineral	*PLAGIOCLASE*													
Drill core	**UMT_335**													
Lithology	**UG-2 Chromitite**				**Wehrlite (Footwall assimilation Zone)**									
Sample	**SD-02-1**	**SD-02-2**	**SD-02-3**	**SD-02-4**	**SD-06-1**	**SD-06-2**	**SD-15B-1**	**SD-17-1**	**SD-17-2**	**SD-17-3**	**SD-17-4**	**SD-17-5**	**SD-17-6**	**SD-17-7**
SiO_2	50.57	51.52	49.22	52.37	52.27	51.76	47.60	57.89	57.16	59.79	57.57	57.90	57.55	58.93
TiO_2	0.01	0.03	0.01	0.04	0.02	0.07	0.10	0.05	0.03	0.08	0.07	0.04	0.03	0.06
Al_2O_3	29.80	31.42	32.42	28.49	29.04	28.94	31.12	24.52	25.22	25.96	24.65	24.54	24.79	23.99
Cr_2O_3	0.11	0.03	0.00	0.03	0.00	0.03	0.01	0.03	0.06	0.03	0.03	0.02	0.04	0.06
MgO	0.05	0.02	0.00	0.01	0.03	0.00	0.15	0.01	0.03	0.00	0.01	0.00	0.02	0.01
MnO	0.01	0.00	0.00	0.00	0.00	0.01	0.01	0.00	0.00	0.00	0.03	0.00	0.00	0.03
FeO	0.20	0.15	0.10	0.13	0.21	0.20	0.87	0.14	0.13	0.17	0.15	0.16	0.23	0.12
CaO	12.63	12.06	14.07	13.71	11.35	11.46	15.27	7.21	7.88	7.23	7.42	7.31	7.33	6.49
Na_2O	4.10	4.28	3.82	4.45	4.66	4.52	2.72	7.34	6.73	6.78	7.14	7.28	7.24	7.67
K_2O	0.23	0.18	0.32	0.37	0.34	0.48	0.01	0.23	0.31	0.22	0.36	0.26	0.25	0.42
Total	97.70	99.68	99.96	99.60	97.92	97.46	97.86	97.42	97.54	100.27	97.43	97.51	97.46	97.77
Cations (Calculated on the basis of 6 cations)														
Si	2.40	2.41	2.42	2.43	2.44	2.43	2.18	2.66	2.62	2.65	2.64	2.65	2.64	2.69
Ti	0.00	0.00	0.00	0.00	0.00	0.00	0.00	0.00	0.00	0.00	0.00	0.00	0.00	0.00
Al	1.56	1.57	1.59	1.56	1.54	1.55	1.43	1.33	1.36	1.36	1.33	1.33	1.34	1.29
Cr	0.00	0.00	0.00	0.00	0.00	0.00	0.00	0.00	0.00	0.00	0.00	0.00	0.00	0.00
Fe	0.01	0.01	0.00	0.00	0.01	0.01	0.00	0.00	0.00	0.01	0.01	0.01	0.01	0.00
Mn	0.00	0.00	0.00	0.00	0.00	0.00	0.00	0.00	0.00	0.00	0.00	0.00	0.00	0.00
Mg	0.00	0.00	0.00	0.00	0.00	0.00	0.00	0.00	0.00	0.00	0.00	0.00	0.00	0.00
Ca	0.64	0.61	0.58	0.58	0.57	0.58	1.48	0.35	0.39	0.34	0.37	0.36	0.36	0.32
Na	0.38	0.39	0.36	0.40	0.42	0.41	0.00	0.65	0.60	0.58	0.64	0.65	0.64	0.68
K	0.01	0.01	0.02	0.02	0.02	0.03	0.00	0.01	0.02	0.01	0.02	0.02	0.01	0.02
Cation ratios														
An	62.12	60.21	60.26	57.97	56.23	56.72	100.00	34.72	38.56	36.57	35.72	35.17	35.37	31.10
Ab	36.52	38.71	37.64	39.87	41.76	40.44	0.00	63.97	59.63	62.09	62.22	63.36	63.22	66.49
Or	1.36	1.09	2.09	2.16	2.01	2.83	0.00	1.31	1.81	1.34	2.06	1.48	1.41	2.40

Mineral	*PLAGIOCLASE*														
Drill core	UMT_335					UMT-094									
Lithology	Lower Chromitite seam					UG-2 Chromitite					Olivine Gabbronorite				
Sample	SD-09-1	SD-09-2	SD-09-3	SD-09-4	SD-09-5	SD-25-1	SD-25-2	SD-25-3	SD-25-4	SD-25-5	SD-30-1	SD-30-2	SD-30-3	SD-30-4	SD-30-5
SiO_2	50.32	50.86	51	51	51	50.57	50.32	50.86	51	51	48.01	47.89	49.74	48.83	48.97
TiO_2	0.01	0.00	0	0	0	0.02	0.01	0.00	0	0	0.03	0.01	0.03	0.00	0.02
Al_2O_3	29.40	29.81	29	29	29	29.33	29.40	29.81	29	29	31.53	31.33	30.33	31.04	30.51
Cr_2O_3	0.00	0.06	0	0	0	0.17	0.00	0.06	0	0	0.01	0.01	0.01	0.01	0.01
MgO	0.03	0.02	0	0	0	0.04	0.03	0.02	0	0	0.02	0.04	0.04	0.04	0.04
MnO	0.01	0.00	0	0	0	0.01	0.01	0.00	0	0	0.00	0.00	0.00	0.00	0.00
FeO	0.24	0.14	0.35	0.43	0.42	0.29	0.24	0.14	0.35	0.43	0.35	0.43	0.42	0.42	0.43
CaO	13.48	13.51	13	13	13	13.27	13.48	13.51	13	13	15.86	15.88	14.57	15.40	14.87
Na_2O	3.94	4.03	4	4	5	4.19	3.94	4.03	4	4	2.67	2.55	3.24	2.79	3.06
K_2O	0.32	0.07	0	0	0	0.01	0.32	0.07	0	0	0.09	0.21	0.34	0.29	0.27
Total	97.74	98.50	97.85	98.27	98.32	97.91	97.74	98.50	97.85	98.27	98.57	98.35	98.72	98.82	98.17
Cations (Calculated on the basis of 6 cations)															
Si	2.35	2.35	2.35	2.36	2.36	2.35	2.35	2.35	2.35	2.36	2.23	2.24	2.30	2.26	2.28
Ti	0.00	0.00	0.00	0.00	0.00	0.00	0.00	0.00	0.00	0.00	0.00	0.00	0.00	0.00	0.00
Al	1.62	1.62	1.61	1.60	1.60	1.61	1.62	1.62	1.61	1.60	1.73	1.72	1.66	1.70	1.68
Cr	0.00	0.00	0.01	0.01	0.02	0.01	0.00	0.00	0.01	0.01	0.00	0.00	0.00	0.00	0.00
Fe	0.01	0.01	0.02	0.01	0.01	0.01	0.01	0.01	0.02	0.01	0.01	0.02	0.01	0.01	0.02
Mn	0.00	0.00	0.00	0.00	0.00	0.00	0.00	0.00	0.00	0.00	0.00	0.00	0.00	0.00	0.00
Mg	0.00	0.00	0.00	0.00	0.01	0.00	0.00	0.00	0.00	0.00	0.00	0.00	0.00	0.00	0.00
Ca	0.67	0.67	0.65	0.64	0.64	0.66	0.67	0.67	0.65	0.64	0.79	0.79	0.72	0.77	0.74
Na	0.36	0.36	0.40	0.41	0.42	0.38	0.36	0.36	0.40	0.41	0.24	0.23	0.29	0.25	0.28
K	0.02	0.00	-0.02	-0.03	0.01	0.00	0.02	0.00	-0.02	-0.03	0.01	0.01	0.02	0.02	0.02
Cation ratios															
An	64.26	64.70	63.47	63.12	62.77	63.56	64.26	64.70	63.47	63.12	76.24	76.58	69.92	74.07	71.76
Ab	33.95	34.89	37.49	38.70	39.93	36.36	33.95	34.89	37.49	38.70	23.26	22.24	28.12	24.28	26.71
Or	1.79	0.41	0.00	0.00	0.00	0.08	1.79	0.41	0.00	0.00	0.49	1.18	1.97	1.65	1.53

Mineral	*PLAGIOCLASE*									
Drill core	**UMT-345**				**UMT-094**					
Lithology	**Olivine Gabbronorite**				**Pegmatoidal Troctolite**					
Sample	**SD-30-6**	**SD-30-7**	**SD-30-8**	**SD-30-9**	**SD-48-1**	**SD-48-2**	**SD-48-3**	**SD-48-4**	**SD-48-5**	**SD-48-6**
SiO_2	48.66	49.29	47.54	48.05	49.46	49.34	50.99	48.92	49.43	49.76
TiO_2	0.02	0.01	0.00	0.02	0.02	0.02	0.02	0.03	0.02	0.02
Al_2O_3	31.12	30.12	31.37	31.29	30.61	30.96	29.88	30.87	30.60	30.36
Cr_2O_3	0.00	0.00	0.00	0.01	0.00	0.00	0.00	0.01	0.00	0.00
MgO	0.04	0.03	0.04	0.04	0.02	0.01	0.01	0.03	0.01	0.02
MnO	0.01	0.01	0.01	0.01	0.01	0.01	0.00	0.02	0.00	0.01
FeO	0.41	0.37	0.40	0.40	0.20	0.17	0.20	0.19	0.19	0.19
CaO	15.51	14.51	15.84	15.63	14.65	14.88	13.52	15.00	14.71	14.56
Na_2O	2.76	3.22	2.55	2.66	3.18	3.18	3.84	3.01	3.21	3.32
K_2O	0.23	0.29	0.17	0.20	0.29	0.21	0.34	0.28	0.22	0.32
Total	98.75	97.84	97.93	98.32	98.44	98.81	98.81	98.36	98.39	98.55
Cations (Calculated on the basis of 6 cations)										
Si	2.26	2.30	2.23	2.24	2.30	2.28	2.35	2.28	2.30	2.31
Ti	0.00	0.00	0.00	0.00	0.00	0.00	0.00	0.00	0.00	0.00
Al	1.70	1.66	1.73	1.72	1.68	1.69	1.62	1.69	1.68	1.66
Cr	0.00	0.00	0.00	0.00	0.00	0.00	0.00	0.00	0.00	0.00
Fe	0.01	0.01	0.01	0.01	0.01	0.01	0.01	0.01	0.01	0.01
Mn	0.00	0.00	0.00	0.00	0.00	0.00	0.00	0.00	0.00	0.00
Mg	0.00	0.00	0.00	0.00	0.00	0.00	0.00	0.00	0.00	0.00
Ca	0.77	0.73	0.80	0.78	0.73	0.74	0.67	0.75	0.73	0.72
Na	0.25	0.29	0.23	0.24	0.29	0.29	0.34	0.27	0.29	0.30
K	0.01	0.02	0.01	0.01	0.02	0.01	0.02	0.02	0.01	0.02
Cation ratios										
An	74.66	70.16	76.65	75.58	70.58	71.22	64.73	72.21	70.80	69.51
Ab	24.01	28.17	22.35	23.26	27.76	27.57	33.30	26.20	27.94	28.69
Or	1.33	1.66	1.00	1.16	1.67	1.20	1.97	1.59	1.26	1.80

Appendix C: Whole-rock major geochemistry data

.

Lithology abbreviations

FPXY	Feldspathic pyroxenite
UG-2 CHRM	UG2 chromitite
CHRM	Lower chromitite seam
WEHR	Wehrlite
SERP	Serpentinite
OL-GBN	Olivine gabbronorite
TROCT	Pegmatoidal Troctolite
PPX	Parapyroxenite
Skarn	Calc-silicate skarn

Sample	*SD-01*	*SD-02*	*SD-03*	*SD-04*	*SD-05*	*SD-06*	*SD-07*	*SD-08*	*SD-09*	*SD-10*
Depth	**1715.50**	**1718.00**	**1720.75**	**1723.75**	**1726.30**	**1726.80**	**1729.50**	**1733.00**	**1734.60**	**1737.20**
Drill core	**UMT-335**	**UMT-335**	**UMT-335**	**UMT-335**	**UMT-335**	**UMT-335**	**UMT-335**	**UMT-335**	**UMT-335**	**UMT-335**
Lithology	**FPXY**	**UG-2 CHRM**	**FPXY**	**FPXY**	**Skarn**	**WEHR**	**WEHR**	**FPXY**	**CHRM**	**FPXY**
Al2O3	4.84	14.87	2.29	5.24	16.86	5.23	9.82	6.06	5.81	11.81
CaO	3.91	2.80	2.20	3.88	18.55	10.24	13.11	4.79	3.28	6.96
Cr2O3	0.50	21.91	0.46	0.47	0.19	0.74	0.74	0.42	3.90	0.80
Fe2O3	10.22	22.79	13.30	10.73	4.82	15.44	9.27	10.87	13.61	9.18
K2O	0.07	0.00	0.17	0.07	1.29	0.19	0.18	0.09	0.06	0.19
MgO	25.64	13.87	26.49	24.99	8.42	22.07	16.33	23.67	24.39	17.86
MnO	0.19	0.21	0.24	0.20	0.12	0.21	0.16	0.20	0.20	0.16
Na2O	0.47	0.99	0.24	0.48	0.75	0.65	1.19	0.61	0.41	1.29
P2O5	0.01	0.00	0.02	0.00	0.01	0.03	0.01	0.01	0.01	0.01
SiO2	53.98	21.80	54.31	53.77	48.76	44.96	48.96	53.13	48.15	51.60
TiO2	0.16	0.74	0.27	0.15	0.22	0.24	0.22	0.14	0.18	0.14
Total	100	100	100	100	100	100	100	100	100	100
Total LOI	0.06	BDL	0.82	0.17	2.06	1.39	0.82	0.19	-0.03	0.17
Ba	24.30	24.30	19.60	30.40	439.90	91.60	70.10	38.50	23.20	76.30
Be	0.08	0.10	0.16	0.11	0.20	0.15	0.19	0.10	0.07	0.17
Ce	2.14	2.27	5.15	2.45	8.98	9.98	7.87	2.61	1.81	4.77
Co	84.07	187.00	101.59	87.10	32.56	187.00	88.54	88.62	141.12	80.89
Cr	3868.00	4500.00	3542.00	3741.00	1535.00	4500.00	4500.00	3214.00	4500.00	4500.00
Cs	1.24	0.46	1.58	1.17	1.84	1.61	1.62	1.55	0.67	1.02
Cu	89.10	961.80	46.90	68.80	142.70	1701.50	633.70	196.10	1044.80	409.20
Dy	0.66	0.26	1.08	0.60	1.58	1.94	1.73	0.60	0.43	0.52
Er	0.46	0.23	0.83	0.46	0.81	1.03	0.98	0.42	0.33	0.41
Eu	0.18	0.16	0.13	0.17	0.53	0.53	0.53	0.18	0.10	0.31
Ga	5.65	40.20	4.51	5.62	12.88	6.09	9.34	5.76	9.90	9.45
Gd	0.45	0.28	0.98	0.53	1.57	2.11	1.88	0.51	0.30	0.58
Hf	0.22	0.20	1.11	0.19	0.63	0.74	0.50	0.21	0.16	0.31
Ho	0.15	0.08	0.25	0.14	0.32	0.40	0.35	0.13	0.10	0.13
La	1.00	1.20	2.40	1.20	4.00	4.00	3.00	1.50	0.90	2.60
Li	7.30	7.00	3.70	5.90	28.60	8.60	13.40	7.50	5.30	8.20
Lu	0.09	0.04	0.14	0.08	0.11	0.12	0.13	0.08	0.05	0.07
Mo	0.40	0.83	0.32	0.43	0.24	0.43	0.30	0.39	0.44	0.43
Nb	0.16	0.41	1.61	0.16	0.40	0.62	0.22	0.11	0.14	0.60
Nd	1.46	1.10	2.99	1.39	6.07	7.27	5.70	1.44	0.98	2.54
Ni	583.80	1818.60	580.60	547.60	218.90	3413.40	909.50	494.20	2128.10	662.80
Pb	1.12	6.25	1.45	3.49	8.92	52.59	9.19	4.16	4.74	3.12
Pr	0.26	0.29	0.67	0.33	1.28	1.53	1.26	0.33	0.24	0.58
Rb	2.32	1.64	10.85	2.57	75.00	8.10	6.80	3.44	1.36	4.78
Sc	26.00	14.70	31.40	25.30	30.70	34.40	39.70	27.80	24.40	22.90
Sm	0.36	0.25	0.78	0.40	1.44	2.00	1.49	0.34	0.22	0.54
Sr	65.90	82.40	11.80	70.20	348.60	95.80	185.50	85.60	53.00	188.60
Ta	0.01	0.02	0.10	0.01	0.03	0.04	0.01	0.01	0.01	0.04
Tb	0.09	0.04	0.16	0.09	0.25	0.32	0.28	0.09	0.06	0.09
Th	0.09	0.12	0.96	0.08	0.34	0.49	0.16	0.10	0.07	0.52
Ti	1052.00	4488.00	1701.00	949.00	1416.00	1399.00	1495.00	907.00	1185.00	806.00
Tl	0.04	0.07	0.14	0.04	0.25	0.12	0.08	0.06	0.09	0.07
Tm	0.07	0.04	0.13	0.07	0.11	0.13	0.14	0.07	0.06	0.05
U	0.02	0.03	0.24	0.03	0.12	0.12	0.05	0.03	0.02	0.17
V	108.30	370.00	123.50	100.10	135.20	168.60	183.70	100.80	234.40	110.70
Y	4.09	1.99	7.06	3.68	8.15	10.16	10.05	3.44	3.17	3.51
Yb	0.48	0.22	0.87	0.55	0.69	0.91	0.89	0.51	0.38	0.41
Zn	74.2	419.2	83.1	80.6	62	97.9	70.6	71.6	120.8	67.1
Zr	7	6	51	7	20	24	15	7	6	12

Sample	*SD-11*	*SD-12*	*SD-13*	*SD-14*	*SD-15*	*SD-16*	*SD-17*	*SD-18*	*SD-19*	*SD-20*
Depth	**1740.00**	**1743.10**	**1745.50**	**1747.90**	**1752.60**	**1755.90**	**1759.10**	**1760.20**	**1762.20**	**1765.40**
Drill core	**UMT-335**	**UMT-335**	**UMT-335**	**UMT-335**	**UMT-335**	**UMT-335**	**UMT-335**	**UMT-335**	**UMT-335**	**UMT-335**
Lithology	**PPX**	**PPX**	**Skarn**	**WEHR**	**WEHR**	**WEHR**	**WEHR**	**Skarn**	**PPX**	**FPXY**
Al2O3	14.63	14.87	23.83	5.95	9.04	2.20	3.87	11.04	15.79	6.71
CaO	12.33	17.06	19.18	12.42	8.38	8.98	14.65	23.09	20.45	4.37
Cr2O3	0.21	0.13	0.00	2.96	0.92	0.52	0.42	0.12	0.16	0.28
Fe2O3	11.84	5.77	9.58	16.47	16.08	16.09	13.97	11.85	7.65	15.42
K2O	0.51	0.94	0.02	0.05	0.15	0.16	0.06	0.04	1.14	0.23
MgO	12.26	9.74	6.60	19.63	22.67	24.95	20.60	9.11	7.19	21.73
MnO	0.10	0.14	0.17	0.22	0.27	0.24	0.23	0.17	0.14	0.21
Na2O	1.51	1.61	0.08	0.25	0.70	0.44	0.43	0.12	0.55	0.71
P2O5	0.02	0.02	0.09	0.03	0.01	0.04	0.03	0.02	0.04	0.01
SiO2	46.43	49.49	40.45	41.60	41.64	46.14	45.40	43.70	46.61	50.19
TiO2	0.16	0.25	0.01	0.42	0.15	0.25	0.32	0.74	0.30	0.14
	100	100	100	100	100	100	100	100	100	100
Total LOI	3.08	2.31	6.35	3.21	3.03	4.18	1.79	0.70	1.78	1.85
Ba	186.00	257.50	7.50	22.40	165.10	57.30	40.30	23.80	636.80	97.80
Be	0.12	0.32	0.41	0.08	0.13	0.19	0.16	0.26	0.21	0.12
Ce	8.26	15.55	6.30	9.62	5.92	10.49	11.76	7.42	9.18	2.59
Co	128.23	50.34	20.82	123.74	138.53	150.53	128.99	112.79	58.78	144.68
Cr	1702.00	1031.00	10.00	4500.00	4500.00	3934.00	3148.00	901.00	1168.00	2088.00
Cs	2.80	2.44	0.48	1.35	3.37	4.52	2.05	0.51	2.89	7.08
Cu	426.60	976.10	7.30	710.70	852.90	784.80	1433.40	1952.40	910.20	603.30
Dy	1.41	1.87	0.65	1.81	0.75	2.07	1.63	1.07	1.58	0.50
Er	0.84	1.09	0.38	1.20	0.46	1.26	1.03	0.62	0.89	0.42
Eu	0.56	0.74	0.10	0.48	0.34	0.37	0.45	0.34	0.49	0.28
Ga	10.52	11.40	15.52	10.87	8.67	4.13	5.67	13.40	13.43	6.95
Gd	1.41	2.02	0.67	1.65	0.78	1.91	1.48	1.08	1.48	0.34
Hf	0.38	0.70	0.14	0.91	0.25	0.59	0.91	3.20	0.76	0.14
Ho	0.28	0.41	0.13	0.38	0.17	0.46	0.37	0.21	0.32	0.12
La	3.80	7.70	3.40	3.70	3.00	4.30	5.50	3.00	3.90	1.60
Li	22.30	48.00	45.90	9.30	8.90	12.20	13.50	31.70	33.40	17.70
Lu	0.10	0.15	0.02	0.17	0.08	0.20	0.17	0.12	0.13	0.08
Mo	0.47	0.33	0.36	0.36	0.30	0.36	0.38	0.57	1.58	0.33
Nb	0.36	0.94	0.47	0.76	0.27	1.19	0.81	0.75	0.41	0.19
Nd	4.96	7.84	2.93	6.31	3.19	6.70	6.33	4.69	5.24	1.14
Ni	1516.40	468.90	72.80	1119.50	1139.40	1579.40	1427.50	1979.60	857.00	1395.90
Pb	11.91	29.71	0.83	9.47	14.18	15.63	22.05	44.43	33.77	13.27
Pr	1.10	1.96	0.73	1.46	0.69	1.45	1.59	1.08	1.24	0.27
Rb	19.93	63.82	0.53	2.81	5.09	10.64	2.98	2.22	85.65	10.88
Sc	18.20	26.90	1.10	26.80	17.40	40.30	34.00	62.20	24.90	21.60
Sm	1.20	1.83	0.52	1.53	0.66	1.65	1.32	0.96	1.27	0.31
Sr	429.20	463.70	28.00	73.80	434.00	54.10	155.60	144.30	333.50	149.30
Ta	0.03	0.08	0.01	0.07	0.02	0.09	0.10	0.08	0.04	0.01
Tb	0.23	0.30	0.10	0.30	0.13	0.32	0.27	0.16	0.24	0.08
Th	0.38	0.83	0.40	0.74	0.20	1.13	0.95	0.61	0.44	0.13
Ti	998.00	1581.00	91.00	2456.00	870.00	1498.00	1982.00	4477.00	1825.00	889.00
Tl	0.30	0.16	0.01	0.10	0.16	0.24	0.10	0.10	0.40	0.48
Tm	0.11	0.16	0.04	0.17	0.07	0.18	0.16	0.08	0.12	0.07
U	0.09	0.17	0.13	0.19	0.06	0.29	0.21	0.17	0.09	0.06
V	99.00	137.70	7.00	358.10	159.80	159.20	176.50	208.30	144.40	87.00
Y	8.16	10.97	4.61	10.71	4.54	11.62	10.08	5.36	8.94	3.49
Yb	0.71	0.98	0.17	1.12	0.44	1.27	1.10	0.65	0.86	0.54
Zn	65.4	67.4	60.2	191.5	140.4	135.9	104.6	121.8	80.6	124.4
Zr	14	27	6	32	9	25	34	86	28	6

Sample	*SD-21*	*SD-22*	*SD-23*	*SD-24*	*SD-25*	*SD-26*	*SD-27*	*SD-28*	*SD-29*	*SD-30*
Depth	**1524.90**	**1525.20**	**1531.10**	**1517.8**	**1521.1**	**1523.5**	**1526.2**	**1529.9**	**1531.9**	**1537.5**
Drill core	**UMT-335**	**UMT-335**	**UMT-335**	**UMT-345**	**UMT-345**	**UMT-345**	**UMT-345**	**UMT-345**	**UMT-345**	**UMT-345**
Lithology	**SERP**	**SERP**	**FPXY**	**FPXY**	**UG-2 CHRM**	**SERP**	**SERP**	**SERP**	**Skarn**	**OL-GBN**
Al2O3	2.33	2.12	4.97	6.97	13.37	2.23	4.81	6.53	7.81	22.46
CaO	0.90	1.45	4.01	6.18	2.13	3.22	4.74	4.19	5.03	16.85
Cr2O3	0.83	0.41	0.42	0.38	25.19	0.17	0.31	0.05	0.36	0.04
Fe2O3	19.68	15.95	11.89	16.45	26.75	14.09	13.50	14.44	11.19	8.42
K2O	0.44	0.27	0.10	0.24	0.00	0.04	0.32	0.20	0.10	0.37
MgO	33.42	32.85	24.49	19.35	14.40	34.04	26.29	31.07	22.28	6.22
MnO	0.16	0.19	0.22	0.17	2.33	0.19	0.26	0.20	0.20	0.42
Na2O	0.14	0.15	0.53	0.88	0.00	0.22	0.40	0.38	0.61	1.06
P2O5	0.01	0.01	0.02	0.02	0.01	0.01	0.01	0.01	0.01	0.01
SiO2	41.95	46.50	53.17	49.16	16.46	45.69	49.24	42.88	52.30	44.07
TiO2	0.12	0.10	0.17	0.19	-0.65	0.10	0.12	0.04	0.12	0.08
Total	100	100	100	100	100	100	100	100	100	100
Total LOI	8.26	6.01	0.02	1.79	BDL	8.69	3.12	8.24	0.17	3.16
Ba	34.50	32.20	41.10	41.9	5.6	2.8	41.3	20.9	29	142.2
Be	0.06	0.05	0.14	0.18	0.05	0.07	0.09	0.08	0.08	0.21
Ce	1.92	1.85	4.47	7.17	2.08	3.68	3.55	2.81	2.24	5.15
Co	187.00	187.00	99.16	187	187	187	105.21	168.83	87.17	34.69
Cr	4500.00	2997.00	3382.00	2791	4500	1218	2324	403	2707	307
Cs	6.13	4.32	1.40	0.933	1.618	1.372	3.374	3.678	0.683	2.165
Cu	1723.00	1563.60	162.60	2900	682.1	384.2	244.7	106.9	359.2	489.7
Dy	0.29	0.29	0.79	0.871	0.564	0.69	0.427	0.238	0.36	0.392
Er	0.20	0.29	0.55	0.593	0.333	0.404	0.364	0.125	0.307	0.212
Eu	0.07	0.08	0.20	0.2329	0.1047	0.1543	0.1305	0.1504	0.1213	0.3221
Ga	3.70	2.98	5.40	6.59	41.68	2.2	4.6	4.05	6.77	14.76
Gd	0.22	0.28	0.64	0.794	0.476	0.663	0.371	0.176	0.294	0.418
Hf	0.14	0.20	0.33	0.41	0.28	0.25	0.2	0.15	0.18	0.3
Ho	0.06	0.08	0.17	0.1963	0.1092	0.1485	0.0953	0.0479	0.0787	0.0862
La	0.90	0.90	2.20	3.9	0.8	1.4	1.6	1.4	1.2	2.7
Li	6.20	4.90	9.50	6	17.3	7.4	31.8	14.8	5.5	43.5
Lu	0.03	0.04	0.10	0.083	0.049	0.063	0.057	0.02	0.049	0.034
Mo	0.22	0.21	0.49	0.59	0.7	0.25	0.28	0.3	0.8	0.66
Nb	0.29	0.21	0.33	1.258	0.322	0.176	0.41	0.185	0.257	0.446
Nd	0.78	0.92	2.25	3.59	1.45	2.37	1.55	1.14	1.23	2.11
Ni	4100.00	4100.00	497.80	4100	1638.9	3151.7	1022.6	1632.8	507.2	443.4
Pb	3.80	3.58	2.63	8.6	4.24	9.15	5.65	8.3	3.58	22.16
Pr	0.25	0.24	0.56	0.887	0.334	0.544	0.397	0.256	0.269	0.571
Rb	37.31	19.83	3.48	12.24	2.06	2.54	20.96	9.53	2.56	11.14
Sc	11.00	15.30	29.40	27	19.8	19.4	24.4	9.1	25.5	7.9
Sm	0.21	0.29	0.47	0.735	0.287	0.621	0.286	0.187	0.305	0.459
Sr	8.90	10.30	65.10	78.5	25.5	10.8	48.5	62	109.8	416.6
Ta	0.02	0.01	0.02	0.098	0.018	0.015	0.021	0.012	0.015	0.029
Tb	0.03	0.05	0.12	0.1337	0.0801	0.1016	0.068	0.0312	0.0504	0.0584
Th	0.24	0.21	0.25	1.05	0.093	0.127	0.357	0.142	0.196	0.377
Ti	661.00	565.00	1159.00	1152	3802	529	725	294	759	480
Tl	0.45	0.24	0.06	0.147	0.068	0.206	0.221	0.167	0.02	0.112
Tm	0.04	0.04	0.10	0.0888	0.0479	0.0567	0.0585	0.0216	0.0466	0.0323
U	0.10	0.06	0.07	0.454	0.032	0.075	0.09	0.065	0.043	0.081
V	84.10	70.80	112.90	94.1	370	57.8	89.8	28.3	91.6	37.8
Y	1.82	2.18	5.19	5.48	3.06	3.87	2.74	1.2	2.37	2.42
Yb	0.24	0.30	0.58	0.604	0.302	0.366	0.341	0.161	0.323	0.195
Zn	157.1	97.7	75.6	83.2	510	96.5	134.8	87.2	77.8	147.8

Sample	*SD-31*	*SD-32*	*SD-33*	*SD-34*	*SD-35*	*SD-36*	*SD-37*	*SD-38*	*SD-39*	*SD-40*
Depth	**1538.9**	**1543.6**	**1547.2**	**1553.3**	**1561**	**1567.4**	**1575**	**1583.2**	**1584.6**	**1595.3**
Drill core	**UMT-345**	**UMT-345**	**UMT-345**	**UMT-345**	**UMT-345**	**UMT-345**	**UMT-345**	**UMT-345**	**UMT-345**	**UMT-345**
Lithology	**OL-GBN**	**OL-GBN**	**OL-GBN**	**OL-GBN**	**FPXY**	**FPXY**	**FPXY**	**FPXY**	**FPXY**	**FPXY**
Al2O3	3.76	6.86	6.78	4.07	5.63	3.15	5.64	8.77	15.08	6.16
CaO	9.81	8.42	8.71	5.51	4.46	4.54	4.92	6.16	9.44	4.87
Cr2O3	0.43	0.54	0.41	0.52	0.64	0.44	0.67	0.45	0.22	0.40
Fe2O3	12.50	16.50	13.23	12.60	11.55	14.77	13.04	11.64	12.05	12.46
K2O	0.06	0.10	0.06	0.05	0.04	0.04	0.03	0.07	0.17	0.08
MgO	23.20	23.16	25.37	24.46	24.52	24.99	23.47	20.58	12.01	22.89
MnO	0.21	0.22	0.17	0.22	0.23	0.26	0.23	0.21	0.13	0.21
Na2O	0.26	0.41	0.59	0.33	0.43	0.26	0.45	0.72	1.81	0.61
P2O5	0.01	0.01	0.01	0.00	0.00	0.00	0.00	0.00	0.01	0.00
SiO2	49.60	43.65	44.58	52.06	52.35	51.36	51.39	51.27	48.95	52.15
TiO2	0.15	0.14	0.10	0.17	0.14	0.18	0.15	0.12	0.12	0.16
Total	100	100	100	100	100	100	100	100	100	100
Total LOI	0.59	5.17	4.31	0.39	0.29	0.48	0.01	0.13	1.29	0.08
Ba	24.6	36	18	13.7	14.3	17.4	12.6	27.3	95.9	31.3
Be	0.04	0.11	0.06	0.05	0.06	0.08	0.04	0.06	0.18	0.09
Ce	2.98	4.53	2.1	2.77	1.1	2.39	0.96	1.77	4.89	2.35
Co	121.21	186.7	154.19	116.17	99.44	157.75	128.52	112.59	187	117.69
Cr	3318	4089	3194	4079	4500	3324	4500	3600	1741	3067
Cs	0.643	0.22	0.196	0.071	0.018	0.072	0.075	0.099	0.161	0.172
Cu	959.8	2703.7	1168.5	1244.1	719.9	1927.6	1184.1	925.6	2041.2	851.4
Dy	0.975	0.696	0.602	0.751	0.407	0.713	0.469	0.447	0.563	0.528
Er	0.577	0.455	0.42	0.477	0.385	0.618	0.398	0.403	0.371	0.458
Eu	0.2293	0.2355	0.1724	0.1499	0.1039	0.1661	0.106	0.1325	0.3568	0.183
Ga	4.3	5.8	5.5	5.23	6.2	5.03	6.2	7.46	11.97	6.63
Gd	0.846	0.724	0.566	0.66	0.328	0.603	0.306	0.308	0.584	0.449
Hf	0.26	0.35	0.19	0.29	0.14	0.26	0.14	0.14	0.19	0.2
Ho	0.2061	0.1481	0.1208	0.172	0.1039	0.1954	0.107	0.1033	0.1305	0.1375
La	1.2	2.3	0.9	1.1	0.5	0.9	0.4	1	2.6	1.2
Li	2.5	7.6	5.6	3.9	2.8	3.5	2.8	3.5	4.9	4.5
Lu	0.08	0.063	0.056	0.076	0.077	0.093	0.071	0.066	0.069	0.077
Mo	0.41	0.3	0.34	0.44	0.71	0.7	0.57	0.97	0.45	0.56
Nb	0.26	0.668	0.093	0.253	0.086	0.269	0.074	0.149	0.175	0.136
Nd	2.34	2.66	1.59	1.73	0.78	1.65	0.7	0.95	2.35	1.35
Ni	1065	2338.2	1492.3	1255.3	1244.4	2110.5	1962.5	1149.4	4100	1279.3
Pb	13.52	15.37	8.89	8.55	5.35	10.13	8.73	10.12	28.6	9.05
Pr	0.459	0.589	0.299	0.394	0.139	0.363	0.16	0.22	0.557	0.291
Rb	2.05	2.37	0.84	1.16	0.33	1.19	0.28	0.83	2.3	0.97
Sc	41.9	25.7	24.9	33.8	25	28.2	27.5	27.1	20.8	29.9
Sm	0.725	0.56	0.507	0.492	0.136	0.491	0.274	0.214	0.454	0.371
Sr	43	83.8	95.3	42.7	67.3	30.3	72.3	143.1	285.5	101.5
Ta	0.015	0.04	0.007	0.013	0.007	0.013	0.007	0.007	0.01	0.007
Tb	0.1434	0.1297	0.0963	0.115	0.0588	0.1016	0.0601	0.0629	0.091	0.0976
Th	0.241	0.494	0.066	0.144	0.023	0.119	0.042	0.095	0.125	0.086
Ti	988	830	599	1090	890	1128	900	788	819	998
Tl	0.057	0.142	0.042	0.044	0.023	0.06	0.035	0.035	0.109	0.049
Tm	0.0866	0.0668	0.052	0.0738	0.0583	0.0809	0.0533	0.0627	0.0584	0.0677
U	0.051	0.119	0.016	0.05	0.012	0.04	0.011	0.022	0.032	0.022
V	137.7	97.8	80.1	113.3	92.1	104.9	99.6	88	69	95.2
Y	5.18	4.56	3.65	4.52	2.71	4.52	3.09	2.88	3.49	3.99
Yb	0.566	0.426	0.341	0.516	0.422	0.607	0.413	0.381	0.383	0.505
Zn	82.8	111.5	82.2	96.3	94.8	106.1	101.2	92	60	92.4
Zr	7	13	6	9	6	8	6	6	6	6

Sample	*SD-41*	*SD-42*	*SD-43*	*SD-44*	*SD-45*	*SD-46*	*SD-47*	*SD-48*	*SD-49*	*SD-50*	*SD-51*
Depth	**1331.4**	**1334.7**	**1336.9**	**1341.8**	**1347.3**	**1348.5**	**1354.1**	**1360.3**	**1362.3**	**1365.7**	**1372.3**
Drill core	**UMT-094**	**UMT-094**	**UMT-094**	**UMT-094**	**UMT-094**	**UMT-094**	**UMT-094**	**UMT-094**	**UMT-094**	**UMT-094**	**UMT-094**
Lithology	**FPXY**	**WEHR**	**FPXY**	**FPXY**	**FPXY**	**FPXY**	**TROCT**	**TROCT**	**WEHR**	**WEHR**	**WEHR**
Al2O3	5.68	7.26	7.04	6.39	5.20	5.56	6.68	3.91	2.95	6.70	5.68
CaO	5.43	4.14	8.49	5.78	4.96	5.40	4.90	6.00	13.91	12.44	5.43
Cr2O3	0.45	0.12	0.70	0.84	1.21	0.75	0.67	1.06	0.88	4.53	0.45
Fe2O3	12.19	15.94	12.68	12.35	14.47	14.88	13.13	18.66	11.82	14.46	12.19
K2O	0.10	0.07	0.12	0.11	0.07	0.08	0.07	0.13	0.18	0.02	0.10
MgO	22.50	27.58	21.02	21.96	23.79	25.17	25.67	28.25	24.15	22.57	22.50
MnO	0.22	0.21	0.20	0.22	0.23	0.23	0.24	0.22	0.18	0.19	0.22
Na2O	0.58	0.60	0.73	0.58	0.44	0.51	0.54	0.45	0.40	0.27	0.58
P2O5	0.03	0.01	0.01	0.01	0.01	0.01	0.01	0.02	0.01	0.01	0.03
SiO2	52.65	44.01	48.85	51.61	49.45	47.28	47.98	41.12	45.20	38.53	52.65
TiO2	0.17	0.06	0.17	0.16	0.17	0.13	0.11	0.18	0.32	0.28	0.17
Total	100	100	100	100	100	100	100	100	100	100	100
Total LOI	0.03	0.30	0.40	-0.17	0.19	1.01	2.01	6.44	2.28	3.36	0.03
Ba	51.1	24.5	36.6	35.1	25.1	22.8	27.5	56.6	6.2	4.8	2.7
Be	0.12	0.08	0.12	0.1	0.07	0.07	0.09	0.11	0.11	0.11	0.37
Ce	4.3	1.39	4.06	3.51	2.58	2.49	1.65	5.23	13.52	9.24	13.78
Co	108.19	187	140.54	119.3	147.28	148.25	115.46	187	117.26	115.39	93.86
Cr	3460	977	4500	4500	4500	4500	4500	4500	4500	4500	4082
Cs	0.143	0.115	0.503	0.522	0.433	0.052	0.048	0.331	0.684	0.182	0.111
Cu	555.4	1758.9	1191.3	954.9	1010.2	1081.3	156.4	2632.2	801	495.6	553.1
Dy	0.625	0.188	0.856	0.618	0.547	0.565	0.374	0.811	1.812	1.412	1.717
Er	0.435	0.128	0.534	0.476	0.403	0.382	0.248	0.495	1.079	0.882	0.983
Eu	0.214	0.1238	0.2303	0.1898	0.133	0.1437	0.1347	0.2565	0.5398	0.3908	0.4322
Ga	6.1	5.72	7.53	7.34	6.72	6.03	6.49	5.57	6.23	11.46	5.34
Gd	0.56	0.154	0.784	0.545	0.564	0.494	0.273	0.86	1.966	1.488	1.642
Hf	0.27	0.14	0.33	0.24	0.23	0.18	0.14	0.33	1.27	0.49	1.01
Ho	0.1442	0.0438	0.1919	0.1469	0.1363	0.1266	0.0808	0.1682	0.3726	0.2931	0.3259
La	2.3	0.7	1.7	1.5	1.3	1	0.9	2.6	5.1	3.7	6.3
Li	3.5	5.1	5.6	3.7	3.2	4.7	8.1	5.9	6.8	4.6	1
Lu	0.077	0.031	0.075	0.086	0.066	0.069	0.048	0.064	0.146	0.105	0.126
Mo	0.59	0.68	0.53	0.61	0.54	0.44	0.45	0.31	0.53	0.53	0.24
Nb	0.341	0.127	0.292	0.221	0.211	0.157	0.112	0.42	0.407	0.354	0.886
Nd	2.23	0.59	2.59	1.85	1.65	1.54	0.94	2.67	8.13	5.33	7.28
Ni	1250.4	3263.4	2192.5	1378.4	1884.3	2170.2	1118.6	4100	1625.8	849.4	912.3
Pb	3.41	8.13	5.42	4.48	5.67	8.12	2.85	13.03	9.44	6.58	4.45
Pr	0.541	0.175	0.576	0.462	0.391	0.354	0.25	0.706	1.934	1.361	1.762
Rb	1.92	0.93	4.21	3.25	1.59	1.01	1.02	4.11	7.68	0.64	0.4
Sc	32.9	12.3	32.6	30.1	27.1	22.7	20.3	20.1	26.9	27.9	17.2
Sm	0.459	0.091	0.68	0.5	0.429	0.575	0.273	0.809	2.007	1.36	1.716
Sr	82.7	119.1	110.4	94.2	75.6	88.1	117.6	69.6	38.7	52.3	38.5
Ta	0.021	0.007	0.018	0.014	0.012	0.01	0.007	0.027	0.037	0.04	0.082
Tb	0.1011	0.0213	0.1455	0.0932	0.0877	0.0845	0.0531	0.1239	0.2991	0.2801	0.2537
Th	0.332	0.115	0.232	0.174	0.14	0.126	0.091	0.343	0.396	0.432	0.959
Ti	1026	380	1026	964	957	797	637	1053	1961	1607	1595
Tl	0.027	0.03	0.042	0.042	0.037	0.035	0.012	0.141	0.33	0.047	0.1
Tm	0.0676	0.0218	0.0854	0.0739	0.07	0.0608	0.0361	0.0783	0.1578	0.124	0.1325
U	0.082	0.021	0.056	0.046	0.04	0.031	0.023	0.087	0.08	0.068	0.118
V	123.6	45.3	139.6	142.3	156.3	111	88.7	143.1	138.3	259.7	68.3
Y	4.28	1.17	5.05	3.8	3.54	3.47	2.31	4.65	10.24	8.15	9.65
Yb	0.515	0.177	0.554	0.507	0.436	0.423	0.315	0.482	0.968	0.717	0.829
Zn	85.5	113.3	87.8	99.3	109.3	109.1	105.9	175.8	87.3	156.4	31.4
Zr	10	6	11	8	7	6	6	12	40	22	34

Sample	*SD-52*	*SD-53*	*SD-54*	*SD-55*	*SD-56*	*SD-57*	*SD-58*	*SD-59*	*SD-60*	*SD-61*
Depth	**1375.8**	**1385.9**	**1390.3**	**1395.2**	**1400.1**	**1402.9**	**1409.9**	**1415.4**	**1417.1**	**1423.2**
Drill core	**UMT-094**	**UMT-094**	**UMT-094**	**UMT-094**	**UMT-094**	**UMT-094**	**UMT-094**	**UMT-094**	**UMT-094**	**UMT-094**
Lithology	**WEHR**	**WEHR**	**WEHR**	**WEHR**	**WEHR**	**WEHR**	**WEHR**	**Skarn**	**Skarn**	**Skarn**
Al2O3	4.10	12.56	16.25	19.42	14.89	1.92	15.74	12.98	13.19	7.78
CaO	14.32	6.41	13.27	11.03	14.79	5.43	23.67	13.96	25.29	14.87
Cr2O3	0.20	0.02	0.01	0.01	4.03	0.33	0.04	0.00	0.01	0.01
Fe2O3	13.44	11.98	10.80	11.85	12.20	16.02	9.34	6.13	5.42	6.15
K2O	0.12	0.14	0.15	0.27	0.04	0.03	0.02	0.02	0.01	0.02
MgO	22.40	28.26	19.28	21.18	17.91	34.27	14.45	29.00	18.69	35.91
MnO	0.19	0.16	0.14	0.18	0.17	0.16	0.07	0.04	0.38	0.14
Na2O	0.45	0.48	0.43	0.40	0.30	0.12	0.09	0.02	0.02	0.02
P2O5	0.01	0.01	0.03	0.02	0.01	0.01	0.04	0.00	0.01	0.00
SiO2	44.47	39.95	39.17	35.26	35.25	41.54	36.06	37.65	36.59	35.00
TiO2	0.30	0.02	0.47	0.37	0.43	0.16	0.47	0.19	0.39	0.10
Total	100	100	100	100	100	100	100	100	100	100
Total LOI	3.60	7.07	3.93	6.89	1.43	8.71	2.47	11.30	7.69	13.36
Ba	74.8	83.9	163.5	83.1	6.1	11.9	10.8	0.9	1	0.8
Be	0.11	0.06	0.19	0.12	0.12	0.05	0.18	1.18	1.84	0.22
Ce	9.22	2.36	14.03	9.1	11.89	4.24	18.38	20.63	34	2.56
Co	182.47	89.8	99.6	100.35	93.97	187	108.11	28.31	17.08	40.35
Cr	1537	186	94	50	4500	2363	328	20	100	52
Cs	0.592	0.91	1.524	2.452	0.501	0.137	0.133	0.013	0.013	0.013
Cu	2425.5	417.4	841.7	382.8	341.5	1029.7	2623.8	10.1	1059.6	54.1
Dy	1.887	0.11	1.967	1.405	2.016	0.888	2.264	1.235	2.065	0.915
Er	1.179	0.069	1.217	0.83	1.26	0.57	1.332	0.567	1.309	0.831
Eu	0.5099	0.0932	0.5383	0.3685	0.5074	0.1979	0.6642	0.3682	0.554	0.0992
Ga	5.12	9.73	27.18	28.53	28.35	2.57	19.53	13.43	12.19	9.7
Gd	1.938	0.1	2.134	1.387	2.116	0.889	2.34	1.5	2.133	0.651
Hf	0.83	0.14	2.13	1.76	1.39	0.34	2.25	0.46	1.17	0.28
Ho	0.3694	0.0223	0.4186	0.2914	0.4333	0.1816	0.4363	0.2339	0.4339	0.2388
La	3.5	1.8	6.1	4.1	4.6	1.6	7.4	11.1	17.1	1
Li	8.5	10.7	10.7	7.5	9.7	5	8.2	0.6	0.6	0.8
Lu	0.143	0.021	0.157	0.125	0.164	0.073	0.174	0.066	0.172	0.171
Mo	0.54	0.3	0.5	0.3	0.51	0.22	0.4	0.4	0.69	0.17
Nb	0.314	0.048	0.914	0.618	0.461	0.151	1.573	1.154	2.07	0.336
Nd	6.68	0.77	8.07	5.42	8.18	3.09	10.76	8.62	14.18	1.67
Ni	2413.9	878.5	881.4	804.5	627.9	1636.6	1155.4	101.9	239.8	410.3
Pb	15.95	7.81	16.15	14.86	7.84	7.04	13.74	2.22	17.32	3.22
Pr	1.397	0.245	1.937	1.229	1.777	0.663	2.462	2.31	3.904	0.366
Rb	2.84	6.83	8.8	17.65	1.32	0.64	1.54	0.11	0.12	0.11
Sc	37.5	2.5	18	12.7	22	20.4	11.7	3.7	7.3	9.7
Sm	1.902	0.127	1.967	1.436	2.212	0.873	2.186	1.562	2.599	0.486
Sr	95.8	172.3	177.3	141.3	38	21.6	35.7	8	67.1	2.6
Ta	0.023	0.007	0.105	0.058	0.044	0.013	0.114	0.201	0.313	0.089
Tb	0.2978	0.02	0.3447	0.229	0.3295	0.1407	0.3861	0.1961	0.3516	0.1324
Th	0.235	0.07	0.92	0.499	0.381	0.121	0.979	4.935	3.592	1.777
Ti	1796	156	2873	2211	2588	891	2874	1103	2338	641
Tl	0.168	0.123	0.281	0.371	0.09	0.068	0.464	0.01	0.058	0.021
Tm	0.1462	0.013	0.1677	0.1313	0.165	0.0851	0.1805	0.0766	0.1974	0.1397
U	0.066	0.011	0.163	0.086	0.072	0.029	0.349	0.237	0.639	0.093
V	156.4	14	144.4	89.7	230.5	83.5	126	10.9	13	5.9
Y	10.73	0.65	11.93	9.23	11.76	5.39	14.13	5.99	13.06	7.48
Yb	0.978	0.111	1.101	0.81	1.099	0.513	1.265	0.418	1.168	1.019
Zn	112.9	76.3	178.8	299.6	256.8	104.5	142	85.6	1044.1	43
Zr	23	6	69	51	46	11	85	15	49	7